UNIVERSITY OF SOUTHAMPTON

Faculty of Social Sciences
School of Mathematical Sciences

Gravitational waves from timing irregularities of radio pulsars

by

Garvin Yim
ORCiD: 0000-0001-8548-9535

A thesis for the degree of
Doctor of Philosophy

February 2022

University of Southampton

Abstract

Faculty of Social Sciences
School of Mathematical Sciences

Doctor of Philosophy

Gravitational waves from timing irregularities of radio pulsars

by Garvin Yim

Radio pulsars are rotating neutron stars (NSs) identified by a periodic detection of radio emission with intervals of seconds to milliseconds. The periodicity of the emission is closely tied to the NS's spin frequency such that timing a pulsar allows its spin frequency to be accurately determined.

The spin frequency is generally predictable except for the case of two timing irregularities: glitches and timing noise. Both represent phenomena that occur on different time-scales with glitches affecting short-term evolution and timing noise affecting long-term evolution. Glitches are sudden increases in the spin frequency which is sometimes followed by a post-glitch recovery. Timing noise is the term used for the residuals left over after the predictable spin evolution is subtracted from observations.

There are existing models that can explain glitches, their recovery as well as timing noise, but in this thesis, we focus on creating two more, one for the post-glitch recovery and another for timing noise. The key aspect of these models is their connection to gravitational waves (GWs), which is an idea not well explored.

In the first part of this thesis, we create the "transient mountain" model which can explain post-glitch recoveries and make falsifiable predictions for the GWs that come off. This is based off the idea that a NS "mountain" would create an extra braking torque on the NS, hence, spinning it down during the post-glitch recovery.

For the second part of this thesis, we create a model for timing noise which we propose is caused by successive (micro)glitches which cause the NS to oscillate. These glitches excite the f-modes on the NS which are known to emit GWs. In modelling these two types of timing irregularities, we hope to strengthen the bridge between theory, radio observations and GW observations.

Contents

List of Figures

List of Tables

Declaration of Authorship

I declare that this thesis and the work presented in it is my own and has been generated by me as the result of my own original research.

I confirm that:

1. This work was done wholly or mainly while in candidature for a research degree at this University;
2. Where any part of this thesis has previously been submitted for a degree or any other qualification at this University or any other institution, this has been clearly stated;
3. Where I have consulted the published work of others, this is always clearly attributed;
4. Where I have quoted from the work of others, the source is always given. With the exception of such quotations, this thesis is entirely my own work;
5. I have acknowledged all main sources of help;
6. Where the thesis is based on work done by myself jointly with others, I have made clear exactly what was done by others and what I have contributed myself;
7. Parts of this work have been published as:

   Yim, G. and Jones, D. I. (2020). Transient gravitational waves from pulsar post-glitch recoveries. *Monthly Notices of the Royal Astronomical Society*.

   Yim, G. and Jones, D. I. (2022). Gravitational radiation back-reaction from f-modes on neutron stars. *Monthly Notices of the Royal Astronomical Society*.

Signed:..... Date:.....

Acknowledgements

First of all, I would like to say a huge thank you to my supervisor, Ian Jones, for his guidance, wisdom and never-ending patience. His kind quality meant I was always at ease when asking questions, no matter how trivial they may have been, and his responses were always given with incredible clarity and thought. I have learnt a lot from him and I will treasure his guidance forever. For that, I am eternally grateful.

I would also like to take this chance to thank Nils Andersson, who often brought a smile to my face during our stimulating group meetings with his entertaining (yet valuable) comments. I looked forward to these meetings every week. He certainly enhanced my PhD experience and I am grateful to have been a part of his group.

There is also Emma, Alex, Patrick, Olly and Tom of Room 2019. Thank you all for the moral support and for accompanying me whenever I needed my coffee fix. As well as the times in the office, I also enjoyed the times out of the office, whether it was at Stags, the snooker hall, the badminton courts or the climbing wall. If I ever needed help, I always knew they were just a chair swivel away.

I would also like to give a special thanks to my dearest, Yasmin, who has been close by my side through all the ups and downs. She is truly very special to me and her unwavering belief gave me great encouragement throughout my PhD. I am incredibly grateful to have her in my life.

To my late porpor (grandma), thank you for all the loving care that you gave me. Although she never fully understood what I did, she always gleamed with happiness whenever there was a success, no matter how big or small, and this drove me to be where I am today.

Lastly, I would like to thank my parents, Angela and Ben, for supporting me in a whole manner of ways. They showed their love in subtle ways, like in the food they cooked or the little jobs they did around the house, and this made my life a little easier. This did not go unnoticed and it is because of their acts of love have I been able to get this far. Thank you for all that you have done.

Chapter 1

Introduction

1.1 A history and overview of neutron stars

The idea of neutron stars (NSs) were first proposed by Baade and Zwicky (1934), just two years after the discovery of the neutron by Chadwick (1932). In their paper, Baade and Zwicky said

> *"With all reserve we advance the view that a super-nova represents the transition of an ordinary star into a neutron star, consisting mainly of neutrons. Such a star may possess a very small radius and an extremely high density."*
>
> - Baade & Zwicky, 1934.

It seemed like the scientific community did not appreciate Baade and Zwicky's findings until the unexpected discovery of the first pulsar by PhD student and supervisor pair, Bell and Hewish, in 1967 (Hewish et al., 1968). What they had intended to find were distant quasars which were affected by scintillation in the radio band. Instead, a repeating radio source with a period of 1.337 s was discovered which was unlike the characteristic scintillations they had previously observed. The short period suggested the source was a compact object. This was seen by comparing the period to the light-crossing time across the theoretical object and realising that radio photons travelling across the object must not surpass the speed of light. As a result, they concluded the repeating radio source was caused by vibrational modes of either a NS or a white dwarf.

Unbeknown to Bell and Hewish, Pacini (1967) had created a model of how a rotating NS with a strong dipolar magnetic field could power a supernova remnant, just 3 months before the pulsar discovery paper. Independent of Pacini, Gold (1968) had written a theory suggesting that a radio pulsar was in fact a rotating NS (even though at the time they were essentially in adjacent offices). The theory consisted of radio photons being emitted from a jet above the magnetic poles of the NS. The magnetic axis was

inclined to the rotation axis such that when the NS rotated and the jet passed across the observer's line of sight, a pulse of radio waves would be detected. This was the first time that someone had made the connection between a NS and a pulsar and in hindsight, proved to be critical in understanding pulsars.

Both the vibrational mode theory and the rotating NS theory were plausible explanations of the repeating radio source at the time and so further observations were needed to distinguish which was correct. Most scientists preferred the idea of white dwarfs being the source as they were well understood at the time, whereas the existence of NSs was purely hypothetical and so was mainly accepted by just theorists. It was in late 1968 that the Vela pulsar (Large et al., 1968) and the Crab pulsar (Staelin and Reifenstein, 1968) were discovered, having periods of 89 ms and 33 ms respectively. To have such short periods eliminated any theories built around white dwarfs so as a result, NS theories were favoured. However, there was still the problem of distinguishing whether it was a vibrating NS or a rotating NS. Pacini (now collaborating with Gold) realised their rotating NS model predicted the frequency of radio pulses should decrease over time whereas there would be no decrease in frequency for the vibrational mode model (Pacini, 1968). Soon enough, there were indeed observations of the Crab pulsar slowing down by 36.48 ns per day (Richards and Comella, 1969) which then gave strong evidence in support of the rotating NS model.

To this day, we still use the rotating NS model to explain radio pulsars and it has been successful enough to predict when the next pulse will arrive with great accuracy (in the absence of glitches, see Section 2.2). There are also many back-of-the-envelope calculations one could perform to estimate the minimum period (P), minimum mean density ($\bar{\rho}$) and maximum radius (R) of a NS. The derivation of these properties begin with enforcing the radial gravitational acceleration of the NS to be greater than the centripetal acceleration required to keep the NS bound

$$\Omega^2 R < \frac{GM}{R^2} \tag{1.1}$$

where Ω is the NS's angular frequency, G is Newton's gravitational constant and M is the mass of the NS. Then, we substitute $\Omega = \frac{2\pi}{P}$ and assume that the NS is perfectly spherical and uniformly-dense such that $\bar{\rho} = \frac{3M}{4\pi R^3}$. We can then derive the minimum period (or maximum frequency if we invert) a pulsar can have before the NS's gravitational force can no longer hold itself together

$$P > \sqrt{\frac{3\pi}{G\bar{\rho}}}\,. \tag{1.2}$$

If we were to observe a certain period, then we could rearrange Equation (1.2) to find the implied minimum mean density as being

$$\bar{\rho} > \frac{3\pi}{GP^2} \,. \tag{1.3}$$

Note that this is a rather conservative lower limit for the minimum mean density because in reality the NS will oblate in shape due to its fast rotation. Also, due to the complex nature of the interior of NSs, the density is far greater than what is calculated in this simple calculation. Nevertheless, for a more oblate NS, matter on the equator will be further from the rotation axis meaning the gravitational acceleration would be weaker but the centripetal acceleration must be greater to keep that matter bound. Taking this effect into account makes the right hand side of Equation (1.3) more positive, hence, a conservative lower limit. For the first pulsar discovered, $P = 1.337$ s making the minimum mean density equal 7.9×10^{10} kg m^{-3} (or 7.9×10^{7} g cm^{-3} in CGS units). This certainly agrees with Baade and Zwicky's predictions about a NS having high density (c.f. the densest metal on Earth, osmium, which has a density of 2.259×10^{4} kg m^{-3}).

Finally, to get the maximum radius, we need to make an assumption about the mass. We know that white dwarfs are supported by electron degeneracy pressure which prevents the white dwarf from collapsing under its own gravity. The electron degeneracy pressure is a result of the Pauli exclusion principle where no two identical fermions (such as electrons) are allowed to be in the same quantum state. There becomes a certain mass, known as the Chandrasekhar limit, whereby the electron-degeneracy pressure can no longer withstand the gravitational pressure and causes the white dwarf to collapse into a NS, where now, neutron degeneracy pressure prevents any further collapse. The Chandrasekhar limit is about 1.4 $M_\odot$. Assuming the mass is kept the same throughout the collapse (meaning no mass has been ejected or converted into radiative energy), then it is justified to say that the mass of the newly formed NS will be around 1.4 $M_\odot$ (Shapiro and Teukolsky, 1983). From more detailed calculations, the mass is theorised to be between 1 $M_\odot$ and 3 $M_\odot$ (Özel and Freire, 2016). From the observational side, the most massive NS observed so far has a mass of $(2.08^{+0.07}_{-0.07})$ $M_\odot$ (Cromartie et al., 2020; Fonseca et al., 2021; Riley et al., 2021; Miller et al., 2021). This type of collapse whereby a white dwarf accretes matter from a binary counterpart until it passes the Chandrasekhar limit is known as a Type Ia supernova. Using this information along with Equation (1.1), we deduce the back-of-the-envelope maximum radius of a NS which is

$$R < \left(\frac{GMP^2}{4\pi^2}\right)^{\frac{1}{3}} \tag{1.4}$$

which for a pulsar having a period of $P = 1.337$ s yields a maximum radius of 2030 km. This is still large relative to our current estimate of the NS radii of being around 10 km, but at least it eliminates the chance of the source being a white dwarf which typically

have radii of 7000 km. The difference between 2030 km and 10 km is not an issue as Equation (1.4) refers to the maximum radius a NS of period $P = 1.337$ s can have. To find the most general maximum radius, we should use the smallest period which belongs to a pulsar of frequency 716 Hz corresponding to a period of $P = 1.4 \times 10^{-3}$ s (Hessels et al., 2006). Equation (1.4) then leads to the maximum radius being 21 km. This gives further support of Baade and Zwicky's prediction that a NS's radius is small. Realistically, NSs are not uniformly-dense and have an equation of state (EOS) which tells us how the pressure varies with the mass density (or energy density) within the NS. Including the EOS into the calculation brings the maximum radius down to $10 - 15$ km depending on which EOS you use (Özel and Freire, 2016). Along with the typical value of the mass (1.4 $M_\odot$), a typical moment of inertia, I, can be calculated too assuming the NS is a solid, uniform sphere, $I = \frac{2}{5}MR^2 \approx 10^{38}$ kg m^2 $= 10^{45}$ g cm^2. This large moment of inertia is what is responsible for a NS to spin with little deviation over long periods except in the case of catastrophic events such as a glitches as we will learn about in Section 2.2.

The other known channel to create a NS is through a Type II supernova whereby a main sequence star of mass between $8.5^{+1}_{-1.5}$ $M_\odot$ and $16.5^{+1.5}_{-1.5}$ $M_\odot$ undergoes core-collapse (Smartt, 2009). When a main sequence star of radius $\sim 10^6$ km collapses into a NS of radius 10 km, there are two developments which occur. The moment of inertia decreases (since $I \propto R^2$) and from the conservation of angular momentum, the angular frequency must therefore increase. This is the first development and there is strong evidence to support this as there are observations of NSs with frequencies between 0.043 Hz (Tan et al., 2018) to 716 Hz (Hessels et al., 2006) which are considerably higher than the rotational frequencies of main sequence stars. The upper and lower frequencies were sourced from the ATNF Pulsar Catalogue which is a complete catalogue of all known pulsars and it is regularly updated (Manchester et al., 2005).

The second development arises from the conservation of magnetic flux, $\Phi_B = \int \mathbf{B} \cdot d\mathbf{S}$, where $\mathbf{B}$ is the magnetic field flux density (or simply magnetic field) and $\mathbf{S}$ is the vector surface area. Since the radius is decreasing by a factor of 10^5, the area decreases by a factor of 10^{10} meaning the magnetic field strength increases by a factor of 10^{10}. For a typical main sequence star, the magnetic field stength is $\sim 10^2$ G (1 G $= 10^{-4}$ T) so for the resultant NS, the magnetic field would be $\sim 10^{12}$ G. Typically, isolated NSs have magnetic fields between 10^{10} G and 10^{13} G. There are objects known as magnetars which are thought to be very similar to NSs with the exception that their magnetic field is 10^{14} G to 10^{15} G. Due to this high magnetic field, rather than being rotationally-powered (see Section 2.1.2), these magnetars are powered from the decay of its magnetic field. See Kaspi and Beloborodov (2017) for a recent review of magnetars.

1.2 Motivation and aims of the project

The motivation of this PhD project is to attempt to find the cause of the widespread, and often not well understood, timing irregularities seen in radio pulsar astronomy. This means trying to understand more about glitches and timing noise, both of which are discussed in Sections 2.2 and 2.3. In particular, there has been little theoretical modelling of how timing noise arises and so we make an attempt to do so in the latter part of this thesis.

Another topical event which motivates our work is the recent detection of gravitational waves (GWs) and electromagnetic emission from the binary NS merger, GW170817 (Abbott et al., 2017b). This opened up a whole new field of physics known as multi-messenger astronomy. Multi-messenger astronomy unites our attempts in understanding a system by looking at it both electromagnetically and gravitationally via GWs (and also through cosmic rays and neutrino observations). With upcoming electromagnetic telescopes/satellites (e.g. SKA, eXTP) and new GW detectors (e.g. KAGRA, aLIGO India, DECIGO, LISA, Einstein Telescope, Cosmic Explorer), there will certainly be more synergy between the different disciplines which makes it an interesting field to be in.

The models we create delve into the field of multi-messenger astronomy and in doing so, we aim to explain glitch recoveries and timing noise in radio data but also have testable predictions for GW data. Specifically, we create the "transient mountain" model to explain glitch recoveries and we model timing noise as lots of unresolved glitches with each glitch triggering short-lived f-mode oscillations on the NS.

This thesis is split up into three main parts. Chapters 2 - 4 go over relevant and established ideas from radio astronomy, GW astronomy and fluid dynamics respectively. Chapter 5 discusses the project on glitch recoveries and how they can be explained with glitch-induced transient mountains, which resulted in a published paper (Yim and Jones, 2020). Chapters 6 and 7 are spin-offs from Chapter 5, where we apply the transient mountain model to more scenarios as well as consider the energetics involved.

This leads nicely onto the other project which is about NS oscillations and starts from Chapter 8 onwards. In that chapter, we look at oscillations on non-rotating, incompressible, uniformly-dense NSs. This leads to the first analytic calculation of the gravitational radiation reaction from non-axisymmetric f-modes, with both energy and angular momentum conservation consistently accounted for. In doing so, one finds that GW emission from a prograde (retrograde) mode causes the NS to rotate in the retrograde (prograde) direction, something we term the "GW back-reaction".

Connected to this is Chapter 9, where we explore how NS oscillations could explain small glitch-like features that have previously been observed, which ultimately could be the cause for timing noise. Finally, Chapter 10 summarises the main findings presented in this thesis.

Chapter 2

Radio astronomy overview

2.1 Overview of pulsars and pulsar timing

2.1.1 Why radio?

First of all, we should establish the type of pulsars were are interested in. Pulsars can either be in a binary system or they could be isolated. For now, it makes sense to focus on the simpler case of isolated pulsars which we call "NSs" most of the time.

Isolated NSs can be seen in the radio, γ-ray and even the ultraviolet, optical and infrared (UVOIR) parts of the electromagnetic spectrum (Mignani, 2011). NSs in binaries also have X-ray emission given the companion is near enough for the NS to accrete matter. The problem with observing with UVOIR frequencies is that there is only a small population of isolated NSs that exhibit UVOIR emission. What is even more important is we wish to see both short and long-term timing phenomena (relating to glitches and timing noise respectively) but UVOIR observations either have an observational cadence not great enough to see any short-term phenomena, or have observations with long integration times (of a few days) but are infrequent meaning we do not see phenomena which have durations longer than a few days. In essence, we do not have a large enough volume of UVOIR data for it to be useful for our needs. We cannot use γ-ray data for the same reason but the cause is slightly different. This is due to current γ-ray detectors not being sensitive enough to have large counts of γ-ray photons to make statistically significant conclusions. As γ-ray detectors become more sensitive and greater in number, we could eventually use them to study the timing of isolated NSs. What remains are radio observations which have been operating since the discovery of the first pulsar and can provide us with effectively real-time data with daily observations of certain pulsars. There are over 3000 radio pulsars[1] and many of them have been tracked long enough that timing noise can be seen (Hobbs et al., 2010;

[1] Value taken from the ATNF Pulsar Catalogue (Manchester et al., 2005).

Parthasarathy et al., 2019; Lower et al., 2020). Similarly, over 190 radio pulsars[2] have been seen to glitch so overall, there is a large volume and rich phenomena to work with in the radio.

2.1.2 Magnetic dipole radiation

To understand pulsar timing, we take a closer look at the long-term (secular) spin evolution of a NS. It was mentioned in Section 1.1 that the Crab pulsar was seen to slow down (spin-down) over time and that Gold and Pacini had predicted this was because of magnetic dipole radiation. We show in Figure 2.1 what such a NS would look like for a magnetic dipole inclined to the rotational axis by an angle α.

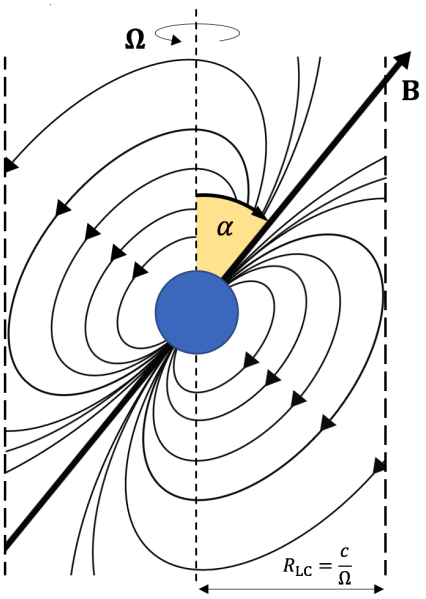

FIGURE 2.1: A diagram showing the dipolar nature of the magnetic field around a NS. The magnetic axis (**B**) is inclined to the rotation axis (**Ω**) by angle α. The light-cylinder radius (R_{LC}) is marked on the diagram and it is the radius from the rotation axis where the furthest part of the magnetosphere co-rotates with the NS at the speed of light. By that definition, it is also where the last closed magnetic field line is tangent to the light-cylinder.

The power radiated from an oscillating magnetic dipole is a standard calculation and can be found in Griffiths (2013), for example. However, if the magnetic dipole is rotating instead of oscillating, then the power output is twice that of the oscillating case. In SI units, the rotating magnetic dipole radiation power is

$$P_{\text{mag.dip.}} = \frac{\mu_0 |\ddot{\mathbf{m}}|^2 \sin^2 \alpha}{6\pi c^3} \tag{2.1}$$

[2]Value taken from the JBCA Glitch Catalogue (Espinoza et al., 2011).

where μ_0 is the permeability of free space and $\ddot{\mathbf{m}}$ is the second time-derivative of the magnetic dipole moment, $\mathbf{m}$. The rotating magnetic field has a magnetic dipole moment of $\mathbf{m} = \mathbf{m}_0 e^{-i\Omega t}$ where $\mathbf{m}_0$ is the magnetic dipole moment at some arbitrary time which rotates around at angular frequency, Ω.

Carrying out the time-derivatives and squaring, we find a Ω^4 dependence for $P_{\text{mag.dip.}}$

$$P_{\text{mag.dip.}} = \frac{\mu_0 |\mathbf{m}_0|^2 \Omega^4 \sin^2 \alpha}{6\pi c^3} \,. \tag{2.2}$$

We can convert the magnetic dipole moment into the magnetic field strength which is of more physical interest. In a spherical coordinates, the magnetic field of a dipole is

$$\mathbf{B}_{\text{dip}} = \frac{\mu_0 |\mathbf{m}_0|}{4\pi r^3} \left[2\cos\theta \hat{\boldsymbol{r}} + \sin\theta \hat{\boldsymbol{\theta}} \right] \,, \tag{2.3}$$

which, at the magnetic poles of the NS ($\theta = 0$) and on the surface ($r = R$), we find the polar magnetic field strength is

$$B_{\text{p}} = \frac{\mu_0 |\mathbf{m}_0|}{2\pi R^3} \,. \tag{2.4}$$

We rearrange Equation (2.4) for $|\mathbf{m}_0|$ and substitute into Equation (2.2) to get the magnetic dipole radiation power in terms of the polar magnetic field which is

$$P_{\text{mag.dip.}} = \frac{2\pi R^6 B_{\text{p}}^2 \sin^2 \alpha}{3\mu_0 c^3} \Omega^4 \,. \tag{2.5}$$

From the conservation of energy, we know that this emitted energy must take energy away from the NS. The most natural form of energy to reduce would be the NS's rotational kinetic energy, E_{rot}, which would explain why the NS spins-down. The rate at which rotational kinetic energy changes is

$$\frac{dE_{\text{rot}}}{dt} = \frac{d}{dt}\left(\frac{1}{2} I \Omega^2 \right) = I \Omega \dot{\Omega} \,. \tag{2.6}$$

We can equate the radiated power to the rate of loss of rotational kinetic energy to get

$$\begin{aligned} P_{\text{mag.dip.}} &= -\frac{dE_{\text{rot}}}{dt} \\ \frac{2\pi R^6 B_{\text{p}}^2 \sin^2 \alpha}{3\mu_0 c^3} \Omega^4 &= -I \Omega \dot{\Omega} \\ \rightarrow \dot{\Omega} &= -\frac{2\pi R^6 B_{\text{p}}^2 \sin^2 \alpha}{3\mu_0 c^3 I} \Omega^3 \,. \end{aligned} \tag{2.7}$$

We see the right hand side of Equation (2.7) is always negative so magnetic dipole radiation always spins the NS down. In addition, Equation (2.7) says a faster spinning NS will have a larger spin-down rate. Whilst we have Equation (2.7) handy, we can rearrange to find the magnetic field strength as a function of the period $P = \frac{2\pi}{\Omega}$ and its

derivative, $\dot{P} = -\frac{2\pi\dot{\Omega}}{\Omega^2}$, giving

$$B_{\rm p} = \sqrt{\frac{3\mu_0 c^3 I}{8\pi^3 R^6 \sin^2\alpha} P\dot{P}}\,. \tag{2.8}$$

If we substitute typical values of $I = 10^{38}$ kg m^2 and $R = 10^4$ m, we get

$$\begin{aligned} B_{\rm p} &= 6.4\times10^{15}\sqrt{\frac{P\dot{P}}{\sin^2\alpha}} \quad \text{[Tesla]} \\ B_{\rm p} &= 6.4\times10^{19}\sqrt{\frac{P\dot{P}}{\sin^2\alpha}} \quad \text{[Gauss]} \\ B_{\rm p} &> 6.4\times10^{19}\sqrt{P\dot{P}} \quad \text{[Gauss]} \end{aligned} \tag{2.9}$$

since $0 < \sin^2\alpha < 1$. For the Crab pulsar, $P = 0.0334$ s and $\dot{P} = 4.21\times10^{-13}$ s s^{-1} so the minimum polar magnetic field strength is $B_{\rm p,\,min} = 7.6\times10^{12}$ G which agrees with our earlier order-of-magnitude prediction of a typical magnetic field in Section 1.1.

Motivated by Equation (2.7), we can define the braking index, n. In general, the relation between the angular frequency derivative and the angular frequency can be written as

$$\dot{\Omega} \propto -\Omega^n \tag{2.10}$$

Depending on what emission mechanisms are involved, the value of the braking index varies. For example, we have shown the braking index is $n = 3$ for magnetic dipole radiation and later in Section 5, we will see that $n = 5$ for non-axisymmetric rigid NSs emitting GWs. Another well-studied method of spin-down gives $n = 7$ due to unstable r-modes being driven by GW emission (Andersson, 1998; Lindblom et al., 1998; Owen et al., 1998).

Working from the other direction, one can often determine Ω, $\dot{\Omega}$ and $\ddot{\Omega}$ from pulsar timing observations and use them to calculate n. To see how, let us differentiate Equation (2.10) and rearrange to find

$$\begin{aligned} \ddot{\Omega} = -nk\Omega^{n-1}\dot{\Omega} = n(-k\Omega^n)\frac{\dot{\Omega}}{\Omega} = n\frac{\dot{\Omega}^2}{\Omega} \\ \rightarrow n = \frac{\Omega\ddot{\Omega}}{\dot{\Omega}^2} \end{aligned} \tag{2.11}$$

where k is a constant of proportionality. Typically, the majority of pulsars are observed to have $n \lesssim 3$ but, as we will see in Section 2.3, there can be large deviations from this due to timing noise. These deviations from $n = 3$ suggests that magnetic dipole radiation cannot be the only radiative mechanism affecting the spin evolution of pulsars if all else has been correctly been accounted for.

There is one final derived quantity which is commonly used when talking about pulsar timing and it is the characteristic age, τ_c. This is a rough estimate of the age of a pulsar under the assumption that all spin-down has been due to magnetic dipole radiation. Rearranging Equation (2.8), we find

$$P\dot{P} = \frac{8\pi^3 R^6 B_p^2 \sin^2\alpha}{3\mu_0 c^3 I} \,. \tag{2.12}$$

Assuming the magnetic field strength and angle between the magnetic and rotation axes do not change with time, we see that $P\dot{P}$ is constant which allows us to do the following

$$\begin{aligned} P\dot{P} &= P\frac{dP}{dt} \\ \int_0^{\tau_c} P\dot{P}dt &= \int_{P_0}^{P} P'dP' \\ P\dot{P}\int_0^{\tau_c} dt &= \frac{P^2 - P_0^2}{2} \\ \tau_c &= \frac{P^2 - P_0^2}{2P\dot{P}} \end{aligned} \tag{2.13}$$

where P_0 is the period of the NS when it is born. If $P \gg P_0$, which would be the case long after birth, then we can ignore the second term in Equation (2.13) to yield

$$\tau_c = \frac{P}{2\dot{P}} = -\frac{\Omega}{2\dot{\Omega}} \tag{2.14}$$

which is the definition of the characteristic age of a pulsar. This simple calculation describes observed pulsars fairly well. This is seen in Figure 2.2 in what is known as a P-$\dot{P}$ diagram, with a pulsar's period on the horizonal axis and period derivative on the vertical axis. The dashed lines with years stated at the base represent lines of constant characteristic ages. As pulsars age, we expect their characteristic age to increase so they move down the diagram. It appears that at a certain characteristic age, we stop observing pulsars. The implication of this might be because the they have "died". In fact, there is a zone at the bottom right of the diagram (shaded in yellow in Figure 2.2) which is known as the pulsar graveyard. The line which seperates the graveyard is calculated from the condition that living pulsars must have a strong enough magnetic field to create an electric potential difference strong enough to initiate pair production which eventually leads to radio emission. As a result, the "death line" is an key aspect in the understanding pulsar emission mechanisms and even the EOS of NSs (Harding et al., 2002).

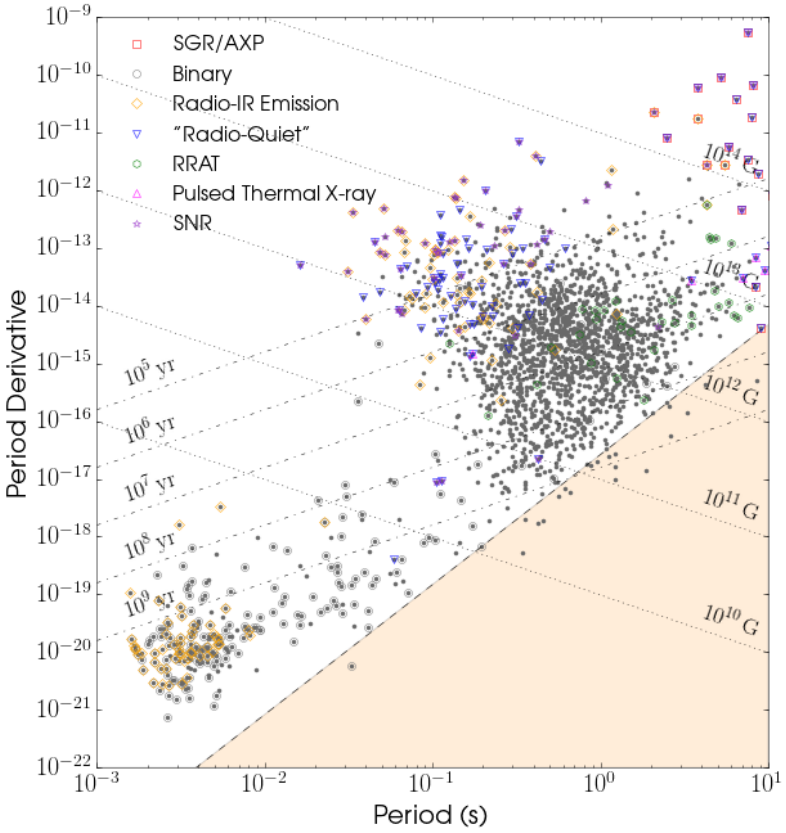

FIGURE 2.2: A P-$\dot{P}$ diagram where the period of a pulsar P and its derivative $\dot{P}$ are plotted on the axes. Each point represents a single pulsar and in the diagram, there are a total of 2636 pulsars. There are some special types of pulsars which have different icons but this thesis does not concern these. The legend in the top left states these types of pulsars. The shaded yellow region in the bottom right is known as the pulsar graveyard. The data was taken from the ATNF Pulsar Catalogue (Manchester et al., 2005). The diagram was created by an open-sourced Python module created by Pitkin (2018).

2.1.3 Pulsar timing

NSs have a large moment of inertia which is responsible for their stable rotation but over long durations, there is a secular deviation due to magnetic dipole radiation as shown in Section 2.1.2. This effect is not obvious when comparing consecutive radio pulses as the fractional deviation is minuscule and the time between each pulse is small. However, we see the effect more clearly when we look over longer time-scales (weeks to years) which is the idea behind pulsar timing.

There is always some reference date in pulsar timing known as the reference epoch. We need to be able to have a model of what the average radio pulse looks like at the reference epoch in order for future pulses to be compared to it. This allows us to compare some feature (say the peak of the pulse) to the reference to see what has changed. For

pulsar timing, we would be interested to know whether future pulses arrive earlier or later than expected.

When we measure radio emission from a pulsar, we measure the radio flux density as a function of time. Radio flux densities are measured conventionally in units of Janskys (Jy) where 1 Jy $= 10^{-26}$ W m^{-2} Hz^{-1}. Individual radio pulses generally arrive with flux densities of differing shapes which makes it difficult to find a stable reference point. To reduce this variability, an average of a set of pulses is taken. This creates what is known as a pulse profile which is incredibly stable for a given pulsar. Each pulse profile is unique so some call it the "fingerprint" of a pulsar. Figure 2.3 shows schematically the stages of converting raw data into a pulse profile.

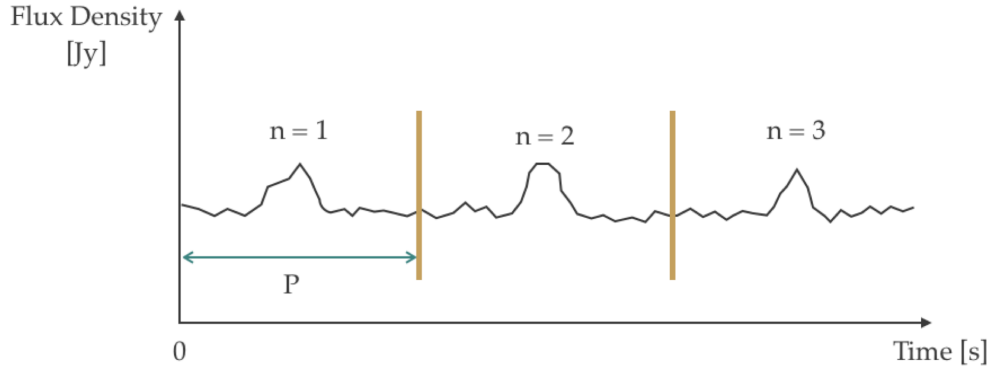

(A) An example of what radio pulsar data would look like from a radio telescope. It shows flux density as a function of time. Each pulse is seperated by one period, P, and each pulse is numbered with n.

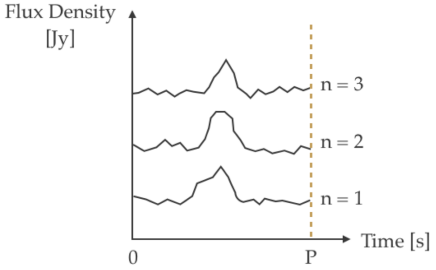

(B) This shows a pulse stack where each individual pulse is stacked on top of one another.

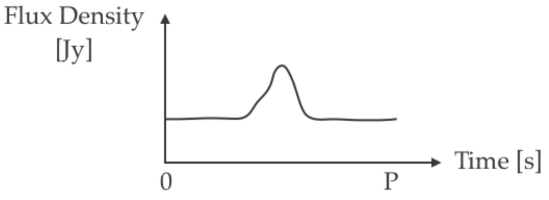

(C) When individual pulses are averaged, such as those in Subfigure 2.3B, the resultant averaged pulse is known as the pulse profile of a pulsar.

FIGURE 2.3: Subfigures (A), (B) and (C) show how to get from raw data to a pulse profile for a given pulsar. The graphs all show flux density as a function of time with each graph presenting the same data differently.

We now have a stable reference to compare any timing deviations from. Statistically, the best point to take as the reference is the sharpest peak on the pulse profile. Also, the more pulses we receive, the more accurate and precise the pulse profile reference point will be. This is one reason why, for precise timing, such as for gravitational wave detection in pulsar timing arrays (see Section 3.5), we use millisecond pulsars with sharp peaks in their pulse profiles.

Since all pulsars have different periods, it is useful to standardise the measurements so that we can make comparisons between pulsars. Since pulsars rotate 360° during each period, we can rescale one period as $1P = 360°$. We call this angle of rotation the pulse phase or longitude (ϕ) and by convention, the pulse phase of greatest flux density is set to have $\phi = 0$ and $t = 0$ (unlike Figure 2.3). The pulse phase also "wraps around" every 360° so that $\phi + 360° = \phi$.

All timing (and hence pulse phase) variations are measured with respect to a fixed reference point on the pulse profile. This reference point does not necessarily have to be the point of highest flux density or the sharpest peak, but could be any arbitrary point. Between pulses, the phase of this reference point changes by a small amount so the first few terms of a Taylor expansion is appropriate. It follows that the phase of the n'th pulse for the i'th integration (a dataset taken over time $\tau_{\text{int}}^{(i)}$, as in the integration time), $\phi_{(i)}(t^{(n)})$, about an arbitrary reference time, $t_0^{(i)}$, such as the start time of the integration, is given by

$$\phi_{(i)}(t^{(n)}) = \phi_{(i)}(t_0^{(i)}) + \frac{d\phi_{(i)}}{dt}(t^{(n)} - t_0^{(i)}) + \frac{1}{2!}\frac{d^2\phi_{(i)}}{dt^2}(t^{(n)} - t_0^{(i)})^2 + \frac{1}{3!}\frac{d^3\phi_{(i)}}{dt^3}(t^{(n)} - t_0^{(i)})^3 + \cdots \tag{2.15}$$

where $\frac{d\phi_{(i)}}{dt}$, $\frac{d^2\phi_{(i)}}{dt^2}$ and $\frac{d^3\phi_{(i)}}{dt^3}$ are parameters to be found numerically. The time $t^{(n)}$ falls in the range of $[t_0^{(i)}, t_0^{(i)} + \tau_{\text{int}}^{(i)}]$. The time $t_0^{(i)}$ is in the range $[0, \infty]$ and will be different for each integration. The notation is slightly subtle so it might help to take a look at Figure 2.4.

At this point, we should be clear that for a given integration, $\phi_{(i)}(t^{(n)})$ represents a discrete dataset since n consists of natural numbers going up to N which is the total number of pulses in one integration. $\phi_{(i)}$ in itself is another discrete set. This discrete set is caused by radio telescopes not always being able to observe the pulsar of interest meaning integrations can be unequally spaced. Above, we could have measured all times relative to one period such that $t^{(n)}$ and $t_0^{(i)}$ are both in the range $[0, P]$, but we see it is best for our understanding to keep it unchanged. In reality, we might want to use the latter method since it is best to keep numbers small whilst solving problems numerically.

We know the rate of change in pulse phase is equal to the angular frequency of the pulsar ($\frac{d\phi_{(i)}}{dt} = \Omega_{(i)}$) and so we write the following

$$\phi_{(i)}(t^{(n)}) \approx \phi_{(i)}(t_0^{(i)}) + \Omega_{(i)}(t^{(n)} - t_0^{(i)}) + \frac{1}{2}\dot{\Omega}_{(i)}(t^{(n)} - t_0^{(i)})^2 + \frac{1}{6}\ddot{\Omega}_{(i)}(t^{(n)} - t_0^{(i)})^3 \tag{2.16}$$

where $\Omega_{(i)}$ is the angular frequency determined from the i'th integration. Equation (2.16) captures exactly what we want to describe. Say a pulsar does not spin-down, we expect $t^{(n)} = t_0^{(i)} + (n-1)P$ since pulses would come at regular intervals. This means

on the left hand side of Equation (2.16) we have $\phi_{(i)}(t_0^{(i)} + (n-1)P) = \phi_{(i)}(t_0^{(i)})$ where the equality is because the pulse phase repeats every period by definition. Also, $\Omega_{(i)}$ is constant here ($\Omega_{(i)} = \frac{2\pi}{P}$) so together with the periodic property of $\phi_{(i)}$, the $\Omega_{(i)}$ term has zero contribution. If the left hand side of Equation (2.16) equals $\phi_{(i)}(t_0^{(i)})$, then the only solution to satisfy the right hand side of Equation (2.16) is if the terms with $\dot{\Omega}_{(i)}$ and $\ddot{\Omega}_{(i)}$ (and higher order terms) sum to zero. The trivial solution would be $\dot{\Omega}_{(i)} = 0$ which means no observed spin-down, recovering the information we put in.

We know pulsars are dynamic systems which evolve at different time-scales so as a result, if we obtain values of $\Omega_{(i)}$, $\dot{\Omega}_{(i)}$ and $\ddot{\Omega}_{(i)}$ at a later time, we would find the results vary noticeably. However, these secular changes are sufficiently small which again allows us to use a Taylor expansion about an arbitrary time. For these secular changes, the arbitrary time will be a reference epoch as mentioned earlier, but for simplicity, one can think of it as when the pulsar was first observed, t_{epoch}, which leads to

$$\phi(t_{\text{TOA}}^{(i)}) \approx \phi(t_{\text{epoch}}) + \Omega(t_{\text{TOA}}^{(i)} - t_{\text{epoch}}) + \frac{1}{2}\dot{\Omega}(t_{\text{TOA}}^{(i)} - t_{\text{epoch}})^2 + \frac{1}{6}\ddot{\Omega}(t_{\text{TOA}}^{(i)} - t_{\text{epoch}})^3 \tag{2.17}$$

where

$$\phi(t_{\text{TOA}}^{(i)}) = \frac{1}{N}\sum_{n=1}^{N} \phi_{(i)}(t^{(n)}) \tag{2.18}$$

$$t_{\text{TOA}}^{(i)} = t_0^{(i)} + \frac{1}{N}\sum_{n=1}^{N} t^{(n)} \,. \tag{2.19}$$

In other words, the phase $\phi(t_{\text{TOA}}^{(i)})$ is the average of the individual pulse phases of a given integration and contributes to one datapoint on a graph of ϕ as a function of t. The time corresponding to this datapoint is at $t_{\text{TOA}}^{(i)}$ and is called the time of arrival (TOA). The spacing between the TOAs need not be the same which is why we compare to the reference epoch t_{epoch} and this comes back to radio telescopes not being able to observe at every possible moment in time. The spacing between TOAs are usually on order of a few days, whereas the spacing between $t^{(n)}$ is on order of a period. Figure 2.4 shows the graphical representation of the all the quantities described in this calculation.

Similar to fitting Equation (2.16) to timing data from one integration, we can fit Equation (2.17) to TOA data to determine Ω, $\dot{\Omega}$ and $\ddot{\Omega}$ which ultimately is the objective of pulsar timing. It is these parameters which allow us to test our understanding of pulsars and they are the values we use to determine the braking index (Equation (2.11)).

We have gone from observations to deriving quantities of Ω, $\dot{\Omega}$ and $\ddot{\Omega}$, but we can work from the opposite direction and propose Ω, $\dot{\Omega}$ and $\ddot{\Omega}$ to determine what we expect to observe. When we set values of Ω, $\dot{\Omega}$ and $\ddot{\Omega}$, the resultant phase model (Equation (2.17)) is known as a timing model. Not only are Ω, $\dot{\Omega}$ and $\ddot{\Omega}$ included in the timing model but there are many different parameters which we need to include. There are

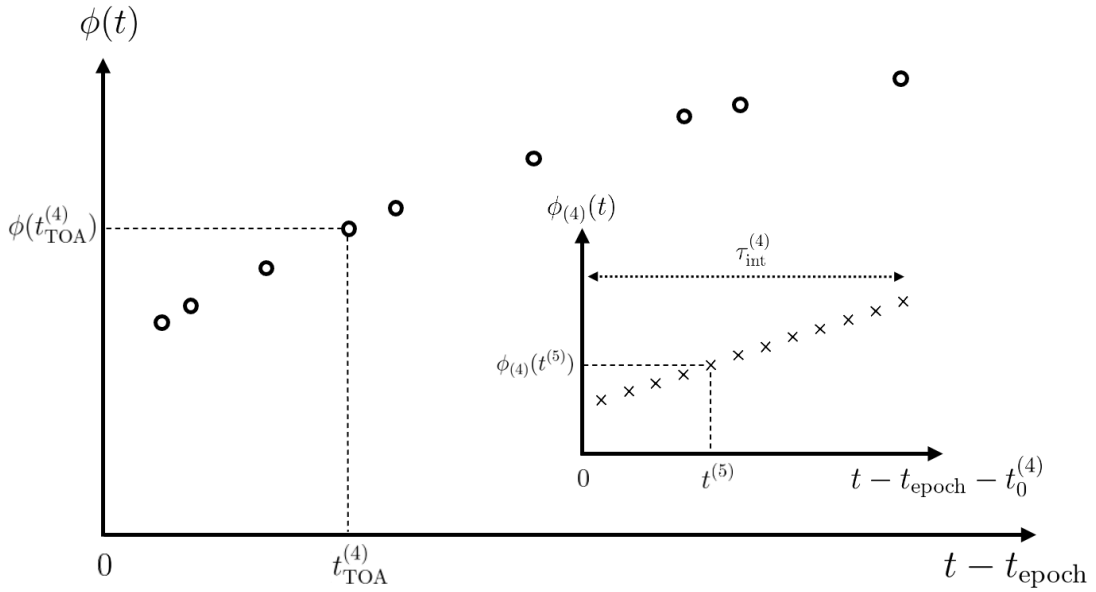

FIGURE 2.4: A diagram pictorially showing the graphical interpretations of the terms introduced in Equations (2.15) - (2.19). The larger graph displays a pulsar's phase as a function of time. The same applies to the smaller graph in the top right except the time-scale is much smaller. Each open circle in the larger graph represents a single TOA and each cross in the smaller graph represents an individual pulse. Identified here is the fourth TOA and the corresponding integration for that TOA is displayed in the smaller graph. The fifth pulse in the integration has been identified and the associated notation labelled. If a numerical fit were to be applied to the smaller graph, it would yield values of $\Omega_{(4)}$, $\dot{\Omega}_{(4)}$ and $\ddot{\Omega}_{(4)}$ whereas a numerical fit to the larger graph produces Ω, $\dot{\Omega}$ and $\ddot{\Omega}$.

parameters such as the sky location, proper motion (transverse velocity), dispersion measure (essentially the distance) and its derivative (essentially the radial velocity). There are also relativistic effects such as the Einstein delay and Shapiro decay as well as a classical effect known as the Rømer delay which requires us to correctly model the Earth's motion around the Sun. For that reason, all incoming timing observations are always taken relative to the Solar System's barycentre. This standardises the observations to allow for meaningful and easy comparisons between studies. A small deviation from true astrometric or dispersive parameters could lead to systematic errors in the timing model's results which normally would be seen as characteristic signatures in the residuals.

So, we need to define what is meant by a residual. It is simply the observed phase minus the predicted phase from our timing model. If the timing model provides an exact description, the residuals would equal zero resembling a flat line on a residual-time graph. However, observations are generally not well-described with the simple theoretical work developed in previous sections. Each pulsar is very different and so the residuals we observe do not give us zeroes, even with our best values for timing parameters. Not only could the emission process be different in different pulsars, but there are also temporal variations too which we need to consider. The next section

describes short time-scaled events known as glitches and the section after that is on timing noise which is a long time-scale phenomenon.

2.2 Glitches

2.2.1 Introduction

Glitches are sudden events where a pulsar will rapidly spin-up and increase its angular frequency by $\frac{\Delta\Omega}{\Omega} = 10^{-12} - 10^{-5}$ (Espinoza et al., 2011). The event was first seen in the Vela pulsar in a glitch of size $\frac{\Delta\Omega}{\Omega} = 2 \times 10^{-6}$ reported in back-to-back papers in 1969 (Radhakrishnan and Manchester, 1969; Reichley and Downs, 1969). As of today, there are 581 glitches from 191 different pulsars[3] meaning this phenomenon affects roughly 6% of the known pulsar population. Typically, a pulsar's glitch size distribution follows a power law (with different pulsars having different power indices) and waiting times between glitches are exponentially distributed (Melatos et al., 2008; Fuentes et al., 2019). There are however some exceptions which include the Vela pulsar, J0537-6910 and J1341-6220 where glitches occur quasi-periodically (Melatos et al., 2008; Howitt et al., 2018; Fuentes et al., 2019). These population studies should be taken lightly as only a few tens of glitches have been observed for even the most frequent glitchers.

For glitches in young (small τ_c) pulsars, after increasing in angular frequency, there is normally an exponential recovery back to, but never quite reaching, the pre-glitch angular frequency in a time-scale of a few tens of days, whereas for older pulsars, there is not normally this exponential recovery (Shemar and Lyne, 1996). Sometimes, there is a permanent change to the spin-down rate too which accompanies the glitch (e.g. Lyne et al., 2000). Graphs of Ω and $\dot{\Omega}$ and their residuals as functions of time are shown in Figure 2.5 to show what a typical glitch looks like.

The above is the description for typical glitches though in general, the field is widely diverse and has a rich phenomenology. An instance of this is seen in the Crab pulsar, thought to be created in 1054 AD. It had 3 large glitches which all showed an extra resolved spin-up typically a day after the main spin-up (Lyne et al., 2015; Shaw et al., 2018). The first 2 of these 3 large glitches and another large glitch in 2004 showed a standard exponential recovery but then the frequency exponentially increased asymptotically such that at long times (about a year), there was a permanent frequency increase relative to the pre-glitch value which was much larger than the permanent offset often found in smaller glitches (Lyne et al., 2015). The last of the 3 large glitches was only recently discovered and is the largest Crab glitch ever detected. Due to how recent this observation was, we still need to wait to confirm whether it will have the exponential permanent increase in frequency like the other large glitches (Shaw et al.,

[3] Value taken from the JBCA Glitch Catalogue Espinoza et al. (2011).

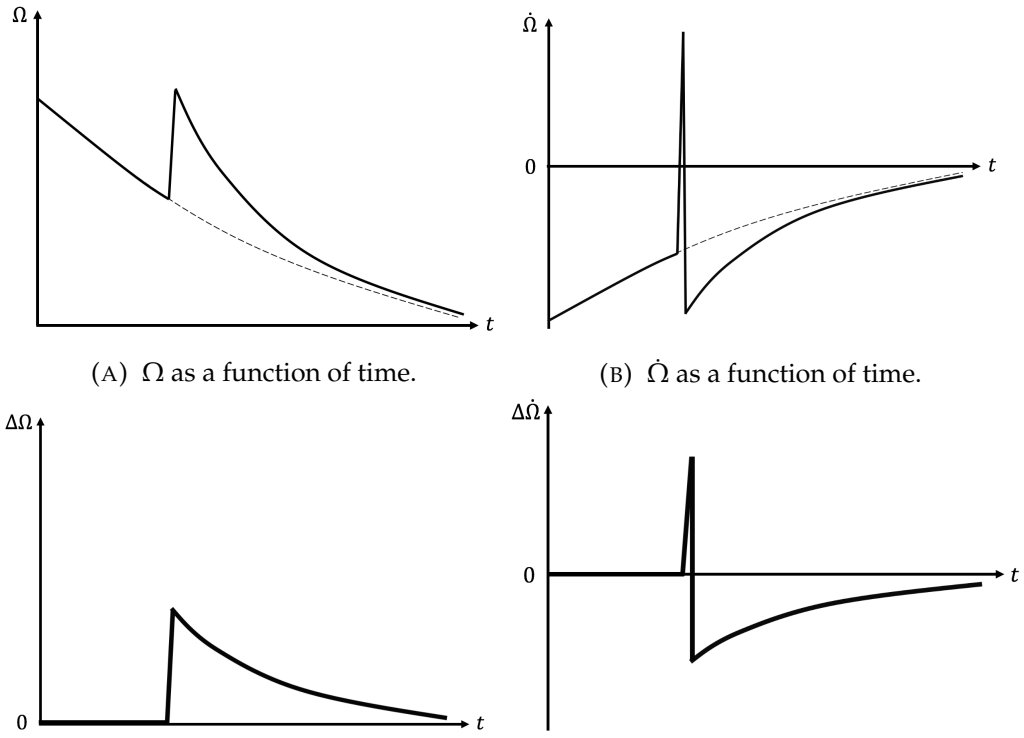

(A) Ω as a function of time.

(B) $\dot{\Omega}$ as a function of time.

(C) Residual Ω as a function of time.

(D) Residual $\dot{\Omega}$ as a function of time.

FIGURE 2.5: The subfigures above show what a glitch would look like in that respective graph. For Subfigures (A) and (B), the dashed lines represent the the secular spin-down of the NS. The solid line shows what would be observed if there were a glitch. In the above examples, the permanent change in spin-down rate is set to zero.

2018). Though there have been attempts (e.g. Gügercinoğlu and Alpar, 2019), features like these are still not well understood and so there are many possibilities for research.

There is a lot of timing research based around the Crab pulsar since it is one of the longest-recorded in history with daily observations of up to 12 hours per day from Jodrell Bank Centre for Astrophysics (JBCA) since 1984 (Lyne et al., 2015). Before that, other observatories also observed the Crab but with not on a daily basis. It is also one of the youngest pulsars we know about meaning there are numerous glitches occurring. There is yet another well-monitored pulsar which is the Vela pulsar (Dodson et al., 2007). Vela's glitches have many differences to the Crab's but the most noticeable is that Vela's glitches are much larger in size compared to the Crab's, perhaps indicative of a different glitch mechanism. This variation amongst different pulsars adds to the challenge of understanding glitches fully.

2.2.2 Current theories of glitches

From seeing different types of glitches, numerous glitching mechanisms have been proposed (see Haskell and Melatos (2015) for a recent review). Here we will only discuss the main two models, the starquake model and the vortex unpinning model.

We begin with describing the starquake model which was first conceptualised by Ruderman (1969). He proposed NSs are born with intrinsic spin and due to this, the NS has an oblate shape about the rotational axis. Soon after a NS is born, the outer layers cool forming a solid crystalline crust which is oblate in shape. As the NS spins-down, the centrifugal force decreases and the NS wants to become more spherical but it is prevented from doing so due to the solid crust. Instead, shear stresses build in the crust until a critical threshold is reached which is when the crust cracks. The cracking of the crust results in a sudden release of the shear stresses and the NS rapidly becomes more spherical reducing the moment of inertia and causes the NS to glitch in order to conserve angular momentum.

This model was generally accepted for a few years until it was realised that starquakes could only explain small glitches and not larger ones, especially at the rate we were seeing large glitches from Vela (Baym et al., 1969b; Baym and Pines, 1971). Another prediction of the model is that glitch sizes should be correlated with the waiting time before the glitch. This is because the further away the stress energy is to the critical threshold, the longer one must wait before that threshold is reached. However, it was soon realised that there was no such correlation (except the case of PSR J0537-6910 (Espinoza et al., 2011)) and so a new theory of vortex unpinning was created by Anderson and Itoh (1975).

Their model required that a NS has two components: a superfluid interior and a normal matter crust (Baym et al., 1969a). Due to the irrotational property of superfluids, when a NS rotates, quantised superfluid vortices form which lie parallel to the rotation axis (e.g. Graber et al., 2017). These vortices hold the circulation of the superfluid meaning that on a macroscopic scale, the superfluid can rotate. Subsequently, the area density of vortices becomes proportional to the angular velocity of the local superfluid so that the creation or destruction of these vortices is the only way the NS can change its angular velocity.

As the NS spins-down, these vortices migrate outwards from the rotational axis in an attempt to reduce the angular velocity of the NS. However, near the crust-core boundary, there are pinning sites where these vortices can get pinned, stopping them from their migration. Eventually, a build up of vortices at this boundary causes the core to rotate at a different angular velocity to the crust (which is constantly being spun-down by an external braking torque, primarily due to magnetic dipole radiation) and a lag develops.

Once pinned, a vortex experiences the Magnus force which acts to unpin the vortex. It is proportional and acts perpendicular to the relative velocity between the pinned vortices and the background superfluid. Once the lag between the core and crust becomes large enough, the Magnus force causes a collective unpinning of vortices which rapidly transfers angular momentum from the core to the crust, to which the magnetic field is

thought to be "frozen" to (Goldreich and Julian, 1969), leading to an observed spin-up – a pulsar glitch.

2.2.3 Current theories of glitch recoveries

We have explored models which cause the glitch but we have yet to address the recovery back to (almost) the pre-glitch frequency. The generally accepted model is the vortex creep model which is an extension to the Anderson and Itoh (1975) vortex unpinning model (Alpar et al., 1984, 1989).

In the vortex creep model, once a vortex is pinned, it is allowed to "hop" or "creep" to another pinning location which, on average, is radially further out due to it being more energetically favourable. The creep rate is proportional to the Boltzmann factor and the exponential of the lag between the core and crust. Therefore, at a finite temperature, there is always a non-zero transfer of angular momentum from the pinned superfluid to the normal matter in the crust, with the angular momentum transfer being faster for hotter NSs or for larger lags. When there is vortex creep (and hence pinned vortices), the superfluid and crust are said to be "dynamically coupled", even though both components are rotating at different rates (Gügercinoğlu and Alpar, 2020). For clarity, dynamically coupled components (confusingly) mean the components are uncoupled in the usual sense, in that they rotate at different rates.

When a glitch occurs, vortices collectively unpin and the lag between the core and crust momentarily becomes zero causing the creep rate to decrease, possibly stopping entirely. During this split second, the superfluid and normal matter dynamically decouple (or couple in the usual sense) since there is no longer any creep. Now, during the post-glitch recovery, the external braking torque acts on a smaller moment of inertia, causing a negative jump to the time derivative of the spin frequency (alternatively, an increase in the spin-down rate). The spin-down rate recovers as the creep re-establishes itself.

Another way to think of the vortex creep model is through an analogy created by Alpar and collaborators linking it to electrical circuits containing a capacitor (Alpar et al., 1996; Akbal and Alpar, 2018; Gügercinoğlu and Alpar, 2019). The idea goes that the lag between the superfluid and crust acts like a potential difference driving charge carriers (vortices) to the capacitor (pinning sites). Any resistive elements have a current going through them which represents vortex creep. Then, when the potential difference drops, the capacitor discharges which constitutes a glitch. This analogy does not quite handle the complexities of the vortex creep model, but nevertheless, it does help to visualise what is happening.

The vortex creep model is generally the most accepted model for glitch recoveries, but there are others too which include mutual friction (Jones, 1991; Haskell et al., 2012), Ekman pumping (van Eysden and Melatos, 2008; Bennett et al., 2010; Singh, 2017), vortex slippage (Link, 2014) and transient mountains (Yim and Jones, 2020) which is a novel model created as part of this thesis, as we will see in Chapter 5.

2.3 Timing noise

2.3.1 Introduction

We have covered the short time-scale effects to pulsar timing so now let us look at the long time-scale effects, i.e. on the order of years. Timing noise is unlike glitches in the fact that we do not really have a solid theoretical understanding of how it arises. By definition, timing noise is observed as non-zero residuals which suggests our timing models are incomplete. Most of the time, we see it as long time-scale variations to residuals, examples of which are found in Figure 2.6. Some of these residual plots, like the bottom-right plot in Figure 2.6 (PSR B1700-18), show a fairly even scatter of residuals averaging about zero. The residual range is small and there are no obvious patterns within the data. This would be classified as well-modelled and any deviations would be attributed to the intrinsic system noise in the telescope which is white (has noise components at all frequencies).

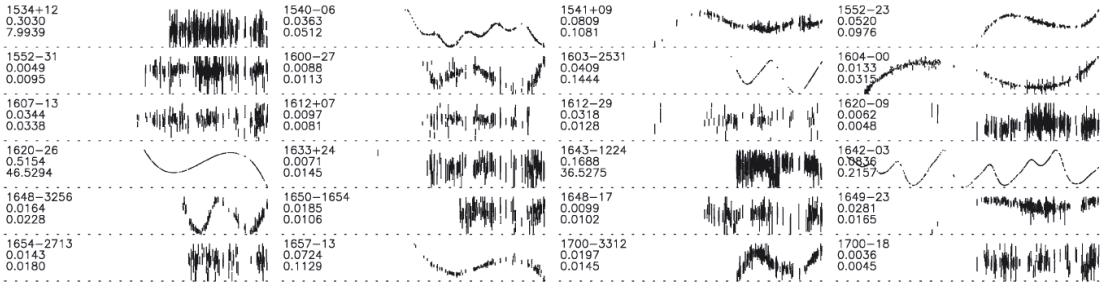

FIGURE 2.6: A collection of residual-time plots for several pulsars. The three labels on each plot show the name of the pulsar, the range between the maximum and minimum residuals in seconds, and the range between the maximum and minimum residuals as a fraction of the pulsar's period. This figure was taken from Hobbs et al. (2010).

However, if we take a residual plot of a pulsar affected by timing noise and take a Fourier transform of it, we would find that rather than having a white spectrum (shown by a flat line in the Fourier transform), the spectrum will be red meaning there is an overabundance of low frequency phenomena which is characteristic of timing noise. An example of this red spectrum in shown in Figure 2.7 for B1826-17.

In 2004, Hobbs et al. wrote a paper on the long-term timing of 374 pulsars (Hobbs et al., 2004). In their research, they found braking indices to vary between $-2.6 \times 10^8 < n <$

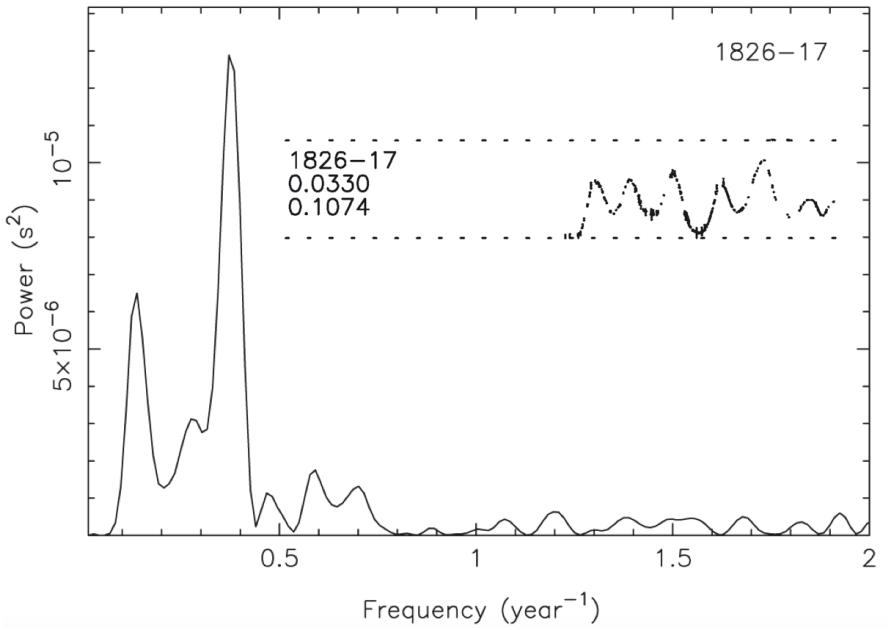

FIGURE 2.7: A power spectrum (Fourier transform of residual-time plot) of the residuals of B1826-17. The original residual-time plot is shown between the dashed lines and one can see apparent long-term fluctuations in the residuals. According to the power spectrum, the residuals are dominated by an effect of about 2.5 years in period. There are also other effects at different time-scales and together, they form what is known as timing noise. This figure was taken from Hobbs et al. (2010).

2.5×10^8. Clearly, this is orders of magnitude larger than $n = 3$ predicted earlier for magnetic dipole radiation in Section 2.1.2. They concluded such large values of n are caused by the domination of timing noise which goes to show timing noise can hide the underlying physics found from pulsar timing. What is also interesting is that 46% of the studied pulsars had negative n meaning 54% had positive n. The symmetry between the magnitudes and distribution of positive and negative n sure is intriguing and maybe hints a symmetric nature of timing noise.

In the same paper, $\ddot{\Omega}$ (which is related to n by Equation (2.11)) was found to vary across seven orders of magnitude ranging from 1×10^{-29} rad s^{-3} $< |\ddot{\Omega}| <$ 4×10^{-22} rad s^{-3}. The issue with $\ddot{\Omega}$ was that is was found to vary depending on the timespan of data you measure it from. This suggests that timing noise is time-scale dependent.

To eliminate effects from timing noise to get clean data, Hobbs et al. created an algorithm incorporated into a common pulsar timing software, TEMPO2 (Hobbs et al., 2006), which eliminated the effect of timing noise. The way in which they did this was they subtracted low-frequency harmonically-related sinusoids from the residuals to whiten the data[4]. From this analysis, they were able to correctly recover astrometric data consistent with very-long baseline interferometry (VLBI) methods. They used this

[4]One can also whiten residuals by subtracting (red) power laws (e.g. Coles et al., 2011; Lentati et al., 2014; Lower et al., 2020) or a high number of terms from a Taylor series (e.g. Abbott et al., 2020).

to justify their subtraction of harmonic sinusoids but they did not provide an analysis of what they removed until years later.

Hobbs et al. (2010) eventually analysed the timing noise which they had subtracted from their previous paper. They used two diagnostics, Δ_8 and $\sigma_z(T)$, to measure how much timing noise affected a pulsar

$$\Delta_8 = \log_{10}\left(\frac{1}{6\Omega}|\ddot{\Omega}|T_8^3\right) \tag{2.20}$$

$$\sigma_z(T) = \frac{T^2}{2\sqrt{5}}\left\langle c^2\right\rangle^{\frac{1}{2}} \tag{2.21}$$

where $T_8 = 10^8$ s (an arbitrary length of time corresponding to the length of data the creators of the Δ_8 diagnostic had (Arzoumanian et al., 1994)), T is the length of data being used and c is the amplitude of the cubic term in Equation (2.17). The angled brackets around c represents the average value of the cubic term over many realisations of data with length T.

The Δ_8 diagnostic was created based on finding out how much the cubic term in Equation (2.17) influences a timing model when only the Ω and $\dot{\Omega}$ terms are accounted for. It is worth noting that there is a Ω in the denominator of Δ_8 (which makes the argument of the logarithm have units of s) and this makes the argument of the logarithm equal the pulsar clock error (Arzoumanian et al., 1994).

The Δ_8 diagnostic does have its issues though. If different pulsars have different lengths of data, then comparing Δ_8 would no longer be meaningful as Hobbs et al. (2004) found $\ddot{\Omega}$ depended on the duration of data used (Namkham et al., 2019). It all goes back to timing noise being time-scale dependent. This is why the $\sigma_z(T)$ diagnostic was used in the 2010 follow-up paper which allowed a measure of timing noise on any time-scale. The $\sigma_z(T)$ diagnostic was adapted from the Allan variance which is traditionally used to measure a clock's stability (Matsakis et al., 1997). For a time-scale of 10 years, Hobbs et al. found the empirical relation

$$\log_{10}\left(\sigma_z(10\text{ yr})\right) = 1.37\log_{10}(\Omega^{-0.29}|\dot{\Omega}|^{0.55}) + 0.52 \tag{2.22}$$

based on a linear regression fit of $\log_{10}\left(\sigma_z(10\text{ yr})\right)$ against $\log_{10}(\Omega^{\alpha}|\dot{\Omega}|^{\beta})$ where α and β were constants found numerically. The correlation coefficient was 0.77 for this relation. This result supports the general consensus that timing noise has a larger effect for pulsars with a larger spin-down rate (Cordes and Helfand, 1980). Hobbs et al. also found timing noise to be inversely proportional to the characteristic age of a pulsar, with the exception of those with $\tau_c < 10^5$ yr, where they found pulse timings were consistent with glitch recoveries.

2.3.2 Current theories of timing noise

In 1972, Boynton et al. were the first group to report seeing timing noise (Boynton et al., 1972). The timing noise was found in none other than the Crab pulsar, but in their case, it was observed in optical wavelengths with a total of 2 years of data. Back then, residuals were not calculated in phase-space but instead in terms of the derivative in angular frequency. It meant whatever measured $\dot{\Omega}$ they had, they subtracted Equation (2.10) away from it and set $n = 3$ since magnetic dipole radiation was the most dominant effect seen in pulsar timing.

Within that group was Groth, who had just submitted a thesis on the optical timing of the Crab pulsar (Groth, 1971). He proposed a model which suggested that timing noise was one of "phase noise", "frequency noise" or "slowing-down noise". This is the same as saying timing noise is due to noise in ϕ, Ω or $\dot{\Omega}$. The model stated that at random times, one of the quantities has an unresolved discontinuous jump, with the amplitude of each jump also randomly distributed. This is why the term "random walk" is often used when explaining this model.

Later in 1975, Groth confirmed the Crab's timing noise was most consistent with a random walk in the pulse frequency (Groth, 1975). The model gained support and by 1980, Cordes & Helfand reported that timing noise was a characteristic of many pulsars and not just the Crab (Cordes and Helfand, 1980). With more pulsars to look at, Cordes & Downs extended Groth's model and said that timing noise was not just a noise in the phase, frequency or spin-down but in fact a mixture of all of them (Cordes and Downs, 1985). Another finding was that Cordes and Downs (1985) was able to model timing noise in some pulsars as microglitches. Out of 17 pulsars available, there were thought to be 42 microglitch events (Cordes and Downs, 1985).

Around the same time, Cheng came up with the theory that timing noise could be caused by magnetospheric fluctuations (Cheng, 1987a,b). In his first paper, he suggested the natural fluctuation in pair production in the outer gap of the magnetosphere could give rise to timing noise (Cheng, 1987a). In the paper which immediately followed, he suggested microglitches could somehow excite the magnetosphere which results in timing noise (Cheng, 1987b).

Fast-forward to 2010 where Lyne et al. found observational evidence to suggest timing noise is due to a NS's magnetosphere quasi-periodically switching states (Lyne et al., 2010). This explanation is not too far from Cheng's theory, though the time-scales do not quite match. The evidence for magnetospheric switching was shown by a strong correlation between changes to the pulse profile (the shape of which is strongly related to the magnetosphere) and the angular frequency derivative, $\dot{\Omega}$. It was these quasi-periodic changes to $\dot{\Omega}$ that they said explained the timing noise residuals. The research

was quite a breakthrough in our understanding but on the other hand, it was only 6 pulsars which showed evidence of magnetospheric switching.

Besides these phenomenological noise and magnetospheric models, there have been attempts at explaining timing noise as due to effects within the interior of the NS. Jones (1990) proposed the variability in the coupling between the superfluid and crust could possibly be the reason. More recently, Melatos and Link (2014) suggested superfluid turbulence may be the cause. It is clear there is still uncertainty in the mechanism behind timing noise and so in the latter part of the thesis, we create our own model which involves microglitches exciting NS oscillations, see Chapter 8 onwards.

2.3.3 Connecting glitches with timing noise

2.3.3.1 Alpar, Nandkumar & Pines (1986)

Groth's model was more of a phenomenological one and as timing noise became more mysterious, there was more pressure on the theorists to explain the physics behind it all. It has already been hinted that there may be some connection between glitches and timing noise in the last section (Cordes and Downs, 1985; Cheng, 1987b).

In Sections 2.2.2 and 2.2.3, we saw how the vortex creep/unpinning model could explain glitches and their subsequent recoveries. Alpar et al. (1986) had the idea to use the vortex model to test whether timing noise could be explained with it.

They concluded that the mechanism responsible for large glitches, specifically vortex unpinning, played no role in the timing noise of the 25 pulsars they studied which included the Crab and Vela. As a result of this conclusion, they suggested that there maybe a minimum size for glitches produced by vortex unpinning. Another conclusion was that the microglitches are not simply scaled down versions of (macro)glitches. As we will see shortly, both these conclusions are consistent with the recent work of Espinoza et al. (2014, 2021).

2.3.3.2 Cheng (1987) and Cheng et al. (1988)

After the conclusion of Alpar, Nandkumar & Pines, Cheng (1987b) did not want to give up the idea of internal vortex dynamics being the cause of timing noise so he attempted to describe timing noise slightly differently. He modified the vortex unpinning model by saying microglitches caused by vortices unpinning perturb the magnetosphere which causes changes to the braking torque on the NS. Cheng said any white noise found in the power spectrum of the residuals would be attributed directly to the microglitches and the red timing noise is due to the microglitch-induced changes to the magnetosphere. He compared his theoretical predictions of the "slow-down noise

strength parameter" to observational values (Cordes and Helfand, 1980) for 22 pulsars and found that within a factor of a few, his theory was consistent. The main uncertainty was due to a lack of understanding between how magnetosphere responds to the microglitches.

Soon after, Alpar and collaborators saw potential in Cheng's research and partnered up with him to continue the quest of explaining timing noise with superfluid vortices (Cheng et al., 1988). They had to find a reason to why microglitches could exist and they suggested different pinning sites had different values of critical lag before a glitch occurred. As such, they concluded that "structural inhomogeneities in the crust of neutron stars may be responsible for frequent microglitches which lead to pulsar timing noise".

2.3.3.3 Janssen & Stappers (2006)

Another more direct piece of observational evidence that glitches may be the same phenomenon as timing noise was reported by Janssen and Stappers (2006). Their paper reported 30 glitches in 7 slow-spinning pulsars. From the $P - \dot{P}$ diagram in Figure 2.2, we see that pulsars observed to be slowly rotating typically have higher characteristic ages and we know from Section 2.2.1 that older pulsars tend not to show an exponential recovery. This was indeed what was found so they modelled the glitches without an exponential recovery and just as a permanent, discontinuous change to Ω and $\dot{\Omega}$. Any exponential recovery would have been difficult to spot anyway since most glitches were small.

There was one pulsar which was of particular interest, B1951+32. After taking away the secular spin-down (Equation (2.17)), the residuals measured in milliturns (1000 milliturns $= 360°$ of phase) showed timing noise features and are shown in Figure 2.8.

Janssen & Stappers found that B1951+32's timing noise was best modelled by 4 consecutive glitches, each a few hundred days apart. In doing this, they reduced the residuals by a factor of 10 and the resultant residual plot had no obvious features. Another interesting point was that the sizes of the glitches ranged from $0.51 \times 10^{-9} < \frac{\Delta\Omega}{\Omega} < 2.25 \times 10^{-9}$ which is on the smaller side for glitch sizes.

2.3.3.4 Espinoza at al. (2014, 2021)

There are two more related papers which are of interest to us. The first is a paper from Espinoza et al. (2014) and it discusses the minimum glitch size observable in the Crab pulsar. They claim the smallest glitch size possible for the Crab pulsar is $\frac{\Delta\Omega}{\Omega} \sim 2 \times 10^{-9}$, which is above detection limits of current telescopes. They create a criterion for glitch detection by defining a glitch occurs when $\Delta\Omega > 0$ and $\Delta\dot{\Omega} < 0$ simultaneously which

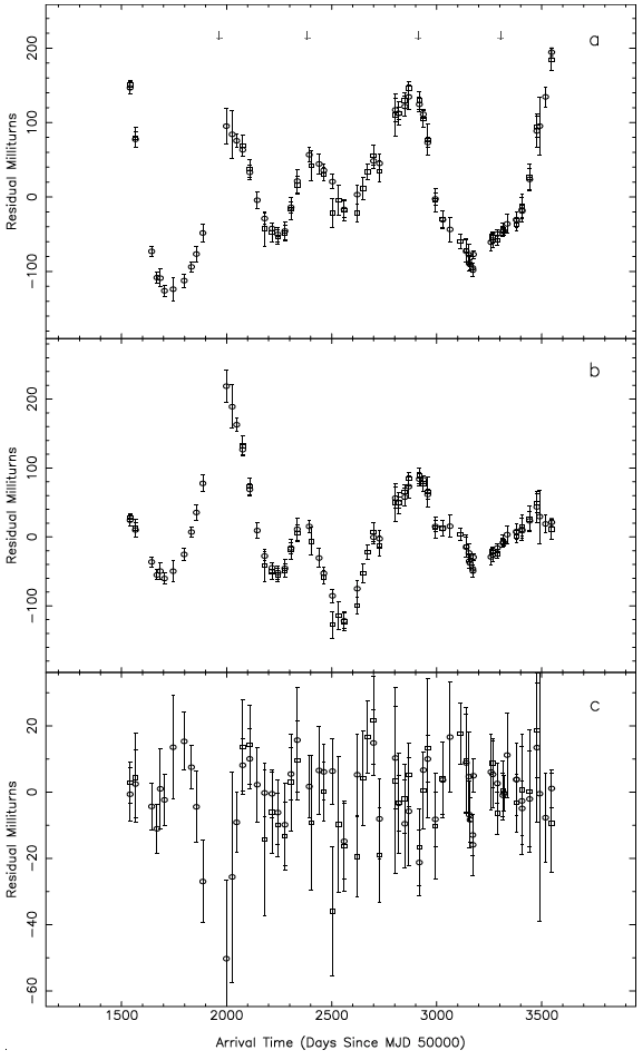

FIGURE 2.8: The top graph shows the residuals of B1951+32 when the ϕ, Ω and $\dot{\Omega}$ terms are accounted for in the timing model which has been subtracted (Equation (2.17)). The middle graph is the same but with the $\ddot{\Omega}$ term also removed. The bottom graph shows the residuals after 4 glitches have been included in the model and notice the vertical scale is 10 times smaller. This figure was taken from Janssen and Stappers (2006).

is how we defined a glitch in Section 2.2.1 and is seen visually in Figure 2.5. For a glitch at time t_g, the phase residual relative to if there was not a glitch, $\Delta\phi_g$, is

$$\Delta\phi_g = -\Delta\Omega(t_{TOA} - t_g) - \frac{1}{2}\Delta\dot{\Omega}(t_{TOA} - t_g)^2 \tag{2.23}$$

where $t_{TOA} > t_g$. Here, $\Delta\Omega$ and $\Delta\dot{\Omega}$ are step changes and do not have a time dependence. Figure 2.9 shows Equation (2.23) in a residual-time graph for when a glitch has occurred.

We see from Equation (2.23) that $\Delta\Omega > 0$ leads to a linear decrease in $\Delta\phi_g$ whereas $\Delta\dot{\Omega} < 0$ leads to a quadratic increase in $\Delta\phi_g$ with both effects being visible in Figure 2.9.

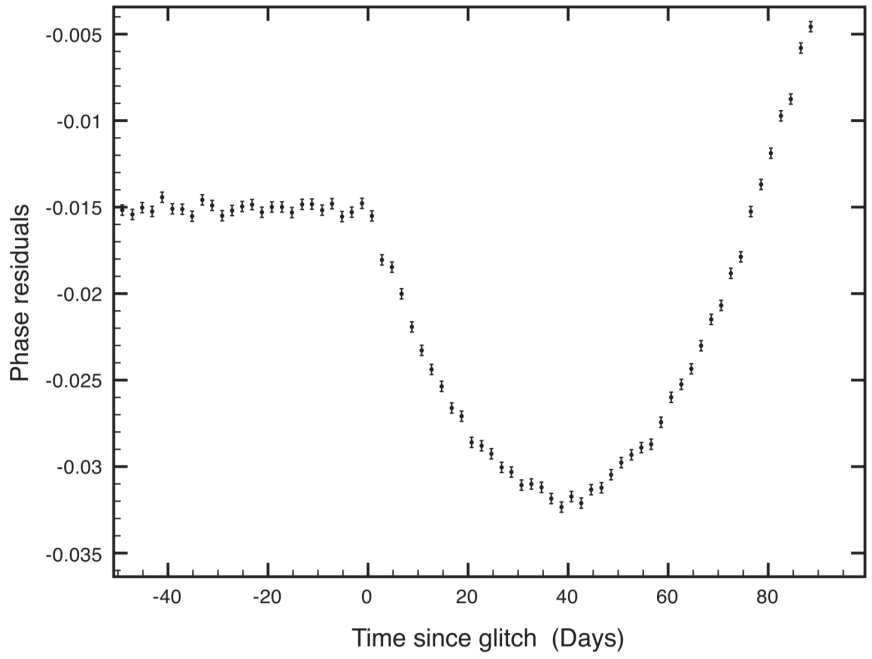

FIGURE 2.9: An example of a glitch as seen in a phase residual-time graph. This figure was taken from Espinoza et al. (2014).

So, the first constraint Espinoza et al. stated was that there must be a dominant effect from the linear term compared to the quadratic term so that a dip in $\Delta\phi_g$ is seen. The second constraint was that this dip had to be greater than the root-mean-square of the residuals prior to t_g. From just these two constraints, they were able to create an algorithm to process timing data from as far back as 1984 which totalled 8862 TOAs.

From their analysis, they re-discovered all but one of the glitches already known totalling 19 out of a possible 20. They attributed the missed detection to the missed glitch occurring only 63 days after the previous, and so the residuals were still in the process of recovering. They also found 381 "glitch candidates" (GCs) which satisfied the two criteria required to be classed as a glitch. They altered the program to find "anti-glitch candidates" (AGCs) which would have a bump instead of a dip in $\Delta\phi_g$ and they found 383 of them. When arranged by glitch size, the known glitches were clearly larger in size ($\frac{\Delta\Omega}{\Omega} \gtrsim 2 \times 10^{-9}$) compared to the candidates which all had sizes below $\frac{\Delta\Omega}{\Omega} \sim 1 \times 10^{-9}$. This is what drove them to test whether the candidates and known glitches came from the same distribution. They found the candidates were well-described by a log-normal distribution, whereas the glitches, as we have already established in Section 2.2.1, were well-described by a power law. There seems to be a striking symmetry for these GCs and AGCs and it offers a chance to investigate timing noise, which according to this study, would have sizes of $\frac{\Delta\Omega}{\Omega} < 1 \times 10^{-9}$ and have a log-normal distribution.

Then in their second paper, they re-did the analysis but for the Vela pulsar (Espinoza et al., 2021). A very similar conclusion was reached in that there was an intrinsic lack of

Vela glitch sizes smaller than $\frac{\Delta\Omega}{\Omega} \sim 9 \times 10^{-7}$, consistent with the findings of Shannon et al. (2016). There were 83 GCs and 66 AGCs for 24 years of data. Again, a log-normal distribution was favoured and it had a maximum size of $\frac{\Delta\Omega}{\Omega} \lesssim 9 \times 10^{-10}$.

There was a slight difference between the two papers though. In the Crab analysis, there was a 4% chance that GCs and AGCs *were not* from the same distribution but for Vela, there was only a 16.5% chance the GCs and AGCs *were* from the same distribution. However, Espinoza et al. (2021) did mention the lower end of the distributions were poorly constrained, in this case, due to noise in the residuals.

Chapter 3

Gravitational waves overview

We should now have enough knowledge about pulsar timing, glitches and timing noise so in this section, we will focus on the theory behind GWs. Ultimately, we would like to have models for glitch recoveries and timing noise, but in order for a model to be useful, it should have testable predictions. We wish to test our models by comparing to GW observations so it is imperative to know more about GWs. We will begin with a quick overview of general relativity (GR).

3.1 General relativity

Einstein first came up with the idea of GR in 1915. His theory was one which explained gravity as some geometric property of space and time. From his work on special relativity in 1905, his two postulates led him to say that space and time were actually inseparable and always had to be considered together, as spacetime. Then, when you place matter within this spacetime, it causes the spacetime to curve. This curvature tells other matter how to move which is what we know as gravity. This theory can be seen from Einstein's field equations

$$R_{\mu\nu} - \frac{1}{2}Rg_{\mu\nu} = \frac{8\pi G}{c^4}T_{\mu\nu} \tag{3.1}$$

where $R_{\mu\nu}$ is the Ricci tensor, R is the Ricci scalar, $g_{\mu\nu}$ is the spacetime metric tensor, G is Newton's gravitational constant, c is the speed of light in a vacuum and $T_{\mu\nu}$ is the stress-energy tensor. We will go through what each of the more unfamiliar terms are later but for now, we see the right hand side of Equation (3.1) depends only on the stress-energy tensor. This stress-energy tensor is non-zero whenever we have some matter (or equivalently, energy) within our spacetime. On the left hand side, we have the Ricci tensor and scalar and both are measures of how curved the spacetime is. We therefore see that having matter within spacetime causes curvature.

$g_{\mu\nu}$ is the spacetime metric tensor and can be thought of as the "fabric" of spacetime which is being curved. This tells us everything about our system. We will see later that $R_{\mu\nu}$ and R are made up of essentially second derivatives of $g_{\mu\nu}$ which highlights why $R_{\mu\nu}$ and R measure curvature. This means the left hand side of Equation (3.1) is completely known if $g_{\mu\nu}$ is known.

$g_{\mu\nu}$ can be defined in terms of the line element (or spacetime interval)

$$ds^2 = g_{\mu\nu}dx^\mu dx^\nu \tag{3.2}$$

which essentially is "Pythagoras' theorem" in a general spacetime which could possibly be curved. It reduces to exactly to Pythagoras' theorem if we only look at the spatial components (which we know we cannot do in relativity) of a spacetime which is flat, known as the Minkowski spacetime and is symbolised by $g_{\mu\nu} = \eta_{\mu\nu}$.

$g_{\mu\nu}$ also has the property that it can raise and lower indices on tensors. Non-relativistic classical physics was always done in Euclidean space and time was distinct from it. In such a space, there is no difference between upper and lower indices but in relativity, it is important we make this distinction. We are capturing the effects of the curvature of spacetime by doing this. The way in which the spacetime metric raises and lowers indices is

$$dx_\mu = g_{\mu\nu}dx^\nu \quad \text{and} \quad dx^\mu = g^{\mu\nu}dx_\nu \,. \tag{3.3}$$

Next, we look at the covariant derivative. The covariant derivative is used to find the derivative of some object (scalars, vectors, tensors) along a specified tangent vector in a curved spacetime. This is non-trivial as the two points used for the derivative will belong to different tangent spaces (due to curvature) and so one must account for this by using connection coefficients, $\Gamma^\rho_{\mu\nu}$. By definition, the covariant derivative is

$$\nabla_\nu \boldsymbol{e}_\mu = \Gamma^\rho_{\mu\nu}\boldsymbol{e}_\rho \tag{3.4}$$

where ∇_ν represents the covariant derivative, $\boldsymbol{e}_\mu$ are the basis vectors and $\Gamma^\rho_{\mu\nu}$ are the connection coefficients. One can think of the connection coefficients as encoding how the basis vectors change as they move around. For instance, the basis vectors in cylindrical coordinates are $\hat{\mathbf{r}}$, $\hat{\boldsymbol{\theta}}$ and $\hat{\mathbf{z}}$. At all positions, the direction of $\hat{\mathbf{z}}$ always remains the same, however, the direction of $\hat{\mathbf{r}}$ and $\hat{\boldsymbol{\theta}}$ change depending on where you are. In GR, the basis vectors can change due to the curvature of the spacetime you are moving through.

Coming back to the covariant derivative, one wants to be able to compare two points in spacetime but this is meaningless if they belong to different tangent spaces, each having a different local curvature. One needs to parallel transport which essentially takes the local geometry of one region and moves it to another place, whilst keeping angles between basis vectors the same. This then allows the correct comparison when

evaluating the derivative. The scalar product of the basis vectors is another definition of metric tensor

$$g_{\mu\nu} = \boldsymbol{e}_\mu \cdot \boldsymbol{e}_\nu \tag{3.5}$$

and we want the right hand side to be constant during parallel transport (for constant angles), which means we have the condition

$$\nabla_\rho g_{\mu\nu} = 0\,. \tag{3.6}$$

Along with the assumption of a torsion-free metric[1], it can be shown (e.g. Misner et al., 1973) that

$$\Gamma^\rho_{\mu\nu} = \frac{1}{2} g^{\rho\lambda}(g_{\lambda\mu,\nu} + g_{\lambda\nu,\mu} - g_{\mu\nu,\lambda}) \tag{3.7}$$

where in this special case, $\Gamma^\rho_{\mu\nu}$ are called the Christoffel symbols. The commas in Equation (3.7) are best understood when we look at the covariant derivative of the vector, $\boldsymbol{A} = A^\rho \boldsymbol{e}_\rho$.

$$\begin{aligned}
\nabla_\nu \boldsymbol{A} = \nabla_\nu(A^\rho \boldsymbol{e}_\rho) &= (\nabla_\nu A^\rho)\boldsymbol{e}_\rho + (\nabla_\nu \boldsymbol{e}_\rho)A^\rho \\
&= (\nabla_\nu A^\rho)\boldsymbol{e}_\rho + (\Gamma^\lambda_{\rho\nu}\boldsymbol{e}_\lambda)A^\rho \\
&= (\nabla_\nu A^\rho + \Gamma^\rho_{\lambda\nu}A^\lambda)\boldsymbol{e}_\rho \\
\rightarrow A^\rho{}_{;\nu}\boldsymbol{e}_\rho &= (A^\rho{}_{,\nu} + \Gamma^\rho_{\lambda\nu}A^\lambda)\boldsymbol{e}_\rho \\
\rightarrow A^\rho{}_{;\nu} &= A^\rho{}_{,\nu} + \Gamma^\rho_{\lambda\nu}A^\lambda
\end{aligned} \tag{3.8}$$

Here we introduced the semi-colon notation but this should help us understand the comma notation. Equation (3.8) is like the "total derivative" we encounter in calculus. The total derivative always has a term which is a partial derivative and this says to explicitly differentiate with respect to some variable. Then, there are other terms which carry the implicit dependence of the variable you are differentiating with respect to. In this regard, the comma represents a partial derivative of the object, and the second term accounts for effects from gradients in the metric (one can see that $\Gamma^\rho_{\mu\nu}$ depends on the first derivative of the metric from Equation (3.7)). The second term is also there to ensure the covariance of the equation, i.e. if the left hand side is a tensor, then the right hand side must be a tensor too.

The beauty with GR is that you can always transform to another reference frame and the law of physics will be the same. One simplifies the calculation if one selects a local reference frame with $\Gamma^\rho_{\mu\nu} = 0$. This means semi-colons and commas no longer have a difference. This type of reference frame is where the observer is freely-falling in the curved spacetime and is called a local Lorentz frame. The effects of $\Gamma^\rho_{\mu\nu}$ could then be brought back into the end result if needs be.

[1]Practically, this means the order in which you differentiate a mixed 2nd order derivative does not matter. It also means the connection coefficients are symmetric in its lower two indices. i.e. $\Gamma^\rho_{\mu\nu} = \Gamma^\rho_{\nu\mu}$.

Next, we introduce the Riemann tensor which eventually contracts into the Ricci tensor followed by the Ricci scalar. The Riemann tensor can be written entirely out of Christoffel symbols

$$R^{\rho}{}_{\lambda\mu\nu} = \Gamma^{\rho}{}_{\lambda\nu,\mu} - \Gamma^{\rho}{}_{\lambda\mu,\nu} + \Gamma^{\rho}{}_{\sigma\mu}\Gamma^{\sigma}{}_{\lambda\nu} - \Gamma^{\rho}{}_{\sigma\nu}\Gamma^{\sigma}{}_{\lambda\mu} \tag{3.9}$$

and notice the Riemann tensor is made up from a "partial derivative" of the Christoffel symbols. This means that the Riemann tensor is proportional to the "second partial derivative" of the spacetime metric making it a measure of curvature. We show this explicitly by substituting Equation (3.7) into Equation (3.9) and using the properties that $g_{\mu\nu}$ is symmetrical and "partial differentials" commute, we get

$$R^{\rho}{}_{\lambda\mu\nu} = \frac{1}{2}g^{\rho\sigma}(g_{\sigma\nu,\lambda\mu} - g_{\sigma\mu,\lambda\nu} + g_{\lambda\mu,\sigma\nu} - g_{\lambda\nu,\sigma\mu}) \,. \tag{3.10}$$

We then contract the 1st and 3rd indices to attain the Ricci tensor

$$R_{\lambda\nu} = R^{\mu}{}_{\lambda\mu\nu} \tag{3.11}$$

and contract the remaining indices to get the Ricci scalar

$$R = R^{\nu}{}_{\nu} \tag{3.12}$$

where we applied the spacetime metric $g^{\nu\lambda}$ on to the Ricci tensor in Equation (3.11) to raise the λ and change it to a ν.

The Ricci tensor and scalar make up the left hand side of Equation (3.1) but the Einstein field equations can be further simplified. We define the Einstein tensor

$$G_{\mu\nu} = R_{\mu\nu} - \frac{1}{2}Rg_{\mu\nu} \tag{3.13}$$

meaning the Einstein field equations now take a simpler form

$$G_{\mu\nu} = \frac{8\pi G}{c^4}T_{\mu\nu} \,. \tag{3.14}$$

From geometric principles, one can show

$$\nabla \cdot G_{\mu\nu} = 0 \tag{3.15}$$

which is known as the contracted Bianchi identity. Together with Equation (3.14), one can see that the conservation of energy and momentum comes out as a result of this geometric statement and is shown by

$$\nabla \cdot T_{\mu\nu} = 0 \,. \tag{3.16}$$

3.2 Linearising Einstein's field equations

If we go back to the picture of masses causing curvature to spacetime, GWs are a result of moving masses about and are seen as ripples in spacetime. This is analogous to how we see ripples radiating outwards on the surface of a pond when we throw a stone into it.

To see how GWs arise from the theory of GR, we need to use first-order perturbation theory. This regime only works when the GWs are far from their source such that the radius of the curvature of spacetime is much larger than the wavelength of the GWs. When we are in such a regime, the GWs can be thought of as plane waves and will be small perturbations on the flat Minkowski metric. This means the perturbation is shown by a total spacetime metric of

$$g_{\alpha\beta} = \eta_{\alpha\beta} + h_{\alpha\beta} \tag{3.17}$$

where $\eta_{\alpha\beta} = \text{diag}(-1, 1, 1, 1)$ and $h_{\alpha\beta}$ is the metric perturbation with the property $|h_{\alpha\beta}| \ll 1$. We also define the trace-reversed metric perturbation

$$\bar{h}_{\alpha\beta} = h_{\alpha\beta} - \frac{1}{2}\eta_{\alpha\beta}h \tag{3.18}$$

where $h = h^{\alpha}_{\ \alpha}$ and $\bar{h}^{\alpha}_{\ \alpha} = -h$ hence the name "trace-reversed". Once we use Equation (3.17) in Equation (3.10), keeping only 1st order terms in $h_{\alpha\beta}$, and calculate the Einstein tensor using Equations (3.13) and (3.18), we get

$$G_{\alpha\beta} = -\frac{1}{2}(\bar{h}_{\alpha\beta,\mu}{}^{,\mu} + \eta_{\alpha\beta}\bar{h}_{\mu\nu}{}^{,\mu\nu} - \bar{h}_{\alpha\mu,\beta}{}^{,\mu} - \bar{h}_{\beta\mu,\alpha}{}^{,\mu}) \,. \tag{3.19}$$

This is quite a complex expression but we can get rid of the 2nd, 3rd and 4th terms if we set $\bar{h}^{\mu\nu}{}_{,\mu} = 0$. This is known as the Lorentz gauge and means we fix what coordinate system we are using. Once we make this gauge choice, Equation (3.19) looks a lot less intimidating and reduces to

$$G_{\alpha\beta} = -\frac{1}{2}\bar{h}_{\alpha\beta,\mu}{}^{,\mu} \,. \tag{3.20}$$

Like in electromagnetism, we define the d'Alembertian operator

$$\Box\psi = \psi^{,\mu}{}_{,\mu} = \left(-\frac{1}{c^2}\frac{\partial^2}{\partial t^2} + \frac{\partial^2}{\partial x^2} + \frac{\partial^2}{\partial y^2} + \frac{\partial^2}{\partial z^2}\right)\psi \tag{3.21}$$

where the last equality is the d'Alembertian in standard Cartesian coordinates. This then allows us to write Equation (3.20) as

$$G_{\alpha\beta} = -\frac{1}{2}\Box\bar{h}_{\alpha\beta} \,. \tag{3.22}$$

Substituting this into Einstein's field equations (Equation (3.14)), we get

$$\Box \bar{h}_{\alpha\beta} = -\frac{16\pi G}{c^4} T_{\alpha\beta} \,. \tag{3.23}$$

This is in the form of a sourced wave equation. However, in regions where the radius of spacetime curvature is much greater than the wavelength of GWs (typically in regions of low mass), GWs are known to propagate as if they were travelling through a vacuum (at the speed of light). This has recently been supported by GW170817 where they found the difference between the speed of GWs and the speed of light to be no more than 3×10^{-15} times the speed of light (Abbott et al., 2017c). Therefore, we model GWs (far from their source) as travelling through a vacuum, meaning the matter term on the right hand side of Equation (3.23) vanishes leading to

$$\Box \bar{h}_{\alpha\beta} = 0 \,. \tag{3.24}$$

A solution to the homogeneous wave equation is given by the plane wave solution

$$\bar{h}^{\alpha\beta} = A^{\alpha\beta} e^{ik_\mu x^\mu} \tag{3.25}$$

where $A^{\alpha\beta}$ represents the amplitude of the trace-reversed metric perturbation and $k^\mu = (\frac{\omega}{c}, \boldsymbol{k})^{\mathrm{T}}$ which is the 4-wavevector, with ω being the wave angular frequency. When we substitute this solution back into Equation (3.24), we find $k^\mu k_\mu = 0$ meaning GWs have a null worldline which is the statement that they travel at the speed of light. With the solution, we can also substitute into the Lorentz gauge condition ($\bar{h}^{\alpha\beta}{}_{,\alpha} = 0$) to find

$$A^{\alpha\beta} k_\alpha = 0 \,. \tag{3.26}$$

We divert slightly now to count the number degrees of freedom within our system. As we know, once we have $g_{\alpha\beta}$, we will know everything about the system. By Equation (3.17), it means if we know $h_{\alpha\beta}$ (or $\bar{h}_{\alpha\beta}$), we too will know everything since $\eta_{\alpha\beta}$ is already known. In one temporal and three spatial dimensions, $\bar{h}_{\alpha\beta}$ (and hence $A^{\alpha\beta}$) has 16 possible components. However, due to $\bar{h}_{\alpha\beta}$ being symmetrical, we only need to know 10 of the components (say the top right triangle of the matrix) since we could reflect in the diagonal line to recover 16 components. If we say our GW propagates only in the z direction ($k^\mu = (\frac{\omega}{c}, 0, 0, k)^{\mathrm{T}}$), then the relation we found through the Lorentz gauge (Equation (3.26)) reduces to

$$A^{0\beta} = -A^{3\beta} \tag{3.27}$$

with the help of $k^\mu k_\mu = 0$. This statement means the temporal row of the upper triangle will be known if we know the z row of $A_{\alpha\beta}$. This means 4 of the (temporal row) components are no longer degrees of freedom. From the Lorentz gauge alone, we have reduced $A_{\alpha\beta}$ to only 6 independent components, all of which are spatial.

It can be proven (e.g. p. 205 of Schutz (1985)) that we can add an extra gauge condition to the system (apply more constraints to lower the number of degrees of freedom) without affecting the Lorentz gauge we have already applied. This gauge is known as the transverse-traceless gauge and we denote we are using it by having a superscript "TT" on top of $\bar{h}_{\alpha\beta}$. This gauge is the statement that $\bar{h}_{\alpha\beta}$ must be traceless ($\bar{h}^{\alpha}_{\ \alpha} = 0$) and transverse ($\bar{h}_{\alpha\beta}U^{\beta} = 0$ where U^{β} is an arbitrary constant time-like 4-vector) meaning the effects of the GWs are in a direction perpendicular to the direction of propagation (i.e. GWs affect the $x-y$ plane when travelling in the z direction). Since $\bar{h}_{\alpha\beta}$ is purely spatial (space-like), in order to satisfy $\bar{h}_{\alpha\beta}U^{\beta} = 0$, U^{β} must be purely time-like (due to the scalar product). Therefore if we take $U^{\beta} = \delta^{\beta}_{\ 0}$, then we find

$$A_{\alpha 0} = 0\,. \tag{3.28}$$

This sets all the components in the temporal column to zero which has the effect of setting all but the inner-most 4 components to zero when combined with $\bar{h}_{\alpha\beta}$ being symmetric and Equation (3.27). Equation (3.28) alone removes 3 more degrees of freedom and the traceless condition gives

$$A_{22} = -A_{11} \tag{3.29}$$

which gets rid of 1 more degree of freedom. In total, only 2 degrees of freedom remain and there is no more gauge freedom left within our system. This means the 2 components must have a physical meaning and they are the 2 polarisations which a GW can have. The polarisations are separated by a rotation by 45° which is why one is called the "plus" polarisation and the other the "cross" polarisation. In order to write our final perturbed metric tensor, we need to convert from $\bar{h}_{\alpha\beta}$ to $h_{\alpha\beta}$. However in the transverse-traceless gauge, the trace of $\bar{h}^{\mathrm{TT}}_{\alpha\beta}$ is zero. Therefore, we can say $h^{\mathrm{TT}}_{\alpha\beta} = \bar{h}^{\mathrm{TT}}_{\alpha\beta}$ giving

$$h^{\mathrm{TT}}_{\alpha\beta} = \begin{pmatrix} 0 & 0 & 0 & 0 \\ 0 & h_+ & h_\times & 0 \\ 0 & h_\times & -h_+ & 0 \\ 0 & 0 & 0 & 0 \end{pmatrix} e^{ik_\mu x^\mu}\,. \tag{3.30}$$

3.3 Energy from gravitational waves

To calculate the energy of GWs, one must do more than first-order perturbation theory on a flat Minkowski metric but here we will go over the main results (e.g. Thorne and Blandford, 2017). The main reason for this is because we cannot localise the energy of a GW to a particular part of the GW, i.e. the crest, trough or anywhere in between. We therefore take an average over many wavelengths to find the average energy. Since GWs have a sinusoidal form in spatial coordinates (Equation (3.25)), any 1st order terms

will average out to zero meaning we must go to 2nd order. Also, the existence of GWs within a system will perturb the background metric which is an effect not captured in first-order perturbation theory. In terms of Einstein's field equations, this is written as

$$G^{(B)}_{\alpha\beta} = \frac{8\pi G}{c^4} T^{\mathrm{GW}}_{\alpha\beta} \,. \tag{3.31}$$

From Equation (3.22), we see a homogeneous wave equation only exists if $\langle G_{\alpha\beta} \rangle = 0$, where the angled brackets represents an average over several wavelengths. $G_{\alpha\beta}$, which measures curvature, can be expanded to 2nd order for a general spacetime metric and when we take the average over several wavelengths, we get

$$\langle G_{\alpha\beta} \rangle = G^{(B)}_{\alpha\beta} + \langle G^{(2)}_{\alpha\beta} \rangle = 0 \tag{3.32}$$

where the superscript "(B)" and "(2)" represent the background and 2nd order expansion in $h_{\alpha\beta}$ of $G_{\alpha\beta}$ respectively. The 1st order term vanishes after averaging for the reasons given above. Then, if we substitute Equation (3.32) into Equation (3.31), we find

$$T^{\mathrm{GW}}_{\alpha\beta} = -\frac{c^4}{8\pi G} \langle G^{(2)}_{\alpha\beta} \rangle \tag{3.33}$$

which defines the stress-energy tensor for GWs. After finding the 2nd order expression for $G_{\alpha\beta}$ in terms of $h_{\alpha\beta}$, and if we use the transverse-traceless gauge, Equation (3.33) becomes

$$T^{\mathrm{GW}}_{\alpha\beta} = \frac{c^4}{32\pi G} \langle h^{\mathrm{TT}}_{\mu\nu,\alpha} h^{\mu\nu}_{\mathrm{TT},\beta} \rangle \tag{3.34}$$

which reduces to

$$T^{\mathrm{GW}}_{\alpha\beta} = \frac{c^4}{16\pi G} \langle h_{+,\alpha} h_{+,\beta} + h_{\times,\alpha} h_{\times,\beta} \rangle \tag{3.35}$$

when we use Equation (3.30). Since our GWs are set to propagate in the z direction, we have $h_+ = h_+(kz - \omega t)$ and $h_\times = h_\times(kz - \omega t)$ so the non-zero terms in the stress-energy tensor are

$$T^{\mathrm{GW}}_{00} = \frac{T^{\mathrm{GW}}_{03}}{c} = T^{\mathrm{GW}}_{30} c = \frac{T^{\mathrm{GW}}_{33}}{c^2} = \frac{c^2}{16\pi G} \langle (\dot{h}_+)^2 + (\dot{h}_\times)^2 \rangle \tag{3.36}$$

where T^{GW}_{00} is the energy density, T^{GW}_{03} is the energy flux in the z direction, T^{GW}_{30} is density of the z component of momentum and T^{GW}_{33} is the momentum flux in the z direction.

Since we are interested in the energy of GWs, we can take a closer look at T^{GW}_{03}

$$T^{\mathrm{GW}}_{03} = F_{\mathrm{GW}} = \frac{c^3}{16\pi G} \langle (\dot{h}_+)^2 + (\dot{h}_\times)^2 \rangle \tag{3.37}$$

which is the same as the GW energy flux. The dots represent time derivatives. If we let h_+ and $h_\times$ have the same amplitude, h_0, and they vary sinusoidally with an angular

frequency of $\omega = 2\pi f$, we find the GW energy flux is given by

$$F_{\rm GW} = \frac{\pi}{4}\frac{c^3}{G} f^2 h_0^2 \,. \tag{3.38}$$

Finally, to get a luminosity from this, we need to multiply by some surface area which the GWs irradiate. One might want to multiply by a factor of $4\pi d^2$ where d is the distance between the observer and the GW source however this assumes isotropic GW emission from the source. This is not the case for GWs (see p. 975 of Misner et al., 1973). Once the GW flux is integrated across the correct (quadrupolar) surface area, then for a source where $|h_+| = |h_\times| = h_0$, the GW luminosity is

$$L_{\rm GW} = \frac{2\pi^2}{5}\frac{c^3}{G} d^2 f^2 h_0^2 \,. \tag{3.39}$$

Alternatively, the GW luminosity can be written in terms of the trace-reduced mass quadrupole moment, $I\!\!I_{ij}$, defined as

$$I\!\!I_{ij} \equiv \int_V \rho \left(x_i x_j - \frac{1}{3}\delta_{ij} r^2 \right) d^3x \tag{3.40}$$

where $r^2 = x^k x_k$. It can be shown that $h^{\rm TT}_{\mu\nu}$ in Equation (3.34) can be simplified in terms of $I\!\!I_{ij}$. From Equation (3.30), we see that $h^{\rm TT}_{0\nu} = h^{\rm TT}_{\mu 0} = 0$ so $h^{\rm TT}_{\mu\nu}$ can be fully represented by its spatial part, $h^{\rm TT}_{ij}$. Then, it can be shown that $h^{\rm TT}_{ij}$ is proportional to the second time derivative of $I\!\!I^{\rm TT}_{ij}$

$$h^{\rm TT}_{ij} = \frac{2}{r}\frac{G}{c^4} \ddot{I\!\!I}^{\rm TT}_{ij} \left(t - \frac{r}{c} \right) \tag{3.41}$$

where $\ddot{I\!\!I}^{\rm TT}_{ij}$ is evaluated at the retarded time and is also in the transverse-traceless gauge (see Misner et al., 1973). When substituted into Equation (3.34) and $T^{\rm GW}_{03}$ is correctly integrated, we get a GW luminosity of

$$L_{\rm GW} = \frac{1}{5}\frac{G}{c^5} \left\langle \dddot{I\!\!I}_{ij} \dddot{I\!\!I}^{ij} \right\rangle \,. \tag{3.42}$$

Finally, GWs can carry angular momentum away from a system, at a rate, $\mathcal{N}^i_{\rm GW}$, which is equal to the GW torque. One can show (e.g. Andersson, 2019) that this rate of change in angular momentum is

$$\mathcal{N}^i_{\rm GW} = \frac{2}{5}\frac{G}{c^5} \left\langle \varepsilon^{ijk} \ddot{I\!\!I}^l_j \dddot{I\!\!I}_{kl} \right\rangle \tag{3.43}$$

where ε^{ijk} is the Levi-Civita symbol. The convention we have used here is if GWs are carrying away angular momentum away from the system, then $\mathcal{N}^i_{\rm GW}$ would be positive. Likewise, if GWs carry energy away from the system, then $L_{\rm GW}$ would be positive.

3.4 Types of gravitational waves

We have looked at the mathematical approach to GWs but in this subsection, we will look more at the qualitative properties of different types of GWs. GWs are created whenever there is a time-varying mass multipole or current multipole, in the most generic case. For a multipole labelled by l, the GW luminosity from the l'th current multipole is smaller by a factor of $\mathcal{O}(v^2/c^2)$ compared to the l'th mass multipole. We will therefore consider low velocity systems where the $l = 2$ current multipole is much less than the $l = 2$ mass quadrupole, allowing us to focus entirely on the $l = 2$ mass quadrupole.

There are several astrophysical systems that have a time-varying mass quadrupole. It is important that these sources are astrophysical (so they have a lot of mass) because GWs are incredibly weak. The very first GW detection came from the coalescence of two black holes (BHs) producing $h_0 \sim 10^{-21}$ (Abbott et al., 2016). GWs have the effect where they squeeze and stretch fixed distances so $h_0 \sim 10^{-21}$ means that a 1 metre ruler changes its length by 1 zeptometre, $\Delta L \sim 1 \times 10^{-21}$ m. The more massive the system, the larger h_0 will be.

There are 4 main groups of GWs which GW detectors are looking for. The first are compact binary coalescence (CBC) GWs and as the name suggests, they are the result of the coalescence of two compact binary objects (NS-NS, BH-BH or NS-BH). These GWs are the ripples in spacetime that come off as the two massive objects spiral into one another. As the two objects get closer, their orbital frequency increases and as a result, so does the GW frequency. This gives rise to the "chirp" that some people refer to when talking about CBC GWs. Our current GW detectors are only sensitive to the final moments of a CBC and so the duration of the CBC GWs we detect last no longer than ~ 100 s.

Next are the GWs which will be the focus of this thesis, continuous GWs (CWs). CWs are quasi-monochromatic and last for a quasi-infinite duration. A leading candidate for these CWs are long-lasting "mountains" that form on NSs. These mountains "hook" on to the fabric of spacetime and as the NS rotates, GWs radiate away at a seemingly fixed frequency (twice the spin frequency) (Bonazzola and Gourgoulhon, 1996). Another two possible mechanisms for CWs are precessing NSs (Jones and Andersson, 2002) and long-lived oscillation modes on NSs (Andersson, 1998).

Stochastic GWs are always present whenever making GW observations, much like the cosmic microwave background. The stochastic GW background is thought to be the accumulation of GWs generated from random unresolved events. Candidates for these events are unresolved CBCs, rotating NSs, cosmic string interactions, inflationary models of the early universe and phase transitions of the universe (Abbott et al., 2017a). Finally, burst GWs have short durations like CBC GWs, but are not caused by a CBC.

Burst GWs have been suggested to be produced by supernovae or gamma-ray bursts, but there are countless other possibilities (Schutz, 1989).

3.5 Detecting gravitational waves

As mentioned in Section 3.4, GWs squeeze and stretch fixed distances. However, due to the quadrupolar nature of GWs, whenever we see a stretch in one direction, we see a squeeze in the perpendicular direction. This is best shown in Figure 3.1 which shows how a GW travelling in the z direction influences a circular ring of test masses in the x-y plane. This property means our detector must see changes in length in two

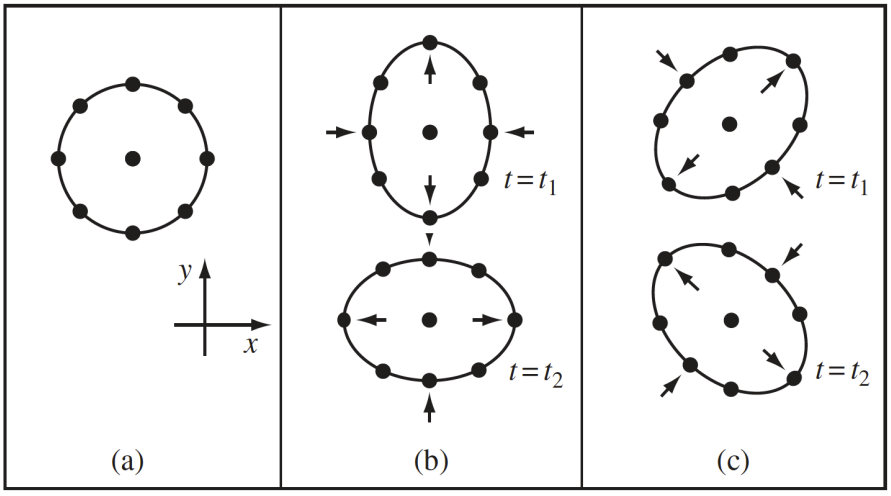

FIGURE 3.1: A diagram showing how a GW travelling in the z direction influences a circular ring of test masses at time t_1 and a later time t_2. Subfigure (a) shows the circular ring of test masses without any influence of a GW. Subfigure (b) shows the effect of a GW purely in the "+" polarisation. Subfigure (c) shows the effect of a GW purely in the "×" polarisation. This figure was taken from *A First Course in General Relativity* by Schutz (1985).

spatial directions to have a chance of detecting GWs. The largest deformation occurs at right angles which is why current ground-based detectors, like Advanced LIGO, have arms which are perpendicular. Future GW detectors, like the Einstein Telescope, will have arms with a 60° opening angle and, with three of them, can arranged in a triangular configuration. The triangular detector would need to be larger to detect the same deformation as a perpendicular detector but there are some important scientific advantages, such as having a "null stream" and better sky localisation, as well as some financial advantages too, such as two arms being able to share the same infrastructure along one of the sides of the triangle (Sathyaprakash et al., 2012; Maggiore et al., 2020).

Our detector needs to be able to measure small changes in length incredibly accurately. A Michelson interferometer does exactly this and is what ground-based and space-based GW detectors are based on, just on a much larger scale. A Michelson interferometer uses a powerful laser which is split by a beam-splitter and sent down both arms. The beams travel down the arms and reflect off freely-suspended mirrors at the end and come back to the beam-splitter where there is a semi-transparent mirror. This semi-transparent mirror reflects most of the light back into the arms to be recycled but some gets sent to a photodiode. If the light from both arms are out of phase (which is the case by default), then the light would destructively interfere and there would be almost no photons being detected on the photodiode. This is why sometimes it is called the "dark port". If a GW passes by, the arms would change lengths and then the light beams will become slightly more in phase and constructively interfere meaning photons would be detected on the photodiode. We can compare the output of the photodiode to models of what is expected and if there is an agreement, then we can confirm a GW detection.

We have not mentioned much about the size of these detectors yet. The size of these detectors determine what GW wavelengths (and thus frequencies) they are sensitive to. Generally, the larger the detector, the lower the GW frequency it can detect. For instance, current ground-based telescopes have 3-4 km arms and future ground-based telescopes, like the Einstein Telescope and Cosmic Explorer, have proposed arms of length 10 km and 40 km, respectively. These ground-based telescopes are most sensitive to GW frequencies between $10 - 10^3$ Hz. Then, there are (future) space-based detectors, like LISA and Taiji, that will have arm lengths of 2.5×10^6 km and 3.0×10^6 km, respectively. These will be sensitive to GW frequencies between $10^{-4} - 10^{-1}$ Hz. Clearly, we need different GW detectors to detect the different GW frequencies that arise from different astrophysical sources.

There is one other type of GW detector that has been gaining momentum recently and is even provided free to us by nature – pulsar timing arrays. Contrary to what was said in Sections 2.2 and 2.3, pulsars are still very stable clocks. They outperform the best atomic clocks on Earth. Their regular pulses means we can predict when the next pulse will arrive with great accuracy. If everything is well-modelled for the outgoing photons from the pulsar, and we observe a delay or early arrival of multiple pulses, then we could attribute that to the distance changing between us and the pulsar. This means the arm length is the distance between Earth and the pulsar, which is typically a few hundred parsecs to a few kiloparsecs, resulting in the greatest GW sensitivity between $10^{-9} - 10^{-7}$ Hz. Again, we need to see length changes in two spatial directions so we cross-correlate the TOAs from different pulsars across the sky. The requirement of stable timing from the pulsars is paramount in the success of pulsar timing arrays and this is another reason why it is so important to understand more about glitches and timing noise.

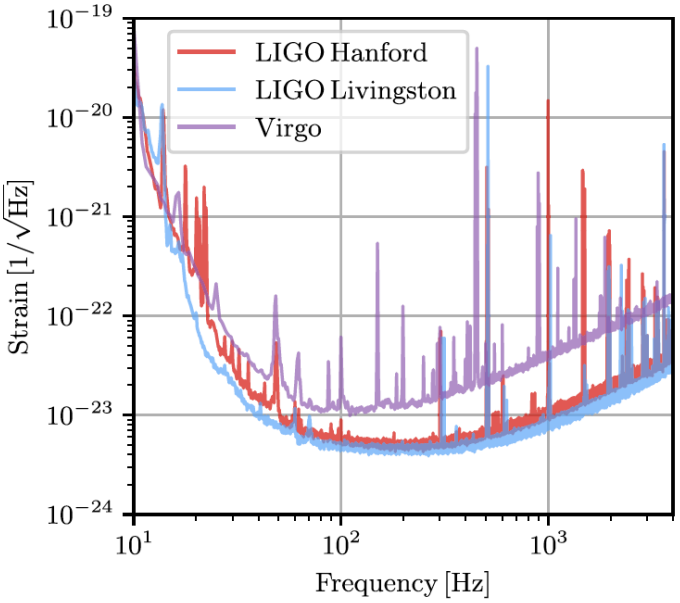

FIGURE 3.2: An example of some sensitivity curves, $\sqrt{S_n(f)}$, measured in units of $\text{Hz}^{-\frac{1}{2}}$. Large values of $\sqrt{S_n(f)}$ means there is more noise at that particular GW frequency. These sensitivity curves represent Hanford and Livingston (both aLIGO detectors in the US) and Virgo (in Italy) in their O3 phase. This figure was taken from Abbott et al. (2021a).

As mentioned, a given GW detector has certain GW frequencies which it is more sensitive to. In fact, we can measure this in what is known as a noise amplitude spectral density graph or a sensitivity curve, symbolised by $\sqrt{S_n(f)}$. It tells us how much noise there is at a given frequency. The higher the value, the more noise there is (or the less sensitive we are) and vice versa. An example of a sensitivity curve is given in Figure 3.2.

Whenever a GW detection is made, the signal-to-noise ratio (SNR) is normally quoted, or at least some detection statistic which is related (e.g. Jaranowski et al., 1998). This is a measure of how significant the signal is when in the presence of noise. To calculate the optimal SNR, ρ_0, we define

$$\rho_0 = \sqrt{(h||h)} \tag{3.44}$$

where h is the GW signal and the double vertical bar represents a scalar product defined as

$$(x||y) = 4\Re\left\{\int_0^\infty \frac{\tilde{x}(f)\tilde{y}^*(f)}{S_n(f)}df\right\} \tag{3.45}$$

where the asterisk (*) represents the complex conjugate, the tilde ($\tilde{}$) represents a Fourier transform[2], f is the GW frequency and $S_n(f)$ is the one-sided noise power spectral density measured in Hz^{-1}. The SNR is referred to as optimal when the matched-filtering template (the GW waveform model) fits the data perfectly (e.g. Prix et al., 2011). One can see why Equation (3.44) represents the SNR when you realise that the numerator

[2]In this thesis, we define a forward Fourier transform of the function $g(t)$ as $\tilde{g}(f) = \int_{-\infty}^{\infty} g(t)e^{i2\pi ft}dt$.

of Equation (3.45) equals the GW power (as a function of frequency) and the denominator is the power due to noise (also as a function of frequency). By integrating, we are adding all the contributions at all frequencies to give the total signal power divided by the noise power. Taking the square root then gives the SNR.

Typically, a GW detector receives a signal $x(t)$ comprised of a noise part $n(t)$ and if fortunate, a GW part $h(t)$, i.e. $x(t) = n(t) + h(t)$. To make any sense of the raw data, we calculate the expectation value of the product of two signals at two different times, $\langle x(t_1)x(t_2)\rangle$, and once we make the assumptions that the noise has a Gaussian distribution with zero mean and that the covariance of $n(t_i)$ and $h(t_j)$ is zero for all i, j, we get

$$\langle x(t_1)x(t_2)\rangle = \langle n(t_1)n(t_2)\rangle + \langle h(t_1)h(t_2)\rangle \,. \tag{3.46}$$

If the noise is stationary (the property where a segment of noise at a given time has the same behaviour as a segment of the same duration at a different time), then the first term on the right hand side of Equation (3.46) is purely a function dependent on the duration of the observation, $\tau = |t_1 - t_2|$. Explicitly, we have

$$\kappa(\tau) = \langle n(t_1)n(t_2)\rangle \,. \tag{3.47}$$

Then by definition, the one-sided noise power spectral density is twice the Fourier transform of Equation (3.47)

$$S_{\mathrm{n}}(f) = 2\int_{-\infty}^{\infty} \kappa(\tau)e^{i2\pi f\tau}d\tau \tag{3.48}$$

for $f \geq 0$ and is $S_{\mathrm{n}}(f) = 0$ for $f < 0$. The factor of 2 comes in because we consider only positive values of frequency hence the name "one-sided". The noise power which would have been in the negative frequencies is added to the positive frequencies and so there is a factor of 2. This prevents any noise power information from being lost. Up to a scaling factor of 2, $S_{\mathrm{n}}(f)$ can also be thought of as the Fourier transform of the autocorrelation function of the noise amplitude data. By calculating $\sqrt{S_{\mathrm{n}}(f)}$ using Equation (3.48), one can generate the sensitivity curves seen in Figure 3.2.

Chapter 4

Fluid dynamics overview

4.1 Equations of motion

It is believed that NSs are born as hot balls of fluid that rotate at great speed. As the NS cools over time, a solid crust forms but the core remains fluid. With the crust being ~ 1 km thick from a radius of ~ 10 km, the whole NS can be approximately governed by fluid dynamics. For something to be fluid means that it does not build a strain whenever stress is applied to it. In this section, we state the basic fluid equations for a non-relativistic (Newtonian) fluid. Of course, this is not the case for a real NS as the strong gravity around it gives rise to relativistic effects, but for us, we will keep within the Newtonian regime for simplicity. One can re-do the analysis in GR once the proof of concept has been established but we will not do this here.

A non-dissipative fluid can be described solely by its mass density $\rho(\mathbf{x}, t)$, velocity $\mathbf{v}(\mathbf{x}, t)$, pressure $P(\mathbf{x}, t)$ and gravitational potential $\Phi(\mathbf{x}, t)$. There are 4 equations that connects all 4 variables to each other and they are: the continuity equation, Euler's equation, Poisson's equation for gravity and the equation of state (EOS). Overall, they encompass the behaviour of fluids and encode the conservation of energy and momentum.

First is the continuity equation

$$\frac{\partial \rho}{\partial t} + \boldsymbol{\nabla} \cdot (\rho \mathbf{v}) = 0 \,. \tag{4.1}$$

This is a statement about the conservation of mass. It says that the rate at which fluid mass enters a region is equal to the mass which leaves the same region. Next is Euler's equation

$$\rho \frac{d\mathbf{v}}{dt} = -\boldsymbol{\nabla} P - \rho \boldsymbol{\nabla} \Phi \tag{4.2}$$

which is essentially Newton's 2nd law but for a fluid. The left hand side represents the resultant force (per unit volume) due to pressure gradients and gravitational potential gradients. The left hand side of Equation (4.2) uses the total (or convective) derivative defined as

$$\frac{d}{dt} = \frac{\partial}{\partial t} + \mathbf{v} \cdot \boldsymbol{\nabla} \, . \tag{4.3}$$

This convective derivative captures changes to a variable as we follow a fluid element around. The first term represents the changes to a fluid element if it were not following the fluid and the second term represents additional changes due to the movement of the fluid element. For this reason, sometimes $\frac{d}{dt}$ is called the Lagrangian time derivative and $\frac{\partial}{\partial t}$ is called the Eulerian time derivative, as will become clear in Section 4.2.

Poisson's equation for gravity is

$$\nabla^2 \Phi = 4\pi G \rho \, . \tag{4.4}$$

This is a type of field equation that relates how a field (gravitational potential field) behaves in the presence of a source term (mass density). This is exactly the same as Einstein's field equations (Equation (3.1)) but in the Newtonian limit.

Finally, we have the EOS, which generically for a non-dissipative fluid is

$$P = P(\rho) \, . \tag{4.5}$$

The exact form of the EOS depends on the detailed microscopic modelling of the physics within the fluid.

4.2 Eulerian and Lagrangian perturbations

Along with a set of initial conditions, stationary solutions for a fluid system can found using the 4 equations in Section 4.1. However, to find out more about the system, one might want to perturb it to see what results (e.g. Chandrasekhar, 1969). For a fluid variable, Q, there are two formalisms for the perturbations we apply: Eulerian perturbations (δQ) and Lagrangian perturbations (ΔQ). Throughout this subsection and the next, we will keep to 1st order in our small expansion parameter, $\boldsymbol{\xi}$, which will be defined shortly.

The Eulerian formalism measures the change of a variable at a fixed point in space. For example, if we had a 2D Cartesian coordinate system, we would always be measuring how the mass density changes at (1,0). If Q_0 is the value of the variable before the perturbation, then an Eulerian perturbation to Q_0 is defined as

$$\delta Q(\mathbf{x}, t) \equiv Q(\mathbf{x}, t) - Q_0(\mathbf{x}, t) \, . \tag{4.6}$$

Alternatively, we have the Lagrangian formalism where we measure changes to a variable as we follow a fluid element around (like the convective derivative in Equation (4.3)). Using the same example as before, if we wanted to know the Lagrangian change to the mass density at (1,0) for a fluid which has been perturbed by a radial enlargement of factor 2, then we would measure the mass density at (2,0) and subtract the mass density at (1,0). Mathematically, this is written as

$$\Delta Q(\mathbf{x}, t) \equiv Q(\mathbf{x} + \boldsymbol{\xi}, t) - Q_0(\mathbf{x}, t) \tag{4.7}$$

where $\boldsymbol{\xi}$ is the (spatial) displacement vector, which can be a function of position and time, $\boldsymbol{\xi} = \boldsymbol{\xi}(\mathbf{x}, t)$ and is much smaller in magnitude when compared to the position vector, $|\boldsymbol{\xi}| \ll |\mathbf{x}|$. We can relate Eulerian and Lagrangian perturbations when we Taylor expand Equation (4.7)

$$\Delta Q(\mathbf{x}, t) \approx [Q(\mathbf{x}, t) + \boldsymbol{\xi} \cdot \boldsymbol{\nabla} Q(\mathbf{x}, t)] - Q_0(\mathbf{x}, t) \tag{4.8}$$

which, with the help of Equation (4.6), simplifies down to the 1st order operator relation

$$\Delta = \delta + \boldsymbol{\xi} \cdot \boldsymbol{\nabla} \tag{4.9}$$

when operating on fluid variable Q.

4.3 Perturbed integral quantities

Say an integral in an unperturbed fluid is (e.g. Shapiro and Teukolsky, 1983)

$$I_0 \equiv \int_V Q_0(\mathbf{x}, t) d\mathbf{x} \tag{4.10}$$

where V represents the unperturbed volume, then the equivalent integral but in a perturbed fluid is

$$I \equiv \int_{V+\Delta V} Q(\mathbf{x}, t) d\mathbf{x} \tag{4.11}$$

where ΔV is the additional volume created by perturbing the boundary of V by $\boldsymbol{\xi}$. The first variation of the integral is written as δI (not to be confused with an Eulerian perturbation) and is defined as

$$\delta I \equiv \int_{V+\Delta V} Q(\mathbf{x}, t) d\mathbf{x} - \int_V Q_0(\mathbf{x}, t) d\mathbf{x} \,. \tag{4.12}$$

We can simplify this further by making both integrals over the same volume which we choose to be the unperturbed volume, V. This requires us to make the transformation, $\mathbf{x}' = \mathbf{x} - \boldsymbol{\xi}(\mathbf{x})$, which ensures the first integral is conducted over the unperturbed volume. Substituting $\mathbf{x} = \mathbf{x}' + \boldsymbol{\xi}(\mathbf{x})$ and introducing the Jacobian, J, due to our change in

coordinates, we get

$$\delta I = \int_V Q(\mathbf{x}' + \boldsymbol{\xi}, t) J d\mathbf{x}' - \int_V Q_0(\mathbf{x}, t) d\mathbf{x} \,. \tag{4.13}$$

The Jacobian is given by

$$J = \frac{\partial \mathbf{x}}{\partial \mathbf{x}'} = \frac{\partial(\mathbf{x}' + \boldsymbol{\xi}(\mathbf{x}))}{\partial \mathbf{x}'} = 1 + \boldsymbol{\nabla}' \cdot \boldsymbol{\xi}(\mathbf{x}) \approx 1 + \boldsymbol{\nabla}' \cdot \boldsymbol{\xi}(\mathbf{x}') \tag{4.14}$$

to 1st order in $\boldsymbol{\xi}$ and where $\boldsymbol{\nabla}'$ represents the gradient operator in $\mathbf{x}'$ coordinates. Applying Equations (4.14) and (4.7) to Equation (4.13) and relabelling $\mathbf{x}' \to \mathbf{x}$, we get the final result of

$$\delta I \approx \int_V \left[\Delta Q(\mathbf{x}, t) + (\boldsymbol{\nabla} \cdot \boldsymbol{\xi}) Q(\mathbf{x}, t)\right] d\mathbf{x} \tag{4.15}$$

where again, we have kept only 1st order terms in $\boldsymbol{\xi}$. For an incompressible fluid, $\boldsymbol{\nabla} \cdot \boldsymbol{\xi} = 0$ so we can simplify to

$$\delta I = \int_V \Delta Q(\mathbf{x}, t) d\mathbf{x} \,. \tag{4.16}$$

There is one final perturbed integral quantity which we will see multiple times so we will highlight it now. The aforementioned perturbed integral is any of the form $\delta \int_V \rho Q \, d\mathbf{x}$. To simplify this, we first need to look at the conservation of mass. We know that mass can be written as

$$M = \int_V \rho d\mathbf{x} \tag{4.17}$$

and when we perturb a system, we wish to conserve mass, so

$$\delta M = \delta \int_V \rho d\mathbf{x} = 0 \,. \tag{4.18}$$

Setting $Q \to \rho$ in Equation (4.15) and invoking the conservation of mass, we get the relation

$$\Delta\rho + (\boldsymbol{\nabla} \cdot \boldsymbol{\xi})\rho = 0 \,. \tag{4.19}$$

Repeating the same procedure but setting $Q \to \rho Q$ in Equation (4.15) will give us

$$\delta \int_V \rho Q \, d\mathbf{x} = \int_V \left[\rho \Delta Q + Q \left\{\Delta\rho + (\boldsymbol{\nabla} \cdot \boldsymbol{\xi})\rho\right\}\right] d\mathbf{x} \tag{4.20}$$

but we know the terms in the braces equate to zero by Equation (4.19). This then leaves the simple relation

$$\delta \int_V \rho Q \, d\mathbf{x} = \int_V \rho \Delta Q \, d\mathbf{x} \,. \tag{4.21}$$

Chapter 5

Gravitational waves from transient mountains

From here on in, we cover topics that are novel and original. As mentioned previously, in this thesis we are looking to create models that are based off astrophysical observations and have some element of GW emission. The first of the new models is the transient mountain model which can explain glitch recoveries and give rise to *transient* CWs (Prix et al., 2011). This work led to a paper being published in Monthly Notices of the Royal Astronomical Society (Yim and Jones, 2020) and a large part of this chapter is taken from there.

5.1 Introducing the transient mountain model

As mentioned in Section 2.2, NSs glitch from time to time. This means its spin frequency, ν, measured in Hz, rapidly increases and is thought to be due to vortex unpinning or starquakes (Section 2.2.2). Then, for some glitches, especially from younger NSs, there often follows an exponential recovery where the spin frequency recovers back to, but never quite reaches, the spin frequency prior to the glitch. This recovery is commonly associated with vortex creep (Section 2.2.3).

Accompanying the positive change to the spin frequency, $\Delta\nu(t_g) > 0$, there is normally a simultaneous negative change to the time derivative of the spin frequency, $\Delta\dot{\nu}(t_g) < 0$, or alternatively, an increase to the spin-down rate, $\Delta|\dot{\nu}|(t_g) > 0$, where t_g is the time of the glitch. In this chapter, the Δ represents changes due to the glitch.

As for GWs, we learnt in Section 3.4 that there are GWs of different types and different time-scales. CBC GWs and burst GWs are both short relative to CWs which last much longer than the time spent observing them. Stochastic GWs are the most extreme in the sense that they are always present.

The longer a GW signal lasts, the more chance you have of detecting it (the SNR increases as the square-root of the time spent observing the signal). However, unlike CBC GWs and CWs, burst GWs and stochastic GWs are unmodelled which makes them more difficult to detect. CBC GWs and CWs are typically modelled so matched-filtering can be used to detect them. This means getting a template (matched-filter) and matching it to the data. A goodness-of-fit can be evaluated for each template and when the match statistic exceeds a threshold, one can say a detection has been made. So far only CBC GWs have been detected (Abbott et al., 2019a).

Besides the above types of GWs, there is another category of modelled GWs which Prix et al. (2011) named "transient CWs". These are GWs with durations between CBC GWs and CWs, meaning on the order of hours to weeks. As to how they are modelled, transient CWs are essentially shorter versions of conventional CWs so have the same quasi-monochromatic behaviour. This means, generally, transient CWs have signals of the form

$$h(t) = h_0(t_s)\mathcal{W}(t; t_s, t_f)\sin(2\pi f \Delta t) \tag{5.1}$$

where $h_0(t_s)$ is the GW amplitude at the start of the signal, $\mathcal{W}(t; t_s, t_f)$ is some window function starting at $t = t_s$ and finishing at $t = t_f$, f is the GW frequency and $\Delta t = t - t_s$ is the time elapsed since the signal began.

So far, there has been little theoretical modelling of how these transient CWs come about. It has been suggested that pulsar glitches could be the trigger since glitch recovery time-scales naturally fall within the range covered by transient CWs. Models using glitches include Ekman flow[1] within the NS (van Eysden and Melatos, 2008; Bennett et al., 2010; Singh, 2017) and also a toy model where the excess superfluid energy from a glitch could seed a non-axisymmetric deformation leading to transient CW emission (Prix et al., 2011). It has been suggested that magnetar flares producing polar Alfvén waves could cause transient CWs too (Kashiyama and Ioka, 2011).

It is clear there are not many models for transient CWs but nevertheless, there have been attempts to detect them. Most recently, Keitel et al. (2019) tried to find transient CWs in the glitch recoveries of the Crab and Vela pulsars but unfortunately, no transient CWs were detected. Abbott et al. (2019c) did a similar search but for unmodelled transient GWs after the binary NS merger GW170817, for durations of up to 8.5 days. Again, no transient GWs were detected.

So, there is an interest to detect transient CWs but the theory is lacking. This is especially the case when it comes to trying to explain both the transient CWs and the observed glitch recovery simultaneously. Those that exist generally depend on some internal mechanism for it to work and quite often, this leads to models being difficult

[1] Ekman flow is the bulk movement of fluid due to some tangential force. In a two-component NS, the tangential force comes from the viscous shear force between the crust and core.

to falsify since the interior of NSs cannot be directly observed. We therefore task ourselves with creating a new model which is simple and makes precise and falsifiable predictions.

In its most basic form, our model, the transient mountain model, only concerns the *glitch recovery* and is *agnostic to what causes the glitch*[2]. The sudden increase to the spin-down rate at the moment of the glitch we propose is due to the *instantaneous* formation of a non-axisymmetric mountain (a $l = 2$, $m = 2$ deformation in the language of spherical harmonics). Such a mountain would create a braking torque on the NS which acts to spin the NS down. Then, we propose the mountain decays away exponentially, on a time-scale similar to the glitch recovery time-scale. As the mountain decays, the braking torque, and hence the rate of spin-down, is reduced and it is this which results in the observed exponential glitch recovery. For a mountain that completely decays away, the spin-down rate will recover to the pre-glitch value. On the other hand, a remnant or "permanent" mountain causes the spin-down rate to be greater after the glitch has fully recovered, leading to a more negative gradient of the spin frequency at times long after the glitch. Right now, we do not focus on the mechanism which creates the mountain or causes it to decay, rather, we are looking at the consequences if such a transient mountain exists. In Chapter 7, we will return to this matter and explore the plausibility of building the mountain from an energetics point of view.

This chapter will be divided as follows. Section 5.2 introduces the relevant equations from radio pulsar astronomy that explain glitches and their subsequent recovery. Section 5.3 looks at the dynamics of the system which allows us to calculate the ellipticity required to cause the glitch recovery. This, in turn, tells us the GW strain achievable. In Section 5.4, we find an expression for the total GW energy radiated away by a transient mountain. In Section 5.5, we calculate the SNR achievable in a GW detector. In Section 5.6, we apply our model to radio data and give a table of results including the SNRs for Crab and Vela glitches for both aLIGO and the Einstein Telescope (ET). In Section 5.7, we discuss the predictions and limitations of our model. Finally, Section 5.8 summarises the results of this work and concludes with some final remarks on future prospects of this research.

5.2 The glitch model from radio astronomy

Timing a pulsar requires accurate modelling of the rotational dynamics of a NS. One well-known property of NSs is that they spin-down on secular time-scales. This is thought to be primarily due to magnetic dipole radiation (Section 2.1.2) though searches are being performed to see if CWs could also play a role (e.g. Abbott et al., 2020). This

[2]Possible glitch mechanisms include starquakes and vortex unpinning, but these precise details are not covered since we are concerned only with the post-glitch recovery. Future improvements to the model will look to incorporate a specific glitch mechanism.

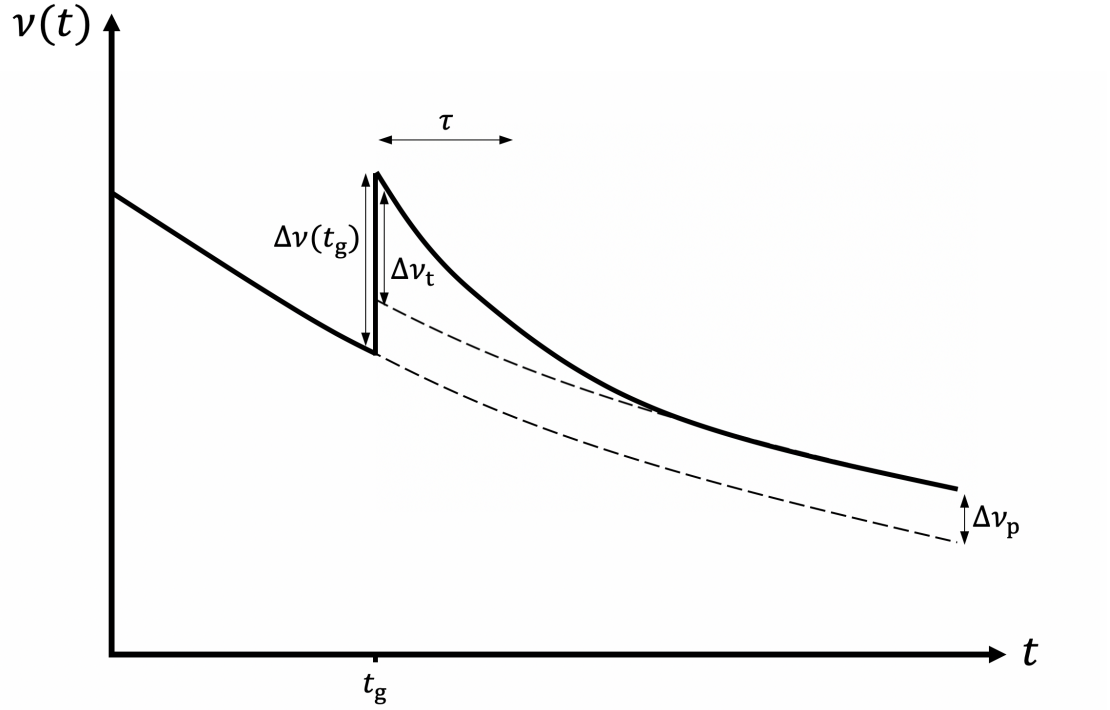

FIGURE 5.1: The graph shows how the spin frequency of a NS changes as a function of time when there is a glitch. There are two parts, one being the secular spin-down (shown by the lower dashed line) and the other being the glitch. $\Delta\nu(t_g)$ is the total change in spin frequency at the time of the glitch, which is made up of a permanent part, $\Delta\nu_p$, and a transient part, $\Delta\nu_t$. $\Delta\nu_t$ exponentially decays away with a time-scale of τ. Also, the permanent change to the time derivative of the spin frequency, $\Delta\dot{\nu}_p$, has been set to $\Delta\dot{\nu}_p = 0$ in the above graph, which has been assumed for most of our analysis.

secular spin-down is represented by the lower dashed line in Figure 5.1. Since we are only interested in glitches (which have much shorter time-scales), we can subtract the secular spin-down to leave the change in the spin frequency due to the glitch, $\Delta\nu(t)$, represented phenomenologically by

$$\Delta\nu(t) = \begin{cases} 0\,, & \text{if } t < t_g \\ \Delta\nu_p + \Delta\dot{\nu}_p \cdot \Delta t + \Delta\nu_t e^{-\frac{\Delta t}{\tau}}\,, & \text{if } t \geq t_g \end{cases} \tag{5.2}$$

where $\Delta t = t - t_g$ is the time elapsed after the glitch with t_g being the time of the glitch. $\Delta\nu_p$ refers to the change in spin frequency which is permanent due to the glitch and $\Delta\nu_t$ is the same but refers to the transient part, i.e. the change in the spin frequency which fully recovers on time-scales much larger than the recovery time-scale of the glitch, τ. The product $\Delta\dot{\nu}_p \cdot \Delta t$ represents the contribution to $\Delta\nu(t)$ due to a permanent change in the spin-down rate caused by the glitch, $\Delta\dot{\nu}_p$. From this formulation, it is seen at $t = t_g$, we get the relation

$$\Delta\nu(t_g) = \Delta\nu_p + \Delta\nu_t\,. \tag{5.3}$$

We can then differentiate Equation (5.2) to get the time derivative of the spin frequency,

$\Delta\dot{\nu}(t)$, and in the regime of $t \geq t_g$, we have

$$\Delta\dot{\nu}(t) = \Delta\dot{\nu}_p - \frac{\Delta\nu_t}{\tau} e^{-\frac{\Delta t}{\tau}} . \tag{5.4}$$

From this, we associate the coefficient of the time-dependent term to be equal to the transient change in the spin-down rate, $\Delta\dot{\nu}_t$, which is given by

$$\Delta\dot{\nu}_t \equiv -\frac{\Delta\nu_t}{\tau} \tag{5.5}$$

such that $\Delta\dot{\nu}(t) = \Delta\dot{\nu}_p + \Delta\dot{\nu}_t e^{-\frac{\Delta t}{\tau}} = \Delta\dot{\nu}_p + \Delta\dot{\nu}_t(t)$. There is a slight subtlety in the notation here since we have explicitly used parentheses to represent a time-dependence, e.g. $\Delta\dot{\nu}_t(t)$ depends on time but $\Delta\dot{\nu}_t = \Delta\dot{\nu}_t(t_g)$ is a constant. The phenomenological glitch model above (or slight variants of it) have been established for a long time, having been used to model the first few glitches of the Crab pulsar (Boynton et al., 1972) and the Vela pulsar (Downs, 1981). Even now, it is still being used in pulsar timing softwares such as TEMPO2 (Edwards et al., 2006).

Our analysis uses publicly available glitch data from the JBCA Glitch Catalogue (Espinoza et al., 2011). Within this catalogue are values for $\frac{\Delta\nu(t_g)}{\nu_0}$ and $\frac{\Delta\dot{\nu}(t_g)}{\dot{\nu}_0}$ for each glitch of a given pulsar. Respectively, ν_0 and $\dot{\nu}_0$ are the measured values of the spin frequency and the time derivative of the spin frequency immediately before the glitch. However, there is an issue using this data since we are not told exactly how much of $\Delta\nu(t_g)$ and $\Delta\dot{\nu}(t_g)$ is due to a transient part and how much of it is due to a permanent part. We therefore require more data and for us, it will be in the form of the healing parameter, $\mathcal{Q}$.

By definition, $\mathcal{Q}$ is defined as

$$\mathcal{Q} \equiv \frac{\Delta\nu_t}{\Delta\nu(t_g)} \tag{5.6}$$

where the numerator represents the change in spin frequency which will "heal" at $t \gg t_g$ and the denominator represents the total change in spin frequency at $t = t_g$ which is the sum of permanent and transient parts, as seen in Equation (5.3). Therefore, a glitch which recovers completely has $\mathcal{Q} = 1$ and a glitch showing no recovery whatsoever has $\mathcal{Q} = 0$.

We can substitute Equation (5.6) into Equation (5.5) to relate our unknowns ($\Delta\dot{\nu}_t$, $\Delta\nu_t$) to our observables ($\mathcal{Q}$, $\Delta\nu(t_g)$) to get the relations

$$\Delta\dot{\nu}_t\tau = -\Delta\nu_t = -\mathcal{Q}\Delta\nu(t_g) . \tag{5.7}$$

τ makes an appearance in Equation (5.7) and it can either be treated as known or unknown. It is known when radio observations are frequent enough to acquire τ directly

from the data. However, this is not the case for most glitches as the exponential recovery is sometimes missed, or if too few observations are made during the glitch recovery to allow a reliable fit. If it is unknown, then we can use Equation (5.7) to approximate τ, see Section 5.7. Throughout this analysis, we will treat τ as unknown but if it is known in reality, then our model provides an independent value of τ which can be checked for consistency and guide future transient CW searches.

5.3 Ellipticity and gravitational wave strain

In this section, we focus on calculating the ellipticity and GW strain obtainable from transient mountains in terms of our observables. It will help at this point if we remind ourselves of the steps of the model: 1) a NS glitches (we are agnostic to what causes this), 2) a transient mountain immediately forms, 3) transient CWs are emitted whilst the transient mountain decays away at a similar rate as the glitch recovery.

It is well-known that a NS mountain will emit CWs at twice the NS's spin frequency, $f = 2\nu$ (e.g. Shapiro and Teukolsky, 1983). A mountain also creates an extra braking torque on the system which we assume explains the glitch recovery. Basic mechanics tells us that the torque, $\mathcal{N}$, is related to power (or in our case GW luminosity) by the equation $L = -\mathcal{N}\Omega$ (for $L > 0$) where Ω is the angular velocity of the NS. It can also be shown (e.g. Shapiro and Teukolsky, 1983) that the GW luminosity due to a mountain is

$$L_{\mathrm{GW}}(t) = \frac{(2\pi)^6}{10}\frac{G}{c^5} I^2 f^6 \varepsilon^2(t) \tag{5.8}$$

where I represents the moment of inertia about the rotation axis, f is the GW frequency of the emitted CWs and $\varepsilon(t)$ is the dimensionless *equatorial* ellipticity of the NS (see Equation (B.5) for the definition in terms of moment of inertias about the principal axes).

By taking out a factor of $\Omega = 2\pi\nu = \pi f$ from Equation (5.8), multiplying throughout by -1 and using $f \approx 2\nu_0$, we get the torque due to a NS mountain

$$\mathcal{N}_{\mathrm{mountain}}(t) = -\frac{32(2\pi)^5}{5}\frac{G}{c^5}\, I^2 \nu_0^5 \varepsilon^2(t)\,. \tag{5.9}$$

Also from mechanics, we know $\mathcal{N} = \dot{I}\Omega + I\dot{\Omega}$ in general. However, as we show in Appendix A, during the glitch recovery we can associate the change in torque solely to a change in the spin-down rate caused by a transient mountain which means

$$\Delta\mathcal{N}(t) = 2\pi I \Delta\dot{\nu}_{\mathrm{t}}(t) \tag{5.10}$$

where we have ignored the effect of $\Delta\dot{I}$, $\Delta\Omega$ and ΔI and specialised to transient mountains only. The physical reasoning for this is because changes in the torque caused by

changes in the moment of inertia or spin frequency are negligible when compared to changes caused by the spin-down rate. This is shown numerically for two very different glitchers, the Crab and Vela pulsars, in Appendix A. It is also worth noting that the internal superfluid is important during glitches and can cause changes to the NS's moment of inertia (e.g. Link et al., 1999; Andersson et al., 2012). However, our model only concerns the change of the shape of the NS during the glitch recovery and omits details about the interior, as the change in shape is what we ascribe to the glitch recovery.

Since our model associates the change in torque purely to a transient mountain, we equate the left hand sides of Equations (5.9) and (5.10). This allows us to find an expression for the ellipticity for $t \geq t_g$ which is

$$\varepsilon(t) = \sqrt{-\frac{5}{32(2\pi)^4}\frac{c^5}{G}\frac{1}{I}\frac{\Delta\dot{\nu}_t(t)}{\nu_0^5}}\,. \tag{5.11}$$

Note that this means our model will only apply to pulsars rotating fast enough, as slow rotators will give a value of $\varepsilon(t)$ that would be problematically large in terms of the physics. Conventional long-lasting mountains have a maximum possible size that is linked to the maximum strain the crust can endure and typically yields maximum values of $\varepsilon_{\max} \sim 10^{-6} - 10^{-5}$ (e.g. Johnson-McDaniel and Owen, 2013). However, as our transient mountains exists for a shorter duration, there may be some non-stationary solution that permits their existence, even if greater than $\varepsilon_{\max}$. The best situation would be to have a pulsar that rotates fast enough such that $\varepsilon(t)$ falls below the maximum allowed for conventional mountains, though this is not essential if there are non-stationary mechanisms at play. Assuming $\varepsilon_{\max} \sim 10^{-5}$, then for both Crab-like and Vela-like glitches, we require $\nu \gtrsim 40$ Hz.

Since $\Delta\dot{\nu}_t(t)$ is in the expression for $\varepsilon(t)$ and $\Delta\dot{\nu}_t(t)$ is unknown, we will set $\Delta\dot{\nu}_t(t) = \Delta\dot{\nu}(t)$ to give us an approximation for the ellipticity from a transient mountain. This means we assume the entire change in the spin-down rate is purely transient, i.e. no permanent mountains are formed which would be associated with $\Delta\dot{\nu}_p$ within the framework of our model. As mentioned later in a footnote of Section 5.7, this is true for most glitches besides the largest glitches from the Crab where there appears to be a linear relationship between $\Delta\dot{\nu}_p$ and $\Delta\nu$ (Lyne et al., 2015). We can then rearrange in terms of how the JBCA Glitch Catalogue reports glitch values, as well as setting $t = t_g$, to get the ellipticity at the moment of the glitch which is

$$\varepsilon_{\text{approx}}(t_g) = \sqrt{-\frac{5}{32(2\pi)^4}\frac{c^5}{G}\frac{1}{I}\frac{\dot{\nu}_0}{\nu_0^5}\left(\frac{\Delta\dot{\nu}(t_g)}{\dot{\nu}_0}\right)}\,. \tag{5.12}$$

Now that we have the ellipticity, we can calculate the GW strain, $h_0(t)$. In general, a given $\varepsilon(t)$ sources a GW strain of

$$h_0(t) = (2\pi)^2 \frac{G}{c^4} \frac{If^2}{d} \varepsilon(t) \tag{5.13}$$

where d is the distance to the source (e.g. Jaranowski et al., 1998). We can then substitute the ellipticity, Equation (5.11), into Equation (5.13) to find the corresponding GW strain at $t \geq t_g$ which is

$$h_0(t) = \sqrt{-\frac{5}{2} \frac{G}{c^3} \frac{I}{d^2} \frac{\Delta\dot{\nu}_t}{\nu_0}} e^{-\frac{\Delta t}{2\tau}} \tag{5.14}$$

where we have used $\Delta\dot{\nu}_t(t) = \Delta\dot{\nu}_t e^{-\frac{\Delta t}{\tau}}$. Note that $h_0(t) \propto e^{-\frac{\Delta t}{2\tau}}$ and not $h_0(t) \propto e^{-\frac{\Delta t}{\tau}}$ as one might originally think. This implies $\tau_{GW} = 2\tau_{radio}$, see Section 5.7. This is due to $\Delta\dot{\nu}_t(t)$ being square-rooted in the expression for $\varepsilon(t)$, as per Equation (5.11). Finally, we can get an approximation for the GW strain at the moment of the glitch by using $\Delta\dot{\nu}_t = \Delta\dot{\nu}(t_g)$ which gives

$$h_{0,\text{approx}}(t_g) = \sqrt{-\frac{5}{2} \frac{G}{c^3} \frac{I}{d^2} \frac{\dot{\nu}_0}{\nu_0} \left(\frac{\Delta\dot{\nu}(t_g)}{\dot{\nu}_0} \right)} \,. \tag{5.15}$$

5.4 Total gravitational wave energy from the glitch recovery

We now proceed on to calculating how much energy is available for the emission of GWs due to the loss of kinetic energy during the glitch recovery. We do not include in our calculation any energy which might be liberated during the glitch or required for the formation of transient mountains since these values require more detailed calculations. We will return to this in Chapter 7.

We begin with the simple expression for the rotational kinetic energy, $E_{rot} = \frac{1}{2} I\Omega^2$. Any instantaneous loss (hence minus sign) of rotational kinetic energy we can write as a luminosity $L(> 0)$ by differentiating with respect to time leading to

$$L = -4\pi^2 I \nu \dot{\nu} \,. \tag{5.16}$$

In particular, we are interested in the GW luminosity achievable due to a mountain which we attribute to having a negative $\Delta\dot{\nu}$. We can also get a change in the luminosity if there is a change in I or ν. However, as demonstrated in Appendices A and B, we are allowed to ignore the contributions due to ΔI and $\Delta\nu$ as these will be negligible.

The change in luminosity due to the glitch, ΔL, can therefore be written as

$$\Delta L(t) = -4\pi^2 I \nu_0 \Delta\dot{\nu}_t(t) \tag{5.17}$$

where we have put time-dependence into the equation and specialised to transient mountains only. This means we are only tracking the GWs due to transient mountains and not from any permanent mountains which arise due to a permanent change in the spin-down rate (these would give conventional CWs).

We can now integrate Equation (5.17) across all time to get the GW energy due to a transient mountain and using $\Delta\dot{\nu}_{\rm t}(t) = \Delta\dot{\nu}_{\rm t} e^{-\frac{\Delta t}{\tau}}$, we get

$$E_{\rm GW} = -4\pi^2 I \nu_0 \Delta\dot{\nu}_{\rm t} \tau = 4\pi^2 I \nu_0 \Delta\nu_{\rm t} \tag{5.18}$$

and using Equation (5.7) we can relate the unknowns to our observables giving the final result of

$$E_{\rm GW} = 4\pi^2 I \nu_0 \mathcal{Q} \Delta\nu(t_{\rm g}) \tag{5.19}$$

or when put in terms of how the JBCA Glitch Catalogue reports measurements, we get

$$E_{\rm GW} = 4\pi^2 I \nu_0^2 \mathcal{Q} \left(\frac{\Delta\nu(t_{\rm g})}{\nu_0} \right) . \tag{5.20}$$

Note that Equation (5.19) can be seen as the answer you would get if you were to naïvely find the change in the rotational kinetic energy, but with an additional factor of $\mathcal{Q}$ to account for the partial recovery of the glitch.

5.5 Signal-to-noise ratio

Next, we relate the GW energy to the optimal[3] SNR achievable. We follow the steps of Prix et al. (2011) but apply it to our transient mountain model instead of their superfluid excess energy model. Additionally, we account for the effects of having multiple detectors and non-perpendicular interferometer arms which were not considered previously.

For a CW with a time-varying GW amplitude, $h_0(t)$, the geometrical-average of the optimal SNR squared, $\langle \rho_0^2 \rangle$, is commonly written as

$$\langle \rho_0^2 \rangle = \frac{4}{25} \frac{1}{S_{\rm n}(f)} \int_0^{T_{\rm obs}} h_0^2(t) dt \tag{5.21}$$

where the angled brackets represents an average over geometrical parameters which are the right ascension, declination, polarisation angle and inclination of the source. This is what is responsible for the factor of $\frac{4}{25}$ which otherwise would not be there if the SNR was not averaged (Jaranowski et al., 1998; Prix et al., 2011). $S_{\rm n}(f)$ is the GW detector's noise power spectral density which is a measure of how much noise the

[3] The SNR is optimal when the matched-filter exactly describes the data. Whenever there is a mismatch, the SNR becomes sub-optimal. See Figure 1 of Prix et al. (2011).

detector picks up at a given GW frequency, f. T_{obs} is the duration for which we observe the source. We eventually set $T_{\text{obs}} \to \infty$ to ensure we capture the entire transient CW.

Equation (5.21) is used frequently within the literature though it does not fully capture the effects which apply to us here in this analysis. The ET is a 3rd-generation GW detector which will consist of three identical interferometers, each with a pair of arms with an opening angle of 60°, arranged in a triangle such that two arms share the same side of the triangle (Freise et al., 2009). The fact that we have multiple detectors increases the SNR and an opening angle less than 90° decreases the SNR. Combining both these effects changes Equation (5.21) into

$$\langle \rho_0^2 \rangle = \frac{4}{25} \frac{N \sin^2 \zeta}{S_{\text{n}}(f)} \int_0^{T_{\text{obs}}} h_0^2(t) dt \tag{5.22}$$

where N is the number of independent interferometers and ζ is the opening angle between the arms of the interferometer. The $\sin^2 \zeta$ factor can also be found in Jaranowski et al. (1998). It is important we account for this as the $S_{\text{n}}(f)$ data for the ET is for a single 90° interferometer[4], even though in reality the ET is made up of three 60° interferometers (Hild et al., 2011).

We now need to evaluate the integral in Equation (5.22). To do this, we directly substitute for $h_0(t)$ using Equation (5.14) followed by Equation (5.7) to get

$$\langle \rho_0^2 \rangle = \frac{2}{5} \frac{G}{c^3} \frac{N \sin^2 \zeta}{S_{\text{n}}(2\nu_0)} \frac{I}{d^2} \mathcal{Q} \left(\frac{\Delta \nu(t_{\text{g}})}{\nu_0} \right) \tag{5.23}$$

which is the SNR (squared) in terms of the observables within our model.

Alternatively, we can utilise the GW energy we calculated in Section 5.4. Equation (5.8) gives the GW luminosity as a function of $\varepsilon(t)$, but $\varepsilon(t)$ is related to $h_0(t)$ through Equation (5.13). We can therefore write the GW luminosity as a function of $h_0(t)$ and integrate to get an expression for the GW energy. This gives

$$E_{\text{GW}} = \frac{2\pi^2}{5} \frac{c^3}{G} f^2 d^2 \int_0^{T_{\text{obs}}} h_0^2(t) dt \, . \tag{5.24}$$

We rearrange for the integral and substitute the integral into Equation (5.22) to get

$$\langle \rho_0^2 \rangle = \frac{2}{5\pi^2} \frac{G}{c^3} \frac{N \sin^2 \zeta}{S_{\text{n}}(f)} \frac{E_{\text{GW}}}{f^2 d^2} \tag{5.25}$$

Finally, we substitute in the GW energy calculated in Equation (5.19) and we get the same answer as Equation (5.23). This alternative method is perhaps more powerful than the first as Equations (5.24) and (5.25) are completely agnostic with regard to the

[4]The ET-D sensitivity curve was taken from `http://www.et-gw.eu/index.php/etsensitivities`.

time-dependence of $h_0(t)$ (since we substituted the entire integral). For the same reason, Equation (5.25) is valid even if we integrate over a short period of time. In other words, it means that we accumulate more SNR the longer the observation is. Equation (5.25) agrees with Equation (4) in Prix et al. (2011) besides the factor of $N \sin^2 \zeta$ which we added in here.

To bring familiarity to all this, we can also express our results in terms of a measure of the GW strain used in burst searches, since after all, transient CWs are essentially just a long burst. The measure used is called the root-sum-squared of the GW *amplitude*, $h_{0,\mathrm{rss}}$, which is defined as

$$h_{0,\mathrm{rss}}^2 \equiv \int_0^{T_{\mathrm{obs}}} h_0^2(t) dt \, . \tag{5.26}$$

Similarly, we can define the geometrically-averaged $h_{0,\mathrm{rss}}^2$ as

$$\langle h_{0,\mathrm{rss}}^2 \rangle \equiv \frac{4}{25} \int_0^{T_{\mathrm{obs}}} h_0^2(t) dt = \frac{4}{25} h_0^2(t_{\mathrm{g}}) \tau \tag{5.27}$$

such that

$$\langle \rho_0^2 \rangle \equiv N \sin^2 \zeta \frac{\langle h_{0,\mathrm{rss}}^2 \rangle}{S_{\mathrm{n}}(f)} = \frac{4}{25} N \sin^2 \zeta \frac{h_0^2(t_{\mathrm{g}}) \tau}{S_{\mathrm{n}}(f)} \tag{5.28}$$

where the last equalities in Equations (5.27) and (5.28) come from using our transient mountain model and setting $T_{\mathrm{obs}} \to \infty$. The first equality in Equation (5.28) can be seen from combining Equation (5.22) and the definition in Equation (5.27).

We can check for consistency by substituting our expression for $h_0(t_{\mathrm{g}})$ from Equation (5.13) and then using Equation (5.7) to get the SNR in terms of observables. After doing that, we find that the right hand side of Equation (5.28) gives the same answer as Equation (5.23). In terms of our observables, $\langle h_{0,\mathrm{rss}}^2 \rangle$ can explicitly be written as

$$\langle h_{0,\mathrm{rss}}^2 \rangle = \frac{2}{5} \frac{G}{c^3} \frac{I}{d^2} \mathcal{Q} \left(\frac{\Delta \nu(t_{\mathrm{g}})}{\nu_0} \right) \, . \tag{5.29}$$

The benefit of calculating $\langle h_{0,\mathrm{rss}}^2 \rangle$ is that it has the same units as $S_{\mathrm{n}}(f)$ which are units of Hz^{-1}. This then allows us to plot both quantities on the same set of axes allowing a visual comparison between the two terms. In fact, if we plot $\sqrt{\langle h_{0,\mathrm{rss}}^2 \rangle}$ and $\sqrt{\frac{S_{\mathrm{n}}(f)}{N \sin^2 \zeta}}$ on the same axes, then the ratio of the two gives exactly the SNR.

In reality, there is some SNR threshold, ρ_{thres}, which we must exceed before confidently accepting a detection. It varies depending on what search method is used, whether the data is stacked coherently and how large the search parameter space is (Walsh et al., 2016; Dreissigacker et al., 2018). For a conventional targeted coherent CW search, this threshold[5] is $\rho_{\mathrm{thres}} \approx 11.4$ (Abbott et al., 2004).

[5]This particular SNR threshold gives a single trial false alarm rate of 1% and a false dismissal rate of 10% (see Section 3.2 of Jaranowski et al., 1998).

However, as we are dealing with transient CWs, it is difficult to accumulate such a large SNR (the SNR increases with the square root of the signal duration). For example, if a transient signal lasted only half as long as it normally would, then only about 70% of the SNR would be accumulated. Even though a signal is shorter in duration, there is still a signal present so we need to *decrease* the SNR threshold to ensure it is detected. i.e. we would decrease the threshold to around 70% of its prior value (e.g. Keitel et al., 2019). There is one other factor we need to account for. As the signal we are looking for is now shorter, there is a greater chance of accidentally reporting a false positive, so the threshold should *increase* to account for the greater number of trials. The amount this increases by is sensitive to the transient signal parameters such as the start time and signal duration (Prix et al., 2011). The details are clearly complicated and there is no simple analytical method to determine the SNR threshold for each glitch so we will take the conservative blanket approach and adopt the same threshold used in conventional CW searches, namely $\rho_{\text{thres}} \approx 11.4$. However, to highlight the potential differences, we refer to Keitel et al. (2019) who used an $\mathcal{F}$-statistic analysis to try to detect transient CWs. Their $\mathcal{F}$-statistic threshold was $\mathrm{E}\left[2\mathcal{F}_{\text{thres}}\right] = 48$, where $\mathrm{E}\left[...\right]$ represents the expectation value, and using Equation (40) of Prix et al. (2011), one can cast this to a SNR threshold of $\rho_{\text{thres}} \approx 6.6$, which is lower than our conservative threshold of 11.4.

Bringing this all together, if we plot $\sqrt{\langle h_{0,\text{rss}}^2 \rangle}$ and $\sqrt{\frac{S_{\text{n}}(f)\rho_{\text{thres}}^2}{N \sin^2\zeta}}$ on the same axes, any signal which lies above the modified sensitivity curve will be confidently detectable, with a SNR greater than 11.4.

5.6 Applying the transient mountain model to data

We will now take our model and apply it to observed radio data. First we need to select which pulsars to use in our model. Obviously the pulsar must glitch so that constrains us to 191 pulsars[6]. However, the most limiting factor requires us to resolve the recovery of the glitch which requires a high cadence of observations, i.e. pulsars which are observed frequently enough to see changes due to the glitch recovery. There are two outstanding candidates which satisfy these constraints and they are the Crab pulsar (B0531+21) and the Vela pulsar (B0833-45). As mentioned in Section 2.2.1, these two pulsars are observed daily at the Jodrell Bank Observatory (Lyne et al., 2015) and at the Mount Pleasant Radio Observatory (Dodson et al., 2007) respectively. Therefore, our analysis will focus on the Crab and Vela pulsars, though the model is applicable to any glitching pulsar where $\mathcal{Q}$ can be obtained and is rotating fast enough to prevent unphysically large mountains, see Equation (5.11).

[6]Value taken from `http://www.jb.man.ac.uk/pulsar/glitches/gTable.html`.

TABLE 5.1: The values for the spin frequency, its time derivative and the distance to the Crab and Vela pulsars. These values were calculated in mid-1991 and early-2000 for the Crab and Vela pulsars respectively. Data taken from the ATNF Pulsar Database (Manchester et al., 2005).

Crab	Vela
$\nu_0 = 29.947$ Hz $\dot{\nu}_0 = -3.77 \times 10^{-10}$ Hz s^{-1} $d = 2.00$ kpc	$\nu_0 = 11.195$ Hz $\dot{\nu}_0 = -1.567 \times 10^{-11}$ Hz s^{-1} $d = 0.28$ kpc

We used radio data from three main sources: JBCA Glitch Catalogue for $\frac{\Delta\nu(t_g)}{\nu_0}$ and $\frac{\Delta\dot{\nu}(t_g)}{\dot{\nu}_0}$ (Espinoza et al., 2011), Crawford and Demiański (2003) for $\mathcal{Q}$ and the ATNF Pulsar Database for ν_0, $\dot{\nu}_0$ and d (Manchester et al., 2005). The value for ν_0 needed to be modified to account for the secular spin-down of the NS[7], but $\dot{\nu}_0$ and d were taken as what was reported in the ATNF Pulsar Catalogue. The secular spin-down model we used included the first time derivative of the frequency only, namely

$$\nu_0(t_g) = \nu_{0,\mathrm{ATNF}} + \dot{\nu}_{0,\mathrm{ATNF}} \cdot (t_g - t_{\mathrm{ATNF}}) \tag{5.30}$$

where the subscript "ATNF" represents the value taken from the ATNF Pulsar Catalogue. t_{ATNF} is the epoch corresponding to when the ATNF values were calculated. This was mid-1991 for the Crab and early-2000 for Vela (Manchester et al., 2005). The left hand side of Equation (5.30) is what was used for ν_0 in all calculations.

t_g was set as the date of the glitch when calculating E_{GW}, $\varepsilon_{\mathrm{approx}}(t_g)$ and $h_{0,\mathrm{approx}}(t_g)$. However, when calculating SNRs for the different detectors, $t_g =$ MJD 57856 for O2 detectors, $t_g =$ MJD 59761 for aLIGO at design sensitivity and $t_g =$ MJD 64693 for the ET. These correspond to the middle of the O2 run, the middle of 2022 and the middle of the 2030s respectively, which are the approximate times for when these detectors may be operational. This step of converting from the catalogue frequency to the predicted frequency is required because over decades, a NSs spin can change considerably and this affects the detector's sensitivity estimates which is required for the SNR calculation.

The values for ν_0, $\dot{\nu}_0$ and d from the ATNF Pulsar Catalogue are found in Table 5.1 and the remaining data from the other two data sources can be found in Tables 5.2 and 5.3. Any unknown $\mathcal{Q}$'s were set to the average $\mathcal{Q}$ from existing known values. For the Crab, this was $\mathcal{Q} \approx 0.84$ and for Vela, it was $\mathcal{Q} \approx 0.17$.

Crawford and Demiański (2003) provides a comprehensive list of $\mathcal{Q}$'s compiled from a large collection of literature. Each glitch has a $\mathcal{Q}$ value and for some glitches, there are several $\mathcal{Q}$'s, each from a different research group. Whenever there was more than one

[7] We found that if one used the value of ν_0 for the Crab from the ATNF Pulsar Catalogue *without* accounting for secular spin-down, then the GW frequency fell within the 60 Hz mains power line spike in the sensitivity curves of the O2 detectors.

$\mathcal{Q}$ for a single glitch, we used the average which is the value we report in Tables 5.2 and 5.3.

As for the GW side of the analysis, we will look at the SNRs achievable in the Hanford and Livingston detectors (during the O2 observation run), aLIGO at its design sensitivity and the ET in its 'D' configuration[8]. Like the sensitivity curve of the ET, the aLIGO design sensitivity curve is for a single interferometer (Aasi et al., 2015) and since two 90° interferometers make up aLIGO, we set $N_{\text{aLIGO}} = 2$ and $\zeta = 90°$. As established in Section 5.5, $N_{\text{ET}} = 3$ and $\zeta = 60°$ for the ET. We will treat each of the Hanford and Livingston detectors in O2 as individual interferometers since they have slightly different sensitivity curves, hence, $N = 1$ and $\zeta = 90°$for both. One can simply multiply the SNR of either Hanford or Livingston by $\sqrt{2}$ to get an approximate combined SNR (or add in quadrature for a more accurate value), but as we will see, this makes little difference in detecting transient CWs outlined in our model for these two detectors.

Together, this data was used to calculate E_{GW}, $\sqrt{\langle\rho_0^2\rangle}$, $\varepsilon_{\text{approx}}(t_{\text{g}})$, $h_{0,\text{approx}}(t_{\text{g}})$ and $\sqrt{\langle h_{0,\text{rss}}^2\rangle}$. The results are shown in Tables 5.2 and 5.3.

Finally, Figure 5.2 shows the detectability of the different glitch-induced transient mountains superimposed on modified sensitivity curves of the GW detectors of interest. The data-points (grey filled circles and light red crosses) represent the square root of the root-sum-squared GW amplitude, $\sqrt{\langle h_{0,\text{rss}}^2\rangle}$, and the modified sensitivity curve is given by $\sqrt{\frac{S_{\text{n}}(f)\rho_{\text{thres}}^2}{N\sin^2\zeta}}$. The grey filled circles correspond to glitches we had $\mathcal{Q}$ for, and the light red crosses refer to glitches where we did not have $\mathcal{Q}$ and so the average $\mathcal{Q}$ for that pulsar was used. If a data-point lies above the modified sensitivity curve, then the SNR would be greater than our threshold of 11.4 and would be classified as detectable. In reality, this detection threshold is only a guide and will differ depending on the confidence which you assign to the detection. The left bunch of data-points represents glitches from Vela and the right bunch belongs to the Crab.

From this visual representation of the detectability, we can see immediately that the Hanford detector would not have detected transient CWs from glitch-induced transient mountains from the Crab and Vela pulsars, irrespective of whether the glitches occurred during the O2 run or not. To be clear, all but 2 glitches *did not* happen in O2. This corresponds as expected with the numerical values of the SNR in Tables 5.2 and 5.3.

For the other detectors, we see that some data-points are situated higher than the detector's sensitivity curve so we will look at the tabulated SNR values to identify these. For Livingston (O2), the Crab had 1 glitch and Vela had 10 glitches which exceeded the threshold SNR. These would have been detectable if they occurred in the O2 run, but again, those 11 glitches *did not* occur in during the O2 run.

[8]The sensitivity curves of Hanford, Livingston and aLIGO at design sensitivity were taken from `https://dcc.ligo.org/LIGO-G1701570/public`, `https://dcc.ligo.org/LIGO-G1701571/public` and `https://dcc.ligo.org/LIGO-T1800044/public` respectively.

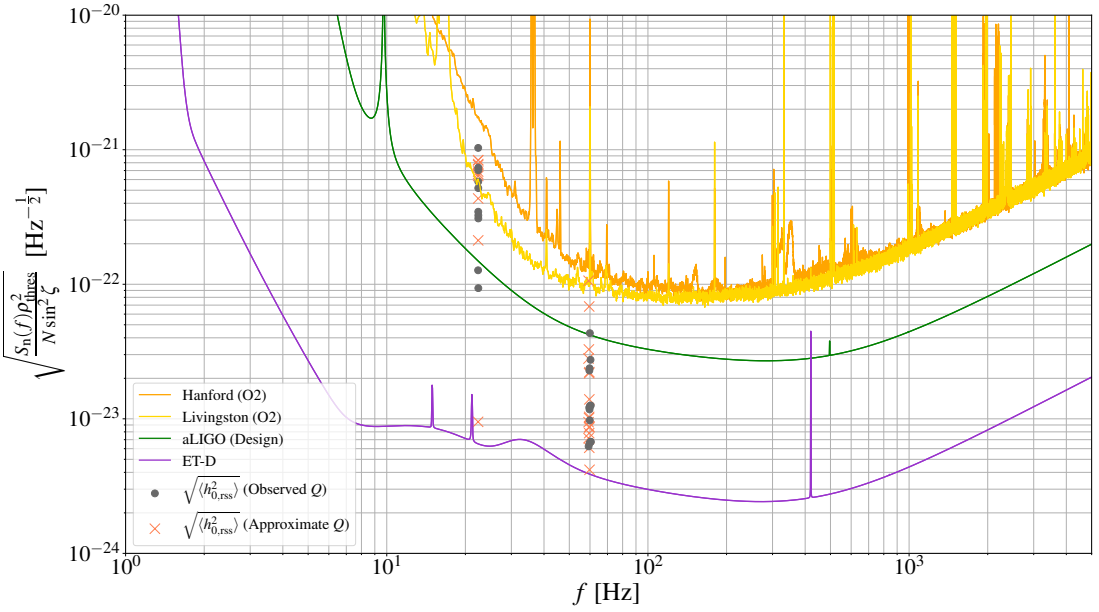

FIGURE 5.2: The above graph shows *modified* sensitivity curves of ET in its 'D' configuration (purple), aLIGO (green), Livingston in O2 (yellow) and Hanford in O2 (orange). The square root of the root-sum-squared GW amplitude of each transient CW is plotted as a grey filled circle. The light red crosses are the same but for the glitches we estimated $\mathcal{Q}$ for. If a data-point lies above the modified sensitivity curve, then that transient CW signal would give a SNR greater than our threshold which is set to $\rho_{\text{thres}} = 11.4$, meaning it would be confidently detectable. The x-axis refers to the GW frequency which is twice the pulsar's spin frequency for a NS mountain.

There were only 2 glitches which *did* occur during the O2 run, MJD 57839 (Crab) and MJD 57734 (Vela), and both had SNRs smaller than the 11.4 threshold in both the Hanford and Livingston detectors. This is consistent with the null findings of Keitel et al. (2019).

Furthermore, there was a glitch from the Crab (MJD 58687) which *did* occur during the O3 observation run. Although the change in the spin-down rate due to the glitch has not yet been published, using our model and assuming the value of $\mathcal{Q} \approx 0.84$, we predict transient CWs from this glitch should not be detectable, as $\sqrt{\langle \rho_0^2 \rangle} = 7.5 < \rho_{\text{thres}}$ for the optimistic case of the O3 detectors having aLIGO's design sensitivity.

Moving onto aLIGO at design sensitivity, our calculations have shown that 3 Crab glitches would be detectable if these glitches were to occur when aLIGO is operational at design sensitivity. For Vela, 17 out of its 20 glitches would be detectable. This is indeed promising for upcoming transient CW searches. However, in general it seems like transient CWs from the Crab are unlikely to be detected, except for the very largest of glitches. Looking into the near future, we should focus on finding transient CWs from Vela's glitches, or any other sufficiently rapidly-rotating pulsar which is near, has a large glitch size $\left(\frac{\Delta\nu(t_g)}{\nu_0}\right)$, has a large glitch recovery ($\mathcal{Q}$) or ideally some combination of all three.

Finally, for 3rd-generation detectors like the ET, we should almost certainly see transient CWs from both the Crab and Vela if glitch recoveries are even partly explained by our transient mountain model. If we do not see transient CWs with the next generation of GW detectors, one could put an upper limit on how much a glitch's recovery is due to a transient mountain.

TABLE 5.2: Summary of results for the Crab pulsar. Columns 1 - 3 are taken from the JBCA Glitch Catalogue (Espinoza et al., 2011) and Column 4 is the average $\mathcal{Q}$ per glitch from Crawford and Demiański (2003). Columns 5 - 10 are calculated from Equations (5.20), (5.23) using $\zeta = 90°$, (5.23) using $\zeta = 60°$, (5.12), (5.15) and (5.29) respectively. The 3 values for the SNR for aLIGO represent Hanford (in O2), Livingston (in O2) and aLIGO at design sensitivity from left to right. [O2]This glitch occurred during the O2 run of aLIGO. [O3]This glitch occurred during the O3 run of aLIGO. *These values of $\mathcal{Q}$ were not found in the literature so the average value of the observed $\mathcal{Q}$'s was used. †Calculated from data in Shaw et al. (in prep).

Crab									
MJD	$\frac{\Delta\nu(t_g)}{\nu_0}$	$\frac{\Delta\dot{\nu}(t_g)}{\dot{\nu}_0}$	$\mathcal{Q}$	E_{GW} [erg]	$\sqrt{\langle\rho_0^2\rangle}_{aLIGO}$	$\sqrt{\langle\rho_0^2\rangle}_{ET}$	$\varepsilon_{approx}(t_g)$	$h_{0,approx}(t_g)$	$\sqrt{\langle h_{0,rss}^2\rangle}$ [$Hz^{-\frac{1}{2}}$]
40491.8	7.2×10^{-9}	4.4×10^{-4}	0.84	2.2×10^{41}	1.1, 1.5, 3.4	36	1.6×10^{-5}	3.0×10^{-26}	1.3×10^{-23}
41161.98	1.9×10^{-9}	1.7×10^{-4}	0.92	6.3×10^{40}	0.6, 0.8, 1.8	20	9.7×10^{-6}	1.9×10^{-26}	6.7×10^{-24}
41250.32	2.1×10^{-9}	1.1×10^{-4}	0.84	6.3×10^{40}	0.6, 0.8, 1.8	20	7.8×10^{-6}	1.5×10^{-26}	6.8×10^{-24}
42447.26	3.57×10^{-8}	1.6×10^{-3}	0.81	1.0×10^{42}	2.4, 3.2, 7.4	80	3.0×10^{-5}	5.7×10^{-26}	2.7×10^{-23}
46663.69	6×10^{-9}	5×10^{-4}	1.00	2×10^{41}	1, 2, 3	40	2×10^{-5}	3×10^{-26}	1×10^{-23}
47767.504	8.10×10^{-8}	3.4×10^{-3}	0.89	2.6×10^{42}	3.8, 5.1, 11.6	130	4.4×10^{-5}	8.3×10^{-26}	4.3×10^{-23}
48945.6	4.2×10^{-9}	3.2×10^{-4}	0.87	1.3×10^{41}	0.8, 1.2, 2.6	28	1.4×10^{-5}	2.6×10^{-26}	9.7×10^{-24}
50020.04	2.1×10^{-9}	2×10^{-4}	0.80	5.9×10^{40}	0.6, 0.8, 1.8	19	1×10^{-5}	2×10^{-26}	6.6×10^{-24}
50260.031	3.19×10^{-8}	1.73×10^{-3}	0.68	7.7×10^{41}	2.1, 2.8, 6.4	69	3.2×10^{-5}	6.0×10^{-26}	2.4×10^{-23}
50458.94	6.1×10^{-9}	1.1×10^{-3}	0.87	1.9×10^{41}	1.0, 1.4, 3.2	34	2.5×10^{-5}	4.8×10^{-26}	1.2×10^{-23}
50489.7	8×10^{-10}	-2×10^{-4}	...	...	...	...	...	...	...
50812.59	6.2×10^{-9}	6.2×10^{-4}	0.92	2.0×10^{41}	1.1, 1.4, 3.3	35	1.9×10^{-5}	3.6×10^{-26}	1.2×10^{-23}
51452.02	6.8×10^{-9}	7×10^{-4}	0.83	2.0×10^{41}	1.0, 1.4, 3.3	35	2×10^{-5}	4×10^{-26}	1.2×10^{-23}
51740.656	2.51×10^{-8}	2.9×10^{-3}	0.80	7.1×10^{41}	2.0, 2.7, 6.1	66	4.1×10^{-5}	7.7×10^{-26}	2.3×10^{-23}
51804.75	3.5×10^{-9}	5.3×10^{-4}	0.84*	1.0×10^{41}	0.8, 1.0, 2.4	25	1.8×10^{-5}	3.3×10^{-26}	8.7×10^{-24}
52084.072	2.26×10^{-8}	2.07×10^{-3}	0.84*	6.7×10^{41}	1.9, 2.6, 6.0	64	3.5×10^{-5}	6.5×10^{-26}	2.2×10^{-23}
52146.758	8.9×10^{-9}	5.7×10^{-4}	0.84*	2.6×10^{41}	1.2, 1.6, 3.7	40	1.8×10^{-5}	3.4×10^{-26}	1.4×10^{-23}
52498.257	3.4×10^{-9}	7.0×10^{-4}	0.84*	1.0×10^{41}	0.7, 1.0, 2.3	25	2.0×10^{-5}	3.8×10^{-26}	8.6×10^{-24}
52587.2	1.7×10^{-9}	5×10^{-4}	0.84*	5.0×10^{40}	0.5, 0.7, 1.6	18	2×10^{-5}	3×10^{-26}	6.1×10^{-24}
53067.078	2.14×10^{-7}	6.2×10^{-3}	0.84*	6.3×10^{42}	5.9, 8.1, 18.4	200	6.0×10^{-5}	1.1×10^{-25}	6.8×10^{-23}
53254.109	4.9×10^{-9}	2×10^{-4}	0.84*	1.4×10^{41}	0.9, 1.2, 2.8	30	1×10^{-5}	2×10^{-26}	1.0×10^{-23}
53331.17	2.8×10^{-9}	7×10^{-4}	0.84*	8.2×10^{40}	0.7, 0.9, 2.1	23	2×10^{-5}	4×10^{-26}	7.8×10^{-24}
53970.19	2.18×10^{-8}	3.1×10^{-3}	0.84*	6.4×10^{41}	1.9, 2.6, 5.9	63	4.3×10^{-5}	8.0×10^{-26}	2.2×10^{-23}
54580.38	4.7×10^{-9}	2×10^{-4}	0.84*	1.4×10^{41}	0.9, 1.2, 2.7	29	1×10^{-5}	2×10^{-26}	1.0×10^{-23}
55875.5	4.92×10^{-8}	...	0.84*	1.4×10^{42}	2.8, 3.9, 8.8	95	...	...	3.3×10^{-23}
57839.92[O2]	2.14×10^{-9}	2.7×10^{-4}	0.70†	5.2×10^{40}	0.5, 0.7, 1.7	18	1.3×10^{-5}	2.4×10^{-26}	6.2×10^{-24}
58064.555	5.1637×10^{-7}	6.969×10^{-3}	0.84*	1.5×10^{43}	9.2, 12.5, 28.6	310	6.5×10^{-5}	1.2×10^{-25}	1.1×10^{-22}
58237.357	4.08×10^{-9}	4.6×10^{-4}	0.84*	1.2×10^{41}	0.8, 1.1, 2.5	27	1.7×10^{-5}	3.1×10^{-26}	9.4×10^{-24}
58470.939	2.36×10^{-9}	3.60×10^{-4}	0.84*	6.9×10^{40}	0.6, 0.8, 1.9	21	1.5×10^{-5}	2.7×10^{-26}	7.2×10^{-24}
58687.59[O3]	3.60×10^{-8}	...	0.84*	1.1×10^{42}	2.4, 3.3, 7.5	81	...	...	2.8×10^{-23}

TABLE 5.3: This contains the same results as Table 5.2 but for the Vela pulsar. [O2]This glitch occurred during the O2 run of aLIGO. [1]The data for this glitch was taken from Xu et al. (2019). *These values of $\mathcal{Q}$ were not found in the literature so the average value of the observed $\mathcal{Q}$'s was used.

Vela									
MJD	$\frac{\Delta\nu(t_g)}{\nu_0}$	$\frac{\Delta\dot{\nu}(t_g)}{\dot{\nu}_0}$	$\mathcal{Q}$	E_{GW} [erg]	$\sqrt{\langle\rho_0^2\rangle}_{aLIGO}$	$\sqrt{\langle\rho_0^2\rangle}_{ET}$	$\varepsilon_{approx}(t_g)$	$h_{0,approx}(t_g)$	$\sqrt{\langle h_{0,rss}^2\rangle}$ [$Hz^{-\frac{1}{2}}$]
40280	2.34×10^{-6}	1.0×10^{-2}	0.034	3.9×10^{41}	2.1, 6.1, 24.8	570	1.8×10^{-4}	3.4×10^{-25}	3.2×10^{-22}
41192	2.05×10^{-6}	1.5×10^{-2}	0.035	3.6×10^{41}	2.0, 5.8, 23.6	540	2.2×10^{-4}	4.2×10^{-25}	3.1×10^{-22}
41312	1.2×10^{-8}	3×10^{-3}	0.55	3.3×10^{40}	0.6, 1.8, 7.1	160	1×10^{-4}	2×10^{-25}	9.4×10^{-23}
42683	1.99×10^{-6}	1.1×10^{-2}	0.21	2.0×10^{42}	4.8, 13.8, 56.2	1300	1.9×10^{-4}	3.6×10^{-25}	7.4×10^{-22}
43693	3.06×10^{-6}	1.8×10^{-2}	0.12	1.9×10^{42}	4.5, 13.2, 53.7	1200	2.4×10^{-4}	4.6×10^{-25}	7.0×10^{-22}
44888.4	1.145×10^{-6}	4.9×10^{-2}	0.177	1.0×10^{42}	3.3, 9.7, 39.6	910	4.0×10^{-4}	7.5×10^{-25}	5.2×10^{-22}
45192	2.05×10^{-6}	2.3×10^{-2}	0.044	4.5×10^{41}	2.2, 6.5, 26.4	610	2.7×10^{-4}	5.2×10^{-25}	3.5×10^{-22}
46257.228	1.601×10^{-6}	1.7×10^{-2}	0.158	1.3×10^{42}	3.7, 10.9, 44.2	1000	2.3×10^{-4}	4.4×10^{-25}	5.8×10^{-22}
47519.8036	1.805×10^{-6}	7.7×10^{-2}	0.17*	1.5×10^{42}	4.1, 12.0, 48.7	1100	5.0×10^{-4}	9.5×10^{-25}	6.4×10^{-22}
48457.382	2.715×10^{-6}	6.0×10^{-1}	0.17*	2.3×10^{42}	5.1, 14.7, 59.7	1400	1.4×10^{-3}	2.6×10^{-24}	7.8×10^{-22}
49559	8.35×10^{-7}	0	0.17*	7.0×10^{41}	2.8, 8.2, 33.1	760	...	...	4.3×10^{-22}
49591.2	1.99×10^{-7}	1.2×10^{-1}	0.17*	1.7×10^{41}	1.4, 4.0, 16.2	370	6.2×10^{-4}	1.2×10^{-24}	2.1×10^{-22}
50369.345	2.11×10^{-6}	5.95×10^{-3}	0.38	4.0×10^{42}	6.7, 19.4, 78.7	1800	1.4×10^{-4}	2.6×10^{-25}	1.0×10^{-21}
51559.319	3.086×10^{-6}	6.736×10^{-3}	0.17*	2.6×10^{42}	5.4, 15.7, 63.7	1500	1.5×10^{-4}	2.8×10^{-25}	8.3×10^{-22}
53193	2.1×10^{-6}	...	0.17*	1.8×10^{42}	4.4, 12.9, 52.5	1200	...	...	6.9×10^{-22}
53960	2.62×10^{-6}	2.3×10^{-1}	0.17*	2.2×10^{42}	5.0, 14.4, 58.7	1300	8.6×10^{-4}	1.6×10^{-24}	7.7×10^{-22}
55408.8	1.94×10^{-6}	7.5×10^{-2}	0.17*	1.6×10^{42}	4.3, 12.4, 50.5	1200	4.9×10^{-4}	9.3×10^{-25}	6.6×10^{-22}
56556	3.1×10^{-6}	1.48×10^{-1}	0.17*	2.6×10^{42}	5.4, 15.7, 63.8	1500	6.9×10^{-4}	1.3×10^{-24}	8.4×10^{-22}
56922	4×10^{-10}	1×10^{-4}	0.17*	3×10^{38}	0.1, 0.2, 0.7	20	2×10^{-5}	3×10^{-26}	1×10^{-23}
57734.485[O2,1]	1.431×10^{-6}	7.335×10^{-2}	0.0085	6.0×10^{40}	0.8, 2.4, 9.7	220	4.9×10^{-4}	9.2×10^{-25}	1.3×10^{-22}

5.7 Discussion

It is interesting to point out that the total GW energy in our transient mountain model (Equation (5.18)) depends on $\Delta\nu_t$, but $\Delta\nu_t$ can be written either as a product of $\Delta\nu(t_g)$ and $\mathcal{Q}$ or $\Delta\dot{\nu}_t$ and τ, by Equation (5.7). This highlights two different degeneracies within our model. The first is that the same GW energy, and hence SNR, can be obtained during the glitch recovery whether it be a large glitch with a small recovery, or a small glitch with a large recovery. This means that we should not neglect searching for transient CWs even if a pulsar has had a small glitch. There could very well be a significant transient CW signal, given the small glitch recovers by a large enough amount.

Secondly, there is a degeneracy between the transient change in the spin-down rate and the recovery time scale. Since $\varepsilon^2(t_g) \propto \Delta\dot{\nu}_t$ by Equation (5.11), the same SNR can be achieved with either a large transient mountain that decays away on a short time-scale, or a small transient mountain that decays on a long time-scale. Taken to the extreme, this statement is how conventional CW searches keep decreasing the upper limit on ε or h_0 for a given pulsar, because not seeing a CW signal for a longer amount of time means the ellipticity must be smaller.

In previous sections, we briefly mentioned the idea of permanent mountains created at the moment of the glitch. They can exist from having a negative $\Delta\dot{\nu}_p$, but with the exception of a few large glitches of the Crab[9], many glitches do not normally show a non-zero $\Delta\dot{\nu}_p$. The only place where we needed to use $\Delta\dot{\nu}(t_g)$ instead of $\Delta\dot{\nu}_t$ was in calculating $\varepsilon_{\text{approx}}(t_g)$ and $h_{0,\text{approx}}(t_g)$, where use of this approximation is clear from the subscript. If one had a value for $\Delta\dot{\nu}_t$, then using that to calculate $\varepsilon(t_g)$ or $h_0(t_g)$ would yield a more accurate result. The same can be said for including the effects of $\Delta\dot{\nu}_p$ in the total GW energy emitted. Permanent mountains would give off conventional CWs which contribute to a constant GW luminosity.

Link et al. (1992) argued that a negative $\Delta\dot{\nu}_p$ could not be explained with the vortex creep model[10] and concluded that there must be either a time-dependent torque during the glitch recovery (e.g. Allen and Horvath, 1997) or the glitch causes a change to the external torque. They preferred the idea of changing the external torque through a rearrangement of the magnetic field (Link et al., 1998; Franco et al., 2000), but our model, if one allows also for the formation of a permanent mountain, provides both the time-dependent torque from transient mountains and the (permanent) change to the external torque from permanent mountains.

[9] It is well-known that large glitches of the Crab exhibit a permanent change to the spin-down rate (Lyne et al., 1993) but this is seemingly the only pulsar which shows this behaviour (Lyne et al., 2000). The Crab had large glitches in the years 1975, 1989, 2011 and 2017 (MJD 42447.26, 47767.504, 55875.5 and 58064.555 respectively) with the first 3 showing a permanent change to $\dot{\nu}$ (Lyne et al., 2015), and the last one too recent to confidently say whether there has been a permanent change to $\dot{\nu}$ (Shaw et al., 2018).

[10] Alpar and collaborators soon added a "vortex depletion region" into their model to explain a negative $\Delta\dot{\nu}_p$ (Alpar and Pines, 1993; Alpar et al., 1996).

In our model, we can also make a prediction for the recovery time-scale by rearranging Equation (5.7) and using the approximation $\Delta\dot{\nu}_{\rm t} \approx \Delta\dot{\nu}(t_{\rm g})$ to give

$$\tau_{\rm approx} \approx -\frac{\mathcal{Q}\Delta\nu(t_{\rm g})}{\Delta\dot{\nu}(t_{\rm g})} = -\frac{\Delta\nu_{\rm t}}{\Delta\dot{\nu}(t_{\rm g})}\,. \tag{5.31}$$

If we were to include the effect of $\Delta\dot{\nu}_{\rm p}$, then the recovery time-scale would be just a rearrangement of Equation (5.5)

$$\tau = -\frac{\Delta\nu_{\rm t}}{\Delta\dot{\nu}_{\rm t}} = -\frac{\Delta\nu_{\rm t}}{\mathcal{Q}'\Delta\dot{\nu}(t_{\rm g})} = \frac{1}{\mathcal{Q}'}\tau_{\rm approx} \tag{5.32}$$

where we follow Weltevrede et al. (2011) in defining

$$\mathcal{Q}' = \frac{\Delta\dot{\nu}_{\rm t}}{\Delta\dot{\nu}(t_{\rm g})} = \frac{\Delta\dot{\nu}_{\rm t}}{\Delta\dot{\nu}_{\rm t} + \Delta\dot{\nu}_{\rm p}} \tag{5.33}$$

which is analogous to $\mathcal{Q}$ but for the spin-down rate. We can then look at $\mathcal{Q}'$ as $\Delta\dot{\nu}_{\rm p}$ varies, with $\Delta\dot{\nu}_{\rm t}$ held as a negative constant. At $\Delta\dot{\nu}_{\rm p} = 0$, we get $\mathcal{Q}' = 1$ leading to $\tau = \tau_{\rm approx}$ as expected. For the case of permanent mountains, $\Delta\dot{\nu}_{\rm p} \lesssim 0$ so $\mathcal{Q}' \lesssim 1$ and $\tau \gtrsim \tau_{\rm approx}$. If there happens to be $\Delta\dot{\nu}_{\rm p} \gtrsim 0$, then $\mathcal{Q}' \gtrsim 1$ and $\tau \lesssim \tau_{\rm approx}$.

It is important to note that $\tau_{\rm approx}$ is the approximate recovery time-scale of the glitch recovery which we see in *radio*. As mentioned in Section 5.3, the GW recovery time-scale from a glitch, $\tau_{\rm GW}$, defined by $h_0(t) \propto e^{-\frac{\Delta t}{\tau_{\rm GW}}}$, is twice the recovery time-scale observed in the radio. Hence, for transient CW searches, one should use

$$\tau_{\rm GW} = \frac{2}{\mathcal{Q}'}\tau_{\rm approx} = -\frac{2}{\mathcal{Q}'}\frac{\nu_0}{\dot{\nu}_0}\mathcal{Q}\left(\frac{\Delta\nu(t_{\rm g})}{\nu_0}\right)\left(\frac{\Delta\dot{\nu}(t_{\rm g})}{\dot{\nu}_0}\right)^{-1} \tag{5.34}$$

or half of this if you are predicting the radio glitch recovery time-scale. Of course, if we already know τ from radio observations then $\tau_{\rm GW}$ would simply be twice the value of τ. This information should certainly help conduct transient CW searches and if, in the future, we detect transient CWs frequently, it could be that GW observations end up aiding radio astronomers in their discoveries instead of the other way around. Generally, GW searches are performed over some plausible range of damping times and not just at this single value (e.g. Keitel et al., 2019).

In both disciplines, it would be insightful to use typical values of $\mathcal{Q}$ and $\mathcal{Q}'$ when a pulsar glitches, so one could immediately predict how the GW waveform/radio timing residuals would appear in data under this model. For instance, we already calculated the average $\mathcal{Q}$ for our two pulsars of interest, $\mathcal{Q}_{\rm Crab} \approx 0.84$ and $\mathcal{Q}_{\rm Vela} \approx 0.17$. We can try to do the same for $\mathcal{Q}'$. Observationally, it appears that $\Delta\dot{\nu}_{\rm p} < 0.2\Delta\dot{\nu}(t_{\rm g})$ for the Crab with the caveat that the glitch is not affected by the previous one (Espinoza et al., 2011; Lyne et al., 2015). This results in $0.8 < \mathcal{Q}'_{\rm Crab} < 1.0$ with larger Crab glitches taking values closer to the lower bound. It is harder to say for Vela as glitches tend to occur

before the spin-down rate has had a chance to fully recover from the previous glitch (Lyne et al., 1996).

When we do calculate $\tau_{\rm GW}$ using $\mathcal{Q}' = 1$, we get average values of $\langle \tau_{\rm GW,\,Crab} \rangle \approx 24$ days and $\langle \tau_{\rm GW,\,Vela} \rangle \approx 298$ days. Keitel et al. (2019) searched for transient CWs of up to 4 months in duration. One can see $\langle \tau_{\rm GW,\,Vela} \rangle$ is longer than 4 months so if a typical glitch from Vela occurred, and it was uninterrupted by another glitch, then it would require a search longer than 4 months to track the first e-fold of its recovery.

In a few cases, there were SNRs greater than our SNR threshold, $\rho_{\rm thres}$. If these glitches occurred during a GW observation run (which they did not), then we could have had a detection if only a fraction of the total signal was detected. With an exponential recovery model, most of the GW energy is emitted within the first few e-folds of the signal, hence, we can reduce how long we need to integrate for. By using Equations (5.22) and (5.14), we get

$$T_{\rm detect} = -\tau \ln \left(1 - \frac{\rho^2_{\rm thres}}{\langle \rho^2_0 \rangle} \right) \tag{5.35}$$

where $T_{\rm detect}$ is the time it takes to confidently detect a signal and $\langle \rho^2_0 \rangle$ is given by Equation (5.23), which is the SNR (squared) you would get if you could capture the entire transient CW uninterrupted. $\langle \rho^2_0 \rangle$ can be predicted at the glitch if we use an approximate value of $\mathcal{Q}$. One should note $\langle \rho^2_0 \rangle$ is different for every glitch, pulsar and GW detector so consequently $T_{\rm detect}$ will be different in each case too. If a transient CW was detected confidently before $\Delta t = T_{\rm detect}$ was reached, then our model would not be a viable explanation for that particular transient CW. In practical terms, if another glitch occurred before $\Delta t = T_{\rm detect}$, but we were still able to confidently detect a transient CW signal from the first glitch, then this model fails to explain that transient CW. A reason for this to happen is if more GW energy is emitted immediately after the glitch and so an exponential form for the GW amplitude is not representative of the physics which cause the GWs.

As a proof of concept on how to use Equation (5.35), we can set $T_{\rm detect} = 4$ months and τ to the average we would expect from Vela, so $\tau = \langle \tau \rangle = \frac{1}{2} \langle \tau_{\rm GW,\,Vela} \rangle = 149$ days, to find what a 4 month search would be sensitive to if a typical Vela glitch with $\tau = 149$ days were to occur. For $\rho_{\rm thres} = 11.4$, the calculation shows that a 4 month search on a typical Vela glitch would only be detectable if the emitted transient CW had $\sqrt{\langle \rho^2_0 \rangle} \geq 15.3$. Explicitly, this means a typical Vela glitch with $11.4 < \sqrt{\langle \rho^2_0 \rangle} < 15.3$ would *not* be detected with a 4 month search, though it would be if we could integrate for longer. Every glitch is different and so if τ was smaller, then the upper limit of the SNR range we are not sensitive to would reduce. It is clear that restricting the length of time searched over limits how many transient CWs we can detect. Therefore, appropriate modelling of transient CWs becomes important in selecting the upper temporal boundary for GW searches.

For the time it takes for a confident detection, the fraction of energy emitted is given by

$$\frac{E_{\text{detect}}}{E_{\text{GW}}} = \frac{\rho^2_{\text{thres}}}{\langle \rho^2_0 \rangle} \tag{5.36}$$

where E_{detect} is the accumulated GW energy emitted up to the detection time T_{detect} and E_{GW} is the total GW energy emitted if the glitch fully recovered. For the Vela case above, a confident detection within a 4 month observation corresponds to detecting at least 55% of E_{GW} for a Vela glitch. Any remaining kinetic energy lost during the glitch recovery could be attributed to elsewhere.

For the ellipticities which we have calculated, it might be natural to want to see how they compare with the spin-down ellipticity of the pulsar. The spin-down ellipticity, ε_{sd}, is the ellipticity a pulsar would have if all of its secular spin-down were due to conventional CW emission. Mathematically, it is found from equating Equations (5.8) and (5.16) and solving for $\varepsilon(t) = \varepsilon_{\text{sd}}$, leading to $\varepsilon^2_{\text{sd}} \propto \dot{\nu}_0$. Also, from Equation (5.11), we know $\varepsilon^2(t_{\text{g}}) \propto \Delta\dot{\nu}_{\text{t}}$. Both the constants of proportionality are the same and so we find the relation

$$\varepsilon^2(t_{\text{g}}) = \left(\frac{\Delta\dot{\nu}_{\text{t}}}{\dot{\nu}_0}\right) \varepsilon^2_{\text{sd}} \tag{5.37}$$

or

$$\varepsilon^2_{\text{approx}}(t_{\text{g}}) = \left(\frac{\Delta\dot{\nu}(t_{\text{g}})}{\dot{\nu}_0}\right) \varepsilon^2_{\text{sd}} \tag{5.38}$$

when we use the approximation $\Delta\dot{\nu}_{\text{t}} \approx \Delta\dot{\nu}(t_{\text{g}})$. Since $\left(\frac{\Delta\dot{\nu}(t_{\text{g}})}{\dot{\nu}_0}\right) < 1$, we can conclude $\varepsilon_{\text{approx}}(t_{\text{g}}) < \varepsilon_{\text{sd}}$ is always true. Therefore, the ellipticities of our transient mountains should never exceed the spin-down ellipticity. This is shown visually in Figure 5.3 using data from the Crab and Vela. Also within Figure 5.3 is a horizontal dashed line which represents the current upper limit on the spin-down ellipticity of the Crab and Vela pulsars, taken from Abbott et al. (2020). It can be seen that many transient mountains have ellipticities which exceed this upper limit. However, this does not disprove our model, as the upper limit is calculated for a conventional CW with a duration on the order of years, whereas our shorter transient CWs may only have $\varepsilon > \varepsilon_{\text{upper}}$ for only some small fraction of time. There would not be enough signal emitted during this short time to accumulate enough SNR to be classified as a detection. This point just highlights the degeneracy between the size of the transient mountain and the time it takes to decay away.

There is nothing in our model to suggest that we cannot have values of $\mathcal{Q} > 1$. This is in contrast to the vortex creep model where Link et al. (1992) showed only $\mathcal{Q} < 1$ was possible. Ultimately though, $\mathcal{Q} < 1$ is what is observed for most pulsars including the Crab and Vela pulsars. Looking at the definition of $\mathcal{Q}$ in Equation (5.6), $\mathcal{Q} > 1$ is mathematically equivalent to having $\Delta\nu_{\text{p}} < 0$ given $\Delta\nu_{\text{t}} > 0$. This would appear as an "over-recovery" and has in fact been seen before in X-ray glitches of magnetars (Livingstone et al., 2010; Gavriil et al., 2011) and the high-magnetic-field radio pulsar

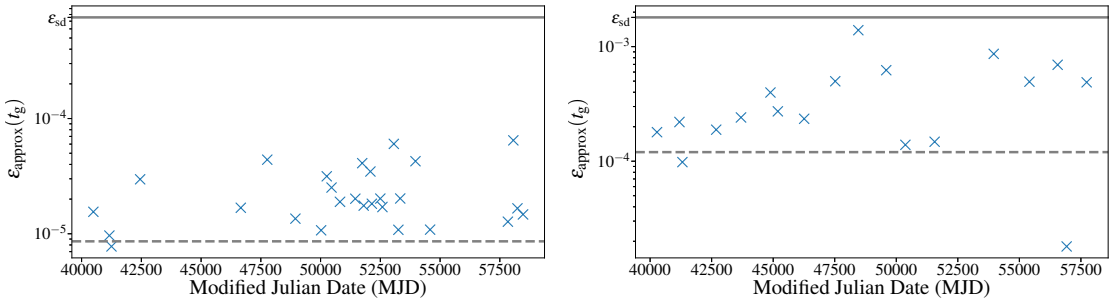

FIGURE 5.3: $\varepsilon_{\rm approx}(t_{\rm g})$ at various MJDs for glitches of the Crab (top) and Vela (bottom). The horizontal solid grey line represents the spin-down ellipticity required to explain the secular spin-down for that given pulsar. For the Crab, $\varepsilon_{\rm sd} = 7.6 \times 10^{-4}$ and for Vela, $\varepsilon_{\rm sd} = 1.8 \times 10^{-3}$. The horizontal dashed grey line represents the latest upper limit on the secular spin-down ellipticity as given in Abbott et al. (2020). These upper limits are $\varepsilon_{\rm upper} = 8.6 \times 10^{-6}$ and $\varepsilon_{\rm upper} = 1.2 \times 10^{-4}$ for the Crab and Vela pulsars respectively.

J1119-6127 (Weltevrede et al., 2011; Antonopoulou et al., 2015). However, it should be noted that magnetars generally rotate too slowly for our model to apply. Although a SNR could be calculated, any ellipticities would end up unphysically large. Additionally, J1119-6127 is one of the very few pulsars which have $\Delta\dot{\nu}_{\rm p} > 0$. This feature cannot be explained by our model.

For glitches with $\mathcal{Q} > 1$, the spin frequency after fully recovering is lower than the pre-glitch frequency. Therefore, if the recovery time-scale of such a glitch were to be shorter than the time between observations, then this over-recovery would be appear as an "anti-glitch". Such an anti-glitch was seen in Archibald et al. (2013), but it was for a magnetar. One explanation for this was an enhanced electromagnetic outflow at the glitch, causing an increase on the external braking torque (e.g. Tong, 2014). If such an anti-glitch were to happen for a rapidly-rotating NS, then our model would associate the anti-glitch with a period of excess braking torque caused by the emission of GWs from a transient mountain. From Equation (5.7), an arbitrarily large $\mathcal{Q}$ can be achieved from having a transient mountain which is large enough, and/or lasts long enough.

Finally, our model is limited to glitches which have $\Delta\nu(t_{\rm g}) > 0$ and $\Delta\dot{\nu}(t_{\rm g}) < 0$. This is true for most glitches but there are a handful of other glitches which have $\Delta\nu(t_{\rm g}) > 0$ and $\Delta\dot{\nu}(t_{\rm g}) > 0$. So far, there is nothing in our model to explain such a glitch and would require more thought.

5.8 Conclusion

To summarise, we have created a simple model whereby pulsar glitch recoveries seen in radio observations are attributed to the instantaneous formation of a transient mountain at the moment of the glitch. This mountain would create a braking torque on the

NS spinning it back down, but not exclusively, to near pre-glitch spin frequencies via the emission of transient CWs. We calculated various quantities like the energy which could go into GW emission, the values for the SNR in different GW detectors as well as the ellipticity and GW strain which could be achieved from our model. All these quantities were expressed in terms of observable parameters from radio astronomy. We found that the greatest chance of detecting a transient CW required a large glitch size, a large glitch recovery and that the pulsar needed to be near to us in distance.

In general, we found that O2-era detectors would not have detected the majority of the Crab's or Vela's glitches, irrelevant of whether they actually occurred during the O2 run. There were however 2 glitches which did occur in O2 but both of these were not detectable according to our model. This is consistent with the recent findings of Keitel et al. (2019). Also, our model predicts that the Crab glitch which occurred in O3 will not be seen when the data from O3 is processed. One disappointing finding is that unless the Crab has a large glitch, it is unlikely we will see transient CWs from the Crab at aLIGO's design sensitivity. Fortunately though, most of Vela's glitches will be detectable at aLIGO's design sensitivity if our model is correct. Finally, with 3rd-generation detectors such as the ET, our results suggests we will see transient CWs from the glitches of both the Crab and Vela pulsars with the caveat that our model is correct, even if partially. If we do not see transient CWs from pulsar glitches at that point, then one could put an upper limit on how much transient mountains actually contribute to the glitch recovery.

A consequence of our model is that large transient mountains which decay away quickly emit the same GW energy as smaller mountains which take longer to decay. This emphasises why it is important to search the uncharted territory between burst GWs and conventional CWs. To this end, we reported an estimate of the recovery time-scale for which transient CWs emitted via mountains would have. It was found that the GW recovery time-scale is exactly twice the glitch recovery time-scale found in radio observations, i.e. $\tau_{\rm GW} = 2\tau_{\rm radio}$. We provided an expression for $\tau_{\rm GW}$ dependent only on observables and could be quickly calculated either with or without the assumption of a permanent mountain being formed at the glitch. This will help guide future transient CW searches, not least, to give a theoretical explanation of a detection, if we are ever successful.

Finally, we provided a prediction for the minimum time required to accumulate enough SNR to warrant a detection, $T_{\rm detect}$. If future searches do find transient CWs within a time shorter than $T_{\rm detect}$, then this simple model, as it stands, will not be able to explain the newly-discovered phenomenon.

Chapter 6

Other applications of the transient mountain model

In Chapter 5, we developed the transient mountain model which is a model that can generate transient CWs and explain glitch recoveries. In this chapter, we explore other scenarios where we could apply the model. Each extension has its own subsection and has been presented briefly. There is not enough detail in each subsection to warrant separate publications though future publications could stem from these ideas.

We begin with the same calculation that we did in Section 5.6 but applied to another interesting pulsar, J0537-6910. Then, we will look at applying our model to the fast component of the glitch recovery seen in the 2016 Vela glitch (Ashton et al., 2019). Afterwards, we take the case where every pulsar glitch has a fast component, to see whether such a glitch recovery would yield detectable transient CWs. Finally, there was a burst GW candidate detected during O3 known as S200114f. For the case that this burst GW is in fact the emission from a very short-lived transient mountain, we find expressions for the glitch size that we would expect. This then gives pulsar astronomers an indication for what to expect and, with the GW candidate sky localisation, would allow a more informed search for an electromagnetic counterpart.

6.1 Applying the transient mountain model to J0537-6910

It was only after giving a presentation to the CW group at the Albert Einstein Institute (Hannover) were we asked if we had applied the transient mountain model to J0537-6910. It had not crossed our minds to look at J0537-6910 since we primarily focused on radio pulsars. Nevertheless, the transient mountain model still applies no matter what wavelength the pulsar is observed in, and so here we apply the model to the frequently-glitching X-ray pulsar, J0537-6910.

J0537-6910 is a young, Crab-like pulsar that was discovered in 1998 using the Rossi X-ray Timing Explorer (RXTE) (Marshall et al., 1998). It has a spin frequency of around $\nu \approx 62$ Hz and on average, glitches once every ~ 100 days. In 13 years of RXTE data, it was seen to glitch 45 times (Antonopoulou et al., 2018) (or 42 times (Ferdman et al., 2018)). More recently, the Neutron star Interior Composition Explorer (NICER) mission found another 8 more glitches in 2.7 years of X-ray data, starting from August 2017 until April 2020 (Ho et al., 2020a) and another 3 glitches between May 2020 to October 2020 (Abbott et al., 2021b).

The upcoming sections will be arranged as follows. In Section 6.1.1, we apply the same transient mountain SNR calculation as we did for the Crab and Vela previously but for J0537-6910. Then, in Section 6.1.2, we explore how the unusual long-term spin-down behaviour of J0537-6910 could be explained with an extension to our model, using the idea that each glitch contributes a little towards an ever-growing permanent mountain. Finally, in Section 6.1.3, we highlight how transient mountains could be responsible for the short-term braking index behaviour seen immediately after each glitch.

6.1.1 The standard calculation

The standard calculation refers to the question of, "if the glitch recoveries of J0537-6910 are purely due to transient mountains, would the GWs given off be detectable"? To answer this, we simply put the relevant information into Equation (5.23) to find the SNR and see whether it surpasses the threshold for detection.

To do this, we need the glitch size and the healing parameter, $\mathcal{Q}$. We will take glitch sizes of the 45 glitches that occurred during the RXTE mission from Antonopoulou et al. (2018). Then, the further 11 glitches during the NICER mission we will take from Ho et al. (2020a) and Abbott et al. (2021b).

We do not however have values of $\mathcal{Q}$, but this is expected since the rotational evolution of J0537-6910 is so heavily dominated by glitches. Often, there is not enough time to observe the glitch recovery before another glitch arrives so there is no accurate measurement of $\mathcal{Q}$. Since this is the case, we will take the optimistic view that every glitch fully recovers which means we will set $\mathcal{Q} = 1$.

From the ATNF Pulsar Catalogue, the required pulsar parameters are $\nu_0 \approx 62$ Hz, $\dot{\nu}_0 \approx -2 \times 10^{-10}$ Hz s^{-1} and $d \approx 49.7$ kpc (Manchester et al., 2005). Putting all this data into the calculations, we get values for E_{GW}, $\sqrt{\langle \rho_0^2 \rangle}$, $\varepsilon_{\mathrm{approx}}(t_{\mathrm{g}})$ and $h_{0,\mathrm{approx}}(t_{\mathrm{g}})$. The results are shown in Table 6.1.

The calculations of the SNR show that aLIGO, even at design sensitivity, is not sensitive enough to detect transient mountains from J0537-6910, if its glitch recoveries are caused by them. This includes the 3 glitches (MJD 58637, 58807, 58868) which occurred

TABLE 6.1: Summary of results for J0537-6910. Columns 1 - 3 are taken from Antonopoulou et al. (2018) (no asterisk), Ho et al. (2020a) (*) and Abbott et al. (2021b) (**). Columns 4 - 8 are calculated from Equations (5.20), (5.23) using $\zeta = 90°$, (5.23) using $\zeta = 60°$, (5.12) and (5.15) respectively. The 3 values for the SNR for aLIGO represent Hanford (in O2), Livingston (in O2) and aLIGO at design sensitivity from left to right. A value of $\mathcal{Q} = 1$ was used throughout the calculations. [O3]This glitch occurred during the O3 run of aLIGO and aVirgo.

J0537-6910							
MJD	$\frac{\Delta\nu(t_g)}{\nu_0}$	$\frac{\Delta\dot{\nu}(t_g)}{\dot{\nu}_0}$	E_{GW} [erg]	$\sqrt{\langle\rho_0^2\rangle}_{aLIGO}$	$\sqrt{\langle\rho_0^2\rangle}_{ET}$	$\varepsilon_{approx}(t_g)$	$h_{0,approx}(t_g)$
51278	6.87×10^{-7}	1×10^{-3}	1.0×10^{44}	0.69, 0.82, 2.0	22.1	2.8×10^{-6}	9.2×10^{-28}
51562	4.50×10^{-7}	7×10^{-4}	6.8×10^{43}	0.56, 0.67, 1.6	17.9	2.4×10^{-6}	7.7×10^{-28}
51711	3.15×10^{-7}	6×10^{-4}	4.8×10^{43}	0.47, 0.56, 1.4	14.9	2.2×10^{-6}	7.1×10^{-28}
51826	1.40×10^{-7}	5×10^{-4}	2.1×10^{43}	0.31, 0.37, 0.9	10.0	2.0×10^{-6}	6.5×10^{-28}
51881	1.40×10^{-7}	7×10^{-4}	2.1×10^{43}	0.31, 0.37, 0.9	10.0	2.4×10^{-6}	7.7×10^{-28}
51960	4.54×10^{-7}	8×10^{-4}	6.9×10^{43}	0.56, 0.67, 1.6	17.9	2.5×10^{-6}	8.2×10^{-28}
52152	2.3×10^{-9}	...	3.5×10^{41}	0.04, 0.05, 0.1	1.3	...	...
52170	1.84×10^{-7}	8×10^{-4}	2.8×10^{43}	0.36, 0.43, 1.0	11.4	2.5×10^{-6}	8.2×10^{-28}
52241	4.26×10^{-7}	2×10^{-4}	6.5×10^{43}	0.54, 0.65, 1.6	17.4	1.3×10^{-6}	4.1×10^{-28}
52378	1.68×10^{-7}	4×10^{-4}	2.5×10^{43}	0.34, 0.41, 1.0	10.9	1.8×10^{-6}	5.8×10^{-28}
52453	2.18×10^{-7}	4×10^{-4}	3.3×10^{43}	0.39, 0.46, 1.1	12.4	1.8×10^{-6}	5.8×10^{-28}
52545	4.20×10^{-7}	5×10^{-4}	6.4×10^{43}	0.54, 0.64, 1.6	17.2	2.0×10^{-6}	6.5×10^{-28}
52731	1.46×10^{-7}	6×10^{-4}	2.2×10^{43}	0.32, 0.38, 0.9	10.2	2.2×10^{-6}	7.1×10^{-28}
52807	2.55×10^{-7}	6×10^{-4}	3.9×10^{43}	0.42, 0.50, 1.2	13.4	2.2×10^{-6}	7.1×10^{-28}
52886	2.346×10^{-7}	4.4×10^{-4}	3.6×10^{43}	0.40, 0.48, 1.2	12.9	1.9×10^{-6}	6.1×10^{-28}
53014	3.38×10^{-7}	7×10^{-4}	5.1×10^{43}	0.48, 0.58, 1.4	15.5	2.4×10^{-6}	7.7×10^{-28}
53125.5	1.7×10^{-8}	4×10^{-4}	2.6×10^{42}	0.11, 0.13, 0.3	3.5	1.8×10^{-6}	5.8×10^{-28}
53145	3.911×10^{-7}	1.9×10^{-4}	5.9×10^{43}	0.52, 0.62, 1.5	16.6	1.2×10^{-6}	4.0×10^{-28}
53288	3.95×10^{-7}	7×10^{-4}	6.0×10^{43}	0.52, 0.62, 1.5	16.7	2.4×10^{-6}	7.7×10^{-28}
53445	2.60×10^{-7}	9×10^{-4}	3.9×10^{43}	0.42, 0.51, 1.2	13.6	2.7×10^{-6}	8.7×10^{-28}
53550	3.21×10^{-7}	7×10^{-4}	4.9×10^{43}	0.47, 0.56, 1.4	15.1	2.4×10^{-6}	7.7×10^{-28}
53696	4.09×10^{-7}	7×10^{-4}	6.2×10^{43}	0.53, 0.63, 1.5	17.0	2.4×10^{-6}	7.7×10^{-28}
53861	2.35×10^{-7}	8×10^{-4}	3.6×10^{43}	0.40, 0.48, 1.2	12.9	2.5×10^{-6}	8.2×10^{-28}
53951.3	1.8×10^{-8}	3×10^{-4}	2.7×10^{42}	0.11, 0.13, 0.3	3.6	1.5×10^{-6}	5.0×10^{-28}
53999	3.52×10^{-7}	4×10^{-4}	5.3×10^{43}	0.49, 0.59, 1.4	15.8	1.8×10^{-6}	5.8×10^{-28}
54094	3.71×10^{-7}	1×10^{-4}	5.6×10^{43}	0.51, 0.60, 1.5	16.2	8.9×10^{-7}	2.9×10^{-28}
54243	1×10^{-9}	...	1.5×10^{41}	0.03, 0.03, 0.1	0.8	...	...
54271	4.88×10^{-7}	8×10^{-4}	7.4×10^{43}	0.58, 0.69, 1.7	18.6	2.5×10^{-6}	8.2×10^{-28}
54448	2.39×10^{-7}	8×10^{-4}	3.6×10^{43}	0.41, 0.49, 1.2	13.0	2.5×10^{-6}	8.2×10^{-28}
54538	1.14×10^{-7}	5×10^{-4}	1.7×10^{43}	0.28, 0.33, 0.8	9.0	2.0×10^{-6}	6.5×10^{-28}
54578	1.47×10^{-7}	0	2.2×10^{43}	0.32, 0.38, 0.9	10.2	...	...
54639	1.287×10^{-7}	4×10^{-4}	2.0×10^{43}	0.30, 0.36, 0.9	9.5	1.8×10^{-6}	5.8×10^{-28}
54712	1.05×10^{-7}	5×10^{-4}	1.6×10^{43}	0.27, 0.32, 0.8	8.6	2.0×10^{-6}	6.5×10^{-28}
54767	3.62×10^{-7}	6×10^{-4}	5.5×10^{43}	0.50, 0.60, 1.4	16.0	2.2×10^{-6}	7.1×10^{-28}
54895	3.41×10^{-7}	5×10^{-4}	5.2×10^{43}	0.48, 0.58, 1.4	15.5	2.0×10^{-6}	6.5×10^{-28}
55043	2.17×10^{-7}	8×10^{-4}	3.3×10^{43}	0.39, 0.46, 1.1	12.4	2.5×10^{-6}	8.2×10^{-28}
55184	2.09×10^{-7}	1.1×10^{-3}	3.2×10^{43}	0.38, 0.45, 1.1	12.2	3.0×10^{-6}	9.7×10^{-28}
55280	5.49×10^{-7}	3×10^{-4}	8.3×10^{43}	0.61, 0.74, 1.8	19.7	1.5×10^{-6}	5.0×10^{-28}
55451	1.69×10^{-7}	4×10^{-4}	2.6×10^{43}	0.34, 0.41, 1.0	10.9	1.8×10^{-6}	5.8×10^{-28}
55519	1.22×10^{-7}	4×10^{-4}	1.8×10^{43}	0.29, 0.35, 0.8	9.3	1.8×10^{-6}	5.8×10^{-28}
55552	8×10^{-9}	-2×10^{-3}	1.2×10^{42}	...	...	...	...
55587	8.7×10^{-8}	1×10^{-3}	1.3×10^{43}	0.24, 0.29, 0.7	7.9	2.8×10^{-6}	9.2×10^{-28}
55615	4.53×10^{-7}	2×10^{-4}	6.9×10^{43}	0.56, 0.67, 1.6	17.9	1.3×10^{-6}	4.1×10^{-28}
55786.1	1.4×10^{-8}	-2×10^{-4}	2.1×10^{42}	...	...	...	...
55819	3.46×10^{-7}	9×10^{-4}	5.2×10^{43}	0.49, 0.58, 1.4	15.7	2.7×10^{-6}	8.7×10^{-28}
58083*	2.61×10^{-7}	7.5×10^{-4}	3.9×10^{43}	0.42, 0.51, 1.2	13.6	2.5×10^{-6}	8.0×10^{-28}
58152*	5.82×10^{-7}	8.0×10^{-4}	8.8×10^{43}	0.63, 0.76, 1.8	20.3	2.5×10^{-6}	8.3×10^{-28}
58363*	1.26×10^{-7}	1.2×10^{-3}	1.9×10^{43}	0.29, 0.35, 0.9	9.5	3.0×10^{-6}	9.9×10^{-28}
58424*	4.09×10^{-7}	1.0×10^{-3}	6.2×10^{43}	0.53, 0.63, 1.5	17.0	2.8×10^{-6}	9.2×10^{-28}
58566*	1.49×10^{-7}	4.5×10^{-4}	2.2×10^{43}	0.32, 0.38, 0.9	10.3	1.9×10^{-6}	6.2×10^{-28}
58637*,O3	4.36×10^{-7}	4.3×10^{-4}	6.6×10^{43}	0.55, 0.66, 1.6	17.6	1.9×10^{-6}	6.1×10^{-28}
58807*,O3	1.22×10^{-7}	1.1×10^{-3}	1.8×10^{43}	0.29, 0.35, 0.8	9.3	3.0×10^{-6}	9.7×10^{-28}
58868*,O3	3.88×10^{-7}	1.2×10^{-3}	5.9×10^{43}	0.52, 0.62, 1.5	16.6	3.1×10^{-6}	1.0×10^{-27}
58993**	6×10^{-9}	1.5×10^{-4}	9.8×10^{41}	0.07, 0.08, 0.2	2.1	1.1×10^{-6}	3.6×10^{-28}
59049**	1.37×10^{-7}	6.5×10^{-4}	2.1×10^{43}	0.31, 0.37, 0.9	9.8	2.3×10^{-6}	7.4×10^{-28}
59103**	5.49×10^{-7}	1.0×10^{-3}	8.3×10^{43}	0.61, 0.73, 1.8	19.7	2.8×10^{-6}	9.2×10^{-28}

in O3. Our model therefore predicts no glitch-induced transient CWs will be found from J0537-6910 when a GW search is performed on O3 data. In fact, there was a recent conventional CWs search on J0537-6910 for O3 data and there was no detection reported (Abbott et al., 2021b). Ideally, a more dedicated transient CW search is required before a fair comparison with our predictions can be made, though the null findings of the conventional CW search is perhaps suggestive of what would result.

Our calculations also suggest that the ET will be sensitive enough to detect these transient CWs should they exist. One can see that a little more than a half of the J0537-6910's glitches would lead to a detection with $\rho_{\text{thres}} = 11.4$. It seems like the main reason for such low SNRs is because of the distance to J0537-6910. It is almost 25 times as far compared to the Crab and this increases to over 170 when compared to Vela.

There is a slight improvement to the detector sensitivity due to the higher spin frequency of J0537-6910 when compared to the Crab and Vela, but it is still not enough to give a significant SNR. However, there is also a negative trade-off because of the faster rotation – the transient mountain ellipticities are smaller (compared to Crab and Vela) and as a result, the SNRs are smaller too.

To summarise, there is nothing immediate to report for J0537-6910 concerning a detectable signal. Even at aLIGO's design sensitivity and with our optimistic assumption of glitches fully recovering, we would not expect to detect transient CWs from the glitch recoveries of J0537-6910 using the transient mountain model. The model, however, will become more relevant for 3rd generation detectors like the ET.

6.1.2 Long-term spin-down behaviour

One other unusual feature of J0537-6910 is that the time derivative of the spin frequency, $\dot{\nu}$, appears to decrease linearly over long time-scales. In other words, an *increase* in the spin-down rate, $|\dot{\nu}|$. This is unusual because pulsars are expected to *decrease* their spin-down rate over long times, as they are thought to spin-down most during their early years shortly after birth.

One can see a graph of the spin-down evolution in Figure 6.1. Antonopoulou et al. (2018) found this corresponded to $\ddot{\nu}_{\text{LT}} = -7.7 \times 10^{-22}$ Hz s^{-2}, where 'LT' means "long-term". This can be transformed into a braking index, n, by Equation (2.11), where the sign of n matches the sign of $\ddot{\nu}$. When the relevant values were put in, Antonopoulou et al. (2018) calculated a value of $n_{\text{LT}} = -1.22$. Ho et al. (2020a) found $\ddot{\nu}_{\text{LT}} = -8.00 \times 10^{-22}$ Hz s^{-2} and $n_{\text{LT}} = -1.25$ when NICER data was incorporated into the calculation.

So, a value of $n_{\text{LT}} = -1.25$ means $\dot{\nu}$ becomes more negative with time. In fact, $\dot{\nu}$ becomes more negative by 8.00×10^{-22} Hz s^{-1} per second on average over long times. In Yim and Jones (2020), a negative $\dot{\nu}$ is caused by the presence of a mountain on the NS.

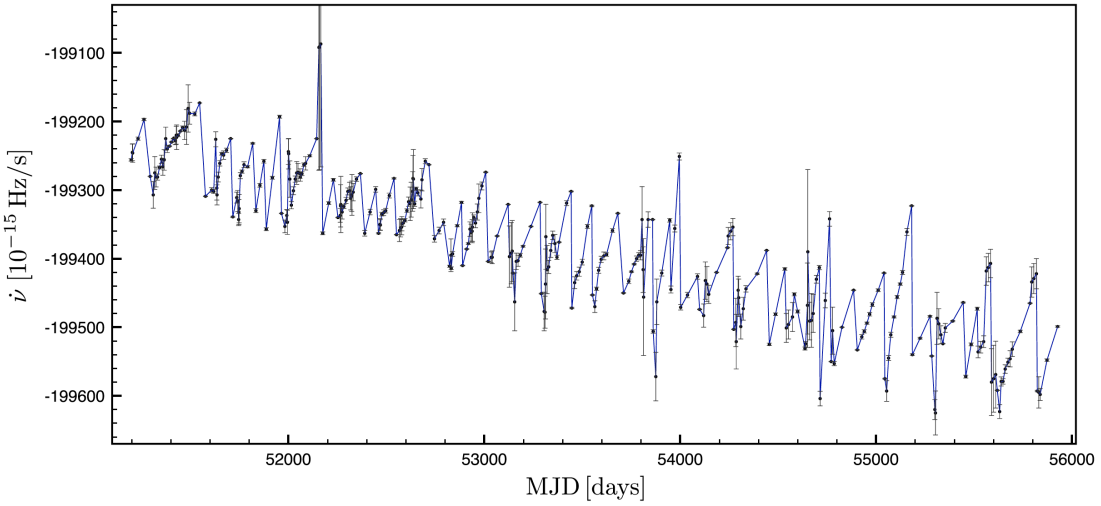

FIGURE 6.1: A graph of the spin-down rate, $\dot{\nu}$, as a function of time for J0537-6910. The data points were fitted to glitch-free observation spans. There is a long-term decrease to $\dot{\nu}$ which was found to have a $\ddot{\nu}$ value of $\ddot{\nu}_{\rm LT} = -7.7 \times 10^{-22}$ Hz s^{-2} and a corresponding braking index of $n_{\rm LT} = -1.22$. Figure taken from Antonopoulou et al. (2018).

What if the long-term spin-down behaviour of J0537-6910 is caused by *an increase in the size of an ever-growing permanent mountain* at every glitch? Running with the idea of transient mountains being responsible for glitch recoveries, it is not implausible to think that a transient mountain does not fully decay away and so a "permanent" mountain remains. Then, whenever another glitch occurs, the permanent mountain gets added to coherently causing it to grow and therefore causes the spin-down rate to increase.

To model this, we can take Equation (5.11) and apply it to the case of permanent mountains. "Permanent" refers to the mountain existing much longer than the recovery time-scale of glitches, but here we propose it *grows* over long times in order to explain the observed $\ddot{\nu}_{\rm LT}$. This then becomes

$$\varepsilon_{\rm p}(t) = \sqrt{-\frac{5}{32(2\pi)^4}\frac{c^5}{G}\frac{1}{I}\frac{\dot{\nu}(t)}{\nu_0^5}} \tag{6.1}$$

where $\varepsilon_{\rm p}(t)$ is the spin-down ellipticity (permanent mountain) and $\dot{\nu}(t)$ is given by $\dot{\nu}(t) = \dot{\nu}(t_{\rm epoch}) + \ddot{\nu}_{\rm LT}\Delta t$ where $\Delta t = t - t_{\rm epoch}$. Taking the time derivative, we get

$$\dot{\varepsilon}_{\rm p}(t) = \sqrt{-\frac{5}{128(2\pi)^4}\frac{c^5}{G}\frac{1}{I}\frac{1}{\nu_0^5}\frac{\ddot{\nu}^2(t)}{\dot{\nu}(t)}}\,. \tag{6.2}$$

One could then define the growth time-scale for the permanent mountains, τ_ε, as

$$\tau_\varepsilon(t) = \frac{\varepsilon_{\rm p}(t)}{\dot{\varepsilon}_{\rm p}(t)} = \frac{2\dot{\nu}(t)}{\ddot{\nu}(t)}\,. \tag{6.3}$$

When we substitute $\dot{\nu}(t) \approx -2 \times 10^{-10}$ Hz s^{-1} and $\ddot{\nu}(t) = \ddot{\nu}_{\rm LT} = -8.00 \times 10^{-22}$ Hz s^{-2}, we get $\tau_\varepsilon \approx 16000$ years. We can compare this to the characteristic age of J0537-6910 which is $\tau_{\rm c} \approx 5000$ years. This tells us that the growth time-scale of the permanent mountain is a few times the pulsar's current characteristic age.

Continuing on, we know how large $\dot{\varepsilon}_{\rm p}(t)$ is from Equation (6.2) and so we can calculate the increase in size of the permanent mountain required, at each glitch, to explain observations. This is done by multiplying the growth rate by the time elapsed to give

$$\Delta\varepsilon_{\rm p}(t) = \sqrt{-\frac{5}{128(2\pi)^4}\frac{c^5}{G}\frac{1}{I}\frac{\ddot{\nu}_{\rm LT}^2}{\nu_0^5\dot{\nu}_0}}\Delta t. \tag{6.4}$$

Over 13 years ($\Delta t = 13$ years), the increase to the permanent mountain size is $\Delta\varepsilon_{\rm p} \approx 7.3 \times 10^{-8}$ so if 45 glitches occurred during that time interval, each glitch must have added a permanent mountain of size $\Delta\varepsilon_{\rm p} \approx 1.6 \times 10^{-9}$, on average.

We can compare this to two other ellipticities. The first is the spin-down ellipticity and is computed using Equation (6.1). This is the ellipticity required to explain the spin-down rate if only mountains were spinning the NS down (so no contribution from magnetic dipole emission). This gives $\varepsilon_{\rm sd} \approx 8.9 \times 10^{-5}$. Also, from Table 6.1, we have the size of the transient mountains that form at each glitch. These transient mountains have ellipticities that are roughly $\Delta\varepsilon_{\rm t} \sim 2 \times 10^{-6}$. We see that the size of the permanent mountains formed at each glitch is small compared to the other two measures and so we can ignore their effects in most scenarios.

In essence, the long term decrease in $\dot{\nu}$ can be explained by a difficult-to-measure permanent mountain. Currently, the upper limit implied by a non-detection of CWs from J0537-6910 is $\varepsilon_{\rm UL} = 3 \times 10^{-5}$ (Abbott et al., 2021b) which is orders of magnitude too large to resolve the increase to the permanent mountain expected here. In the context of our model, the spin-down behaviour of J0537-6910 is governed by transient mountains and these increase the size of the permanent mountain at every glitch. This would explain its glitch recoveries as well as the long term decrease to $\dot{\nu}$.

6.1.3 Short-term braking index behaviour

So far, there has been little attempt to try and explain the short-term behaviour after glitches in J0537-6910. Most papers have been interested in fitting data to the interglitch sections of the data (where effects from glitch recoveries are minimal) and, as a result, there is now evidence to suggest r-mode emission during these interglitch periods (Andersson et al., 2018). Fesik and Papa (2020) and Abbott et al. (2021d) focused on this and conducted CW searches for r-modes during the interglitch periods of J0537-6910. Unfortunately, both groups did not detect any GWs.

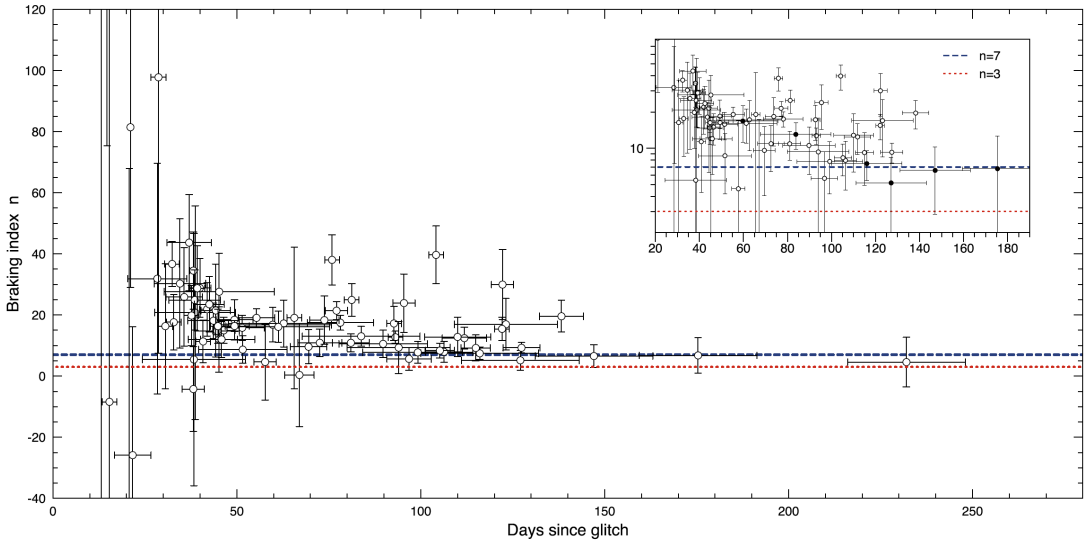

FIGURE 6.2: A graph of the post-glitch braking indices of J0537-6910 as a function of time. The dashed dark blue line represents a value of $n = 7$ and the dotted red line represents a value of $n = 3$. The insert shows a zoomed-in section of the graph with braking indices on a logarithmic scale. Figure taken from Andersson et al. (2018).

Our glitch recovery model has two parts, transient mountains that decay away on short time-scales (days to months) and permanent mountains that last much longer than the decay time-scales of transient mountains. We have seen how permanent mountains might explain the long-term spin-down of J0537-6910, but how about the short-term behaviour? Perhaps transient mountains play a role, an idea we will now explore.

To allow us to compare with the other papers and make comparisons between different braking mechanisms, we will focus on the braking index for the remainder of this section. Figure 6.2 shows how the braking index of J0537-6910 varies as a function of time after its glitches. Each glitch provides multiple datapoints depending on how many observations are made post-glitch (but before the next glitch occurs). We see that at large times after the glitch, but before the next glitch, the braking index tends towards $n \approx 7$, which was the evidence provided to suggest r-mode emission during interglitch periods (Andersson et al., 2018). The asymptotic value was found to be $n = 6.8 \pm 0.2$ when data from Antonopoulou et al. (2018) was used, and $n = 7.4 \pm 0.7$ for Ferdman et al. (2018) data, but it was noted that timing noise could have had an impact on these final values (Andersson et al., 2018). This suggests that $n \approx 5$ may not be ruled out, which is the braking index expected for a non-growing/decaying NS mountain. Furthermore, there was no attempt to explain the behaviour for post-glitch times less than 50 days. We aim to be able to do this with transient mountains.

The idea can be understood quite simply. The braking index essentially tells us how quickly a NS decelerates so we would expect it to suddenly increase if a transient mountain is formed at a glitch. As the transient mountain decays away, it has a weaker effect on the deceleration of the NS and so the braking index also decays.

To see this mathematically, we begin by writing down the general response of the braking index, Δn, to a change of $\Delta\nu$, $\Delta\dot{\nu}$ and/or $\Delta\ddot{\nu}$ which, right now, do not need to be small. This can be done by setting $\nu \to \nu_0 + \Delta\nu$ (and likewise for the other variables) in Equation (2.11)

$$n + \Delta n = \frac{(\nu + \Delta\nu)(\ddot{\nu} + \Delta\ddot{\nu})}{(\dot{\nu} + \Delta\dot{\nu})^2} \tag{6.5}$$

where we have dropped the subscript '0' for ease of reading. Then, if we define $a = \frac{\Delta\nu}{\nu}$, $b = \frac{\Delta\dot{\nu}}{\dot{\nu}}$ and $c = \frac{\Delta\ddot{\nu}}{\ddot{\nu}}$, all of which are time-dependent, then the above can be re-written as

$$\frac{\Delta n}{n} = (1 + a)(1 + c)(1 + b)^{-2} - 1 \tag{6.6}$$

which is still exact and does not require a, b or c to be small. However, we note that one can move the b in the denominator to the numerator by the use of a Taylor expansion which further simplifies the equation. To do so, we need to ensure b is small, i.e. $\Delta\dot{\nu} \ll \dot{\nu}$, but we already know this is true for J0537-6910, see Table 6.1. We do not need to do this for a or c as they are already in the numerator so are not required to be small (even though a is small). As a and b are small for J0537-6910, the large $\Delta n (\gg n)$ observed in Figure 6.2 must be attributed to a large c, i.e. $\Delta\ddot{\nu} \gg \ddot{\nu}$, which in our model means a large rate of change in the size of the transient mountain, $|\dot{\varepsilon}|$.

Doing the Taylor expansion in b, we find

$$\frac{\Delta n}{n} = (1 + a)(1 + c)(1 - 2b + 3b^2 + \cdots) - 1 \tag{6.7}$$

or

$$\frac{\Delta n}{n} \approx (1 + a)(1 + c)(1 - 2b) - 1 \tag{6.8}$$

when $b \ll 1$.

Recall the phenomenological timing model, Equation (5.2), that the transient mountain model is based on

$$\Delta\nu(t) = \Delta\nu_{\rm p} + \Delta\dot{\nu}_{\rm p} \cdot \Delta t + \Delta\nu_{\rm t} e^{-\frac{\Delta t}{\tau}} \ . \tag{6.9}$$

From this, one can write down what a, b and c are

$$a = \frac{\Delta\nu_{\rm p}}{\nu} + \frac{\Delta\dot{\nu}_{\rm p}}{\nu}\Delta t + \frac{\Delta\nu_{\rm t}}{\nu} e^{-\frac{\Delta t}{\tau}} \tag{6.10}$$

$$b = \frac{\Delta\dot{\nu}_{\rm p}}{\dot{\nu}} - \frac{\Delta\nu_{\rm t}}{\dot{\nu}\tau} e^{-\frac{\Delta t}{\tau}} \tag{6.11}$$

$$c = \frac{\Delta\nu_{\rm t}}{\ddot{\nu}\tau^2} e^{-\frac{\Delta t}{\tau}} \tag{6.12}$$

which can then be substituted into Equation (6.7) to yield the exact Δn that one would get from changes in the variables associated with the transient mountain model. In reality, this is not practical as there are infinite terms, but instead, one could use Equation (6.8) if $b \ll 1$. This means we get a (relatively) simple expression for Δn for the

transient mountain model

$$\Delta n(t) = \left(\frac{\ddot{\nu}_0 \Delta\nu_\mathrm{p}}{\dot{\nu}_0^2} - \frac{2\nu_0\ddot{\nu}_0\Delta\dot{\nu}_\mathrm{p}}{\dot{\nu}_0^3}\right) + \left(\frac{\ddot{\nu}_0\Delta\dot{\nu}_\mathrm{p}}{\dot{\nu}_0^2}\right)\Delta t + \left(\frac{\ddot{\nu}_0}{\dot{\nu}_0^2} + \frac{\nu_0}{\dot{\nu}_0^2\tau^2} + \frac{2\nu_0\ddot{\nu}_0}{\dot{\nu}_0^3\tau}\right)\Delta\nu_\mathrm{t} e^{-\frac{\Delta t}{\tau}} \tag{6.13}$$

where we have reinstated the subscript '0' to represent it is the quantity measured immediately before the glitch. This expression for Δn is governed by 7 parameters, $\{\nu_0, \dot{\nu}_0, \ddot{\nu}_0, \Delta\nu_\mathrm{p}, \Delta\nu_\mathrm{t}, \Delta\dot{\nu}_\mathrm{p}, \tau\}$, but ν_0, $\dot{\nu}_0$ and $\ddot{\nu}_0$ are known. Moreover, if we use the relations

$$\Delta\nu(t_\mathrm{g}) = \Delta\nu_\mathrm{t} + \Delta\nu_\mathrm{p} \tag{6.14}$$

$$\Delta\dot{\nu}(t_\mathrm{g}) = \Delta\dot{\nu}_\mathrm{t} + \Delta\dot{\nu}_\mathrm{p} \tag{6.15}$$

$$\Delta\dot{\nu}_\mathrm{t}\tau = -\mathcal{Q}\Delta\nu(t_\mathrm{g}) \tag{6.16}$$

where $\mathcal{Q} = \frac{\Delta\nu_\mathrm{t}}{\Delta\nu(t_\mathrm{g})}$, then τ becomes the only degree of freedom left, since $\Delta\nu(t_\mathrm{g})$, $\Delta\dot{\nu}(t_\mathrm{g})$ and $\mathcal{Q}$ can be taken from radio (or X-ray) observations. In GW searches, there is also a degree of freedom for the time of the glitch, but here we take it as given. The braking index at a given time, $n(t)$, would therefore be the pre-glitch value, n_0, which is unknown and adds a degree of freedom, plus $\Delta n(t)$, so has the general form

$$n(t) = A(n_0, \nu_0, \dot{\nu}_0, \ddot{\nu}_0, \Delta\nu_\mathrm{p}, \Delta\dot{\nu}_\mathrm{p}) + B(\dot{\nu}_0, \ddot{\nu}_0, \Delta\dot{\nu}_\mathrm{p})\Delta t + C(\nu_0, \dot{\nu}_0, \ddot{\nu}_0, \Delta\nu_\mathrm{t}, \tau)e^{-\frac{\Delta t}{\tau}} \tag{6.17}$$

where A, B and C are functions that can be fitted for empirically, or, for the transient mountain model (for small b), would have the values

$$A(n_0, \nu_0, \dot{\nu}_0, \ddot{\nu}_0, \Delta\nu_\mathrm{p}, \Delta\dot{\nu}_\mathrm{p}) = n_0 + \frac{\ddot{\nu}_0\Delta\nu_\mathrm{p}}{\dot{\nu}_0^2} - \frac{2\nu_0\ddot{\nu}_0\Delta\dot{\nu}_\mathrm{p}}{\dot{\nu}_0^3} \tag{6.18}$$

$$B(\dot{\nu}_0, \ddot{\nu}_0, \Delta\dot{\nu}_\mathrm{p}) = \frac{\ddot{\nu}_0\Delta\dot{\nu}_\mathrm{p}}{\dot{\nu}_0^2} \tag{6.19}$$

$$C(\nu_0, \dot{\nu}_0, \ddot{\nu}_0, \Delta\nu_\mathrm{t}, \tau) = \left(\frac{\ddot{\nu}_0}{\dot{\nu}_0^2} + \frac{\nu_0}{\dot{\nu}_0^2\tau^2} + \frac{2\nu_0\ddot{\nu}_0}{\dot{\nu}_0^3\tau}\right)\Delta\nu_\mathrm{t}\,. \tag{6.20}$$

It is clear that there exists an exponential recovery of $n(t)$ within the framework of the transient mountain model. Looking at Figure 6.2, it does appear that this is indeed observed for times shorter than $\Delta t < 50$ days. This is a little clearer in the insert where on a logarithmic scale, it appears like there is a linear relation between the logarithm of n and time for $\Delta t < 50$ days.

In summary, we have highlighted that the transient mountain model could account for the qualitative short-term post-glitch behaviour of J0537-6910, with predictions (at least to leading order) of an exponential recovery to the braking index, having the same time-scale as the glitch recovery. To get a more accurate representation of how the braking index changes, one should include higher order terms in b, especially during the time immediately after the glitch, where higher order terms are required. One could

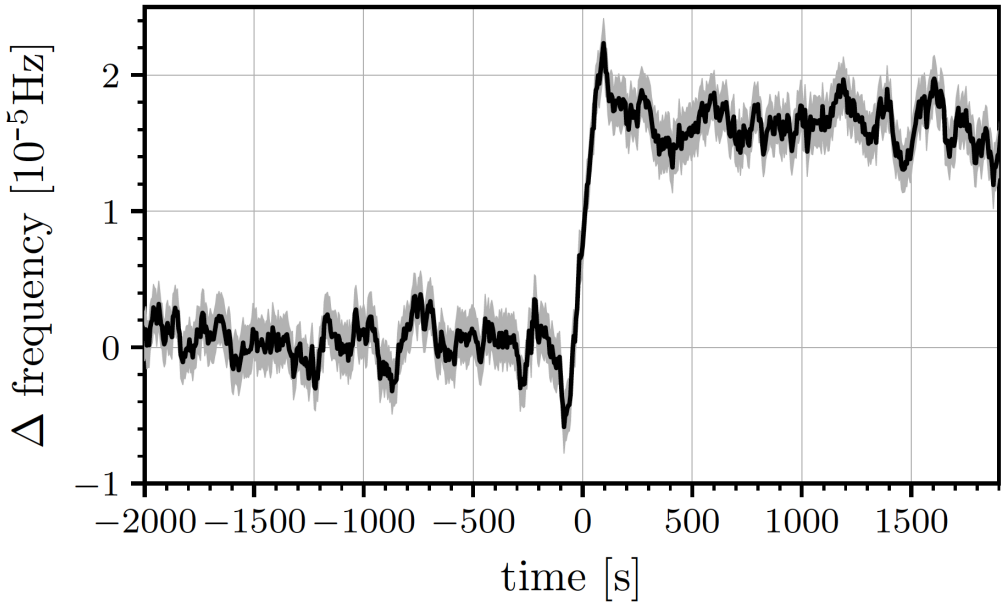

FIGURE 6.3: The 2016 Vela glitch shown in terms of the spin frequency. This was obtained by splitting the time-domain data into 200 s windows then fitting a constant frequency to the truncated data. The window is then slid along and a constant frequency is fitted to the new truncated data. The constant frequency fitted to each 200 s window is what is plotted above as a function of time. Therefore, features appear smeared out in the above graph. Figure taken from Ashton et al. (2019).

also continue the analysis numerically and find the coefficients in Equation (6.17), either phenomenologically (where A, B and C are free parameters) or using the transient mountain model but with higher order terms included.

6.2 Fast recovery of 2016 Vela glitch

6.2.1 Observational information

Recently, Ashton et al. (2019) looked at the rotational evolution of Vela during its most recent glitch in 2016 (MJD 57734), which also overlapped with O2. What was special about this glitch was that radio astronomers were observing the source at the moment it glitched and were able to extract individual pulse data, which had never been done before (Palfreyman et al., 2018). In the frequency domain, Ashton et al. (2019) found a fast ∼100 s recovery after the glitch and also a ∼100 s spin-down prior to the glitch. To emphasize, these time-scales are much shorter than those considered in earlier sections. Figure 6.3 shows what the 2016 Vela glitch looked like in terms of its spin frequency and Figure 6.4 shows the same but magnified around the time of the glitch.

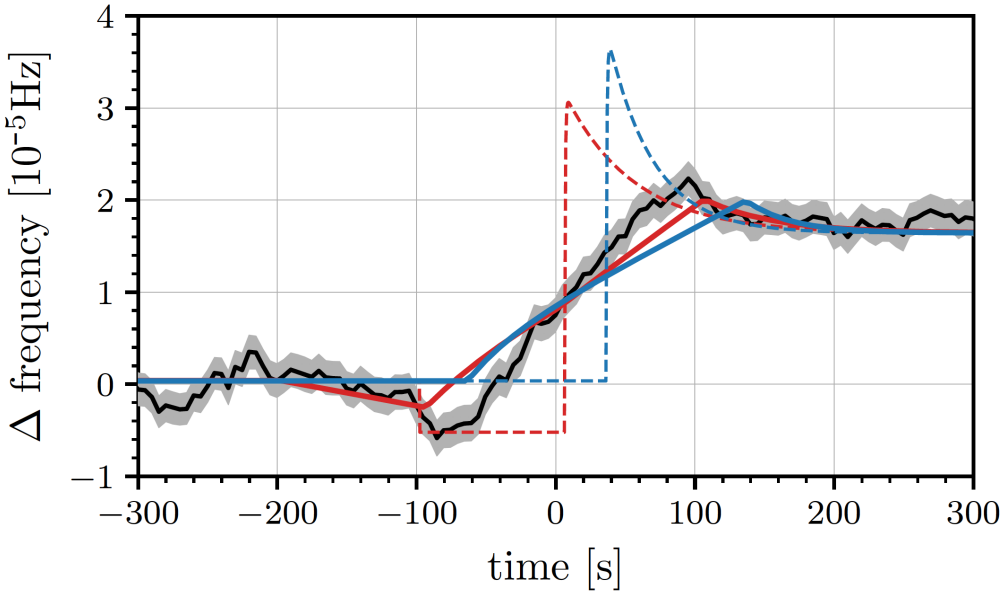

FIGURE 6.4: This figure is a magnified version of Figure 6.3 around the time of the glitch. The black line and grey area is the raw data and its error bars respectively. The solid blue and red curves represent two models fitted to the data. Blue represents a typical glitch where there is a rapid spin-up followed by an exponential recovery and red is the same but with a constant negative offset in spin frequency prior to the glitch. The dashed lines represent what that model would look like if the data was not smeared out with the 200 s window. Figure taken from Ashton et al. (2019).

In Figure 6.4, there are two models fitted to the data. One model represents a typical glitch where there is a rapid spin-up due to the glitch followed by an exponential recovery. This is represented as the blue curve. The other model is the same but with a constant negative off-set in spin frequency prior to the glitch which is represented by the red curve. Ashton et al. (2019) found that the model with a negative off-set prior to the glitch was favoured with a log Bayes factor of 2.8 when compared to 0.38 for the other model. They therefore reported that there was evidence for a spin-down prior to the glitch and suggested that this spin-down triggered the glitch, as the critical lag between the superfluid and normal matter had been reached.

6.2.2 Applying the basic model

In the context of the transient mountain model, the fast glitch recovery is caused by the instantaneous formation of a transient mountain at the moment of the glitch followed by the mountain decaying away, all whilst emitting GWs. This is what was covered in Chapter 5. The calculations there showed how to go from observables to the SNR for the GWs emitted and other derived quantities like the size of the transient mountain.

Applying that here, we first read from Figure 6.4 our observables

$$\begin{aligned} \Delta\nu(t_g) &\sim 3.5 \times 10^{-5}\ \text{Hz} \\ \mathcal{Q} &\sim 0.5 \\ \tau &\sim 100\ \text{s} \\ \nu_0 &\sim 11.2\ \text{Hz} \\ d &\sim 0.28\ \text{kpc} \\ \rightarrow \frac{\Delta\nu(t_g)}{\nu_0} &\sim 3.1 \times 10^{-6} \\ \rightarrow \Delta\dot{\nu}_t &\sim -1.8 \times 10^{-7}\ \text{Hz s}^{-1} \end{aligned}$$

where the values of ν_0 and d were obtained from Table 5.1 and $\Delta\dot{\nu}_t$ was calculated from Equation (5.7).

We also require the sensitivity of the GW detector at $f = 2\nu_0$ to calculate the SNR. Unfortunately, the Livingston detector was being tested/commissioned at the time of the Vela glitch so only the Hanford detector was observing at the time. This means we need to set $N = 1$ in Equation (5.23). We can read off the sensitivity from a daily record[1] of the sensitivity curves. On 16th December 2016, Hanford had a sensitivity of

$$\sqrt{S_n(2\nu_0)} \approx 2 \times 10^{-22}\ \text{Hz}^{-\frac{1}{2}}$$

and Livingston was half as sensitive, i.e. $\sqrt{S_n(2\nu_0)} \approx 4 \times 10^{-22}\ \text{Hz}^{-\frac{1}{2}}$, for when it was operational on that date. Livingston was not observing at 11:36 UTC when the glitch occurred (Palfreyman et al., 2018).

When all this data is substituted into Equations (5.23) and (5.11), for Hanford, we get

$$\begin{aligned} \sqrt{\langle\rho_0^2\rangle} &= 7.2 \\ \varepsilon(t_g) &= 1.9 \times 10^{-1}\ . \end{aligned}$$

The SNR is below our threshold of 11.4 to be classified as a detection. Also, $\varepsilon(t_g)$ is unphysically large making it unlikely that transient mountains are entirely responsible for the fast ∼100 s post-glitch recovery of the 2016 Vela glitch.

6.2.3 Including the spin-down prior to the glitch

In this section, we divert our attention to the spin-down seen immediately before the 2016 Vela glitch. An interesting extension of the transient mountain model is to suggest this spin-down is caused by the presence of a NS mountain. This mountain could either

[1] https://www.gw-openscience.org/detector_status/day/20161212/

grow in size until some critical ellipticity which cracks the crust and triggers the glitch, or, it could be the instantaneous formation of a constant-sized (or growing) mountain that spins-down the normal component of the NS causing the lag between the normal and superfluid components to become critical, triggering vortex unpinning (Anderson and Itoh, 1975). The glitch recovery would then be associated with the mountain decaying away, as previously suggested.

Like before, we do not propose a formation mechanism for the mountain, rather, we only consider the consequences of such a mountain. We look into the energetics of building a mountain in Chapter 7. Further analysis of $\ddot{\nu}$ would be required to distinguish if it was a growing mountain or a constant-sized mountain, similar to what was covered in Sections 6.1.2 and 6.1.3.

This extension of the model implies that there would be GWs emitted at twice the NS's spin frequency *prior* to the glitch, as well as after the glitch. If the crust-cracking idea is correct, it could also explain the symmetry of the observations since the crust would crack at the halfway point between it growing and decaying away, at the mountain's maximum size. Another symmetry is that the spin-down rate before and after the glitch appear to be the same magnitude. This would correspond to the mountain surviving the glitch event before decaying away.

Taking the idea that the growth of the mountain is the same as the decay, the signal would essentially consist of an exponentially growing signal, until $t = t_{\mathrm{g}}$, followed by a exponentially decaying signal afterwards. Both growth/decay time-scales would be similar. Therefore, if we capture this entire signal, the root-sum-squared of the GW amplitude doubles from previous, i.e. $\langle h_{0,\mathrm{rss}}^2 \rangle \rightarrow 2\langle h_{0,\mathrm{rss}}^2 \rangle$ meaning the SNR improves by a factor of $\sqrt{2}$. Also, due to the survival of the mountain throughout the glitch, the ellipticity would be the same as what was calculated in Section 6.2.2. Therefore, we get

$$\begin{aligned} \sqrt{\langle \rho_0^2 \rangle} &= 10.1 \\ \varepsilon(t_{\mathrm{g}}) &= 1.9 \times 10^{-1} \,. \end{aligned}$$

It appears that using the sensitivity curve of Hanford on the day of the glitch leads to a SNR that is below our threshold for detection. This suggests a GW search should not return a detection, according to the transient mountain model, even in the optimistic case of such large mountains. In the most ideal case where both detectors were operating, Livingston would have had half the sensitivity of Hanford (on that day) so the SNR would have been 5.1. Combined in quadrature, the combined sensitivity of Hanford and Livingston would have been 11.3, which would have still been below the detection threshold.

It is worth noting that the input data for our model could have been more accurate which would have led to slightly different answers. It appears like the models (solid

red and blue lines in Figure 6.4) used in Ashton et al. (2019) do not fit the data (solid black line) that well. There are two reasons that might explain this.

It could be that the pre-glitch spin-down event could be better modelled with either a constant negative change in the spin-down rate at $t \approx -100$ s or a negatively-growing exponential. The first suggests the instantaneous formation of a constant-sized mountain at $t \approx -100$ s, and the second suggests an exponentially growing mountain which begins its growth at about the same time.

The second, perhaps more likely reason, is due to the truncation of data into 200 s segments. A constant-frequency model was fitted to each segment and the value of the fitted frequency is what is shown in Figures 6.3 and 6.4. To advance in time is the same as sliding the 200 s window across the data, with a constant-frequency fitted to each segment. We see that the sharp peaks in the raw data (black line in Figure 6.4) is separated by less than 200 s, perhaps just over 180 s when judged by eye.

Then, we realise that a glitch model with a discontinuous jump in spin frequency at the time of the glitch can, at best, have peaks separated by 200 s when smeared out with a 200 s window (allowing direct comparison with the data). This is essentially a convolution of the dashed curves in Figure 6.4 with a uniform distribution of width 200 s. This can be confirmed by looking at Figure 6.4 and seeing the peaks and troughs of the solid red curve and solid blue curve are each separated by 200 s. Therefore, no matter how accurate the frequency evolution model, it would never be able to resolve a 180 s feature in the data when convolved with a 200 s window. It is very much the case of trying to "fit a square peg into a round hole".

The points made above are natural steps to progress the work done here. If the theoretical SNR still ends up being less than 11.4 with more accurate inputs, then greater certainty can be placed on our conclusion of not being able to detect a signal in the GW data, according to the transient mountain model. Also, questions have been raised about the profile of the pre-glitch spin-down and could be another possible avenue to explore. Evidence to suggest the favouring of one profile over another would create questions on *pre-glitch* mechanisms and would offer interesting tests on the extensions of the transient mountain model mentioned here.

Finally and most obviously, we could conduct a directed GW search for the 2016 Vela glitch in O2 data. Surprisingly, the parameter-space of the expected signal ($f_{\mathrm{GW}} \sim 22$ Hz, $\tau_{\mathrm{GW}} \sim 400$ s) has not been searched across before. The nearest searches in terms of parameter-space include a transient CW search from Keitel et al. (2019) and an all-sky search by Abbott et al. (2019b). The shortest GW time-scale Keitel et al. (2019) searched for was 0.5 days and the all-sky search only went to GW frequencies as low as 24 Hz. Although we expect there not to be a GW signal, a null result from such a GW search would place upper limits on the size of the transient mountain before and after the glitch, much like the spin-down limit for the non-detection of CWs.

6.3 Fast recovery of glitches from other pulsars

6.3.1 Outlining the idea

Since no other pulsars besides Vela have been observed whilst glitching, it could be the case that all pulsar glitches have a fast ($\mathcal{O}$(minutes)) recovery. It would simply be observational bias that has prevented us from seeing this phenomenon previously. In this section, we explore this idea a little more and assess whether glitches of other pulsars could be potential GW candidates for the case that they have an unresolved fast recovery caused by a transient mountain.

Generally, for a given $\varepsilon(t_g)$ and τ, one can write the SNR as

$$\sqrt{\langle \rho_0^2 \rangle} = \frac{8(2\pi)^2}{5}\frac{G}{c^4}\sqrt{\frac{N\sin^2\zeta}{S_n(2\nu_0)}}\frac{I}{d}\nu_0^2\sqrt{\tau}\varepsilon(t_g) \tag{6.21}$$

which comes from combining Equations (5.23), (5.11) and (5.7). This clearly shows the degeneracy between $\varepsilon(t_g)$ and τ which was detailed earlier in Section 5.7. Interesting candidates will need to be detectable so require $\sqrt{\langle \rho_0^2 \rangle} > 11.4$.

Having such a transient mountain causes the spin frequency of the pulsar to decrease rapidly, which we will call $\Delta\nu_{\text{calc}}$, and is assumed to be unresolved. One can calculate what this decrease is with

$$\frac{\Delta\nu_{\text{calc}}}{\nu_0} \equiv \frac{32(2\pi)^4}{5}\frac{G}{c^5}I\nu_0^4\tau\varepsilon^2(t_g) \tag{6.22}$$

which comes from combining Equations (5.11) and (5.7). Say a short-duration GW was detected from a glitch but a fast glitch recovery was not seen, then, the above equation tells electromagnetic observers how much of the entire glitch they had missed because they had not caught the glitch as it happened. This information may be useful for those working on glitch mechanisms.

6.3.2 Results

We will now calculate the SNR that comes from unresolved fast recoveries caused by a transient mountain. We initially assume the transient mountain has the same properties as the one determined for the 2016 Vela glitch, i.e. $\varepsilon(t_g) = 0.19$ and $\tau = 100$ s, but each pulsar will have a different ν_0 and d.

To populate our dataset, we first need to find out which pulsars glitch, which can be found in the JBCA Glitch Catalogue (Espinoza et al., 2011). When counted by J-name, there are 191 different pulsars that glitch. Then, to get ν_0 and d, we look at the ATNF

TABLE 6.2: These pulsars are potential candidates for emitters of transient CWs from fast glitch recoveries, under the assumption of $\varepsilon(t_g) = 0.19$ and $\tau = 100$ s.

Rank	**Pulsar**	ν_0 [Hz]	d [kpc]	**SNR**
1	J0613-0200	326.6	0.78	105635.3
2	J1824-2452A	327.4	5.50	15055.0
3	J0534+2200 (Crab)	29.9	2.00	275.2
4	J1952+3252	25.3	3.00	115.2
5	J1913+1011	27.8	4.61	98.2
6	J0835-4510 (Vela)	11.2	0.28	77.7
7	J1302-6350	20.9	2.63	74.8
8	J1813-1246	20.8	2.64	73.3
9	J0537-6910	62.0	49.70	65.0
10	J2229+6114	19.4	3.00	51.3
11	J1105-6107	15.8	2.36	33.0
12	J0205+6449	15.2	3.20	21.2
13	J1833-1034	16.2	4.10	20.4
14	J1915+1606	16.9	4.17	18.8
15	J2022+3842	20.6	10.00	18.6
16	J1112-6103	15.4	4.50	15.7
17	J1410-6132	20.0	13.51	12.6
18	J1718-3825	13.4	3.49	12.3
19	J1617-5055	14.4	4.74	11.8

Pulsar Catalogue (Manchester et al., 2005) but this contains only 180 of the 191 glitching pulsars. Of these 180 pulsars, 2 of them do not have a distance measurement meaning we would not be able to calculate a SNR for them. In the end, 178 pulsars have the necessary measurements required for the SNR calculation.

As for the GW detector, we choose to have only one aLIGO detector (so $N = 1$ and $\zeta = 90°$) and we will assume it has design sensitivity.

Putting in each pulsar's spin frequency and distance into Equation (6.21), we find that 19 pulsars would be potential candidates, given the glitch recoveries of these candidates were caused by a transient mountains with properties $\varepsilon(t_g) = 0.19$ and $\tau = 100$ s. The results are shown in Table 6.2.

The two pulsars with the highest SNR are both millisecond pulsars. This is not surprising considering the SNR is proportional to the square of the spin frequency. Both pulsars have glitched just the once and it will be unlikely that they will glitch again due to their old age (Cognard and Backer, 2004; McKee et al., 2016).

Although both J0613-0200 and J1824-2452A have similar spin frequencies, their SNR differ. This highlights the second important factor to consider which is the distance. Between the two, J0613-0200 is much closer and since the SNR is inversely proportional to the distance, the closer pulsar gives the higher SNR. Therefore, potential candidates will be those that spin fast and/or are close, similar to the conventional CW case.

6.3.3 A more realistic ellipticity

In the previous calculation, we used $\varepsilon(t_g) = 0.19$ which is far too large according to existing research on the maximum mountain size. The generally accepted value is between $\varepsilon \sim 10^{-8} - 10^{-5}$ (Johnson-McDaniel and Owen, 2013; Gittins et al., 2021) which corresponds to when the crust breaks (Horowitz and Kadau, 2009; Baiko and Chugunov, 2018). So, we repeat the above analysis with the still optimistic, but more realistic, value of $\varepsilon(t_g) = 1 \times 10^{-5}$ and $\tau = 100$ s to see what arises.

The result of this calculation is that transient mountains associated with a fast glitch recovery on all pulsars are not detectable with aLIGO at design sensitivity, when $\varepsilon(t_g) = 1 \times 10^{-5}$. This is somewhat expected since upper limits from CW searches have shown that mountains around the same order of magnitude (and even smaller) have not been detected, even when the signal lasts much longer (e.g. Abbott et al., 2021c).

If we ignore these physical arguments about the allowed maximum size, we can ask the question of how large must a transient mountain be in order for it to be detected. We find that, out of all glitching pulsars, J0613-0200 requires the smallest $\varepsilon(t_g)$ before the detection threshold is reached (as expected), and corresponds to $\varepsilon(t_g) = 2.05 \times 10^{-5}$. Next is J1824-2452A, which happens at $\varepsilon(t_g) = 1.44 \times 10^{-4}$. For the Crab and Vela, it is $\varepsilon(t_g) = 7.87 \times 10^{-3}$ and $\varepsilon(t_g) = 2.79 \times 10^{-2}$ respectively. Note that the value for Vela calculated here differs from the earlier value of $\varepsilon(t_g) = 0.19$. This is because we are now using aLIGO at design sensitivity instead of during O2.

Excluding millisecond pulsars, transient mountains need to be at least as big as $\varepsilon(t_g) \sim 1 \times 10^{-3}$ to be detected. Unless there is some mechanism that can sustain a mountain of this size for $\tau = 100\ s$, it appears transient mountains cannot explain a fast recovery, if they are ever observed.

6.4 Finding an electromagnetic counterpart for the S200114f event

During the O3 run of aLIGO and aVirgo the Gravitational-Wave Candidate Event Database (GraceDB) was created which is a public database of GW candidates. GW candidates are added automatically along with basic information such as the expected source of the GW (if a CBC), the pipeline used to detect it, which interferometers detected it, the false alarm rate, as well as physical properties such as the time of the event and a sky map showing the areas in the sky the GW most likely originated from.

Of the 80+ entries in GraceDB, only 3 of them are classified as non-CBC GW events. However, of these 3 events, 2 of them were retracted, leaving just 1 non-CBC event -

S200114f. It was found using the burst search pipeline, cWB, which searches for unmodelled GWs (Klimenko et al., 2016). Currently, the raw data is still with the LIGO-Virgo-KAGRA collaboration (LVK) and so there has not been a published paper that describes what S200114f might be. What has been concluded recently is that it cannot be due to a quasi-circular binary BH (The LIGO Scientific Collaboration et al., 2021). Nevertheless, there has been speculation. Perhaps most well-known and picked up by the media is the idea that Betelgeuse has gone supernova, but right now, Betelgeuse still shines brightly in the night sky.

In this section, we propose the burst GW is from a super short-lived transient mountain and if so, ask what size the glitch must have been to cause it[2]. This then gives pulsar astronomers an idea of the sort of glitch size they might be looking for, if S200114f was triggered by a glitch and its recovery was due to a transient mountain.

6.4.1 Information about S200114f

From the GraceDB webpage[3] for S200114f, we find the following relevant information

$$\begin{aligned} t_{\rm start} &= 1263002916.225766 \text{ s} \\ t_0 &= 1263002916.239300 \text{ s} \\ t_{\rm end} &= 1263002916.252885 \text{ s} \end{aligned}$$

and a false-alarm-rate of 1.226×10^{-9} Hz or 1 false positive event per 25.838 years. Also provided is the sky map of S200114f which gives an area on the sky where pulsar astronomers could search for coincident pulsars. $t_{\rm start}$ is the "time corresponding to the start of the window for grouping events into this superevent", t_0 is the "best estimate of time at which the GW event occurred" and $t_{\rm end}$ is the "time corresponding to the end of the window for grouping events into this superevent"[4]. We will therefore take the duration of the GW event to be

$$\tau_{\rm GW} = t_{\rm end} - t_0 = 0.013585 \text{ s} \tag{6.23}$$

so that

$$\tau = \frac{1}{2}\tau_{\rm GW} = 0.0067925 \text{ s} . \tag{6.24}$$

The reason we divided the GW time-scale by two is because the transient mountain model predicts the glitch recovery time-scale will be half of the GW recovery time-scale (Equations (5.2) and (5.14)).

[2]This idea was inspired from a discussion with Ben Shaw from the University of Manchester. He was interested in seeing whether S200114f could be explained by f-mode oscillations (e.g. Ho et al., 2020b), but here, we use transient mountains instead.

[3]https://gracedb.ligo.org/superevents/S200114f/

[4]https://gracedb.ligo.org/documentation/models.html

Then from a GW alert notice[5], we find the central GW frequency to be $f = 64.69$ Hz meaning

$$\nu_0 = \frac{1}{2} f = 32.345 \text{ Hz} \tag{6.25}$$

where the halving is done because GWs from NS mountains are emitted at twice the spin frequency. Pulsars with spin frequencies around 32.345 Hz which happen to coincide with the GW sky localisation would be suggestive of the transient mountain model. Other models of short GW emission from pulsar glitches include f-modes oscillations (Ho et al., 2020b), but these generally predict kHz GW frequencies which do not match with the reported observed GW frequency of S200114f.

6.4.2 Applying the transient mountain model to S200114f

To answer whether S200114f was due to a transient mountain, we first note that the SNR must have been around 10 or greater, otherwise it would have not been detectable in the first place. We then restate Equation (5.23) but for a network of detectors

$$\langle \rho_0^2 \rangle = \frac{2}{5} \frac{G}{c^3} \frac{1}{S_{\text{n}}^{\text{Network}}(2\nu_0)} \frac{I}{d^2} \mathcal{Q} \left(\frac{\Delta\nu(t_{\text{g}})}{\nu_0} \right) . \tag{6.26}$$

We are required to use the network sensitivity because S200114f was detected in Livingston, Hanford and Virgo, each with a slightly different sensitivity. To combine M independent detectors, we add together the weighted reciprocals of the GW power sensitivity curves (alternatively, add the amplitude sensitivity curves in fractional quadrature) to give

$$S_{\text{n}}^{(M)}(f) = \left(\frac{1}{F(\boldsymbol{\lambda}_1) S_{\text{n},1}(f)} + \frac{1}{F(\boldsymbol{\lambda}_2) S_{\text{n},2}(f)} + \cdots + \frac{1}{F(\boldsymbol{\lambda}_M) S_{\text{n},M}(f)} \right)^{-1} . \tag{6.27}$$

where F is a function similar to an antenna pattern, which is less than or equal to 1, that depends on the source's sky location parameters $\boldsymbol{\lambda}_i$ for $i = 1, 2, \ldots, M$ (e.g. Jaranowski et al., 1998). F is equal to 1 when the source is directly above the detector. As a very crude and optimistic approximation for the network sensitivity, we will look at the case where F is equal to 1 for each detector (which is physically not possible due to there being an angle subtended between different detectors from the perspective of the source). Nonetheless, this provides a simple estimate which can be used to find the maximum value for the SNR. Explicitly, we take

$$S_{\text{n}}^{(M)}(f) \sim \left(\frac{1}{S_{\text{n},1}(f)} + \frac{1}{S_{\text{n},2}(f)} + \cdots + \frac{1}{S_{\text{n},M}(f)} \right)^{-1} . \tag{6.28}$$

[5] https://gcn.gsfc.nasa.gov/notices_l/S200114f.lvc

This can be verified by looking at the case where we have $M = N$ independent GW detectors, all with the same sensitivity. We see the GW power sensitivity improves (value of $S_{\rm n}$ decreases) as N increases, or similarly, the GW amplitude sensitivity improves as $\sqrt{N}$, leading to an improvement to the SNR by $\sqrt{N}$ which is generally well-known.

Looking at the sensitivity curves on the day of the event[6], we find

$$\sqrt{S_{\rm n,Livingston}(64.69\ {\rm Hz})} \approx 6 \times 10^{-24}\ {\rm Hz}^{-\frac{1}{2}}$$
$$\sqrt{S_{\rm n,Hanford}(64.69\ {\rm Hz})} \approx 1 \times 10^{-23}\ {\rm Hz}^{-\frac{1}{2}}$$
$$\sqrt{S_{\rm n,Virgo}(64.69\ {\rm Hz})} \approx 1.5 \times 10^{-23}\ {\rm Hz}^{-\frac{1}{2}}$$

so the combined network sensitivity on the day was

$$\sqrt{S_{\rm n}^{\rm Network}(64.69\ {\rm Hz})} = 4.87 \times 10^{-24}\ {\rm Hz}^{-\frac{1}{2}}\ . \tag{6.29}$$

Going back to Equation (6.26), we see that there is a degeneracy between the glitch size and distance, i.e. a nearby pulsar that has a small glitch would give the same SNR as a far away pulsar that has a large glitch. Therefore, in the optimistic case where the glitch fully recovers (so $\mathcal{Q} = 1$), we have the condition

$$\frac{1}{d}\sqrt{\left(\frac{\Delta\nu(t_{\rm g})}{\nu_0}\right)} > \sqrt{\frac{5}{2}\frac{c^3}{G}S_{\rm n}^{\rm Network}(2\nu_0)\frac{1}{I}\langle\rho_0^2\rangle} \tag{6.30}$$

$$\rightarrow \quad \frac{1}{d}\sqrt{\left(\frac{\Delta\nu(t_{\rm g})}{\nu_0}\right)} > 1.51 \times 10^{-4}\ {\rm kpc}^{-1} \tag{6.31}$$

that we must satisfy for the GW signal to be detectable. If we look at the limiting case of the smallest glitch size currently detectable by telescopes, which is around $\frac{\Delta\nu(t_{\rm g})}{\nu_0} \sim 10^{-11}$, we find that we must have $d < 0.02$ kpc, meaning the pulsar must be within 0.02 kpc otherwise it would not be detectable. Given the nearest detected pulsar is at a distance of 0.09 kpc (Manchester et al., 2005), it makes it highly unlikely that GW detectors would ever be sensitive enough to detect a GW signal from a glitch of size $\sim 10^{-11}$.

What if the glitch was bigger? This would have the effect of increasing the detectable distance, but there is only so much one could increase the glitch size before the size of the transient mountain that causes the (full) glitch recovery becomes too large. This is

[6] https://www.gw-openscience.org/detector_status/day/20200114/

highlighted when we combine Equations (5.11) and (5.7) to give

$$\varepsilon(t) = \sqrt{\frac{5}{32(2\pi)^4}\frac{c^5}{G}\frac{1}{I}\frac{1}{\nu_0^4}\frac{1}{\tau}\left(\frac{\Delta\nu(t)}{\nu_0}\right)}\, e^{-\frac{\Delta t}{2\tau}} \tag{6.32}$$

$$\rightarrow \quad \varepsilon(t_{\rm g}) = \sqrt{\frac{5}{32(2\pi)^4}\frac{c^5}{G}\frac{1}{I}\frac{1}{\nu_0^4}\frac{1}{\tau}\left(\frac{\Delta\nu(t_{\rm g})}{\nu_0}\right)} \tag{6.33}$$

where we have set $\mathcal{Q} = 1$. We know that the maximum allowed size of a mountain is around $\varepsilon_{\rm max} \sim 10^{-5}$ and for S200114f, the equivalent pulsar spin frequency is $\nu_0 = 32.345$ Hz (Equation (6.25)) and the glitch recovery time-scale is $\tau = 0.0067925$ s (Equation (6.24)). Therefore, the largest glitch size possible without violating the largest mountain allowed is

$$\left(\frac{\Delta\nu(t_{\rm g})}{\nu_0}\right) < \frac{32(2\pi)^4}{5}\frac{G}{c^5} I \nu_0^4 \tau \varepsilon_{\rm max}^2 \tag{6.34}$$

$$\rightarrow \quad \left(\frac{\Delta\nu(t_{\rm g})}{\nu_0}\right) < 2.04\times10^{-17}\left(\frac{\nu_0}{32.345\ {\rm Hz}}\right)^4\left(\frac{\tau}{0.0067925\ {\rm s}}\right)\left(\frac{\varepsilon_{\rm max}}{10^{-5}}\right)^2 . \tag{6.35}$$

Clearly, the glitch must be very small and is much smaller than telescope detection limits. However, if telescope limits were not an issue, then together with the constraint in Equation (6.31), we see that we are forced to have implausibly small values of d which are even closer than the 0.02 kpc calculated earlier. Similarly, for more realistic distances of $d > 0.09$ kpc, a glitch large enough to give a detectable GW signal would have a transient mountain too large.

We have shown that the transient mountain model is not a suitable explanation for S200114f. Given the sensitivities of our current GW detectors and telescopes, the only situation where the transient mountain model may be more plausible is if the GW source had a greater ν_0 and/or τ so that the transient mountain is not unphysically large.

Chapter 7

Energetics of the building mountains

In Chapter 5, we proposed that transient mountains could explain the glitch recovery often seen in pulsar glitches. In the model, a transient mountain instantaneously forms at the time of the glitch, causing a braking torque on the NS which spins it down. In essence, we looked at angular momentum conservation and the resulting consequences for GW and electromagnetic observations. We did not however look at whether it could be energetically possible to form the mountain.

In this chapter, we aim to find out if it is energetically possible to form a mountain (regardless of whether it is transient or permanent - it does not matter for the argument here), and if so, explain where this energy comes from. We first go over the Baym and Pines model created for starquakes (Baym and Pines, 1971) followed by sections applying the Baym and Pines' model to fit our purpose.

7.1 The Baym & Pines model

Ruderman (1969) was the first to suggest that pulsar glitches are the result of starquakes (see Section 2.2.2). Then, two years later, Baym and Pines (1971) created the mathematical formalism by considering rotational, elastic and gravitational effects on a self-gravitating, elastic, incompressible NS. These ideal conditions allowed for analytic results without having to focus too much on other details.

The formalism was based on perturbing a non-rotating, spherical NS, with perturbations captured by the small parameter

$$\varepsilon_{20} \equiv \frac{I_{zz} - I_{\text{sph}}}{I_{\text{sph}}} \tag{7.1}$$

which we know is the oblateness parameter (c.f. Equation (B.6)). Here, the "20" represents a $l = 2$, $m = 0$ spherical harmonic perturbation, which is the deformation expected for a spinning NS. This is an axisymmetric perturbation. To clarify, the transient mountains in earlier chapters refer to a $l = 2$, $m = 2$ perturbation so we will need to eventually connect to $l = 2$, $m = 2$ perturbations. I_{zz} is the moment of inertia about the z-axis, which we choose as our axis of rotation, and I_{sph} is the moment of inertia of the NS if it were spherical.

Using the oblateness parameter, Baym and Pines (1971) wrote down the energy of an axisymmetric, elastic, oblate NS[1]

$$E = E_{\text{sph}} + \frac{J^2}{2I_{zz}} + A_{20}\varepsilon_{20}^2 + B_{20}(\varepsilon_{20} - \varepsilon_{\text{ref},20})^2 \tag{7.2}$$

$$E = E_{\text{sph}} + \frac{1}{2}I_{\text{sph}}(1 + \varepsilon_{20})\Omega^2 + A_{20}\varepsilon_{20}^2 + B_{20}(\varepsilon_{20} - \varepsilon_{\text{ref},20})^2 \tag{7.3}$$

where E_{sph} is the energy a spherical NS would possess, $J = I_{zz}\Omega = I_{\text{sph}}(1 + \varepsilon_{20})\Omega$ is the angular momentum of the NS, A_{20} is a positive constant that relates to the change in gravitational potential energy when a spherical NS is perturbed by a $l = 2$, $m = 0$ perturbation, B_{20} is similar but for the elastic energy and $\varepsilon_{\text{ref},20}$ is called the "reference" oblateness, at which the NS is unstrained.

From Baym and Pines (1971), for an incompressible NS, A_{20} was found to be minus one fifth the value of the self gravitational binding energy, meaning

$$A_{20} = \frac{3}{25}\frac{GM^2}{R} \,. \tag{7.4}$$

Moreover, B_{20} is defined as

$$E_{\text{elastic}} \equiv B_{20}(\varepsilon_{20} - \varepsilon_{\text{ref},20})^2 \tag{7.5}$$

such that the elastic energy is proportional to the square of oblateness departure from the unstrained configuration, with the constant of proportionality being B_{20}. Note that the elastic energy does care about whether ε_{20} or $\varepsilon_{\text{ref},20}$ is larger, but rather the relative difference between the two.

We can introduce the mean stress, σ, which is defined as

$$\sigma \equiv \left| \frac{1}{V_{\text{crust}}} \frac{\partial E_{\text{elastic}}}{\partial \varepsilon_{20}} \right| = \mu(\varepsilon_{20} - \varepsilon_{\text{ref},20}) \tag{7.6}$$

[1]This equation is only accurate to the leading terms in the gravitational potential energy and elastic energy. The next leading terms would be 4th order terms in ε_{20}, for NSs in equilibrium. Each new 4th order term would have a new coefficient in front of it, e.g. $A_{20}^{(4)}$ and $B_{20}^{(4)}$. This would need to be considered if we calculate E accurate to 4th order.

where $V_{\rm crust}$ is the volume of the crust and μ is the mean shear modulus of the crust, which is equal to

$$\mu = \frac{2B_{20}}{V_{\rm crust}} \,. \tag{7.7}$$

If we substitute values of $M = 1.4\ \mathrm{M}_\odot$ and $R = 10$ km into Equation (7.4), then $A_{20} \approx 6.3 \times 10^{52}$ erg. Similarly, for $\mu \sim 1 \times 10^{30}$ erg cm^{-3} in the crust (Strohmayer et al., 1991), and a typical crust thickness of 1 km, the value of B_{20} as calculated from Equation (7.7) is $B_{20} \sim 6 \times 10^{47}$ erg. One can see that $B_{20} \ll A_{20}$ which will be useful later. This is the statement that the gravitational potential energy changes by a greater amount for a given change in oblateness, when compared to the changes in the elastic energy.

Going back to the energy, Equation (7.2), one can get from this to the ellipticity of a NS in equilibrium. In equilibrium, the energy of a system is extremised to any changes in the oblateness so we partially differentiate Equation (7.2) with respect to ε_{20}, whilst holding the angular momentum constant, and equate the result to zero. i.e. $\left.\frac{\partial E}{\partial \varepsilon_{20}}\right|_J = 0$. Forcing the equilibrium condition, we find that the oblateness of a NS in equilibrium is

$$\varepsilon_{20} = \frac{I_{\rm sph}\Omega^2}{4(A_{20}+B_{20})} + \frac{B_{20}}{A_{20}+B_{20}}\varepsilon_{\rm ref,20} \,. \tag{7.8}$$

Equations (7.3) and (7.8) are the key results from this section, and they will come up multiple times in the upcoming sections.

7.2 Elastic energy from secular spin-down

So, how do we use Equations (7.3) and (7.8)? In this section, we will use those equations to tell us how much elastic energy can be stored in the crust; firstly, during the spin-down between glitches and secondly, when considering the possibility of a "strain reservoir" which might arise from the early formation of a maximally-deformed crust. Then in the next section, we will compare these energies to the energy required to build a mountain, to see whether mountain formation can be energetically sustained.

7.2.1 Pessimistic estimate of elastic energy

The calculation outlined here will comprise of finding out how much elastic energy can be obtained between glitches, on the assumption that the elastic strain reduces to zero immediately after a glitch. One might expect this in the starquake model where the cracking of the crust relieves all elastic strains (and hence energy) in the crust. The loss of elastic strain causes the NS to become more spherical (from an initially more oblate state) which reduces the moment of inertia which in turn causes the spin to increase in order to conserve angular momentum.

With this assumption of zero strain after a glitch, we end up with a pessimistic estimate of the elastic energy. The reason for this comes from the fact we have not considered a potential "strain reservoir" which may have formed during the early life of the NS when it was spinning much faster. We will cover this optimistic case in more detail in Section 7.2.2.

For now, we focus only on the interglitch period and for the reasons above, we label the (unstrained) oblateness immediately after a glitch as $\varepsilon_{\text{ref},20}$ and as the NS spins-down during the interglitch period, the oblateness decreases to ε_{20} which leads to an increase in stored strain. Clearly, we will have

$$\delta\varepsilon_{20} \equiv \varepsilon_{\text{ref},20} - \varepsilon_{20} > 0 \tag{7.9}$$

where δ represents quantities that are varying across the interglitch period. Then, the amount of elastic energy available during an interglitch period is given as

$$\delta E_{\text{elastic}} = B(\delta\varepsilon_{20})^2 \tag{7.10}$$

where we have used Equation (7.5). We can get $\delta\varepsilon_{20}$ in analytic form by evaluating the oblateness at the start and end of the interglitch period, $\varepsilon_{\text{ref},20}$ and ε_{20}. We will define the rotational frequency at the start of the interglitch period as Ω_{start} and we know the NS is not strained at this moment, so using Equation (7.8), we find

$$\varepsilon_{\text{ref},20} = \frac{I_{\text{sph}}\Omega_{\text{start}}^2}{4A_{20}} \tag{7.11}$$

where we used $B_{20} = 0$ since elasticity does not play a role when there is no strain. The oblateness at the end of the interglitch period does include elasticity so we need to use Equation (7.8) to represent this.

Therefore, taking ε_{20} from $\varepsilon_{\text{ref},20}$, we find

$$\delta\varepsilon_{20} = \frac{I_{\text{sph}}(\Omega_{\text{start}}^2 - \Omega^2)}{4(A_{20} + B_{20})}\,. \tag{7.12}$$

Writing $\Omega = \Omega_{\text{start}} + \delta\Omega$, where $\delta\Omega$ (< 0) is how much the rotational frequency has changed by during the interglitch period, we can rewrite the above to give

$$\delta\varepsilon_{20} = -\frac{1}{2(A_{20} + B_{20})} I_{\text{sph}}\Omega_{\text{start}}^2 \left[\left(\frac{\delta\Omega}{\Omega_{\text{start}}}\right) + \frac{1}{2}\left(\frac{\delta\Omega}{\Omega_{\text{start}}}\right)^2\right] \tag{7.13}$$

and when substituted into Equation (7.10) for the elastic energy, we get

$$\delta E_{\text{elastic}} = \frac{1}{4}\frac{B_{20}}{(A_{20} + B_{20})^2} I_{\text{sph}}^2\Omega_{\text{start}}^4 \left[\left(\frac{\delta\Omega}{\Omega_{\text{start}}}\right)^2 + \left(\frac{\delta\Omega}{\Omega_{\text{start}}}\right)^3 + \frac{1}{4}\left(\frac{\delta\Omega}{\Omega_{\text{start}}}\right)^4\right] \tag{7.14}$$

or if $\delta\Omega \ll \Omega_{\rm start}$, then

$$\delta E_{\rm elastic} \approx \frac{1}{4}\frac{B_{20}}{(A_{20}+B_{20})^2} I_{\rm sph}^2 \Omega_{\rm start}^4 \left(\frac{\delta\Omega}{\Omega_{\rm start}}\right)^2 . \tag{7.15}$$

One can see that when elasticity is weak, i.e. when B_{20} is small, we obtain smaller amounts of elastic energy. Additionally, the elastic energy, to leading order, is quadratic in the amount the NS spins-down by, so a NS that spins-down more stores more elastic energy.

We can now put in numerical values for the Crab and Vela pulsars. Firstly, we state the constants, $A_{20} \approx 6.3 \times 10^{52}$ erg, $B_{20} \sim 6 \times 10^{47}$ erg and $I_{\rm sph} = 1 \times 10^{45}$ g cm^2. Then, for the Crab and Vela, we use their rotational frequencies for $\Omega_{\rm start}$, which are $\Omega_{\rm start} = 186.6$ rad s^{-1} and $\Omega_{\rm start} = 70.4$ rad s^{-1} respectively.

As for $\delta\Omega$, we look at the evolutionary history of the Crab and Vela. The spin frequency of the Crab decreased from $\nu \approx 30.2$ Hz in 1970 to $\nu \approx 29.7$ Hz in 2015, so a total change of $\delta\nu \approx -0.5$ Hz over 45 years, and over this time, it had 24 glitches (Lyne et al., 2015). This means the average change in angular frequency for a typical interglitch period for the Crab is $\delta\Omega \approx -0.13$ rad s^{-1} or $\left(\frac{\delta\Omega}{\Omega_{\rm start}}\right) \approx -7 \times 10^{-4}$.

As for Vela, its spin frequency decreased from $\nu \approx 11.21$ Hz in 1968 to $\nu \approx 11.19$ Hz in 2005, so a total change of $\delta\nu \approx -0.02$ Hz over 37 years, consisting of 17 glitches (Cordes et al., 1988; Espinoza et al., 2021). This means the average change in angular frequency for a typical interglitch period for Vela is $\delta\Omega \approx -7.4 \times 10^{-3}$ rad s^{-1} or $\left(\frac{\delta\Omega}{\Omega_{\rm start}}\right) \approx -1 \times 10^{-4}$.

Using all of this observational data in Equation (7.14) (or Equation (7.15)), one finds that the typical energy that could be harnessed from the build-up of elastic energy between glitches is

$$\delta E_{\rm elastic} \approx 2.2 \times 10^{34} \text{ erg} \quad \text{(Crab)} \tag{7.16}$$

$$\delta E_{\rm elastic} \approx 1.0 \times 10^{31} \text{ erg} \quad \text{(Vela)} . \tag{7.17}$$

Recall that this is a pessimistic estimation of the energy available to build mountains. In the next subsection, we will move onto the optimistic case.

7.2.2 Optimistic estimate of elastic energy

In this section, we will look at a more optimistic estimate of the elastic energy that might be available to build mountains. The main idea was suggested by Jones (2012) and goes as follows. NSs are born hot and spinning very quickly. However, they soon cool down which results in a crust forming (whilst still in an extremely oblate shape). As the NS crust can withstand a strain of up to $u_{\rm max} \sim 0.1$ (Horowitz and Kadau, 2009;

Baiko and Chugunov, 2018), one might expect the strain in the crust to build up to this maximal value as the NS first spins-down (or by some other mechanism). This then acts as a "reservoir" of strain that could be utilised at a later date, given not all the strain is released during glitches. The fact that the strain reservoir can be depleted means that this mechanism is not a steady state solution. This is unlike the mechanism covered in Section 7.2.1 which is self-sufficient and does not require a one-off event needing to take place, i.e. the rapid spin-down shortly after birth to maximally strain the crust.

To evaluate this, it is often easier to think in terms of the strain, which we will define as

$$u \equiv \varepsilon_{\text{ref},20} - \varepsilon_{20} \, . \tag{7.18}$$

During the initial spin-down when strain is being built up, $\varepsilon_{\text{ref},20}$ is the initial oblateness when the crust just forms (so no strain yet) and ε_{20} refers to the oblateness of the strained configuration, with $\varepsilon_{20} < \varepsilon_{\text{ref},20}$. The elastic energy is then given by

$$E_{\text{elastic}} = Bu^2 \, . \tag{7.19}$$

As the maximum strain is $u_{\text{max}} \sim 0.1$, we very quickly see that the maximum elastic energy is $E_{\text{elastic, max}} \sim 6 \times 10^{45}$ erg.

In the most extreme case, all this stored elastic energy could be used to create a single transient (or non-transient) mountain, but this would only be able to explain a single glitch recovery since the strain reservoir would have completely depleted. Instead, we now look at a more realistic situation where there are multiple glitches.

In the starquake model, a sudden decrease in the oblateness leads to a glitch which comes from the conservation of angular momentum. However, one normally assumes the strain leading to the glitch is built up during the spin-down between glitches. The case that we are considering here is different. There already exists a strain reservoir and so we propose the NS is unloading itself of its stored strain by having glitches. We see this clearly from

$$\frac{\Delta\nu}{\nu} = -\frac{\Delta I}{I} = -\Delta\varepsilon_{20} \tag{7.20}$$

where the first equality comes from the conservation of angular momentum and the second equality comes from the definition of ε_{20}, see Equation (7.1).

The change in oblateness, $\Delta\varepsilon_{20}$, can be achieved by saying that glitches are triggered by a decrease in reference oblateness, which in turn causes the actual oblateness to decrease too. This relation between the perturbed oblateness parameters can be seen by perturbing Equation (7.8)

$$\Delta\varepsilon_{20} = \frac{B}{A+B}\Delta\varepsilon_{\text{ref},20} \tag{7.21}$$

which assumes only a change in reference oblateness can cause a change to ε_{20}. Then, it is simple to see

$$\Delta\varepsilon_{20} - \Delta\varepsilon_{\mathrm{ref},20} = -\frac{A}{A+B}\Delta\varepsilon_{\mathrm{ref},20}\,. \tag{7.22}$$

The left hand side is equal to $-\Delta u$ so we find

$$\Delta u = \frac{A}{A+B}\Delta\varepsilon_{\mathrm{ref},20} \tag{7.23}$$

or in words, the change in strain is approximately equal to the change in reference oblateness. Substituting Equations (7.21) and (7.23) into Equation (7.20), one finds

$$\frac{\Delta\nu}{\nu} = -\frac{B}{A}\Delta u \tag{7.24}$$

or similarly

$$\Delta u = -\frac{A}{B}\left(\frac{\Delta\nu}{\nu}\right) \tag{7.25}$$

which says how much strain is released for a given glitch size. One can look at Equation (7.24) and ask the question of how large could the largest glitch be, if all the strain from a maximally strained crust is released all at once. We set $\Delta u = -u_{\mathrm{max}} \sim -0.1$ to find that the largest glitch that could be explained with a maximal strain reservoir is $\frac{\Delta\nu}{\nu} \sim 1\times10^{-6}$ which happens to be the typical size of a Vela glitch. Therefore, from this very simple argument, we have shown that although one of Vela's glitches could be explained by the release of natal strain, it cannot be the full picture as we would not be able to get consecutive glitches.

It is slightly different for the Crab which typically has smaller glitch sizes. For a typical glitch size of $\frac{\Delta\nu}{\nu} \sim 1\times10^{-8}$, the strain released is $\Delta u \sim -1\times10^{-3}$ which suggests that this mechanism could power around 100 glitches before the strain reservoir is fully depleted. This suggests this mechanism is still plausible for the Crab considering only ~ 30 Crab glitches have been observed so far.

We initially set out to find how much energy could be available for building mountains from a strain reservoir and now we have everything to determine this. We have just seen that a glitch could be caused by a change in reference oblateness which in turn changes the actual oblateness, and this results in a change in strain. If we assume this change in strain is small compared to the strain already in the crust ($\Delta u \ll u$), then we only need to consider the linear terms in the perturbed elastic energy

$$\Delta E_{\mathrm{elastic}} = 2Bu\Delta u \tag{7.26}$$

which comes from perturbing Equation (7.19). For the Crab, we saw $\Delta u \sim -1\times10^{-3}$ and if we take the optimistic case of the current strain being equal to the breaking strain ($u \sim 0.1$), then the elastic energy that would be liberated and hence available for

building mountains is

$$|\Delta E_{\text{elastic}}| = 1.2 \times 10^{44} \text{ erg} \quad \text{(Crab)} \,. \tag{7.27}$$

We saw earlier that Vela requires the maximum possible strain to be released in order to explain a typical glitch, so the most energy available for building a mountain for Vela is $E_{\text{elastic, max}} \sim 6 \times 10^{45}$ erg.

7.3 Energy to build a mountain on a non-rotating neutron star

In the last section, we found pessimistic and optimistic estimates of the energy that could become available when a glitch occurs. The question we are trying to answer now is how much energy is required to build a mountain so that we can compare to what is available. It is important to stress that a mountain is represented by an $l = 2$, $m = 2$ deformation, which is non-axisymmetric. We therefore cannot use the oblateness parameter. Instead, we use the equatorial ellipticity which is defined as

$$\varepsilon_{22} \equiv \frac{I_{xx} - I_{yy}}{I_{zz}} \tag{7.28}$$

where I_{xx}, I_{yy} and I_{zz} are the moment of inertias about the x, y and z axes respectively. Like in many cases, the z-axis is the axis of rotation. In principle, the form of the NS's energy would have a similar form to the $l = 2$, $m = 0$ case (Equation (7.3)). This is because the energy of any physical system in equilibrium is situated around a minima, meaning the first non-zero contributions from perturbations only comes in at second order. Therefore, the energy of a NS with a mountain has the following form

$$E = E_{\text{sph}} + \frac{1}{2} I_{zz} \Omega^2 + A_{22} \varepsilon_{22}^2 + B_{22} (\varepsilon_{22} - \varepsilon_{\text{ref},22})^2 \,. \tag{7.29}$$

Note that the positive constants A_{22} and B_{22}, in general, are different to the $l = 2$, $m = 0$ case. Like before, mountains in equilibrium are extremised with respect to changes to the ellipticity whilst holding the angular momentum constant, so like in the $l = 2$, $m = 0$ case, we have

$$\varepsilon_{22} = \frac{\Omega^2}{4(A_{22} + B_{22})} \frac{\partial I_{zz}}{\partial \varepsilon_{22}} + \frac{B_{22}}{A_{22} + B_{22}} \varepsilon_{\text{ref},22} \,. \tag{7.30}$$

For our rough estimate, we will only look at the energy of building a mountain on a non-rotating NS. This means the energy and ellipticity can be written as

$$E = E_{\rm sph} + A_{22}\varepsilon_{22}^2 + B_{22}(\varepsilon_{22} - \varepsilon_{\rm ref,22})^2 \tag{7.31}$$

$$\varepsilon_{22} = \frac{B_{22}}{A_{22}+B_{22}}\varepsilon_{\rm ref,22} \quad \rightarrow \quad \varepsilon_{\rm ref,22} = \frac{A_{22}+B_{22}}{B_{22}}\varepsilon_{22}\,. \tag{7.32}$$

When $\varepsilon_{\rm ref,22}$ is substituted into Equation (7.31), we find that the change in energy due to a mountain on a non-rotating NS, $\Delta E_{\rm mountain} = E - E_{\rm sph}$, is equal to

$$\Delta E_{\rm mountain} = A_{22}\left(1 + \frac{A_{22}}{B_{22}}\right)\varepsilon_{22}^2 \approx \frac{A_{22}^2}{B_{22}}\varepsilon_{22}^2 \tag{7.33}$$

for a mountain of ellipticity ε_{22}. We have assumed $B_{22} \ll A_{22}$ for the approximation and it is only an assumption since the exact forms of A_{22} and B_{22} have not been found. As a first guess, we will assume the values of A_{22} and B_{22} are equal to their $l = 2, m = 0$ counterparts, so that $A_{22} \approx 6.3 \times 10^{52}$ erg and $B_{22} \sim 6 \times 10^{47}$ erg. The calculation of these coefficients will be the study of future work.

What is left to know is the size of the mountain. As we are applying these calculations to see whether the transient mountains in Section 5 can exist, it is instructive to take the ellipticities from there. For the Crab, the smallest and largest transient mountains were $\varepsilon_{22} = 7.8 \times 10^{-6}$ and $\varepsilon_{22} = 6.5 \times 10^{-5}$, and for Vela, they were $\varepsilon_{22} = 2 \times 10^{-5}$ and $\varepsilon_{22} = 1.4 \times 10^{-3}$. Therefore, the energies required to build these mountains are

$$4.0 \times 10^{47}\ \text{erg} < \Delta E_{\rm mountain} < 2.8 \times 10^{49}\ \text{erg} \quad \text{(Crab)} \tag{7.34}$$

$$2.6 \times 10^{48}\ \text{erg} < \Delta E_{\rm mountain} < 1.3 \times 10^{52}\ \text{erg} \quad \text{(Vela)}\,. \tag{7.35}$$

When comparing to our optimistic estimates of the amount of energy available, see Section 7.2.2, it is clear that even the smallest of transient mountains cannot be accounted for by elasticity alone. According to Equation (7.33), the largest mountains that can be formed from the elastic energy released during a glitch, for the Crab and Vela, are $\varepsilon_{\rm max,22} \approx 1.3 \times 10^{-7}$ and $\varepsilon_{\rm max,22} \approx 1.0 \times 10^{-6}$ respectively.

Therefore, we have shown, through a greatly simplified calculation, that it is unlikely mountains of the size found in Section 5 can be explained by elasticity alone. There are many ways to improve this calculation, but perhaps the most important is accounting for the superfluid found within NSs. It has been suggested that a pinned superfluid, on which the Magnus force acts, could potentially strain the crust more leading to an extra source of strain (Jones, 2010). This would allow for larger mountains to be created for the same maximum elastic strain reservoir considered here. Also, another improvement could be to find what A_{22} and B_{22} are analytically, instead of assuming they take the values of A_{20} and B_{20}. The inclusion of rotation may play in important part too,

since rotational kinetic energy is the next most important energy, behind gravitational potential energy and ahead of elasticity (Keer and Jones, 2015).

Chapter 8

Gravitational waves from f-mode oscillations

8.1 Introduction

From this point onwards, we will be discussing GWs from NS oscillations. Specifically, we aim to model pulsar timing noise as due to NS oscillations, an idea which thus far has not been explored to the best of our knowledge. Due to the time-varying mass quadrupole one could get from NS oscillations, one expects GWs to be emitted and so this model connects GWs and electromagnetic observations, making it a part of multi-messenger astronomy.

The field of NS oscillations is vast, complex and is rich with physics. Ultimately, perturbing a NS or causing it to oscillate allows us to find out more about its interior and its composition, which is something we cannot achieve from electromagnetic observations alone. It is because of this complexity that research on this subject often has simplifications, which at times may seem absurd and illogical, but they do eventually get improved on (e.g. Comins, 1979).

Therefore, as a starting point for this novel timing noise model, it is natural to work with the simplest case of a non-rotating, uniformly-dense, incompressible NS which is treated in Newtonian gravity. This allows us to solve problems analytically. Once a proof of concept has been established, then further work could be done to remove these assumptions and extend to GR.

In making these assumptions, only one type of oscillation mode can be excited and they are known as the f-modes or fundamental modes. These are "bulk" oscillations to the NS where the entire shape, including the interior, oscillate at the f-mode frequency. In terms of the radial overtone number, n, the fundamental mode of any oscillating system, has $n = 0$. This means fluid elements along the same radial line from the

origin move in phase with each other. When there are overtones, i.e. $n \geq 1$, we get p-modes (pressure modes) and g-modes (gravity modes). Respectively, the restorative force in each case comes from pressure gradients and gravitational potential gradients (buoyancy). These two types of oscillation modes arise when the incompressibility assumption is relaxed. Oscillation modes are also characterised by their degree, l, which captures how many nodal lines exist on the surface of the NS. These nodal lines are lines where no fluid motion occurs. Oscillation modes also have an order, m, which is the number of longitudinal nodal lines. Therefore, the number of latitudinal nodal lines is given by $l - |m|$.

Finally, a real NS rotates so there is a Coriolis force in the reference frame that rotates with the NS, which is called the "body frame" or "rotating frame". This Coriolis force is the restorative force driving r-modes (Rossby modes). r-modes are particularly interesting for GW astronomers because the emission of GWs from these modes could cause an instability, the CFS instability, named after its discoverers (Chandrasekhar, 1970; Friedman and Schutz, 1978a,b). The instability occurs whenever the rotation rate of the NS exceeds the pattern speed of the oscillation mode (which propagates in the direction opposite to rotation). This causes the mode amplitude to grow in a runaway reaction leading to even more GWs being emitted (Andersson, 1998). Although r-modes are fascinating, we will not discuss them any further as we restrict ourselves to working with non-rotating NSs for simplicity.

Our ultimate aim is to build the foundations of a timing noise model. As discussed in Section 2.3.3, there may be a link between timing noise and microglitches so this will be the main idea that we will build on in the rest of this thesis. One might ask what causes microglitches and instead of the usual glitch models of starquakes or vortex unpinning, we propose that microglitches are caused by the excitation and decay of f-modes, the properties of which are carefully derived in this chapter. (Further details of the model can be found in the introduction of Chapter 9.)

After the careful treatment of f-modes, we move to Chapter 9 where we utilise the findings of Chapter 8 to provide an explanation for the unexplained glitch candidates (GCs) and anti-glitch candidates (AGCs) reported in Espinoza et al. (2014, 2021). There appears to be some symmetry between GCs and AGCs, which may manifest itself as equal but opposite f-modes being excited, e.g. for $l = 2$, the $m = 2$ and $m = -2$ f-modes[1]. These modes have the effect of spinning-up and spinning-down the NS by a small amount since the GWs emitted from them carry away negative and positive angular momentum respectively.

The final part of the model would be to explain how these frequent microglitches, perhaps unresolvable (unlike the GCs and AGCs), may have their effects accumulate to

[1]The convention we will use is $m = 2$ is the retrograde mode and $m = -2$ is the prograde mode, i.e. the oscillations have a form $e^{i(m\phi+\omega t)}$.

give long-term variations to the rotation rate, i.e. timing noise. The mechanism has not yet been fully developed, but as we will see, there is already a lot of interesting physics surrounding the principle ideas of this model.

In this chapter, we outline all the key details of the f-modes used in our model and in particular, how they damp due to the emission of GWs. We begin by solving the fluid equations for the background equilibrium configuration, followed by a calculation of eigenfunctions ($\boldsymbol{\xi}$) and eigenvalues (ω^2) of the f-modes allowed on our NS. Once we have the eigenfunctions and eigenvalues, we will be able to calculate the associated mode energies and angular momenta, using second order perturbation theory (Friedman and Schutz, 1978a,b). What then follows is a calculation of the rate of change of these quantities which forces us to conclude the existence of a "GW back-reaction". The latter half of this chapter is also detailed in our second paper (Yim and Jones, 2022).

8.2 Solving the fluid equations for the background solution

To find out more about NS oscillations, we first need to understand the background solution, i.e. the static solution to the fluid equations, on top of which perturbations are applied to. As mentioned in Section 8.1, we are initially looking at perturbations applied to a non-rotating, uniformly-dense, incompressible, fluid NS. This means the background NS is spherical so we will be specialising to a spherical coordinate system (r, θ, ϕ). There will also be no time dependence for the background solution, since by construction, it is static. Due to spherical symmetry, all background variables will be functions of radius r only.

A uniformly-dense NS with mass M and radius R has a density profile

$$\rho(r) = \bar{\rho}(1 - H(r - R)) \tag{8.1}$$

where $\bar{\rho} = \frac{3M}{4\pi R^3}$ is the average mass density and $H(x)$ is the Heaviside step function which has properties

$$H(x) = \begin{cases} 0 & \text{for } x < 0 \\ \frac{1}{2} & \text{for } x = 0 \\ 1 & \text{for } x > 0\,. \end{cases} \tag{8.2}$$

Also, by construction, we have $P(r;\rho) \neq 0$ for $r < R$ and $P(r;\rho) = 0$ otherwise. Due to there being no time dependence in the system, Euler's equation (Equation (4.2)) reduces to

$$0 = -\boldsymbol{\nabla} P - \rho \boldsymbol{\nabla} \Phi \tag{8.3}$$

and Poisson's equation for gravity (Equation (4.4)) remains the same

$$\nabla^2\Phi = 4\pi G\rho \,. \tag{8.4}$$

Since there is a discontinuous jump in the density at $r = R$, it is best if we find solutions for inside the star ($r < R$) and outside the star ($r > R$) and then match the solutions at the boundary using boundary conditions. Inside the interior of the star, we have

$$0 = -\boldsymbol{\nabla} P^{\text{int}} - \bar{\rho}\boldsymbol{\nabla}\Phi^{\text{int}} \tag{8.5}$$

$$\nabla^2\Phi^{\text{int}} = 4\pi G\bar{\rho} \tag{8.6}$$

and on the exterior, we have

$$\nabla^2\Phi^{\text{ext}} = 0 \,. \tag{8.7}$$

We can solve for Φ^{int} by performing a volume integral on Equation (8.6) over a Gaussian sphere of volume $V(r)$. Then, using the divergence theorem we get

$$\begin{aligned}
\int_{V(r)} \boldsymbol{\nabla}\cdot\boldsymbol{\nabla}\Phi^{\text{int}} dV = \int_{\partial V(r)} \boldsymbol{\nabla}\Phi^{\text{int}}\cdot d\boldsymbol{S} = 4\pi G\bar{\rho}\int_{V(r)} dV \\
\rightarrow \frac{d\Phi^{\text{int}}}{dr}(4\pi r^2) = 4\pi G\bar{\rho}\left(\frac{4}{3}\pi r^3\right) + C_1 \\
\rightarrow \frac{d\Phi^{\text{int}}}{dr} = \frac{4}{3}\pi G\bar{\rho} r + \frac{C_1}{4\pi r^2}
\end{aligned} \tag{8.8}$$

where C_1 is a constant of integration. We demand finite solutions at the origin so the constant of integration must be $C_1 = 0$ meaning

$$\frac{d\Phi^{\text{int}}}{dr} = \frac{4}{3}\pi G\bar{\rho} r \rightarrow \Phi^{\text{int}}(r) = \frac{2}{3}\pi G\bar{\rho} r^2 + C_2 \tag{8.9}$$

with C_2 being another constant of integration. Solving Laplace's equation for the external gravitational potential in spherical coordinates (Equation (8.7)), we get the familiar result

$$\Phi^{\text{ext}}(r) = -\frac{GM}{r} = -\frac{4\pi G\bar{\rho}R^3}{3r} \,. \tag{8.10}$$

We have the boundary condition that $\Phi^{\text{int}}(R) = \Phi^{\text{ext}}(R)$ since the gravitational potential must be continuous across the boundary. If it were not continuous, there would be a discontinuous jump in the gravitational potential meaning an infinite gradient corresponding to an infinite gravitational force at the boundary which is unphysical. Using this boundary condition, we find $C_2 = -2\pi G\bar{\rho}R^2$ meaning the background gravitational potential is

$$\Phi(r) = \begin{cases} \frac{2}{3}\pi G\bar{\rho}(r^2 - 3R^2) & \text{for } r \leq R \\ -\frac{4\pi G\bar{\rho}R^3}{3r} & \text{for } r > R \,. \end{cases} \tag{8.11}$$

We can use the interior gravitational potential in Equation (8.5) to get

$$\frac{dP^{\text{int}}}{dr} = -\frac{4}{3}\pi G\bar{\rho}^2 r$$
$$\rightarrow P^{\text{int}}(r) = -\frac{2}{3}\pi G\bar{\rho}^2 r^2 + C_3 \,. \tag{8.12}$$

By using $P^{\text{int}}(R) = 0$, we find $C_3 = \frac{2}{3}\pi G\bar{\rho}^2 R^2$ meaning the background pressure solution is

$$P(r) = \begin{cases} \frac{2}{3}\pi G\bar{\rho}^2(R^2 - r^2) & \text{for } r \leq R \\ 0 & \text{for } r > R \,. \end{cases} \tag{8.13}$$

8.3 Kelvin modes

Now that we have the background solution, we can see what happens when we perturb the NS. We want to displace all fluid elements by the displacement vector, $\boldsymbol{\xi}(r, \theta, \phi, t)$, which causes changes to the pressure, gravitational potential and, when using Eulerian perturbations (see Section 4.2), the mass density too.

For the assumptions of no rotation, uniform density and incompressibility, the eigenfunctions/displacement vectors that solve the perturbed fluid equations are known as the Kelvin modes. Thompson, who is better known as Lord Kelvin, was the first to derive these results using fairly archaic notation in 1863 (§58 in Thomson (1863)). In this section, we will re-derive the eigenfunctions and eigenvalues of the Kelvin modes but using more modern notation. Then, in the next section, we will use these eigenfunctions to determine the mode energies and angular momenta. As it will become important later, we will make clear here that the entirety of this section is accurate to *first order* in $\boldsymbol{\xi}$.

We begin by defining the associated velocities caused by the displacement vector $\boldsymbol{\xi}$ over some time t. The partial time derivative of the displacement vector is defined as the *Eulerian* change in the velocity

$$\delta\mathbf{v} \equiv \frac{\partial\boldsymbol{\xi}}{\partial t} = \dot{\boldsymbol{\xi}} \tag{8.14}$$

and the total time derivative of the displacement vector is defined as the *Lagrangian* change in the velocity

$$\Delta\mathbf{v} \equiv \frac{d\boldsymbol{\xi}}{dt} = \dot{\boldsymbol{\xi}} + (\mathbf{v}\cdot\boldsymbol{\nabla})\boldsymbol{\xi} \tag{8.15}$$

where we have used Equations (4.3) and (8.14) in the final equality. Since our background NS is static, we have $\mathbf{v} = \mathbf{0}$ which means we get

$$\Delta\mathbf{v} = \delta\mathbf{v} = \dot{\boldsymbol{\xi}} \,. \tag{8.16}$$

The NS is also modelled as incompressible meaning the total Lagrangian volume remains the same at all times when we perturb it (to first order in $\boldsymbol{\xi}$). In terms of our displacement vector, incompressibility is defined as $\boldsymbol{\nabla} \cdot \boldsymbol{\xi} \equiv 0$. Since the Lagrangian volume remains the same, as does the total mass of the NS, we deduce the Lagrangian change to the mass density must zero everywhere (and at all times) which means

$$\Delta\rho = 0 \,. \tag{8.17}$$

Temporarily dropping the time dependence, we use Equation (4.9) to relate Lagrangian perturbations to Eulerian ones, and so Equation (8.17) becomes

$$\delta\rho = -\boldsymbol{\xi}(r,\theta,\phi) \cdot \boldsymbol{\nabla}\rho(r) \tag{8.18}$$

where $\rho(r)$ is the background mass density (Equation (8.1)). Since the background solution is only dependent on the radius from the origin, we only need to consider the radial part of $\boldsymbol{\nabla}\rho(r)$

$$\nabla_r \rho(r) \equiv \frac{d\rho}{dr} = -\bar{\rho}\frac{d}{dr}(H(r-R)) \,. \tag{8.19}$$

The Heaviside step function has another defining property which is $\frac{dH(x)}{dx} = \delta(x)$ where $\delta(x)$ is Dirac's delta function. Therefore, we get

$$\nabla_r \rho(r) = -\bar{\rho}\delta(r-R) \,. \tag{8.20}$$

Since $\boldsymbol{\nabla}\rho(r)$ is purely radial, the scalar product in Equation (8.18) only produces a non-zero value when the radial component of $\boldsymbol{\xi}(r,\theta,\phi)$, which we denote with $\xi^r(r,\theta,\phi)$, takes part in the calculation. As a result, the Eulerian change to the mass density is

$$\delta\rho(r,\theta,\phi) = \bar{\rho}\delta(r-R)\xi^r(r,\theta,\phi) \tag{8.21}$$

which is true for all times. We can see that there is discontinuous behaviour at the surface of the NS so like in the last section, we will treat the interior and exterior separately to the boundary and use boundary conditions to fix any unknowns.

We now make a choice and look at the Eulerian perturbations of the NS's variables. We could very well use Lagrangian perturbations, but the results do not change. It is necessary to put in the time-dependence at this point. The perturbed variables then become

$$\mathbf{v}^{\text{pert}}(r,\theta,\phi,t) = \delta\mathbf{v}(r,\theta,\phi,t) = \dot{\boldsymbol{\xi}}(r,\theta,\phi,t) \tag{8.22}$$

$$\rho^{\text{pert}}(r,\theta,\phi,t) = \rho(r) + \delta\rho(r,\theta,\phi,t) \tag{8.23}$$

$$P^{\text{pert}}(r,\theta,\phi,t) = P(r) + \delta P(r,\theta,\phi,t) \tag{8.24}$$

$$\Phi^{\text{pert}}(r,\theta,\phi,t) = \Phi(r) + \delta\Phi(r,\theta,\phi,t) \,. \tag{8.25}$$

We can substitute these perturbed quantities into the Euler equation (Equation (4.2)) to get

$$[\rho(r)+\delta\rho(r,\theta,\phi,t)]\frac{\partial^2\boldsymbol{\xi}(r,\theta,\phi,t)}{\partial t^2} = -\boldsymbol{\nabla}[P(r)+\delta P(r,\theta,\phi,t)] - [\rho(r)+\delta\rho(r,\theta,\phi,t)]\boldsymbol{\nabla}[\Phi(r)+\delta\Phi(r,\theta,\phi,t)] \tag{8.26}$$

and if we drop all second order terms in the perturbations (e.g. $\delta\rho\boldsymbol{\nabla}\delta\Phi$ would be second order), we find

$$\rho(r)\frac{\partial^2\boldsymbol{\xi}(r,\theta,\phi,t)}{\partial t^2} = \boxed{-\boldsymbol{\nabla}P(r)} - \boldsymbol{\nabla}\delta P(r,\theta,\phi,t)\boxed{-\rho(r)\boldsymbol{\nabla}\Phi(r)} - \rho(r)\boldsymbol{\nabla}\delta\Phi(r,\theta,\phi,t) - \delta\rho(r,\theta,\phi,t)\boldsymbol{\nabla}\Phi(r)\,. \tag{8.27}$$

The terms in the dashed boxes collect to form the equation for the background solution (Equation (8.3)) so we can set the sum of these terms equal to zero. What remains is

$$\rho(r)\frac{\partial^2\boldsymbol{\xi}(r,\theta,\phi,t)}{\partial t^2} = -\boldsymbol{\nabla}\delta P(r,\theta,\phi,t) - \rho(r)\boldsymbol{\nabla}\delta\Phi(r,\theta,\phi,t) - \delta\rho(r,\theta,\phi,t)\boldsymbol{\nabla}\Phi(r)\,. \tag{8.28}$$

However, we saw in Equation (8.21) that $\delta\rho(r,\theta,\phi,t)$ is discontinuous at the surface of the NS and so we will only look at solutions inside the NS ($r < R$) and deal with the surface later. Equation (8.28) then becomes

$$\bar{\rho}\frac{\partial^2\boldsymbol{\xi}(r,\theta,\phi,t)}{\partial t^2} = -\boldsymbol{\nabla}\delta P^{\text{int}}(r,\theta,\phi,t) - \bar{\rho}\boldsymbol{\nabla}\delta\Phi^{\text{int}}(r,\theta,\phi,t) \tag{8.29}$$

for $r < R$. We can perturb Poisson's equation (Equation (4.4)) to find

$$\nabla^2\delta\Phi(r,\theta,\phi,t) = 4\pi G\delta\rho(r,\theta,\phi,t)\,. \tag{8.30}$$

Again, if we are only concerning ourselves with the inside of the NS, Equation (8.30) becomes

$$\nabla^2\delta\Phi^{\text{int}}(r,\theta,\phi,t) = 0 \tag{8.31}$$

for $r < R$. Equations (8.29) and (8.31) are the governing fluid equations of the Eulerian perturbations inside the NS. To solve them, we first take the divergence of Equation (8.29) to get

$$\bar{\rho}\frac{\partial^2}{\partial t^2}(\boldsymbol{\nabla}\cdot\boldsymbol{\xi}(r,\theta,\phi,t)) = -\nabla^2\delta P^{\text{int}}(r,\theta,\phi,t) - \bar{\rho}\nabla^2\delta\Phi^{\text{int}}(r,\theta,\phi,t) \tag{8.32}$$

and because our NS is incompressible ($\boldsymbol{\nabla}\cdot\boldsymbol{\xi} = 0$) and because of Equation (8.31), we find

$$\nabla^2\delta P^{\text{int}}(r,\theta,\phi,t) = 0\,. \tag{8.33}$$

Equations (8.31) and (8.33) are Laplace equations for $\delta\Phi^{\text{int}}(r,\theta,\phi,t)$ and $\delta P^{\text{int}}(r,\theta,\phi,t)$

respectively. From Equations (8.30) and (8.21), we also know the external perturbed gravitational potential $\delta\Phi^{\text{ext}}(r,\theta,\phi,t)$ must follow Laplace's equation. All three quantities will therefore have the same general solution at a fixed time which in spherical coordinates is

$$\delta Q(r,\theta,\phi) = \sum_{l=0}^{\infty}\sum_{m=-l}^{l}\left(A'_{lm}r^{l} + B'_{lm}r^{-(l+1)}\right)Y_{lm}(\theta,\phi) \tag{8.34}$$

for a general variable, Q. A'_{lm} and B'_{lm} are unknown constants to be fixed by using boundary conditions and $Y_{lm}(\theta,\phi)$ are spherical harmonic functions which have a degree, l, and an order, m. For a given l, there are $2l+1$ values of m.

Then, due to the requirement of regular (finite) solutions at $r = 0$ for $\delta\Phi^{\text{int}}(r,\theta,\phi,t)$ and $\delta P^{\text{int}}(r,\theta,\phi,t)$, and regular solutions at $r \to \infty$ for $\delta\Phi^{\text{ext}}(r,\theta,\phi,t)$, we get the solutions

$$\delta P^{\text{int}}(r,\theta,\phi) = A_{lm}r^{l}Y_{lm}(\theta,\phi) \tag{8.35}$$

$$\delta\Phi^{\text{int}}(r,\theta,\phi) = B_{lm}r^{l}Y_{lm}(\theta,\phi) \tag{8.36}$$

$$\delta\Phi^{\text{ext}}(r,\theta,\phi) = C_{lm}r^{-(l+1)}Y_{lm}(\theta,\phi) \tag{8.37}$$

at any point in time. A_{lm}, B_{lm} and C_{lm} are unknown constants. We have dropped the summation symbols but the indices here are not the same as tensor index notation used in Section 3.1, i.e. indices do not contract here. By construction, there is no matter at $r > R$. This means there is no pressure there and since changes in the mass density are only observed inside the NS or on the surface, $\delta P^{\text{ext}} = 0$.

Let us quickly review what is going to happen. We have three unknowns and we will use two boundary conditions to express B_{lm} and C_{lm} in terms of A_{lm}. Once we do that, we will express $\delta P^{\text{int}}(r,\theta,\phi,t)$, $\delta\Phi^{\text{int}}(r,\theta,\phi,t)$ and $\delta\Phi^{\text{ext}}(r,\theta,\phi,t)$ in terms of A_{lm} which we will use in the perturbed Euler equation (Equation (8.29)) to find $\boldsymbol{\xi}(r,\theta,\phi,t)$ in terms of A_{lm}. Once we have $\boldsymbol{\xi}(r,\theta,\phi,t)$ (the eigenfunctions), we eliminate A_{lm} to find ω^2_{lm} (the eigenvalues).

The first boundary condition is

$$\delta\Phi^{\text{int}}(R,\theta,\phi) = \delta\Phi^{\text{ext}}(R,\theta,\phi) \tag{8.38}$$

which keeps the gravitational potential continuous at the boundary after the perturbation has taken place. One can very quickly see from Equations (8.36) and (8.37) that this results in

$$C_{lm} = B_{lm}R^{2l+1}\,. \tag{8.39}$$

Next, the Lagrangian change to the pressure is also zero at the surface (this is what defines the surface) which is the second boundary condition

$$\Delta P(R,\theta,\phi) = 0\,. \tag{8.40}$$

This then leads to an equation similar in form to Equation (8.18)

$$\delta P(R,\theta,\phi) = -\boldsymbol{\xi}(R,\theta,\phi)\cdot\boldsymbol{\nabla}P(R) \tag{8.41}$$

by Equation (4.9). $P(R)$ is the background pressure (Equation (8.13)) evaluated at $r = R$ so doing the calculation and using Equation (8.35) for $\delta P(R,\theta,\phi)$, we get

$$A_{lm}R^{l}Y_{lm}(\theta,\phi) = \frac{4}{3}\pi G\bar{\rho}^{2}R\xi^{r}(R,\theta,\phi)\,. \tag{8.42}$$

We have not yet solved Poisson's equation at the boundary (Equation (8.30)), so we will do so now. Equation (8.30) becomes

$$\nabla^{2}\delta\Phi(r,\theta,\phi) = 4\pi G\bar{\rho}\delta(r-R)\xi^{r}(r,\theta,\phi) \tag{8.43}$$

when we use Equation (8.21) for $\delta\rho(r,\theta,\phi)$. This equation gives boundary information when we do a volume integral over a Gaussian pillbox positioned across the NS surface such that one end of the pillbox is just within the NS's surface, and the other end is just outside of it. In the limit of the ends of the pillbox becoming infinitely close, there is no contribution from the sides of the pillbox and so we pick out only the radial components from the volume integral. This then gives the result

$$\lim_{\varepsilon\to 0}\left[\frac{\partial\Phi^{\text{ext}}(R+\varepsilon,\theta,\phi)}{\partial r} - \frac{\partial\Phi^{\text{int}}(R-\varepsilon,\theta,\phi)}{\partial r}\right] = 4\pi G\bar{\rho}\xi^{r}(R,\theta,\phi) \tag{8.44}$$

which in the absolute limit, using Equations (8.36) and (8.37), we get

$$-(l+1)C_{lm}R^{-(l+2)}Y_{lm}(\theta,\phi) - lB_{lm}R^{l-1}Y_{lm}(\theta,\phi) = 4\pi G\bar{\rho}\xi^{r}(R,\theta,\phi)\,. \tag{8.45}$$

From Equation (8.39), we can relate C_{lm} to B_{lm} to simplify down to

$$-(2l+1)B_{lm}R^{l-1}Y_{lm}(\theta,\phi) = 4\pi G\bar{\rho}\xi^{r}(R,\theta,\phi)\,. \tag{8.46}$$

We now have enough to connect A_{lm} to B_{lm} through Equations (8.42) and (8.46). We do so by eliminating $\xi^{r}(R,\theta,\phi)$ from these two equations to get

$$B_{lm} = -\frac{3}{\bar{\rho}(2l+1)}A_{lm} \tag{8.47}$$

and using Equation (8.39), also get

$$C_{lm} = -\frac{3R^{2l+1}}{\bar{\rho}(2l+1)}A_{lm} \tag{8.48}$$

such that Equations (8.35), (8.36) and (8.37) become

$$\delta P^{\text{int}}(r,\theta,\phi) = A_{lm} r^l Y_{lm}(\theta,\phi) \tag{8.49}$$

$$\delta\Phi^{\text{int}}(r,\theta,\phi) = -\frac{3}{\bar{\rho}(2l+1)} A_{lm} r^l Y_{lm}(\theta,\phi) \tag{8.50}$$

$$\delta\Phi^{\text{ext}}(r,\theta,\phi) = -\frac{3R^{2l+1}}{\bar{\rho}(2l+1)} A_{lm} r^{-(l+1)} Y_{lm}(\theta,\phi)\ . \tag{8.51}$$

Next, we give all our variables oscillatory time dependences, $e^{i\omega_{lm}t}$, such that $\frac{\partial^2\boldsymbol{\xi}(r,\theta,\phi,t)}{\partial t^2} = -\omega_{lm}^2\boldsymbol{\xi}(r,\theta,\phi,t)$. Using this result along with Equations (8.49) and (8.50) in the perturbed Euler equation (Equation (8.29)), we can rearrange for the displacement vector

$$\boldsymbol{\xi}_{lm}(r,\theta,\phi) = \frac{2(l-1)}{2l+1}\frac{A_{lm}}{\bar{\rho}\omega_{lm}^2}\boldsymbol{\nabla}(r^l Y_{lm}(\theta,\phi)) \tag{8.52}$$

which are our eigenfunctions. To find our eigenvalues, which are values of ω_{lm}^2, we need to eliminate A_{lm}. We can do so if we use Equation (8.42) but that requires the radial component of $\boldsymbol{\xi}(r,\theta,\phi)$. We do this by taking the radial part of Equation (8.52) which is

$$\xi_{lm}^r(r,\theta,\phi) = \frac{2l(l-1)}{2l+1}\frac{A_{lm}}{\bar{\rho}\omega_{lm}^2} r^{l-1} Y_{lm}(\theta,\phi)\ . \tag{8.53}$$

Using this in Equation (8.42) and eliminating A_{lm}, we find our eigenvalues to be

$$\omega_{lm}^2 = \omega_l^2 = \frac{8\pi G\bar{\rho}}{3}\frac{l(l-1)}{2l+1}\ . \tag{8.54}$$

where we removed the subscript m from ω_{lm} since we have shown it does not depend on m. Thomson (1863) pointed out that for a given mass density, the oscillation frequency on a spherical fluid sphere is independent of the size of the sphere, which is indeed what is seen above.

It is also worth noting that oscillations cannot form for $l = 0$ or $l = 1$. Therefore, the smallest l that gives a non-zero oscillation frequency is $l = 2$ and this would be the mode that contributes most to GW emission, compared to higher modes with $l > 2$ (Thorne, 1980). For $l = 2$, the Kelvin mode frequency is

$$\omega_2^2 = \frac{16\pi G\bar{\rho}}{15}\ . \tag{8.55}$$

We introduce a new small parameter, α_{lm}, which is the dimensionless amplitude of a Kelvin mode, assumed to be much less than 1, and is defined as

$$\alpha_{lm} \equiv \frac{2(l-1)}{2l+1}\frac{A_{lm}R^{l-2}}{\bar{\rho}\omega_l^2} \tag{8.56}$$

such that the displacement vector takes the simpler form of

$$\boldsymbol{\xi}_{lm}(r,\theta,\phi,t) = \frac{\alpha_{lm}}{R^{l-2}}\boldsymbol{\nabla}(r^l Y_{lm}(\theta,\phi))e^{i\omega_l t} \tag{8.57}$$

which is even simpler in the case of $l = 2$. We defined α_{lm} in such a way that there is a R^{l-2} in the denominator of Equation (8.57). This is to ensure that α_{lm} remains dimensionless for all l. One can see this by looking at the gradient part which is proportional to r^{l-1}. We require $\boldsymbol{\xi}_{lm}$ to be a length so there must be a R^{l-2} in the denominator if α_{lm} is to be dimensionless.

We have set the time-dependence of the Kelvin modes to be $e^{i\omega_l t}$ since we require oscillatory behaviour. It will be important, especially when using second order perturbation theory, to always take the real part of Equation (8.57) because complex functions are only a mathematical tool that represents something which is actually physical. For instance, we use $e^{i\omega_l t}$ to represent the physical time dependence of $\cos(\omega_l t)$. We also need to take the real parts as soon as possible rather than at the end. This can clearly lead to errors as $\mathrm{Re}\left\{e^{2i\omega_l t}\right\} \neq (\mathrm{Re}\left\{e^{i\omega_l t}\right\})^2 \rightarrow \cos(2\omega_l t) \neq \cos^2(\omega_l t)$.

It is also important to note that spherical harmonics are complex functions due to a $e^{im\phi}$ dependence. If we are to take the real parts of $\boldsymbol{\xi}_{lm}$, we need to expand the spherical harmonics to account for the hidden imaginary term. To do this, we write

$$Y_{lm}(\theta,\phi) = Y_{lm}(\theta,0)e^{im\phi} \tag{8.58}$$

where $Y_{lm}(\theta,0)$ is purely real. This then allows us to rewrite $\boldsymbol{\xi}_{lm}$ as

$$\boldsymbol{\xi}_{lm}(r,\theta,\phi,t) = \alpha_{lm}\frac{r^{l-1}}{R^{l-2}}\left[lY_{lm}(\theta,0)\boldsymbol{e}_r + \frac{dY_{lm}(\theta,0)}{d\theta}\boldsymbol{e}_\theta + i\frac{m}{\sin\theta}Y_{lm}(\theta,0)\boldsymbol{e}_\phi\right]e^{i(m\phi+\omega_l t)} \tag{8.59}$$

or when in explicitly real form

$$\begin{aligned}\boldsymbol{\xi}_{lm}(r,\theta,\phi,t) = \alpha_{lm}\frac{r^{l-1}}{R^{l-2}}&\left[lY_{lm}(\theta,0)\cos(m\phi+\omega_l t)\boldsymbol{e}_r\right. \\ &\left.+\frac{dY_{lm}(\theta,0)}{d\theta}\cos(m\phi+\omega_l t)\boldsymbol{e}_\theta - \frac{m}{\sin\theta}Y_{lm}(\theta,0)\sin(m\phi+\omega_l t)\boldsymbol{e}_\phi\right].\end{aligned} \tag{8.60}$$

For completeness, we can express the real parts of δP^{int}, $\delta\Phi^{\mathrm{int}}$ and $\delta\Phi^{\mathrm{ext}}$ as

$$\delta P^{\mathrm{int}} = \frac{4\pi G\bar{\rho}^2 l}{3}\alpha_{lm}\frac{r^l}{R^{l-2}}Y_{lm}(\theta,0)\cos(m\phi+\omega_l t) \tag{8.61}$$

$$\delta\Phi^{\mathrm{int}} = -\frac{4\pi G\bar{\rho}l}{2l+1}\alpha_{lm}\frac{r^l}{R^{l-2}}Y_{lm}(\theta,0)\cos(m\phi+\omega_l t) \tag{8.62}$$

$$\delta\Phi^{\mathrm{ext}} = -\frac{4\pi G\bar{\rho}l}{2l+1}\alpha_{lm}\frac{R^{l+3}}{r^{l+1}}Y_{lm}(\theta,0)\cos(m\phi+\omega_l t)\,. \tag{8.63}$$

At this point, we should also define the pattern speed for non-axisymmetric ($m \neq 0$) modes

$$\omega_{\rm p} \equiv -\frac{\omega_l}{m} \tag{8.64}$$

which comes from tracking a fixed phase of the mode, i.e. from $\frac{d}{dt}(m\phi + \omega_l t) = 0$. This means that modes with negative m propagate in the positive (prograde) direction and modes with positive m propagate in the negative (retrograde) direction.

As we will mainly be focusing on $l = 2$, we list below Equations (8.59) - (8.63) but for $l = 2$. The complex version of $\boldsymbol{\xi}_{2m}$ is

$$\boldsymbol{\xi}_{2m}(r,\theta,\phi,t) = \alpha_{2m} r \left[2Y_{2m}(\theta,0)\boldsymbol{e}_r + \frac{dY_{2m}(\theta,0)}{d\theta}\boldsymbol{e}_\theta + i\frac{m}{\sin\theta}Y_{2m}(\theta,0)\boldsymbol{e}_\phi \right] e^{i(m\phi+\omega_2 t)} \tag{8.65}$$

followed by the real part

$$\begin{aligned}\boldsymbol{\xi}_{2m}(r,\theta,\phi,t) = \alpha_{2m} r \, [&2Y_{2m}(\theta,0)\cos(m\phi+\omega_2 t)\boldsymbol{e}_r \\ &+ \frac{dY_{2m}(\theta,0)}{d\theta}\cos(m\phi+\omega_2 t)\boldsymbol{e}_\theta - \frac{m}{\sin\theta}Y_{2m}(\theta,0)\sin(m\phi+\omega_2 t)\boldsymbol{e}_\phi \Big]\end{aligned} \tag{8.66}$$

and finally

$$\delta P^{\rm int} = \frac{8\pi G\bar{\rho}^2}{3}\alpha_{2m} r^2 Y_{2m}(\theta,0)\cos(m\phi+\omega_2 t) \tag{8.67}$$

$$\delta\Phi^{\rm int} = -\frac{8\pi G\bar{\rho}}{5}\alpha_{2m} r^2 Y_{2m}(\theta,0)\cos(m\phi+\omega_2 t) \tag{8.68}$$

$$\delta\Phi^{\rm ext} = -\frac{8\pi G\bar{\rho}}{5}\alpha_{2m}\frac{R^5}{r^3}Y_{2m}(\theta,0)\cos(m\phi+\omega_2 t)\,. \tag{8.69}$$

8.4 Energies and angular momenta of Kelvin modes from first principles

In this section, we will calculate the energies and angular momenta associated with the $l = 2$ Kelvin modes. In the first subsection, we will provide some background to why this calculation is not as straightforward as one might initially think. Then, we will proceed to calculate the energy and angular momentum from first principles, using equations from Appendix B of Friedman and Schutz (1978a). Throughout the remainder of this chapter, we will make extensive use of equations from Friedman and Schutz (1978a) and Friedman and Schutz (1978b), which we refer to using the shorthand (FSa...) and (FSb...) respectively. A large part of the rest of this chapter can also be found in Yim and Jones (2022).

8.4.1 Background to calculating mode energies

In the 1960s, Chandrasekhar pioneered a method to calculate energies of stars in equilibrium, in what he called the "virial method" (Chandrasekhar, 1961, 1969). This method intended to simplify the relatively harder problem of solving exact equations of motion, especially when gravity or magnetism are involved. It involves taking the first few moments of an equation of motion and looking at each subsequent equation individually. One of the main advantages is that individual terms can often be interpreted as physical quantities, like different energies.

An example can be seen for our system. If we take the first moment of the Euler equation, we get

$$\int_V \rho(\mathbf{x}) x_i \frac{dv_j}{dt} d\mathbf{x} = -\int_V x_i \frac{\partial P}{\partial x_j} d\mathbf{x} - \int_V \rho(\mathbf{x}) x_i \frac{\partial \Phi}{\partial x_j} d\mathbf{x} \tag{8.70}$$

which after some algebra (e.g. Chandrasekhar, 1969) simplifies to

$$\frac{1}{2}\frac{d^2\mathcal{I}}{dt^2} = 2T + W - 3U \tag{8.71}$$

where $\mathcal{I} = \int_V \rho(\mathbf{x})|\mathbf{x}|^2 d\mathbf{x}$ is the *scalar* moment of inertia, T is the kinetic energy of the background, U is the internal energy of the background and W is the gravitational potential energy of the background.

This gives the "virial equation" for the energies in the (unperturbed) background star, but here, we are concerned about the energies of the perturbations. Chandrasekhar and Lebovitz (1962) suggested that the virial method could be further used to study perturbation energies. In their analysis, they perturb the equation above with small changes in the energies, represented by a δ, which have an oscillatory time dependence, to give

$$-\frac{1}{2}\omega^2 \delta\mathcal{I} = 2\delta T + \delta W - 3\delta U \tag{8.72}$$

see also §118 of Chandrasekhar (1961). However, in general, it is not correct to do this. As Friedman and Schutz (1978a) pointed out, perturbation energies are second order meaning they are generally comprised of two terms: one that is quadratic in the first order changes in the fluid variables (ρ, $\mathbf{v}$, P, Φ) and another that is linear in the second order changes in the fluid variables. In the equation above and with how δT, δW and δU are defined, it is assumed that the term linear in the second order changes is zero. The reason is because it has the same form as the first order change in energy, which vanishes identically for stationary solutions. However, as was discovered for the CFS instability, rotating stars are not necessarily stable if a counter-rotating mode with a sufficiently large m is present, so there could indeed be a non-zero contribution from the neglected linear piece.

This oversight was carried into subsequent works throughout the 1960s and 1970s. This included work on another method called the "variational principle" which is distinct from, but is largely consistent with, the virial method (Chandrasekhar, 1964; Clement, 1964; Lynden-Bell and Ostriker, 1967). In the variational principle, which we will be using throughout this chapter, fluid perturbations are described by a displacement vector, $\boldsymbol{\xi}$, meaning we can keep track of our expansions in powers of $\boldsymbol{\xi}$ rather than in changes to the fluid variables.

Eventually, Schutz and Sorkin (1977) realised that there is a class of displacement vectors called the "trivials" that leave the physical fluid variables unchanged, but changed the (apparent) perturbation energy that many used for stability analysis. The trivials amounted to a relabelling of fluid elements, which clearly should not change the energy. This was the first sign that the existing expressions for perturbation energy were not complete.

Friedman and Schutz (1978a) set about fixing this and a year later, provided a complete second order calculation of the energies (and angular momentum) using the variational principle. Moreover, they were able to do this for a displacement vector that only needed to be first order in some small parameter (for us, α_{lm}). Here, we will apply their formalism to the Kelvin modes which, as far as we know, is the first time this has been done.

8.4.2 Mode energies

Recall that the (real) displacement vector for the $l = 2$ Kelvin modes is given by Equation (8.66). This will be used whenever ξ^i appears. It should also be noted that from now on, whenever referring to an accuracy up to a certain order, it means in powers of α_{lm}. Therefore, ξ^i is first order in α_{lm} and the mode energy and angular momentum are second order in α_{lm}.

In their Appendix B, Friedman and Schutz (1978a) give all the formulae that are needed to compute mode energies accurate to second order, using only the first order perturbations, ξ. We simply need to evaluate the relevant formulae for the Kelvin modes. The mode energies calculated here are "physical" in the sense that they represent the actual change in energy when a mode is present and comes from the elementary definitions of the different energies. This is opposed to the "canonical" energies that we will encounter later in Section 8.6.

The total physical change in energy due to a mode, δE, is given by the sum of the kinetic, internal and gravitational pieces (FSaB59)

$$\delta E = \delta T + \delta U + \delta W \tag{8.73}$$

TABLE 8.1: Table of contributions to the total mode energy δE, in units of $\beta \equiv \alpha_{2m}^2 \bar{\rho}\omega_2^2 R^5$. Starting with column 2, we have perturbation in kinetic energy δT, internal energy δU, gravitational energy δW, "total potential energy" $\delta V \equiv \delta U + \delta W$, and total energy $\delta E = \delta T + \delta V$.

	$\delta T/\beta$	$\delta U/\beta$	$\delta W/\beta$	$\delta V/\beta$	$\delta E/\beta$
$l = 2, m = 0$	$\sin^2(\omega_2 t)$	$\frac{5}{4}\cos^2(\omega_2 t)$	$-\frac{1}{4}\cos^2(\omega_2 t)$	$\cos^2(\omega_2 t)$	1
$l = 2, m = \pm 1, \pm 2$	$\frac{1}{2}$	$\frac{5}{8}$	$-\frac{1}{8}$	$\frac{1}{2}$	1

where each term depends on l and m of the mode, but is not explicitly shown here. We give a summary in Table 8.1 of each of these pieces, for the cases of $l = 2$, $m = 0$ and $l = 2$, $m \neq 0$.

The kinetic energy perturbation is given by (FSaB43), which for a non-rotating star takes the simple form

$$\delta T = \frac{1}{2}\int_V \rho \dot{\xi}^i \dot{\xi}_i \, dV \, . \tag{8.74}$$

Substituting for ξ using Equation (8.66), we obtain the results given in the second column of Table 8.1. Note that for $m = 0$, we have $\delta T \propto \sin^2(\omega_2 t)$, whilst for $m \neq 0$, we have $\delta T =$ constant. Both of these results were to be expected. For $m = 0$, the oscillation changes the shape of the star between a prolate and oblate shape, once per mode period. The kinetic energy will be zero when maximally deformed and positive in between. For $m \neq 0$, the mode results in a perturbed shape that rotates at the pattern speed, so that the configuration at different times is related by a rotation about the z-axis. It follows that δT (and also δU and δW) must be constant in time.

The internal energy piece is given by the $\nabla_i \xi^i = 0$ form of (FSaB48)

$$\delta U = \frac{1}{2}\int_V \xi^i \xi^j \nabla_i \nabla_j P \, dV \tag{8.75}$$

where $P(r)$ is the background pressure which can be found in Equation (8.13). From Equation (8.13), one can see that the pressure drops from a finite value to zero at the surface of the star, so $\nabla_j P$ at the stellar surface can be described by a Heaviside step function

$$\nabla_j P(r) = -\frac{4}{3}\pi G \bar{\rho}^2 r_j H(R - r) \tag{8.76}$$

where r_j is the position vector. When differentiated, the step function results in the appearance of a delta function

$$\nabla_i \nabla_j P(r) = -\frac{4}{3}\pi G \bar{\rho}^2 [\delta_{ij} H(R - r) - r_j \hat{r}_i \delta(r - R)] \tag{8.77}$$

where $\hat{r}_i$ is the radial unit vector. The integral to be computed therefore contains both a volume and surface term

$$\delta U = -\frac{2}{3}\pi G\bar{\rho}^2 \int_V \xi^i \xi_i \, dV + \frac{2}{3}\pi G\bar{\rho}^2 R \int_{\partial V} [\xi^r(R)]^2 \, dS \, . \tag{8.78}$$

The result of this calculation is given in the third column of Table 8.1, showing positive non-zero values for δU.

It may seem surprising that δU is not exactly zero for the modes we consider, which are, after all, supposed to be perturbations of an incompressible background star. We attribute the existence of this non-zero δU to the fact that the mode eigenfunctions of Section 8.3 were obtained by solving the equations of motion to *first* order in ξ. As such, they satisfy the incompressibility condition of $\nabla_i \xi^i = 0$, but only to first order. To second order, there will be a non-zero Lagrangian perturbation in the mass density, as is made clear by (FSaB32)

$$\frac{\Delta\rho}{\bar{\rho}} = -\nabla_i \xi^i + \frac{1}{2}(\nabla_i \xi^i \nabla_j \xi^j + \nabla_i \xi^j \nabla_j \xi^i) + \mathcal{O}(\xi^3) \, . \tag{8.79}$$

The last of the three terms on the right hand side is non-zero for our eigenfunctions. Consequently, this leads to a net compression resulting in the positive δU values that we calculated.

The perturbation in gravitational energy is given by (FSaB56)

$$\delta W = \int_V \left[\rho \xi^i \nabla_i \Phi + \rho \xi^i \nabla_i \delta\Phi + \frac{1}{8\pi G} \nabla_i \delta\Phi \nabla^i \delta\Phi + \frac{1}{2} \rho \xi^i \xi^j \nabla_i \nabla_j \Phi \right] dV \, . \tag{8.80}$$

Friedman & Schutz obtained this result by integrating by parts several times, exploiting the fact that surface terms, evaluated at infinity, are zero (see (FSaB49) – (FSaB53)). It follows that the domain of integration V extends to infinity, so one must include the contribution from *outside* the star. The first, second and fourth terms in the above integral vanish outside the star, as $\rho = 0$ there, but the third term has a non-vanishing component, and is calculated by using Equation (8.69) outside the star. Performing the calculations, we obtain the results given in the fourth column of Table 8.1.

In the fifth column of Table 8.1, we give the sum of the internal and gravitational energy perturbations

$$\delta V \equiv \delta U + \delta W \, . \tag{8.81}$$

This can be thought of as the total potential energy, which when summed with the kinetic term gives the full energy perturbation, δE, as recorded in the final column of Table 8.1. For all m, the result can be written as

$$\delta E = \alpha_{2m}^2 \bar{\rho} \omega_2^2 R^5 \, . \tag{8.82}$$

We can perform several checks of these results. Firstly, for $m = 0$, we can see that the δT and δV terms are of equal amplitude, representing an exchange between kinetic and potential energies, with constant total energy. For all m, we can verify that our results are consistent with the "virial equation for perturbations", given by Equation (6.6.14) of Shapiro and Teukolsky (1983)

$$\frac{1}{4}\frac{d^2}{dt^2}\delta I = \delta T - \delta V \tag{8.83}$$

where δI is the trace of the mass quadrupole moment tensor caused by the perturbations. We postpone the calculation of this tensor until Section 8.5.1, where it is required to compute the GW emission, but we note here that this virial equation is indeed satisfied by our solutions. A derivation of this equation is given in Appendix C.

For $m = 0$, we can also compare our result for δE with what is written in Chau (1967), in his Equation (17). Our result for δE is a factor of 2 larger than the result he uses. In fact, Chau does not compute δE. Instead, he takes a result from Rayleigh (1945), but comparing with this original source, Chau seems to have incorrectly copied Rayleigh's result. Specifically, it appears Chau only considers the kinetic energy term, given by Equation (7) of §264 of Rayleigh (1945), and replaces a $\cos^2$ term with a factor of $1/2$ (perhaps with the mindset of taking an average) when in fact, the inclusion of potential energies introduces a $\sin^2$ term which combines with the kinetic energy without the need to take an average.

8.4.3 Mode angular momenta

Friedman and Schutz (1978b) also give all the formulae that are needed to compute mode angular momenta accurate to second order, using only the first order perturbations, ξ.

Combining Equations (FSa61), (FSa47) and (FSa38) for $v^i = 0$ we have

$$\delta J = -\int_V \rho \left[\phi^i \Delta v_i + \frac{\partial \xi^i}{\partial \phi}\frac{\partial \xi_i}{\partial t}\right] dV \tag{8.84}$$

where $\phi^i = r\sin\theta(\boldsymbol{e}_\phi)^i$ and Δv_i is the Lagrangian perturbation in velocity, accurate to second order in ξ, as given in Equation (FSaB40)

$$\Delta v_i = \dot{\xi}_i + \dot{\xi}^j \nabla_i \xi_j = \dot{\xi}_i + \dot{\xi}^j \frac{\partial \xi_j}{\partial x^i} - \dot{\xi}^j \Gamma^k_{ji}\xi_k \tag{8.85}$$

where the minus sign comes from the covariant derivative acting on a covariant vector as opposed to the contravariant vector seen in Equation (3.8). Looking at the integral for δJ, we see the only non-zero term comes from Δv_ϕ if we are in spherical coordinates.

The connection coefficients, Γ^k_{ji}, can be found from a rearrangement of Equation (3.4)

$$\Gamma^k_{ji} = \boldsymbol{e}_k \cdot \nabla_i \boldsymbol{e}_j \tag{8.86}$$

where the right hand side can be calculated explicitly. However, there is a convenient list of connection coefficients for spherical coordinates on p.616 of Thorne and Blandford (2017) which we use instead. When the non-zero connection coefficients are substituted into Equation (8.85) with $i = \phi$, we get

$$\Delta v_\phi = \dot{\xi}_\phi + \dot{\xi}^r \frac{\partial \xi_r}{\partial \phi} + \dot{\xi}^\theta \frac{\partial \xi_\theta}{\partial \phi} + \dot{\xi}^\phi \frac{\partial \xi_\phi}{\partial \phi} - \dot{\xi}^\phi (\Gamma^r_{\phi\phi}\xi_r + \Gamma^\theta_{\phi\phi}\xi_\theta) - (\dot{\xi}^r \Gamma^\phi_{r\phi} + \dot{\xi}^\theta \Gamma^\phi_{\theta\phi})\xi_\phi \tag{8.87}$$

where $\Gamma^r_{\phi\phi} = -\Gamma^\phi_{r\phi} = -\frac{1}{r}$ and $\Gamma^\theta_{\phi\phi} = -\Gamma^\phi_{\theta\phi} = -\frac{\cot\theta}{r}$. Using this along with the $l = 2$ form of ξ from Equation (8.66), we find

$$\delta J = -\frac{1}{2} m \alpha^2_{2m} \bar{\rho} \omega_2 R^5 \tag{8.88}$$

for all m.

Recall our convention for the mode phase, $(m\phi + \omega_l t)$. Consistent with this, we see that modes which propagate in the positive mathematical sense ($m < 0$) have $\delta J > 0$, while modes that propagate in the negative mathematical sense ($m > 0$) have $\delta J < 0$, and $m = 0$ "prolate/oblate" modes have $\delta J = 0$.

8.5 Gravitational wave emission using quadrupole formulae

In the previous section, we found the energy and angular momentum of the $l = 2$ Kelvin modes, neglecting dissipation, i.e. the value of δE and δJ for a mode that is constantly oscillating on the NS. Now, we will compute the rate at which this mode radiates energy and angular momentum via the emission of GWs. This will cause it to damp away. The $m = 0$ case was first studied by Chau (1967) and the $m \neq 0$ case by Detweiler (1975), based on Thorne (1969), but Detweiler's calculations only considered energy conservation and not the full problem which also includes angular momentum.

In Section 8.5.1, we calculate the rate of change of energy due to GW emission. In Section 8.5.2, we calculate the rate of change of angular momentum. In Section 8.5.3, we discuss the significance of these results by considering the implied GW time-scales.

8.5.1 Rate of change of energy

For $l = 2$, the rate of change of energy due to GW emission, $\dot{E}_{\mathrm{GW}}$, is given by the standard quadrupole formula

$$\dot{E}_{\mathrm{GW}} = \frac{1}{5}\frac{G}{c^5}\left\langle \dddot{\mathcal{I}}_{ij}\dddot{\mathcal{I}}^{ij}\right\rangle \tag{8.89}$$

where the dots represent time derivatives in the inertial frame and the angled brackets represent an average over several wavelengths/periods (e.g. Misner et al., 1973; Andersson, 2019). $\mathcal{I}_{ij}$ is the trace-reduced mass quadrupole moment tensor, defined by

$$\mathcal{I}_{ij} \equiv \int_V \rho\left(x_i x_j - \frac{1}{3}\delta_{ij}x^k x_k\right) dV \tag{8.90}$$

where x^i is the position vector in a Cartesian basis. Note that $\dot{E}_{\mathrm{GW}}$ is positive when GWs carry energy away from the system resulting in the system's energy decreasing.

In practice, one would first calculate the mass quadrupole moment tensor

$$I_{ij} \equiv \int_V \rho x_i x_j dV \tag{8.91}$$

before reducing by its trace to give $\mathcal{I}_{ij}$, i.e.

$$\mathcal{I}_{ij} = I_{ij} - \frac{1}{3}\delta_{ij}I^k_{\ k} \tag{8.92}$$

such that $\mathrm{Tr}(\mathcal{I}_{ij}) = 0$. It is useful to decompose the mass quadrupole moment tensor into a term related to the background, which is spherical and constant in time, and a time-dependent term which is caused by the perturbation

$$I_{ij} = I_{\mathrm{sph}}\delta_{ij} + \delta I_{ij} \quad \rightarrow \quad \dot{I}_{ij} = \delta\dot{I}_{ij} \quad \rightarrow \quad \dot{\mathcal{I}}_{ij} = \delta\dot{\mathcal{I}}_{ij} \tag{8.93}$$

and similarly for higher time derivatives. From this, we see that once we obtain δI_{ij}, we can reduce it by its trace, differentiate with respect to time an appropriate number of times and then substitute into Equation (8.89) to get $\dot{E}_{\mathrm{GW}}$. So, our task now is to find δI_{ij}.

We can use the general rule for perturbing integral quantities where the mass density appears in the integrand

$$\delta\int_V \rho Q dV = \int_V \rho\Delta Q dV \tag{8.94}$$

(FSaB12) for some fluid variable Q (see also §15 of Chandrasekhar (1969) or Equation (4.21) for a similar result but using the covariant derivative definition of the Lagrangian change, as opposed to the more natural definition based on Lie derivatives

used by Friedman & Schutz). We obtain

$$\delta I_{ij} = \delta \int_V \rho x_i x_j dV = \int_V \rho \Delta(x_i x_j) dV = \bar{\rho} \int_V (\xi_i x_j + x_i \xi_j + \xi_i \xi_j) dV \tag{8.95}$$

which is exact and where ξ is now in a Cartesian basis. Note that the Lagrangian change to the position vector is exactly ξ by definition so there are no higher order terms to consider. We need only the first order terms of δI_{ij} to calculate the rate of change in GW energy and angular momentum accurate to second order, which are quadratic in (the time derivatives of) δI_{ij}, but we need the second order term to test the virial equation stated earlier in Equation (8.83).

Substituting ξ from Equation (8.66) into Equation (8.95) and after some algebra, we find

$$\begin{aligned} \delta I_{ij}^{2,0} &= \frac{1}{15} \alpha_{2,0} \bar{\rho} R^5 \cos(\omega_2 t) \dots \\ &\dots \begin{pmatrix} -4\sqrt{5\pi} + 5\alpha_{2,0} \cos(\omega_2 t) & 0 & 0 \\ 0 & -4\sqrt{5\pi} + 5\alpha_{2,0} \cos(\omega_2 t) & 0 \\ 0 & 0 & 4(2\sqrt{5\pi} + 5\alpha_{2,0} \cos(\omega_2 t)) \end{pmatrix} \end{aligned} \tag{8.96}$$

$$\delta I_{ij}^{2,\pm 1} = \frac{1}{4} \alpha_{2,\pm 1} \bar{\rho} R^5 \begin{pmatrix} 2\alpha_{2,\pm 1} \cos^2(\omega_2 t) & \mp \alpha_{2,\pm 1} \sin(2\omega_2 t) & \mp \frac{8}{15}\sqrt{30\pi}\, \cos(\omega_2 t) \\ \mp \alpha_{2,\pm 1} \sin(2\omega_2 t) & 2\alpha_{2,\pm 1} \sin^2(\omega_2 t) & \frac{8}{15}\sqrt{30\pi}\, \sin(\omega_2 t) \\ \mp \frac{8}{15}\sqrt{30\pi}\, \cos(\omega_2 t) & \frac{8}{15}\sqrt{30\pi}\, \sin(\omega_2 t) & 2\alpha_{2,\pm 1} \end{pmatrix} \tag{8.97}$$

$$\delta I_{ij}^{2,\pm 2} = \frac{1}{30} \alpha_{2,\pm 2} \bar{\rho} R^5 \begin{pmatrix} 4\sqrt{30\pi} \cos(\omega_2 t) + 15\alpha_{2,\pm 2} & \mp 4\sqrt{30\pi} \sin(\omega_2 t) & 0 \\ \mp 4\sqrt{30\pi} \sin(\omega_2 t) & -4\sqrt{30\pi} \cos(\omega_2 t) + 15\alpha_{2,\pm 2} & 0 \\ 0 & 0 & 0 \end{pmatrix} \tag{8.98}$$

which have traces equal to $2\alpha_{2,0}^2 \bar{\rho} R^5 \cos^2(\omega_2 t)$, $\alpha_{2,\pm 1}^2 \bar{\rho} R^5$ and $\alpha_{2,\pm 2}^2 \bar{\rho} R^5$ for $m = 0, \pm 1, \pm 2$ respectively. The superscripts on δI_{ij} represent values of l and m. As an independent check, we can now take these traces along with the energies in Table 8.1 to show that the virial equation in Equation (8.83) is indeed satisfied by the Kelvin modes for all m.

Taking these δI_{ij}, reducing by their trace, differentiating three times with respect to time and substituting into Equation (8.89), we find

$$\dot{E}_{\mathrm{GW}} = \frac{1}{5c^5} \alpha_{2m}^2 \bar{\rho} \omega_2^8 R^{10} \tag{8.99}$$

for all m and to second order in α_{2m}. To get to this form, we used Equation (8.55) which takes a factor of $\bar{\rho}$ along with some other constants and converts them to ω_2^2. This is why $\dot{E}_{\mathrm{GW}}$ is proportional to ω_2^8 instead of ω_2^6 which would be expected from just the time derivatives alone.

Our $m = 0$ case matches Equation (16) of Chau (1967) if one converts from our amplitude parameter, $\alpha_{2,0}$, to his. This can be done by equating the radial position of the perturbed surface, which is $R + \boldsymbol{\xi}(R, \theta, \phi, t) \cdot \boldsymbol{e}_r$ for our work. As far as we are aware, this is the first time the $m \neq 0$ GW luminosities for the Kelvin modes have been written down analytically (Detweiler (1975) only reported damping time-scales directly and not GW luminosities). For our particular choice of amplitude parameter, the relation for $\dot{E}_{\rm GW}$ is the same for all m, mirroring the behaviour seen in compressible stars (Thorne, 1969).

8.5.2 Rate of change of angular momentum

Moving on, the rate of change of angular momentum taken away by GWs is given by (e.g. Misner et al., 1973; Andersson, 2019)

$$\dot{J}^i_{\rm GW} = \frac{2}{5}\frac{G}{c^5}\varepsilon^{ijk}\left\langle \ddot{I}^l_j \dddot{I}_{kl} \right\rangle \tag{8.100}$$

which is positive when GWs are carrying away positive angular momentum. We find only the z component, $\dot{J}^z_{\rm GW}$, is present so we set $\dot{J}_{\rm GW} = \dot{J}^z_{\rm GW}$. This means angular momentum is only being lost in the z direction (for $m \neq 0$).

We follow the same steps as before where we take δI_{ij}, which we have already from Equations (8.96) – (8.98), reduce by the trace and take an appropriate number of time derivatives to use in the above equation for $\dot{J}_{\rm GW}$. After some algebra, we find

$$\dot{J}_{\rm GW} = -\frac{1}{5c^5} m \alpha^2_{2m} \bar{\rho} \omega_2^7 R^{10} \,. \tag{8.101}$$

8.5.3 Gravitational wave time-scales

Combining our results for the energy perturbation δE (Equation (8.82)) and the angular momentum perturbation δJ (Equation (8.88)) we see that

$$\delta E = 2\omega_{\rm p} \delta J \tag{8.102}$$

for $m \neq 0$, where $\omega_{\rm p}$ is the pattern speed. If instead we combine our results for the rate at which GW energy is radiated to infinity (Equation (8.99)) and the rate at which angular momentum is radiated (Equation (8.101)), we see, for $m \neq 0$, that

$$\dot{E}_{\rm GW} = \omega_{\rm p} \dot{J}_{\rm GW} \,. \tag{8.103}$$

This is a well-known relation that holds true for GW emission from any mass distribution with a well-defined pattern speed, and is an immediate consequence of the standard quadrupole formulae of Equations (8.89) and (8.100). The energy and angular

momentum radiated comes at the expense of the energy and angular momentum of the star.

In the case $m = 0$, we have $\delta J = 0$ and $\dot{J}_{\rm GW} = 0$, and the radiated energy clearly comes at the expense of the mode energy. Given that both δE and $\dot{E}_{\rm GW}$ are quadratic in α_{2m}, the mode decays exponentially on a time-scale

$$\tau_{\rm E} \equiv \frac{2\delta E}{\dot{E}_{\rm GW}} \,. \tag{8.104}$$

Using Equations (8.82) and (8.99), we obtain

$$\tau_{\rm E} = \frac{10c^5}{\omega_2^6 R^5} \,. \tag{8.105}$$

Note that the $m = 0$ result can be compared to Equation (19) of Chau (1967) but since his δE is a factor of 2 too small (see Section 8.4.2), his result for $\tau_{\rm E}$ is also a factor of 2 too small. Equation (8.105) is also valid for $m \neq 0$ and in this case, we can check our results against Detweiler (1975) to which we find our results are consistent.

For $m \neq 0$, the situation is more interesting. Comparing Equations (8.102) and (8.103), we see that while δE is locked to δJ, and $\dot{E}_{\rm GW}$ is locked to $\dot{J}_{\rm GW}$, the constants of proportionality differ by a factor of 2. This mean that, unlike the $m = 0$ case, the response of the star to the GW emission cannot only be to decrease the mode amplitude. More explicitly, for a given non-rotating star, the mode is parametrised by the single variable α_{2m} and its energy by α_{2m}^2. It follows that any other quantity proportional to α_{2m}^2, including δJ, must evolve on the same time-scale as the one given in Equation (8.105). However, if we were to compute the angular momentum analogue of Equation (8.105), we would define

$$\tau_{\rm J} \equiv \frac{2\delta J}{\dot{J}_{\rm GW}} \tag{8.106}$$

which leads to

$$\tau_{\rm J} = \frac{5c^5}{\omega_2^6 R^5} \tag{8.107}$$

i.e. there is a factor of 2 mismatch between the energy-based and angular momentum-based time-scales.

The natural resolution to this seeming contradiction is to realise that the definition of the time-scale in Equation (8.106) implicitly assumes that all of the angular momentum radiated away (i.e. all of $\dot{J}_{\rm GW}$) is at the expense of the mode angular momentum only (i.e. comes entirely from δJ). This suggests that the resolution is to allow for a torque to be exerted on the bulk of the star (i.e. on the background configuration), something which must then be accounted for in the angular momentum balance in order to obtain

consistent results. To leading order in Ω, this changes the angular momentum ($\mathcal{O}(\Omega)$) but not the energy of the background ($\mathcal{O}(\Omega^2)$).

8.6 Canonical mode energies and angular momenta

In the previous section, we showed that for $m \neq 0$, the effect of gravitational radiation reaction is to exert a torque on the star, such that it acquires a non-zero angular velocity. This means one must allow for the development of rotation even though our star is initially non-rotating (though initially has a mode with angular momentum δJ by construction). The complications and subtleties that arise from rotation are precisely those captured by the canonical energy/angular momentum formalism of Friedman and Schutz (1978a,b). We will therefore proceed by using this to carefully calculate the response of the star to GW emission, in terms of both the mode amplitude and the development of rotation. We will calculate the canonical energy of our Kelvin modes in Section 8.6.1 and the canonical angular momentum in Section 8.6.2. Then, in Section 8.7, we will compute the time derivatives of these quantities, which will allow a calculation of the effect of radiation reaction for $m \neq 0$.

8.6.1 Canonical energy

Friedman and Schutz (1978a,b) noted that, in addition to the physical second order energy perturbation δE, it is useful to define a *canonical energy* (described below), particularly when dealing with rotating stars. Although the following equations were originally derived for compressible NSs, we have independently checked from first principles that they remain valid for incompressible NSs. The first part of this section lays out the general equations, and the second part applies them to the Kelvin modes.

8.6.1.1 General equations

Friedman and Schutz (1978a) noted that the equation of motion can be written in the form

$$A^i{}_j \ddot{\xi}^j + B^i{}_j \dot{\xi}^j + C^i{}_j \xi^j \equiv 0 \tag{8.108}$$

(FSa15) where A, B and C are operators that depend on the properties of the background NS. For a non-rotating NS, $B^i{}_j = 0$. However, we keep all terms for now as this subsection is general and applies to all NSs. The form of $A^i{}_j$ and $C^i{}_j$ for our non-rotating incompressible star are given in Section 8.6.1.2 below. By writing the perturbed

equation of motion this way, the Lagrangian density $\mathcal{L}$, can be written as

$$\mathcal{L} = \frac{1}{2}\left(\dot{\xi}_i A^i{}_j \dot{\xi}^j + \dot{\xi}_i B^i{}_j \xi^j - \xi_i C^i{}_j \xi^j\right) \tag{8.109}$$

(FSa35). The canonical energy (in the inertial frame), E_c, is defined as

$$E_c \equiv \int_V \left(\dot{\xi}^i \frac{\partial \mathcal{L}}{\partial \dot{\xi}^i} - \mathcal{L}\right) dV \tag{8.110}$$

(FSa44) where $\dot{\xi}^i = \frac{\partial \xi^i}{\partial t}$ is real. Substituting the Lagrangian into Equation (8.110), we get our first method of calculating E_c (using real ξ)

$$E_c = \frac{1}{2}\int_V \left(\dot{\xi}_i A^i{}_j \dot{\xi}^j + \xi_i C^i{}_j \xi^j\right) dV \,. \tag{8.111}$$

Alternatively, Friedman and Schutz (1978a) found that a "sympletic structure" could more neatly describe a perturbed system. One key difference is that this sympletic structure requires complex ξ, which, for clarity, we will write as $\tilde{\xi}$. From this, Friedman and Schutz (1978a) provided another method to calculate E_c which we will label $\tilde{E}_c$, since it will be calculated with $\tilde{\xi}$. The following equation is true for oscillation modes that carry a $e^{i\omega_l t}$ dependence

$$\tilde{E}_c = \omega_l \left[\mathrm{Re}\{\omega_l\}\langle\tilde{\xi}, A\tilde{\xi}\rangle - \frac{1}{2}\langle\tilde{\xi}, iB\tilde{\xi}\rangle\right] \tag{8.112}$$

(FSa50) where the angled brackets represent a complex inner product, defined as

$$\langle\tilde{\xi}, \tilde{\eta}\rangle \equiv \int_V (\tilde{\xi}^i)^* \tilde{\eta}_i dV \tag{8.113}$$

(above FSa36). To quickly summarise, there are two methods to calculate E_c, one using Equation (8.111) with real ξ and the other using Equation (8.112) with complex ξ.

Friedman and Schutz (1978a) found a simple relation between the physical second order energy perturbation δE and the canonical energy E_c

$$\delta E = E_c + \int_V \rho v^i \Delta v_i dV \tag{8.114}$$

(FSa59) where ρ and v^i are the mass density and velocity of the unperturbed NS, and Δv_i is the second order (covariant) Lagrangian change to the velocity.

One can see from Equation (8.114) that for a static background ($v^i = 0$), the integral vanishes and we are left with the physical energy equalling the canonical energy, i.e. $\delta E = E_c$. We nevertheless proceed to calculate E_c using the formulae given above, as a check on our expression for δE in Equation (8.82). The calculation also provides

a natural precursor to the calculation of the canonical angular momentum in the next section, which does *not* equal the physical perturbation δJ.

8.6.1.2 Application to Kelvin modes

We will now apply the preceding equations to the Kelvin modes. We will calculate the canonical energy, E_c, which should be the same regardless of whether it is calculated with real or complex ξ, and must be equal to δE calculated previously (Equation (8.82)).

We start with the case of using real ξ to calculate E_c, see Equation (8.111). To do so, we recall the form of the equation of motion

$$\rho\frac{\partial \mathbf{v}}{\partial t} + \rho(\mathbf{v}\cdot\boldsymbol{\nabla})\mathbf{v} = -\boldsymbol{\nabla}P - \rho\boldsymbol{\nabla}\Phi \tag{8.115}$$

which we perturb with (Eulerian) perturbations, $Q \rightarrow Q_0 + \delta Q$, keeping first order terms only. Then, we subtract the background solution and enforce our assumptions of a static, uniformly-dense, incompressible NS to get

$$\bar{\rho}\ddot{\boldsymbol{\xi}} + \boldsymbol{\nabla}\delta P + \bar{\rho}\boldsymbol{\nabla}\delta\Phi = 0 \tag{8.116}$$

where we used $\delta\mathbf{v} = \dot{\boldsymbol{\xi}}$. We could have also obtained this from (FSa15) by using the conditions $\nabla_i\xi^i = 0$ and $v^i = 0$, alongside a re-expression of Φ in terms of P. Comparing to Equation (8.108), one immediately finds

$$A^i{}_j = \bar{\rho}\delta^i{}_j \tag{8.117}$$

$$B^i{}_j = 0 \tag{8.118}$$

$$C^i{}_j\xi^j = \nabla^i\delta P + \bar{\rho}\nabla^i\delta\Phi \tag{8.119}$$

where $\delta^i{}_j$ is the Kronecker delta. Note that $B^i{}_j$ is zero as expected for our static background configuration.

The expression for $A^i{}_j$ is straightforward and for $C^i{}_j\xi^j$, we need to know what δP and $\delta\Phi$ are, which were presented earlier in Equations (8.61) and (8.62). Using this along with ξ from Equation (8.60), Equation (8.111) in integral form becomes

$$E_c = \frac{1}{2}\alpha_{lm}^2\bar{\rho}\omega_l^2\int_V r^{2l-2}\left[l^2Y_{lm}^2(\theta,0) + \left(\frac{dY_{lm}(\theta,0)}{d\theta}\right)^2 + \frac{m^2}{\sin^2\theta}Y_{lm}^2(\theta,0)\right]dV \tag{8.120}$$

for all l and m. When we evaluate this integral for $l = 2$ Kelvin modes, we find that the canonical energy is given by

$$\delta E = E_c = \alpha_{2m}^2\bar{\rho}\omega_2^2R^5 \tag{8.121}$$

i.e. we have agreement with the physical second order energy perturbation δE computed in Section 8.4.2.

Alternatively, we can use complex $\tilde{\xi}$ to find $\tilde{E}_{\rm c}$, see Equation (8.112). The form of the complex solution is basically given by Equation (8.57) above, but now we, importantly, insert an additional normalisation factor N

$$\tilde{\boldsymbol{\xi}}(r,\theta,\phi,t) = N\frac{\alpha_{lm}}{R^{l-2}}\boldsymbol{\nabla}[r^l Y_{lm}(\theta,\phi)]e^{i\omega_l t} \tag{8.122}$$

$$\tilde{\boldsymbol{\xi}}(r,\theta,\phi,t) = N\alpha_{lm}\frac{r^{l-1}}{R^{l-2}}\left[lY_{lm}(\theta,0)\boldsymbol{e}_r + \frac{dY_{lm}(\theta,0)}{d\theta}\boldsymbol{e}_\theta + \frac{im}{\sin\theta}Y_{lm}(\theta,0)\boldsymbol{e}_\phi\right]e^{i(m\phi+\omega_l t)}\,. \tag{8.123}$$

Using $A^i{}_j$ (and $B^i{}_j = 0$) in Equation (8.112), along with $\tilde{\xi}$ from Equation (8.123), we find that the canonical energy of the Kelvin modes in integral form is

$$\tilde{E}_{\rm c} = N^2\alpha_{lm}^2\bar{\rho}\omega_l^2\int_V r^{2l-2}\left[l^2Y_{lm}^2(\theta,0) + \left(\frac{dY_{lm}(\theta,0)}{d\theta}\right)^2 + \frac{m^2}{\sin^2\theta}Y_{lm}^2(\theta,0)\right]dV\,. \tag{8.124}$$

Since the canonical energy must be the same regardless of whether ξ is real or complex, i.e. $E_{\rm c} = \tilde{E}_{\rm c}$, we find from comparing Equations (8.124) and (8.120) that

$$N^2 = \frac{1}{2} \quad\rightarrow\quad N = \frac{1}{\sqrt{2}} \tag{8.125}$$

for all l and m. With this considered, Equations (8.124) and (8.120) now give the same canonical energy.

This simple result is useful and necessary whenever there is a mixture of real and complex ξ within an analysis. Since the equation of motion is linear in the perturbation, there is no right or wrong relative normalisation for ξ as such, but one *must* enforce a relative normalisation if one wants to use both real and complex formulae in the same calculation. Without normalising, the calculation of the canonical energy with complex ξ would be twice the value obtained when the calculation is done entirely with real expressions. This clearly cannot be correct. To resolve this, one must put a factor of $\frac{1}{\sqrt{2}}$ in front of each complex ξ (specifically, a factor of $\frac{1}{\sqrt{2}}$ for every α_{lm}). This can be understood intuitively if one thinks of complex ξ as comprising of an equal amount of "power" in its real and imaginary parts. Thus, if we only consider the real part, we only get half the power, and hence $\frac{1}{\sqrt{2}}$ the amplitude.

8.6.2 Canonical angular momentum

8.6.2.1 General equations

We again begin by giving the general equations, to be applied to the Kelvin modes in Section 8.6.2.2. The canonical angular momentum is defined as

$$J_{\rm c} \equiv -\int_V \frac{\partial \xi^i}{\partial \phi}\frac{\partial \mathcal{L}}{\partial \dot{\xi}^i} dV \tag{8.126}$$

(FSa47) where ϕ is the azimuthal angle and ξ is real. Substituting in the Lagrangian from Equation (8.109) gives

$$J_{\rm c} = -\int_V \frac{\partial \xi^i}{\partial \phi}\left(A_{ij}\dot{\xi}^j + \frac{1}{2}B_{ij}\xi^j\right) dV \tag{8.127}$$

which will be the calculation using real ξ.

Alternatively, the sympletic structure can be used to find $J_{\rm c}$ but requires ξ to be complex and have a $e^{i(m\phi+\omega_l t)}$ dependence. Friedman and Schutz (1978a) found this to be

$$\tilde{J}_{\rm c} = -m\left[{\rm Re}\{\omega_l\}\langle\tilde{\xi}, A\tilde{\xi}\rangle - \frac{1}{2}\langle\tilde{\xi}, iB\tilde{\xi}\rangle\right] \tag{8.128}$$

(FSa51) for complex ξ. Comparing this to Equation (8.112), one finds, for $m \neq 0$, that $E_{\rm c}$ and $J_{\rm c}$ are related by the pattern speed

$$E_{\rm c} = -\frac{\omega_l}{m}J_{\rm c} = \omega_{\rm p}J_{\rm c} \tag{8.129}$$

(FSa52) which offers a quick alternative method to calculate $J_{\rm c}$ if one already has $E_{\rm c}$.

Note that whereas, for a non-rotating star, the physical and canonical energy of the perturbations were the same, this is not the case for the physical and canonical angular momenta

$$\delta J = J_{\rm c} + \int_V \rho\phi^i \Delta v_i dV \tag{8.130}$$

(FSa61). This point will be of importance when calculating the effect of gravitational radiation reaction.

8.6.2.2 Application to Kelvin modes

Once again, we specialise to the $l = 2$ Kelvin modes. Since we already have E_c from Equation (8.121), the simplest method would be to utilise Equation (8.129) which gives

$$J_c = -m\alpha_{2m}^2 \bar{\rho}\omega_2 R^5 \,. \tag{8.131}$$

We verified that one obtains the same value when using Equation (8.127) with real ξ or Equation (8.128) with complex ξ (whilst ensuring to account for the extra factor of $\frac{1}{\sqrt{2}}$ for every α_{2m}).

Note that this does indeed differ from the physical angular momentum of the Kelvin modes as given by Equation (8.130), corresponding to non-vanishing of the last term in Equation (8.130)

$$\delta J - J_c = \int_V \rho \phi^i \Delta v_i dV = \frac{1}{2} m\alpha_{2m}^2 \bar{\rho}\omega_2 R^5 \,. \tag{8.132}$$

Related to this, comparing Equations (8.88) and (8.131) we see that

$$J_c = 2\delta J \,. \tag{8.133}$$

8.7 Gravitational wave back-reaction

8.7.1 Mode damping time-scale

8.7.1.1 General equations

The aim here is to highlight a calculation, based on the work of Friedman and Schutz (1978a,b), that can determine the damping time-scale of modes on any NS. After the general calculation, we specialise to the Kelvin modes which will be covered in Section 8.7.1.2. The calculational method described here is similar to one done by Ipser and Lindblom (1991), but we stick rigidly to the formalism of Friedman & Schutz.

Friedman and Schutz (1978a) define the *canonical energy in the rotating frame*, $E_{c,R}$, as

$$E_{c,R} = E_c - \Omega J_c = \delta E - \Omega \delta J \tag{8.134}$$

(FSa62) where Ω is the angular frequency of the rigidly rotating NS. Note that $E_{c,R} = E_c = \delta E$ for non-rotating NSs.

One key reason why we introduced $E_{c,R}$ is because the time derivative of $E_{c,R}$ is easily calculable, thus making the physical mode damping time-scale also easily calculable.

To do this, we first need the perturbed form of the equation of motion of a dissipative system, which is given by

$$A^i{}_j \partial_t^2 \xi^j + B^i{}_j \partial_t \xi^j + C^i{}_j \xi^j = F^i \tag{8.135}$$

(FSb46) where ∂_t represents a time derivative in the inertial frame and crucially, F^i is some dissipative force (per unit volume) acting on the system. From this, one can calculate the time derivative of $E_{\rm c,R}$ with

$$\frac{d}{dt} E_{\rm c,R} = \langle \dot{\tilde{\xi}}, \tilde{F} \rangle \tag{8.136}$$

(FSb49). Formally, the dot here represents a time derivative evaluated in the rotating frame, i.e. $\dot{f} = (\partial_t + \Omega \partial_\phi) f$ (FSb42), but this distinction is not important for the non-rotating stars considered here. This time derivative of $E_{\rm c,R}$ is negative when the system is losing energy. It is also worth remembering that $\dot{\xi}$ and F must be complex in this equation (but the result of taking the inner product will be real, see below).

The mode damping time-scale is then given by

$$\tau_{\rm phys} \equiv -\frac{2E_{\rm c,R}}{\frac{d}{dt} E_{\rm c,R}} \tag{8.137}$$

where the minus sign ensures that the damping time-scale is positive for stable modes. Unlike the earlier definitions of $\tau_{\rm E}$ and $\tau_{\rm J}$, $\tau_{\rm phys}$ has the same quantity in the numerator and denominator, and so is clearly the correct expression for the mode damping time-scale. More explicitly, the numerators of $\tau_{\rm E}$ and $\tau_{\rm J}$ were the physical mode energy and angular momentum whereas the denominators were the rate of emission of GW energy and angular momentum.

There are a few more quantities that can be calculated with this formalism, where the equation of motion explicitly includes a dissipative term. For instance, the rate of change in the canonical energy and angular momentum can be calculated with

$$\frac{d}{dt} E_{\rm c} = {\rm Re}\langle \partial_t \tilde{\xi}, \tilde{F} \rangle \tag{8.138}$$

$$\frac{d}{dt} J_{\rm c} = -{\rm Re}\langle \partial_\phi \tilde{\xi}, \tilde{F} \rangle \tag{8.139}$$

(FSb70 & FSb71), where we have complex quantities on the right-hand side. Both are negative when canonical energy or positive angular momentum is being lost from the system. From this, Friedman and Schutz (1978b) found that the rate of change of $E_{\rm c}$ and $J_{\rm c}$ are related by the pattern speed

$$\frac{d}{dt} E_{\rm c} = \omega_{\rm p} \frac{d}{dt} J_{\rm c} \tag{8.140}$$

(below FSb71) much like the $\dot{E}_{\rm GW}$ and $\dot{J}_{\rm GW}$ in Equation (8.103).

8.7.1.2 Application to Kelvin modes

Like in Section 8.6.1.2, we write down the equation of motion for our system, perturb it, keep first order terms, subtract the background solution and apply our assumptions. What is different now is that we allow for a dissipative force, GW emission in this example, in the equation of motion. For GW emission, the dissipative force is given by

$$F^a = -\bar{\rho}\nabla^a\Phi_{\rm RR} \tag{8.141}$$

where $\Phi_{\rm RR}$ is the Burke-Thorne GW radiation reaction potential

$$\Phi_{\rm RR} = \frac{1}{5}\frac{G}{c^5}x^i x^j \frac{d^5}{dt^5}\text{Ŧ}_{ij} \tag{8.142}$$

(Burke, 1969, 1971; Thorne, 1969; Misner et al., 1973). This equates to having a perturbed equation of motion (8.135) of the form

$$\bar{\rho}\ddot{\xi}^a + \nabla^a\delta P + \bar{\rho}\nabla^a\delta\Phi = -\frac{1}{5}\frac{G}{c^5}\bar{\rho}\nabla^a x^i x^j \frac{d^5}{dt^5}\text{Ŧ}_{ij} \tag{8.143}$$

where a labels a spherical basis and i, j labels a Cartesian basis. When written like this, it is clear we must use real ξ in the preceding equations, including for F^a in Equation (8.141). However, we saw earlier that we need complex F^a in Equations (8.136), (8.138) and (8.139). This reiterates our need to connect real and complex expressions, and as shown in Section 8.6.1.2, we can do so by introducing a factor of $\frac{1}{\sqrt{2}}$ for every α_{lm} when going from real to complex.

To find $\tau_{\rm phys}$, we first need to find an expression for $E_{\rm c,R}$, but this is trivial for a non-rotating NS. For a non-rotating NS, $E_{\rm c,R}$ is simply equal to $E_{\rm c}$ so we read directly from Equation (8.121)

$$E_{\rm c,R} = E_{\rm c} = \alpha_{2m}^2\bar{\rho}\omega_2^2 R^5 \tag{8.144}$$

for all m.

Next is to find $\frac{d}{dt}E_{\rm c,R}$ so we now focus on F^a. For the $l = 2$ Kelvin modes, we get Ŧ_{ij} by manipulating δI_{ij} from Equations (8.96) – (8.98). We follow the same steps as before where we reduce by the trace (to get $\delta\text{Ŧ}_{ij}$) and since $\dot{\text{Ŧ}}_{ij} = \delta\dot{\text{Ŧ}}_{ij}$ (which also holds for

all higher time derivatives), we differentiate δI_{ij} five times and substitute into Equation (8.142) to find

$$\Phi_{\mathrm{RR}} \approx \begin{cases} -\frac{2\sqrt{5\pi}}{75}\frac{G}{c^5}\alpha_{2,0}\bar{\rho}\omega_2^5 R^5 r^2(1+3\cos 2\theta)\sin(\omega_2 t) & \text{for } m=0 \\ \pm\frac{2\sqrt{30\pi}}{75}\frac{G}{c^5}\alpha_{2,\pm1}\bar{\rho}\omega_2^5 R^5 r^2 \sin 2\theta \sin(\pm\phi+\omega_2 t) & \text{for } m=\pm1 \\ -\frac{2\sqrt{30\pi}}{75}\frac{G}{c^5}\alpha_{2,\pm2}\bar{\rho}\omega_2^5 R^5 r^2 \sin^2\theta \sin(\pm 2\phi+\omega_2 t) & \text{for } m=\pm2 \end{cases} \tag{8.145}$$

to first order in α_{2m}. Next, we use the GW radiation reaction potential to calculate the GW radiation reaction force using Equation (8.141)

$$F^a = \frac{4\sqrt{5\pi}}{75}\frac{G}{c^5}\alpha_{2,0}\bar{\rho}^2\omega_2^5 R^5 r \begin{pmatrix} (1+3\cos 2\theta)\sin(\omega_2 t) \\ -3\sin 2\theta \sin(\omega_2 t) \\ 0 \end{pmatrix} \quad \text{for } m=0 \tag{8.146}$$

$$F^a = -\frac{4\sqrt{30\pi}}{75}\frac{G}{c^5}\alpha_{2,\pm1}\bar{\rho}^2\omega_2^5 R^5 r \begin{pmatrix} \pm\sin 2\theta \sin(\pm\phi+\omega_2 t) \\ \pm\cos 2\theta \sin(\pm\phi+\omega_2 t) \\ \cos\theta\cos(\pm\phi+\omega_2 t) \end{pmatrix} \quad \text{for } m=\pm1 \tag{8.147}$$

$$F^a = \frac{2\sqrt{30\pi}}{75}\frac{G}{c^5}\alpha_{2,\pm2}\bar{\rho}^2\omega_2^5 R^5 r \begin{pmatrix} 2\sin^2\theta\sin(\pm 2\phi+\omega_2 t) \\ \sin 2\theta \sin(\pm 2\phi+\omega_2 t) \\ \pm 2\sin\theta\cos(\pm 2\phi+\omega_2 t) \end{pmatrix} \quad \text{for } m=\pm2 \tag{8.148}$$

which is purely real and comes from using real ξ. Here, F^a is written in terms of spherical basis vectors ($\boldsymbol{e}_r$, $\boldsymbol{e}_\theta$, $\boldsymbol{e}_\phi$). This is almost what we want, but Equation (8.136) is only valid for complex F^a. To "complexify" our real expression, we use the following

$$\cos(m\phi \pm \omega_2 t) \;\rightarrow\; \frac{1}{\sqrt{2}}e^{i(m\phi\pm\omega_2 t)} \tag{8.149}$$

$$\sin(m\phi \pm \omega_2 t) \;\rightarrow\; -\frac{1}{\sqrt{2}}ie^{i(m\phi\pm\omega_2 t)} \tag{8.150}$$

where the factor of $\frac{1}{\sqrt{2}}$ comes from Section 8.6.1.2 and from the fact that F^a depends linearly on α_{2m}. This then gives the complex expression for F^a which is

$$\tilde{F}^a = -\frac{1}{\sqrt{2}}\frac{4\sqrt{5\pi}}{75}\frac{G}{c^5}\alpha_{2,0}\bar{\rho}^2\omega_2^5 R^5 r e^{i\omega_2 t}\begin{pmatrix} i(1+3\cos 2\theta) \\ -3i\sin 2\theta \\ 0 \end{pmatrix} \quad \text{for } m=0 \tag{8.151}$$

$$\tilde{F}^a = -\frac{1}{\sqrt{2}}\frac{4\sqrt{30\pi}}{75}\frac{G}{c^5}\alpha_{2,\pm1}\bar{\rho}^2\omega_2^5 R^5 r e^{i(\pm\phi+\omega_2 t)}\begin{pmatrix} \mp i\sin 2\theta \\ \mp i\cos 2\theta \\ \cos\theta \end{pmatrix} \quad \text{for } m=\pm1 \tag{8.152}$$

$$\tilde{F}^a = -\frac{1}{\sqrt{2}}\frac{2\sqrt{30\pi}}{75}\frac{G}{c^5}\alpha_{2,\pm2}\bar{\rho}^2\omega_2^5 R^5 r e^{i(\pm 2\phi+\omega_2 t)}\begin{pmatrix} 2i\sin^2\theta \\ i\sin 2\theta \\ \mp 2\sin\theta \end{pmatrix} \quad \text{for } m=\pm2 \tag{8.153}$$

which can now be used in Equations (8.136) with complex $\dot{\xi}$, which is the time derivative of Equation (8.123) (with $N = \frac{1}{\sqrt{2}}$). Finally, this gives the (purely real) result

$$\frac{d}{dt}E_{\mathrm{c,R}} = -\frac{1}{5c^5}\alpha_{2m}^2\bar{\rho}\omega_2^8 R^{10} \tag{8.154}$$

for all m, where we have also used Equation (8.55). This expression for the rate of change of $E_{\mathrm{c,R}}$ is accurate to leading (second) order in α_{2m} and for the $m = 0$ case, had to be time-averaged. Note that this is equal to -$\dot{E}_{\mathrm{GW}}$ which was calculated with real ξ, i.e. Equation (8.99). It was not obvious to us from the outset that this would be the case, hence the need for this calculation.

Finally, using Equation (8.137), we find

$$\tau_{\mathrm{phys}} = \frac{10c^5}{\omega_2^6 R^5} \tag{8.155}$$

for all m. This is the physical damping time-scale for the Kelvin modes if GW emission is the only dissipative mechanism. The $m = 0$ damping time-scale calculated here agrees with Chau (1967) if one accounts for the factor of 2 that is missing from Chau's expression for his mode energy, see the discussion at the end of Section 8.4.2 for details. Our results also agree with the $m \neq 0$ Kelvin mode damping time-scales found by Detweiler (1975) based on the nearly Newtonian limit of the general relativistic formalism of Thorne (1969). For a typical f-mode frequency of $f_{\mathrm{mode}} = 2$ kHz (where $\omega_2 = 2\pi f_{\mathrm{mode}}$), the physical damping time-scale is $\tau_{\mathrm{phys}} \approx 0.06$ s.

Whilst we have F^a in complex form, we can, for completeness, calculate $\frac{d}{dt}E_{\mathrm{c}}$ and $\frac{d}{dt}J_{\mathrm{c}}$ using Equations (8.138) and (8.139). Doing this, one finds

$$\frac{d}{dt}E_{\mathrm{c}} = -\frac{1}{5c^5}\alpha_{2m}^2\bar{\rho}\omega_2^8 R^{10} = -\dot{E}_{\mathrm{GW}} \tag{8.156}$$

$$\frac{d}{dt}J_{\mathrm{c}} = \frac{1}{5c^5}m\alpha_{2m}^2\bar{\rho}\omega_2^7 R^{10} = -\dot{J}_{\mathrm{GW}}\,. \tag{8.157}$$

The energy result agrees with expectations since the inertial frame and rotating frame of a non-rotating NS are the same, so we would expect $\frac{d}{dt}E_{\mathrm{c}} = \frac{d}{dt}E_{\mathrm{c,R}}$. This result of Equation (8.157) then follows, to maintain consistency between the relations $\dot{E}_{\mathrm{GW}} = \omega_{\mathrm{p}}\dot{J}_{\mathrm{GW}}$ (Equation (8.103)) and $\dot{E}_{\mathrm{c}} = \omega_{\mathrm{p}}\dot{J}_{\mathrm{c}}$ (equation (8.129)).

8.7.2 Torque exerted on the star

In Section 8.5.3, we argued that, for $m \neq 0$, the effect of gravitational radiation reaction could not simply be to damp the mode – the bulk angular momentum of the star must change too. We now have everything to compute this change. To do so, we turn to the conservation of angular momentum. We will imagine the pre-existence of an $m \neq 0$

Kelvin mode on an initially non-rotating star, and then calculate the value of $\dot{\Omega}$ that the GW back-reaction induces. (We will look at the case where the mode is not pre-existing in the next chapter.) Formally, once the star rotates, the mode eigenfunctions will change, which means the mode energies and angular momenta would need to be calculated again. However, in the slow rotation regime this will be a higher order correction (in Ω) so we will not account for it here.

We follow a similar procedure as the r-mode analysis of Owen et al. (1998) and write the total angular momentum of the system as

$$J \equiv I\Omega + \delta J \tag{8.158}$$

where I is the NS's moment of inertia and $I\Omega$ is the angular momentum of the bulk of the NS. The difference here is that we used δJ to label the mode angular momentum, whereas Owen et al. (1998) used J_c. As we showed in Section 8.6.2.2, $J_c \neq \delta J$ and the physical mode angular momentum must be δJ. Differentiating with respect to time, we get a torque-balance equation

$$\dot{J} = I\dot{\Omega} + \delta\dot{J} \tag{8.159}$$

where we have discarded the $\dot{I}$ term since the rotation corrections to I will be of higher order. By conservation of angular momentum, $\dot{J} = -\dot{J}_{\rm GW}$ for our system, so that

$$-\dot{J}_{\rm GW} = I\dot{\Omega} + \delta\dot{J}\,. \tag{8.160}$$

There are two (completely equivalent) ways to find $\delta\dot{J}$. The first is to say $\delta\dot{J} = -\frac{2\delta J}{\tau_{\rm phys}}$ (since the mode exponentially decays over the physical time-scale) and then substitute in δJ and $\tau_{\rm phys}$. Or, we can differentiate the relation $J_c = 2\delta J$ from Equation (8.133) to give

$$\dot{J}_c = 2\delta\dot{J} \tag{8.161}$$

which can be combined with the relation $\dot{J}_c = -\dot{J}_{\rm GW}$ from Equation (8.157) to give

$$\delta\dot{J} = -\frac{1}{2}\dot{J}_{\rm GW}\,. \tag{8.162}$$

We can use this to eliminate $\delta\dot{J}$ from Equation (8.160) to give

$$I\dot{\Omega} = -\frac{1}{2}\dot{J}_{\rm GW}\,. \tag{8.163}$$

Inserting the explicit form of $\dot{J}_{\rm GW}$ from Equation (8.101) we obtain

$$I\dot{\Omega} = \frac{1}{10c^5} m\alpha_{2m}^2 \bar{\rho}\omega_2^7 R^{10}\,. \tag{8.164}$$

This shows that if positive angular momentum is being lost from a prograde ($m < 0$) mode, then we would have $\dot{\Omega} < 0$ which rotates the initially static NS in the retrograde direction. For a retrograde mode ($m > 0$), we have $\dot{\Omega} > 0$, so the NS rotates in the prograde direction.

To gain further insight, one can instead use Equation (8.162) to eliminate $\dot{J}_{\rm GW}$ from Equation (8.160) to give

$$\delta\dot{J} = I\dot{\Omega} \tag{8.165}$$

which can be integrated with respect to time

$$\int_0^\infty \delta\dot{J}\, dt = \int_0^\infty I\dot{\Omega}\, dt\ . \tag{8.166}$$

If we imagine that at $t = 0$ we deposit angular momentum $\delta J(0)$ into a mode on a non-rotating ($\Omega(0) = 0$) star, and integrate to $t = \infty$, so that the mode has completely decayed away, we obtain

$$\delta J(\infty) - \delta J(0) = I\Omega(\infty) - I\Omega(0) \tag{8.167}$$

such that

$$I\Delta\Omega = -\delta J(0) \tag{8.168}$$

where $\Delta\Omega$ is the change in angular velocity of the star as a result of the mode decaying away.

Similarly, we can re-arrange Equation (8.163) to give

$$\dot{J}_{\rm GW} = -2I\dot{\Omega} \tag{8.169}$$

which integrates to give

$$\delta J_{\rm GW} = -2I\Delta\Omega \tag{8.170}$$

where $\delta J_{\rm GW}$ is the angular momentum radiated away as GWs. Substituting for $I\Delta\Omega$ using Equation (8.168), we obtain

$$\delta J_{\rm GW} = 2\delta J(0)\ . \tag{8.171}$$

Therefore, we see that if one deposits angular momentum $\delta J(0)$ into an $m \neq 0$ Kelvin mode on a non-rotating star, a total angular momentum of $2\delta J(0)$ is ultimately radiated away, whilst the star itself "recoils" by acquiring an angular momentum of $-\delta J(0)$. In other words, the GW emission not only acts to reduce the angular momentum in the mode, but actually "over-extracts" what is available, so to compensate, the NS rotates

in the opposite direction of the mode to ensure angular momentum is conserved. As far as we know, this is the first time this GW back-reaction has been reported.

Chapter 9

Applying the oscillation model to observations

In the previous chapter, we computed the physical mode energies and angular momenta associated with the $l = 2$ Kelvin modes. We then computed the rate of change of these quantities as a result of gravitational radiation reaction. From conserving energy and angular momentum, we found, surprisingly, that gravitational radiation reaction from non-axisymmetric modes not only damps the mode, but also produces a rotation to the initially non-rotating star, with the direction of rotation opposing the direction of mode propagation. We name this effect the "GW back-reaction".

In this chapter, we explore the problem that originally inspired us to learn more about Kelvin modes, which is the problem of modelling pulsar timing noise. The initial idea for the model concerned only the angular frequency of a NS and asked the question,"if non-axisymmetric modes, which carry angular momentum, are excited during the spin-down of NSs, and its angular momentum were radiated away via GWs, could these excitations somehow explain pulsar timing noise and could we verify this with GW observations?"

As we saw in the last chapter, is not as simple as assuming that all the initial mode angular momentum is radiated away during the GW damping of the mode, but rather, it is twice the initial mode angular momentum that is radiated away. So, we will need to incorporate this into our model.

Additionally, there were a set of intriguing observational papers by Espinoza et al. (2014, 2021) that reported the existence of glitch candidates (GCs) and anti-glitch candidates (AGCs) which are described in more detail in Section 2.3.3.4. These correspond to small instantaneous positive and negative step changes to the angular frequency which we believe could be explained by mode excitations. Moreover, it is clear from

the papers that these GCs and AGCs form a separate group from normal glitches, suggesting the mechanism producing them need not be the same, e.g. does not have to be vortex unpinning or starquakes.

One notable observation is that these GCs and AGCs show an instantaneous step change in the spin-down rate immediately after they occur, with a sign opposite to that of the change in angular velocity. There are other events too where the changes in spin-down rate and angular frequency have the same sign, but we will not consider these here (see Espinoza et al. (2021) for more details). We had not considered the spin-down rate in our initial model but we provide a possible explanation via the coupling torque that exists between the internal superfluid and normal matter.

The model can be summarised as follows. As a NS spins-down on long time-scales, a mode with angular momentum δJ gets excited by some unspecified mechanism. Assuming the mode angular momentum is taken from the NS's rotational angular momentum, we find that the NS changes its rotational angular momentum by $-\delta J$. Then, as we saw in Chapter 8, GWs cause the mode to damp away (with $2\delta J$ radiated away as GWs) causing the NS's rotational angular momentum to change by a further $-\delta J$ meaning a total change of $-2\delta J$, a result of both excitation and decay of the mode. If $\delta J > 0$, like for an $m = -2$ mode, then one finds that the NS spins down ($\Delta\Omega < 0$). The opposite case is true for $m = 2$. The model as presented is enough the explain changes in just the angular frequency, so may be enough to explain timing noise.

On the other hand, if timing noise is in fact the aggregation of multiple GCs and AGCs, then we also need to explain changes in the spin-down rate observed for GCs and AGCs. When a NS is in steady-state, it is believed that there exists an interior pinned superfluid component which is weakly coupled to the NS's other matter (i.e. the crust plus any unpinned superfluid - we will call this combination the "charged" matter, even though overall it is electrically neutral, but this is in line with other works in the literature (e.g. Andersson et al., 2012)). When there is a change in the relative angular velocity between these two components (the pinned superfluid and charged matter), the coupling torque increases in magnitude and acts to reduce the change.

This can be utilised in our model. We propose the spin-up caused by the excitation and decay of an $m = 2$ mode *only spins-up the charged matter* (to which the magnetic field is thought to be "frozen" to, and hence, electromagnetic observations dependent on). This is expected as any torques cannot affect pinned superfluids. Then, the coupling torque between the two components acts in a way which tries to decrease the angular frequency of the charged matter (likewise, causes an increase to the spin-down rate, i.e. $\Delta\dot{\Omega} < 0$).

Most importantly, since this model depends on non-axisymmetric modes being excited, GWs are expected to be emitted. One could therefore test this model with GW observations.

The rest of the chapter is arranged as follows. In Section 9.1, the total change in angular velocity is computed by considering the excitation and damping of a non-axisymmetric mode. Then, in Section 9.2, we consider a simple model for the coupling torque, which allows us to fit to data from Espinoza et al. (2014, 2021) in Section 9.3. Finally, in Section 9.4, we evaluate the detectability of the modes through GW observations and in Section 9.5, we consider the energy budget that is required to power these modes. The work presented in chapter is intended to be published as a paper in the near future.

9.1 Total change in angular velocity

In our model, we will be considering $l = 2$ Kelvin modes which get excited and then subsequently damp away. It will be important to know the angular momentum of these modes which is given by Equation (8.88) and is repeated below

$$\delta J(t) = -\frac{1}{2} m \alpha_{2m}^2(t) \bar{\rho} \omega_2 R^5 \tag{9.1}$$

where now we have put in an explicit time dependence, with $t = 0$ being the time when some event occurs resulting in a mode being excited. We also learnt in Section 8.7.1 that the mode amplitude gets damped on the physical time-scale, τ_{phys}, such that

$$\alpha_{2m}(t) = \alpha_{2m}(0) e^{-\frac{t}{\tau_{\text{phys}}}} . \tag{9.2}$$

The expression for τ_{phys} for $l = 2$ is given in Equation (8.155) and was found to have a value $\tau_{\text{phys}} \approx 0.06$ s for a mode frequency of $f_{\text{mode}} = \frac{\omega_2}{2\pi} \approx 2$ kHz and a NS radius of $R = 10$ km.

Together, the above two equations give

$$\delta J(t) = -\frac{1}{2} m \alpha_{2m}^2(0) \bar{\rho} \omega_2 R^5 e^{-\frac{2t}{\tau_{\text{phys}}}} \equiv \delta J(0) e^{-\frac{2t}{\tau_{\text{phys}}}} \tag{9.3}$$

where $\delta J(0)$ is dependent on m, but we will suppress any subscripts for clarity.

In our model, we will assume the excitation of a mode of angular momentum $\delta J(0)$ comes at the expense of the rotational angular momentum of the NS. Therefore, the change in the NS's rotational angular momentum due to the excitation is

$$\Delta J = I \Delta \Omega_{\text{excite}} = -\delta J(0) \quad \rightarrow \quad \Delta \Omega_{\text{excite}} = -\frac{\delta J(0)}{I} \tag{9.4}$$

which assumes the moment of inertia does not change during the excitation event. We also saw that the damping of the mode, through GW emission, causes a GW back-reaction on the NS and was found to exert a torque

$$I\dot{\Omega}(t) = \frac{1}{10c^5} m\alpha_{2m}^2(t)\bar{\rho}\omega_2^7 R^{10} \quad \rightarrow \quad \dot{\Omega}(t) = -\frac{2}{\tau_{\text{phys}}}\frac{\delta J(0)}{I} e^{-\frac{2t}{\tau_{\text{phys}}}} \tag{9.5}$$

which can be integrated between $t = 0$ and the time until the next excitation event, t_{next}, which gives

$$\Delta\Omega_{\text{damp}} = \int_0^{t_{\text{next}}} \dot{\Omega}(t)dt = -\frac{\delta J(0)}{I}\left[1 - e^{-\frac{2t_{\text{next}}}{\tau_{\text{phys}}}}\right] \tag{9.6}$$

which is the change in angular frequency due to the damping of the mode. Adding these two effects together, we find that the total change in angular frequency due to the excitation and damping of a mode is

$$\Delta\Omega = \Delta\Omega_{\text{excite}} + \Delta\Omega_{\text{damp}} = -\frac{\delta J(0)}{I}\left[2 - e^{-\frac{2t_{\text{next}}}{\tau_{\text{phys}}}}\right] . \tag{9.7}$$

If the excitation is not instantaneous but instead occurs over some finite time-scale, and if we could resolve time-scales as short as τ_{phys}, then one might expect to see a two-step increase to the angular frequency. However, this would only be possible for pulsars that spin fast enough since τ_{phys} is already on the order of one rotation for the Crab and Vela. It would be necessary to see the angular frequency change across multiple rotations to be confident of such a finding.

Clearly, if the time until the next excitation event is much greater than the mode damping time-scale, i.e. $t_{\text{next}} \gg \tau_{\text{phys}}$, then the change in angular frequency can be well approximated as an instantaneous step change in angular frequency

$$\frac{\Delta\Omega}{\Omega} \approx -\frac{2\delta J(0)}{I\Omega} \tag{9.8}$$

where we have normalised by the NS's angular frequency so that both sides represents the glitch size. Once again, we can see that a mode with positive angular momentum causes a negative change to the angular frequency and vice versa. When we reinstate the mode amplitude using Equation (9.3), we find

$$\frac{\Delta\Omega}{\Omega} \approx \frac{15}{8\pi} m\alpha_{2m}^2(0)\frac{\omega_2}{\Omega} \tag{9.9}$$

where we also used $I = \frac{2}{5}MR^2$ and $\bar{\rho} = \frac{3M}{4\pi R^3}$. For the case of a fixed m and ω_2, the only free parameter left is the mode amplitude which controls how much the angular frequency changes. Or, from the other direction, observations of a given glitch size (or GW strain, see later) corresponds to a certain mode amplitude, if this model is to be believed.

With this model, we can explain changes in the angular frequency of NSs. For a sudden instantaneous change, like a GC, AGC or even a glitch (if the mode amplitude allows), our model would attribute this to the excitation and decay of a single non-axisymmetric mode. There is also the possibility that modes are consecutively excited over some period, which could lead to longer time-scale phenomena, like timing noise. At this point, we will explore perhaps a related phenomena – GCs and AGCs. Maybe these observations will help unravel the mystery behind what timing noise is and so we will now proceed to model them.

9.2 The need for a coupling torque

In this section, we will address the change in spin-down rate observed for GCs and AGCs. Figure 9.1 shows an example of this for the Crab. One can clearly see that GCs and AGCs are distinct from glitches and have smaller changes to the spin frequency. Similar to glitches, they have a measurable change in spin-up/down rate but unlike glitches, these changes are instantaneous step changes and are not modelled (or seen) to exponentially recover.

For the Crab and Vela, Espinoza et al. (2014, 2021) found that the fractional changes in spin-down rate are about 10^4 - 10^5 times larger than the fractional changes in spin frequency. Initially, one might want to see whether "conventional" spin-down, as indicated by some braking index, could explain the difference. One could simply choose a value of $n = 3$ for magnetic dipole radiation, or $n = 5$ for GW emission, but we will keep it general below. From Equation (2.10), the spin-down rate can be written as

$$\dot{\Omega} = -\kappa\Omega^n \tag{9.10}$$

where κ is some constant of proportionality. We want to know how $\dot{\Omega}$ changes in response to a change in the angular frequency, $\Delta\Omega$, so we perturb the above equation to give

$$\Delta\dot{\Omega} = -n\kappa\Omega^{n-1}\Delta\Omega\,. \tag{9.11}$$

Following on, one could substitute in the original equation to find

$$\left(\frac{\Delta\dot{\Omega}}{\dot{\Omega}}\right) = n\left(\frac{\Delta\Omega}{\Omega}\right)\,. \tag{9.12}$$

We see that with most theorised spin-down mechanisms, the braking index is not going to give the required fractional change in $\dot{\Omega}$ which is 10^4 - 10^5 times larger than the fractional change in Ω so we must resort to another mechanism.

In reality, we expect there to be at least two components to a NS, a superfluid component and a normal (also called "charged" above) component (e.g. Baym et al., 1969b).

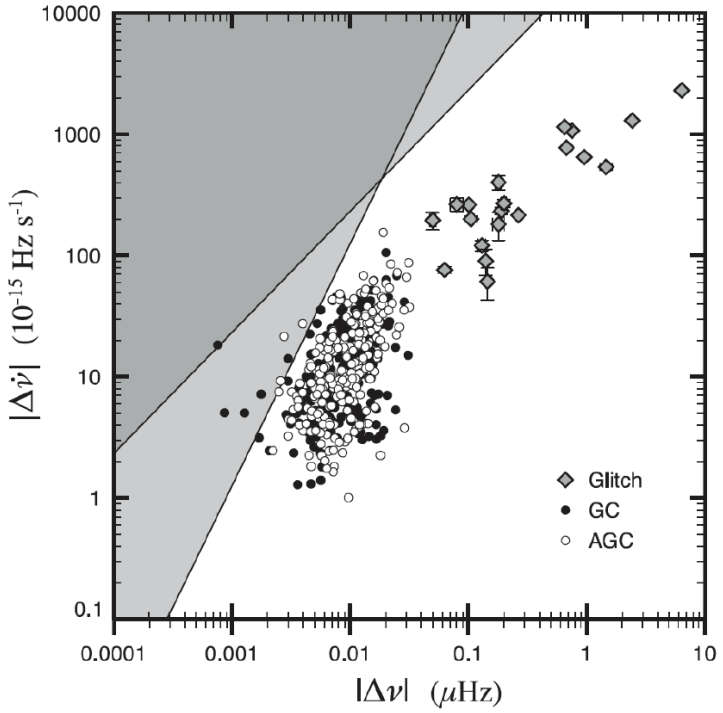

FIGURE 9.1: A graph showing the change in spin frequency and change in spin-up/down rate of different timing events of the Crab pulsar. GCs are marked with black circles, AGCs with white circles and glitches with diamonds. The shaded areas are representative areas in $\Delta\nu$ - $\Delta\dot{\nu}$ parameter space that are not observable, either because the events are too small to be distinguished from noise (steepest slope), or because the observational cadence is not high enough to catch the event happening (smallest slope). Figure taken from Espinoza et al. (2014).

The superfluid component is mainly comprised of superfluid neutrons and the normal component is the crust *plus any other matter strongly coupled to it* such as a proton superconductor. It is thought that the superfluid and normal components are coupled together, but when coupling is weak, the components are allowed to rotate at different speeds. Then, because there is a lag, a coupling torque acts to try to rotate the two components to the same speed, i.e. damps out any lag. We do not specify the cause of the coupling torque, e.g. mutual friction, but keep it as some resistive torque which is linear in the lag.

In the context of our problem, we could imagine, say, a retrograde mode being excited which causes the NS to rotate in the prograde direction. Specifically, this would mean that the normal component of the NS increases in spin frequency, with the superfluid component unchanged due to the weak coupling and the short time-scale of the spin-up ($\sim$ mode damping time-scale). This causes a change in the lag where the normal component now spins faster than what it used to. The coupling torque then acts in the opposite direction so spins the normal component back down (over the coupling time-scale) and, as we will soon see, does so with a spin-down rate large enough to explain the GCs. For AGCs, everything is reversed.

With that in mind, we will set up a set of torque-balance equations for the two separate components, the superfluid component being indicated by a subscript 'n', for neutrons, and the normal component with 'c', for the crust. In general, the crust would have some constant external torque, such as a magnetic dipole torque, acting to spin it down. We will indicate this with $\mathcal{N}_{\rm ext}$. Also acting on the crust would be the coupling torque which spins the crust down when $\Omega_{\rm c} > \Omega_{\rm n}$. For the superfluid, there would be an equal and opposite torque, as required by Newton's 3rd law. Putting everything together, this becomes

$$I_{\rm c}\dot{\Omega}_{\rm c} = \mathcal{N}_{\rm ext} - \frac{I_{\rm c}(\Omega_{\rm c} - \Omega_{\rm n})}{\tau_{\rm coup}} \tag{9.13}$$

$$I_{\rm n}\dot{\Omega}_{\rm n} = \frac{I_{\rm c}(\Omega_{\rm c} - \Omega_{\rm n})}{\tau_{\rm coup}} \tag{9.14}$$

where the choice of $I_{\rm c}$ in the coupling torque sets the interpretation of $\tau_{\rm coup}$ (but could equally be $I_{\rm n}$ or $I = I_{\rm c} + I_{\rm n}$ for a different interpretation) and $\tau_{\rm coup}$ is the coupling time-scale, which is a free parameter in this model. Here, $\tau_{\rm coup}$ can be thought of as the typical time it takes for a change in lag from an event to be damped out by the accompanying change in spin-down rate.

When we solve these coupled ODEs for $\dot{\Omega}_{\rm c}$ and $\dot{\Omega}_{\rm n}$, we find the solutions

$$\dot{\Omega}_{\rm n}(t) = \dot{\Omega}_{\infty} + (\dot{\Omega}_{\rm n,0} - \dot{\Omega}_{\infty})e^{-\frac{I}{I_{\rm n}}\frac{t}{\tau_{\rm coup}}} \tag{9.15}$$

$$\dot{\Omega}_{\rm c}(t) = \dot{\Omega}_{\infty} - \frac{I_{\rm n}}{I_{\rm c}}(\dot{\Omega}_{\rm n,0} - \dot{\Omega}_{\infty})e^{-\frac{I}{I_{\rm n}}\frac{t}{\tau_{\rm coup}}} \tag{9.16}$$

where $\dot{\Omega}_{\infty}$ is the steady-state spin-down rate of system, i.e. when $\dot{\Omega}_{\rm c} = \dot{\Omega}_{\rm n} \equiv \dot{\Omega}_{\infty}$, and is given by

$$\dot{\Omega}_{\infty} \equiv \frac{\mathcal{N}_{\rm ext}}{I} \tag{9.17}$$

and $\dot{\Omega}_{\rm n,0}$ is the initial spin-down rate of the superfluid which is given by

$$\dot{\Omega}_{\rm n,0} \equiv \frac{I_{\rm c}}{I_{\rm n}}\frac{\omega_0}{\tau_{\rm coup}} \tag{9.18}$$

where $\omega_0 \equiv \Omega_{\rm c,0} - \Omega_{\rm n,0}$ is the initial lag. Since our coupled ODEs are linear, we can easily use Equations (9.15) and (9.16) to tell us how the system would behave in response to a perturbation (GC, AGC or glitch)

$$\Delta\dot{\Omega}_{\rm n}(t) = \frac{I_{\rm c}}{I_{\rm n}}\frac{\Delta\omega_0}{\tau_{\rm coup}}e^{-\frac{I}{I_{\rm n}}\frac{t}{\tau_{\rm coup}}} \tag{9.19}$$

$$\Delta\dot{\Omega}_{\rm c}(t) = -\frac{\Delta\omega_0}{\tau_{\rm coup}}e^{-\frac{I}{I_{\rm n}}\frac{t}{\tau_{\rm coup}}} \tag{9.20}$$

where we have assumed the external torque and moment of inertias remain the same after the event. Glitches have a much larger $\Delta\omega_0$ when compared to GCs and AGCs. Now, $t = 0$ corresponds to the time of the event and quantities labelled with Δ represent changes due to the event. We see that for $t \ll \frac{I_n}{I}\tau_{\rm coup}$, the changes in spin-down rates are essentially step changes, but if observed for long enough afterwards, a recovery would be seen with a recovery time-scale of

$$\tau_{\rm EM} \equiv \frac{I_n}{I}\tau_{\rm coup} \, . \tag{9.21}$$

For glitches, $\tau_{\rm EM}$ is the usual post-glitch recovery time-scale. This recovery is typically observed as there is enough time between glitches. On the other hand, GCs and AGCs occur more frequently than glitches, so any recovery would be interrupted by another event which makes the change in spin-down rate appear step-like. We will assume that GCs and AGCs have the same $\tau_{\rm EM}$ as glitches.

We now move on to linking the observed change in spin-down rate (Equation (9.20)) to a change in crustal angular frequency. Taking the change in spin-down rate as being step-like, we can write

$$\Delta\dot{\Omega}_c \approx -\frac{\Delta\Omega_c - \Delta\Omega_n}{\tau_{\rm coup}} \approx -\frac{\Delta\Omega_c}{\tau_{\rm coup}} \tag{9.22}$$

if the change in superfluid angular frequency is much smaller than the change in the crust, i.e. $\Delta\Omega_n \ll \Delta\Omega_c$. This would happen if the angular momentum emitted via GWs affected the crustal component only. Dividing both sides by $\dot{\Omega}_c$ and re-expressing it as the characteristic age on the right hand side, $\tau_c = -\frac{\Omega_c}{2\dot{\Omega}_c}$, we find the simple relation

$$\frac{\Delta\dot{\Omega}_c}{\dot{\Omega}_c} \approx \frac{2\tau_c}{\tau_{\rm coup}}\left(\frac{\Delta\Omega_c}{\Omega_c}\right) \, . \tag{9.23}$$

This equation shows that, using a linear coupling torque, the fractional change in the spin-down rate is $\frac{2\tau_c}{\tau_{\rm coup}}$ larger than the fractional change in the spin frequency. For young pulsars, we might expect $\tau_c \sim 10^4$ - 10^5 years and the coupling time-scale is typically set to the recovery time-scale of a glitch, so anything on the order of months to years. This means the ratio of the two time-scales may give the required factor to explain the vast difference in magnitudes between the observed fractional change in spin-down rate and spin frequency for GCs and AGCs.

9.3 Applying the model to Espinoza et al. (2014, 2021) data

The model is now sufficiently detailed to explain the origin of the GCs and AGCs described in Espinoza et al. (2014, 2021). In this section, we will use our model to make predictions and then make a comparison to observed data.

There are a few assumptions that went into the modelling and we will state them here for clarity. They are:

- The mode decay time-scale is much smaller than the time between events, $\tau_{\rm phys} \ll t_{\rm next}$ – to allow for an instantaneous spin-up/down event
- The time between events is much smaller than the coupling time-scale (weighted by the fractional superfluid moment of inertia), $t_{\rm next} \ll \frac{I_{\rm n}}{I}\tau_{\rm coup}$ – to allow for step-like changes (appear not to recover)
- There is no change to the component moment of inertias or external torque at the event – to make Equation (9.23) simpler
- Any change in the superfluid angular frequency is much smaller than the step change in the crust's angular frequency, $\Delta\Omega_{\rm n} \ll \Delta\Omega_{\rm c}$ – to make Equation (9.23) simpler.

For these assumptions, we found

$$\frac{\Delta\Omega}{\Omega} \approx \frac{15}{8\pi} m\alpha_{2m}^2(0)\frac{\omega_2}{\Omega} \tag{9.24}$$

from Equation (9.9) and

$$\frac{\Delta\dot{\Omega}}{\dot{\Omega}} \approx \frac{2\tau_{\rm c}}{\tau_{\rm coup}}\left(\frac{\Delta\Omega}{\Omega}\right) = \frac{15}{4\pi} m\alpha_{2m}^2(0)\frac{\tau_{\rm c}}{\tau_{\rm coup}}\frac{\omega_2}{\Omega} \tag{9.25}$$

from Equation (9.23). Note that the first equality in Equation (9.25) relates $\Delta\dot{\Omega}$ to $\Delta\Omega$ and is agnostic to whatever causes the change in angular frequency. However, here we will focus on the excitation and decay of modes as what causes $\Delta\Omega$. In this case, we see that we have a two-parameter model, with $\alpha_{2m}(0)$ and $\tau_{\rm coup}$ being the model parameters (for a given m, taken to be $|m| = 2$ here). Since we know how $\tau_{\rm coup}$ relates to $\tau_{\rm EM}$ from Equation (9.21), and we know, from existing glitch recovery literature, the range of values that $\tau_{\rm EM}$ takes, we are able to recast the model parameter from $\tau_{\rm coup}$ to $\frac{I_{\rm n}}{I}$ instead. In the absence of electromagnetically observed glitch recovery time-scales, one can use $\tau_{\rm coup}$ as a model parameter directly.

A collection of glitch recovery time-scales for the Crab and Vela are found in Table 9.1 and Table 9.2 respectively. From these tables, we see that

$$\text{Crab}: \ 2\ \text{d} < \tau_{\rm EM} < 56\ \text{d} \tag{9.26}$$

$$\text{Vela}: \ 1.6\ \text{d} < \tau_{\rm EM} < 351\ \text{d}\ . \tag{9.27}$$

Multiplying by $\frac{I}{I_{\rm n}}$ gives a range of values for $\tau_{\rm coup}$. Typically, glitches require a superfluid fraction of at least $\frac{I_{\rm n}}{I} \gtrsim 0.01$ which is thought to come from either the crustal superfluid alone, or with an additional contribution from part of the core superfluid

TABLE 9.1: A table of glitch recovery time-scales for the Crab pulsar. Note that the recovery time-scales depend on the timing model used so it is expected for there to be variations between two groups reporting on the same glitch. The data in the 2nd to 4th columns come from the JBCA Glitch Database (Espinoza et al., 2011).

Crab					
Date	MJD	$\frac{\Delta\nu}{\nu}$	$\frac{\Delta\dot{\nu}}{\dot{\nu}}$	$\tau_{\rm EM}$ [d]	Reference
27/09/1969	40491.80	7.20×10^{-9}	4.4×10^{-4}	18.7 ± 1.6	Lyne et al. (1993)
				5 ± 2	Lyne et al. (2000)
29/07/1971	41161.98	1.90×10^{-9}	1.7×10^{-4}	...	...
26/10/1971	41250.32	2.10×10^{-9}	1.1×10^{-4}	...	...
04/02/1975	42447.26	3.57×10^{-8}	1.6×10^{-3}	18 ± 2	Lyne et al. (1993)
				15.5 ± 0.2	Lyne et al. (2000)
21/08/1986	46663.69	6.00×10^{-9}	5.0×10^{-4}	9.3 ± 0.2	Lyne et al. (1993)
				9.3 ± 0.2	Lyne et al. (2000)
29/08/1989	47767.504	8.10×10^{-8}	3.4×10^{-3}	18 ± 2	Lyne et al. (1993)
				18 ± 2	Lyne et al. (2000)
19/11/1992	48945.6	4.20×10^{-9}	3.2×10^{-4}	2.0 ± 0.4	Wong et al. (2001)
30/10/1995	50020.04	2.10×10^{-9}	2.0×10^{-4}	$3.2^{+7.3}_{-2.2}$	Wong et al. (2001)
26/06/1996	50260.031	3.19×10^{-8}	1.73×10^{-3}	10.3 ± 1.5	Wong et al. (2001)
10/01/1997	50458.94	6.10×10^{-9}	1.1×10^{-3}	$3.0^{+0.5}_{-1.1}$	Wong et al. (2001)
10/02/1997	50489.7	8.00×10^{-10}	-2.0×10^{-4}	2.2	Wong et al. (2001)
30/12/1997	50812.59	6.20×10^{-9}	6.2×10^{-4}	2.9 ± 1.8	Wong et al. (2001)
01/10/1999	51452.02	6.80×10^{-9}	7.0×10^{-4}	3.4 ± 0.5	Wong et al. (2001)
15/07/2000	51740.656	2.51×10^{-8}	2.9×10^{-3}	4.0	Wang et al. (2001)
17/09/2000	51804.75	3.50×10^{-9}	5.3×10^{-4}	...	...
24/06/2001	52084.072	2.26×10^{-8}	2.07×10^{-3}	...	...
25/08/2001	52146.758	8.90×10^{-9}	5.7×10^{-4}	...	...
12/08/2002	52498.257	3.40×10^{-9}	7.0×10^{-4}	...	...
09/11/2002	52587.20	1.70×10^{-9}	5.0×10^{-4}	...	...
03/03/2004	53067.078	2.14×10^{-7}	6.2×10^{-3}	21.1 ± 0.8	Wang et al. (2012)
				24 ± 1	Ge et al. (2020)
06/09/2004	53254.109	4.90×10^{-9}	2.0×10^{-4}	...	...
22/11/2004	53331.17	2.80×10^{-9}	7.0×10^{-4}	...	...
23/08/2006	53970.190	2.18×10^{-8}	3.1×10^{-3}	7.3 ± 3.4	Wang et al. (2012)
24/04/2008	54580.38	4.70×10^{-9}	2.0×10^{-4}	...	...
10/11/2011	55875.5	4.92×10^{-8}	...	10.6 ± 0.3	Ge et al. (2020)
27/03/2017	57839.92	2.14×10^{-9}	2.7×10^{-4}	...	...
07/11/2017	58064.555	5.16×10^{-7}	6.969×10^{-3}	38.6 ± 3.4	Zhang et al. (2018)
				56 ± 1	Vivekanand (2020)
				45.9 ± 0.3	Ge et al. (2020)
29/04/2018	58237.357	4.08×10^{-9}	4.6×10^{-4}	...	...
18/12/2018	58470.939	2.36×10^{-9}	3.60×10^{-4}	...	...
23/07/2019	58687.59	3.60×10^{-8}	...	...	...

(Andersson et al., 2012). A superfluid fraction of $\frac{I_{\rm n}}{I} \gtrsim 0.01$ means the coupling time-scale will be around 100 times larger than the observed electromagnetic time-scale. However, for GCs and AGCs it is different. As we will see shortly, we require that the superfluid fraction be on the order of unity, $\frac{I_{\rm n}}{I} \sim 1$, to be able to explain GC and AGC data. This suggests that GCs and AGCs utilise all the superfluid in both the core and crust, if the model is correct.

Next, we consider the initial mode amplitude, $\alpha_{2m}(0)$. The initial mode amplitude depends on how these modes are triggered so ideally it would come from detailed modelling of the trigger mechanism. In absence of this, there is an alternative method to proceed. Observationally, a change in spin frequency, $\Delta\nu$, maps onto a corresponding

TABLE 9.2: A table of glitch recovery time-scales for the Vela pulsar. The glitch recovery of the Vela pulsar is normally best fitted with the sum of two or more decaying exponentials, hence why there are two time-scales provided. We have omitted the very shortest of recoveries (< 1 d) and for the glitches fitted by Yu et al. (2013) and Basu et al. (2020), only one exponential was fitted. Note that the recovery time-scales depend on the timing model used so it is expected for there to be variations between two groups reporting on the same glitch. The data in the 2nd to 4th columns come from the JBCA Glitch Database (Espinoza et al., 2011).

Vela						
Date	MJD	$\frac{\Delta\nu}{\nu}$	$\frac{\Delta\dot{\nu}}{\dot{\nu}}$	τ_1 [d]	τ_2 [d]	Reference
28/02/1969	40280	2.34×10^{-6}	1.00×10^{-2}	10.0 ± 1.0	120.0 ± 6.0	Cordes et al. (1988)
29/08/1971	41192	2.05×10^{-6}	1.50×10^{-2}	4.0 ± 1.0	94.0 ± 5.0	Cordes et al. (1988)
27/12/1971	41312	1.20×10^{-8}	3.00×10^{-3}	10.0 ± 0.5	...	Cordes et al. (1988)
28/09/1975	42683	1.99×10^{-6}	1.10×10^{-2}	4.0 ± 0.4	35.0 ± 2.0	Cordes et al. (1988)
04/07/1978	43693	3.06×10^{-6}	1.80×10^{-2}	6.0 ± 0.6	75.0 ± 3.0	Cordes et al. (1988)
11/10/1981	44888.4	1.15×10^{-6}	4.90×10^{-2}	1.6 ± 0.2	233 ± 1	McCulloch et al. (1987)
				6.0 ± 0.6	14.0 ± 2.0	Cordes et al. (1988)
11/08/1982	45192	2.05×10^{-6}	2.30×10^{-2}	3.2 ± 0.5	60 ± 9	McCulloch et al. (1987)
				3.0 ± 0.6	21.5 ± 2.0	Cordes et al. (1988)
11/07/1985	46257.228	1.60×10^{-6}	1.70×10^{-2}	6.5 ± 0.5	332 ± 10	McCulloch et al. (1987)
24/12/1988	47519.804	1.81×10^{-6}	7.70×10^{-2}	4.64 ± 0.02	351 ± 1	McCulloch et al. (1990)
				4.0 ± 0.5	96 ± 5	Flanagan (1990)
20/07/1991	48457.382	2.72×10^{-6}	6.00×10^{-1}	...	...	...
26/07/1994	49559	8.35×10^{-7}	0	...	...	...
27/08/1994	49591.2	1.99×10^{-7}	1.20×10^{-1}	...	...	...
12/10/1996	50369.345	2.11×10^{-6}	5.95×10^{-3}	...	186 ± 12	Yu et al. (2013)
16/01/2000	51559.31	3.09×10^{-6}	6.74×10^{-3}	...	125 ± 83	Yu et al. (2013)
07/07/2004	53193	2.10×10^{-6}	...	...	37 ± 11	Yu et al. (2013)
13/08/2006	53960	2.62×10^{-6}	2.30×10^{-1}	...	73 ± 8	Yu et al. (2013)
31/07/2010	55408.8	1.94×10^{-6}	7.50×10^{-2}	...	...	...
21/09/2013	56556	3.10×10^{-6}	1.48×10^{-1}	...	...	...
22/09/2014	56922	4.00×10^{-10}	1.00×10^{-4}	...	...	...
12/12/2016	57734.485	1.43×10^{-6}	...	...	32 ± 2	Basu et al. (2020)

estimate for the initial mode amplitude, $\alpha_{2m}(0)$, as seen in Equation (9.24), so a value of $\Delta\nu$ can tell us what $\alpha_{2m}(0)$ needs to be.

On a graph of $\Delta\nu$ and $\Delta\dot{\nu}$, the observed range of $\tau_{\rm EM}$ with $\frac{I_{\rm n}}{I} = 1$ permits only a certain region in that parameter space. This is identified as the area between the dashed lines in Figures 9.2 and 9.3, where we have applied our model to the Crab and Vela. To get to any position within the allowable area, one simply chooses the appropriate combination of $\alpha_{2,2}(0)$ and $\tau_{\rm EM}$, within the specified limits for $\tau_{\rm EM}$.

As for how the boundaries set by the dashed lines are determined, we consider the upper and lower boundaries separately. The minimum $\tau_{\rm EM}$ determines the boundary at the top, with smaller minimum $\tau_{\rm EM}$ values pushing the boundary higher. Conversely, the maximum $\tau_{\rm EM}$ determines the boundary at the bottom, with greater maximum $\tau_{\rm EM}$ values pushing the boundary lower. Finally, to move right and left within the dashed lines, one increases or decreases the value of the initial mode amplitude, respectively.

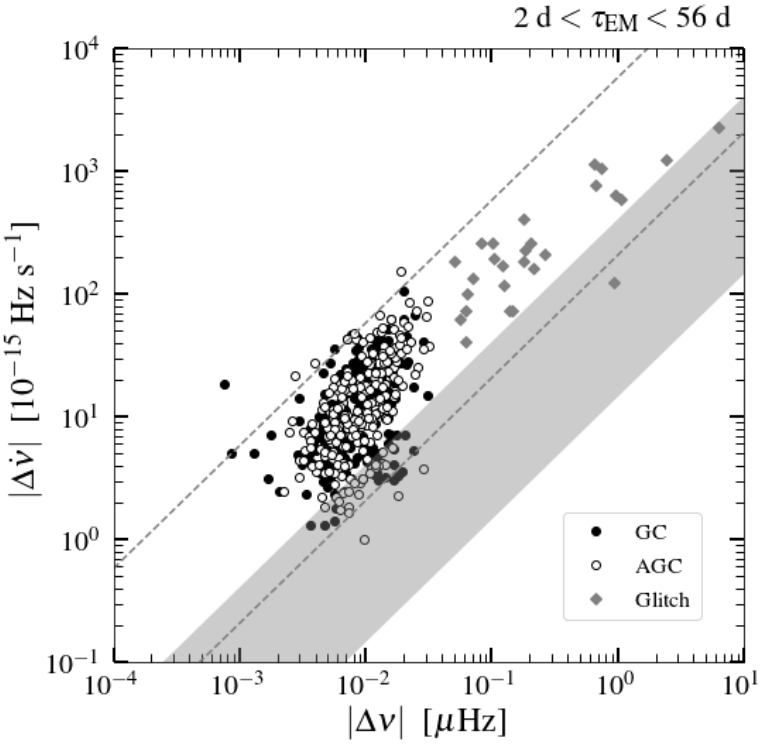

FIGURE 9.2: The area between the dashed lines shows the allowable parameter space that our model permits for the Crab pulsar given the observational constraints on $\tau_{\rm EM}$ and after setting $\frac{I_{\rm n}}{I} = 1$. The grey band is the same but for $\frac{I_{\rm n}}{I} = 0.07$. The filled black circles represent GCs, the filled white circles represent AGCs and the grey diamonds represent glitches. GC and AGC data provided by C. M. Espinoza.

Looking at Figures 9.2 and 9.3, one finds that our model can explain GCs and AGCs remarkably well when $\frac{I_{\rm n}}{I} = 1$, with most GC and AGC events falling within the allowable region. Interestingly, glitches for the Crab also fall into the allowable band when $\frac{I_{\rm n}}{I} = 1$, and only if the mode amplitude is allowed to be large enough. This is not the case for Vela's glitches however. This possibly hints at a different nature between the Crab and Vela's glitches, and in the context of this model, could mean that Vela requires a *smaller* superfluid fraction for glitches. In fact, if we decrease the superfluid fraction to $\frac{I_{\rm n}}{I} = 0.07$, motivated by the findings of Andersson et al. (2012), then the entire allowable band drops downwards on the graph and fits nicely over most of Vela's glitches (and misses most of the GCs and AGCs). This is shown by the grey band in the figures.

For Vela, this suggests its glitches require a smaller superfluid fraction compared to its GC and AGC events. This corresponds to a long coupling time-scale for its glitches and a short coupling time-scale for its GCs and AGCs. For the Crab, the superfluid fraction for glitches and GCs/AGCs are the same. Between the Crab and Vela, Vela's glitches require a smaller superfluid fraction compared to the Crab, assuming this model can be applied to glitches. For both the Crab and Vela, GCs and AGCs require a superfluid fraction of $\frac{I_{\rm n}}{I} = 1$.

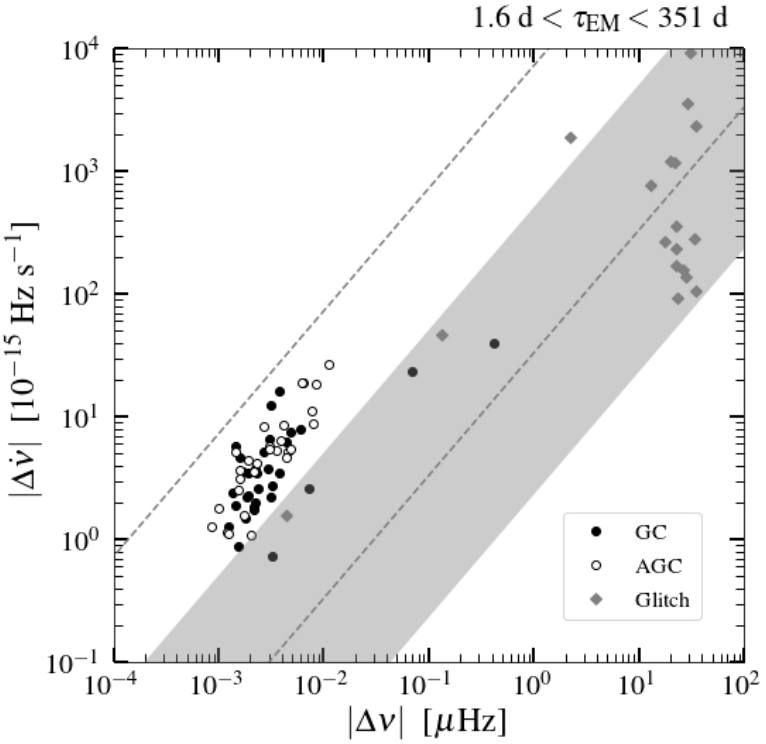

FIGURE 9.3: The area between the dashed lines shows the allowable parameter space that our model permits for the Vela pulsar given the observational constraints on $\tau_{\rm EM}$ and after setting $\frac{I_{\rm n}}{I} = 1$. The grey band is the same but for $\frac{I_{\rm n}}{I} = 0.07$. The filled black circles represent GCs, the filled white circles represent AGCs and the grey diamonds represent glitches. GC and AGC data provided by C. M. Espinoza.

As the crustal superfluid only accounts for about 2% of the total moment of inertia of a 1.4 $M_\odot$ NS (e.g. Ravenhall and Pethick, 1994), we conclude that part of the core superfluid is required to generate GCs, AGCs and glitches within this model. Further improvements to this simple model could help us understand more about the relatively unknown NS core, such as how much superfluid it contains.

9.4 Gravitational wave detectability of the $l = 2$ Kelvin modes

We have just seen that GCs and AGCs can be modelled using the model described here. As we know, non-axisymmetric modes give off GWs so the next natural question to ask is whether the GWs are detectable or not. If so, one could search for these predicted GWs to see if it is possible to falsify this model.

We begin by considering the SNR. From Section 3.5, the optimal SNR, ρ_0, is defined as

$$\rho_0^2 \equiv 4 \int_0^\infty \frac{|\tilde{h}(f)|^2}{S_{\rm n}(f)} df \tag{9.28}$$

where $|\tilde{h}(f)|^2 = \tilde{h}^*(f)\tilde{h}(f)$ and the tilde represents a Fourier transform. For a source that emits a GW signal whose amplitude changes but frequency remains fixed during the change in amplitude, such as a decaying oscillation mode or transient mountain, the power spectral density, $S_{\rm n}(f)$, remains almost constant so can be taken out of the integral. This leads to

$$\rho_0^2 = \frac{4}{S_{\rm n}(f)} \int_0^\infty |\tilde{h}(f)|^2 df \,. \tag{9.29}$$

Note that the frequency in $S_{\rm n}(f)$ is the GW frequency but the f in the integral is only a summation (dummy) variable. We then use Parseval's theorem to write

$$2\int_0^\infty |\tilde{h}(f)|^2 df = \int_{-\infty}^\infty |\tilde{h}(f)|^2 df = \int_{-\infty}^\infty |h(t)|^2 dt \,. \tag{9.30}$$

These relations can be seen from working from the middle outwards, i.e. the first equality is due to the $|\tilde{h}(f)|^2$ being an even function and the final equality is Parseval's theorem. This then allows us to write

$$\rho_0^2 = \frac{2}{S_{\rm n}(f)} \int_{-\infty}^\infty |h(t)|^2 dt \,. \tag{9.31}$$

For a exponentially-decaying GW signal of the form

$$h(t) \equiv h_0(t)\cos\left[\Phi(t)\right] \equiv h_0(0)e^{-\frac{t}{\tau_{\rm GW}}}\cos\left[\Phi(t)\right] \tag{9.32}$$

for $t \geq 0$, where $h_0(t)$ is the GW amplitude and $\Phi(t)$ is the GW phase, the optimal SNR can be shown to be equal to

$$\rho_0^2 = \frac{h_0^2(0)\tau_{\rm GW}}{2S_{\rm n}(f)} \quad \rightarrow \quad \rho_0 = \frac{h_0(0)\sqrt{\tau_{\rm GW}}}{\sqrt{2S_{\rm n}(f)}} \,. \tag{9.33}$$

With this in mind, we now turn our attention to calculating the GW signal we would expect from a decaying Kelvin mode and compare to Equations (9.32) and (9.33) to find the associated SNR.

We begin with the easier task of finding what $\tau_{\rm GW}$ is. We know that $h(t)$ for the Kelvin modes is proportional to the mode amplitude and the mode amplitude decays away on the mode damping time-scale, $\tau_{\rm phys}$. Therefore, it is clear to see that

$$\tau_{\rm GW} = \tau_{\rm phys} = \frac{625}{32}\frac{c^5}{G^3}\frac{R^4}{M^3} \tag{9.34}$$

which we read off from Equation (8.155) and used $\omega_2^2 = \frac{4GM}{5R^3}$ to get into the form above.

Next is to find $h_0(0)$. One can get this by looking at the rate of change in GW energy

which, for the special case of $l = 2$, $|m| = 2$ deformations, is given by the time derivative of Equation (5.24)

$$\dot{E}_{\rm GW} = \frac{1}{10}\frac{c^3}{G}\omega_2^2 d^2 h_0^2 \tag{9.35}$$

where we used $2\pi f = \omega_{GW} = 2\omega_{\rm p} = \omega_2$ with $\omega_{\rm p}$ being the pattern speed. This is also consistent with Equation (21) of Owen (2010). Conveniently, we already have $\dot{E}_{\rm GW}$ for the Kelvin modes which was calculated earlier in Equation (8.99). So, we substitute it into the left hand side of the above equation and rearrange for $h_0(0)$ to give

$$h_0(0) = \frac{4}{25}\sqrt{\frac{30}{\pi}}\alpha_{2,2}(0)\frac{G^2}{c^4}\frac{M^2}{R}\frac{1}{d} \tag{9.36}$$

where again, we used $\omega_2^2 = \frac{4GM}{5R^3}$.

Looking at Equation (9.36), one can place an upper limit on $\alpha_{2,2}(0)$ if GW observations place an upper limit on $h_0(0)$. As an aside, we note that there was a dedicated burst search conducted on Vela's August 2006 glitch (Abadie et al., 2011) which yielded an upper limit of $h_0(0) < 6.3 \times 10^{-21}$. So far, this is the strictest upper limit for GWs from glitches (that match the GW time-scales considered here). This corresponds to an upper limit of $\alpha_{2,2}(0) < 2.6 \times 10^{-4}$. To quickly convert between $h_0(0)$ and $\alpha_{2,2}(0)$, we state

$$\alpha_{2,2}(0) = 1.4 \times 10^{-4}\left(\frac{M}{1.4\,{\rm M}_\odot}\right)^{-2}\left(\frac{R}{10\,{\rm km}}\right)\left(\frac{d}{1\,{\rm kpc}}\right)\left(\frac{h_0(0)}{1\times10^{-21}}\right). \tag{9.37}$$

Next, we ask what the SNR is as a function of $\alpha_{2,2}(0)$. Putting Equations (9.34) and (9.36) into the equation for the SNR (squared), Equation (9.33), we get

$$\rho_0^2 = \frac{15}{2\pi}\alpha_{2,2}^2(0)\frac{G}{c^3}\frac{1}{S_{\rm n}(f)}MR^2\frac{1}{d^2} \tag{9.38}$$

or when we put in representative values of $\alpha_{2,2}(0) = 1 \times 10^{-6}$, $M = 1.4\,{\rm M}_\odot$, $R = 10\,{\rm km}$, $d = 1$ kpc, $\sqrt{S_{\rm n}(f)} = 1 \times 10^{-24}\,{\rm Hz}^{-\frac{1}{2}}$ (the value at $f = 2$ kHz for the ET), we get

$$\rho_0 = 1.3\left(\frac{\alpha_{2,2}(0)}{1\times10^{-6}}\right)\left(\frac{\sqrt{S_{\rm n}(f)}}{1\times10^{-24}\,{\rm Hz}^{-\frac{1}{2}}}\right)^{-1}\left(\frac{M}{1.4\,{\rm M}_\odot}\right)^{\frac{1}{2}}\left(\frac{R}{10\,{\rm km}}\right)\left(\frac{d}{1\,{\rm kpc}}\right)^{-1}. \tag{9.39}$$

Besides from effects of different distances, masses and radii, it is clear that the SNR does not change between different NSs. If we take the distance as given, then it is clear that GWs from mode oscillations can inform us more about the mass and radius, and hence provide constraints for the interior, which highlights one of the main motivations of GW astroseismology.

Instead of writing the SNR as a function of $\alpha_{2,2}(0)$, we can directly write it as a function

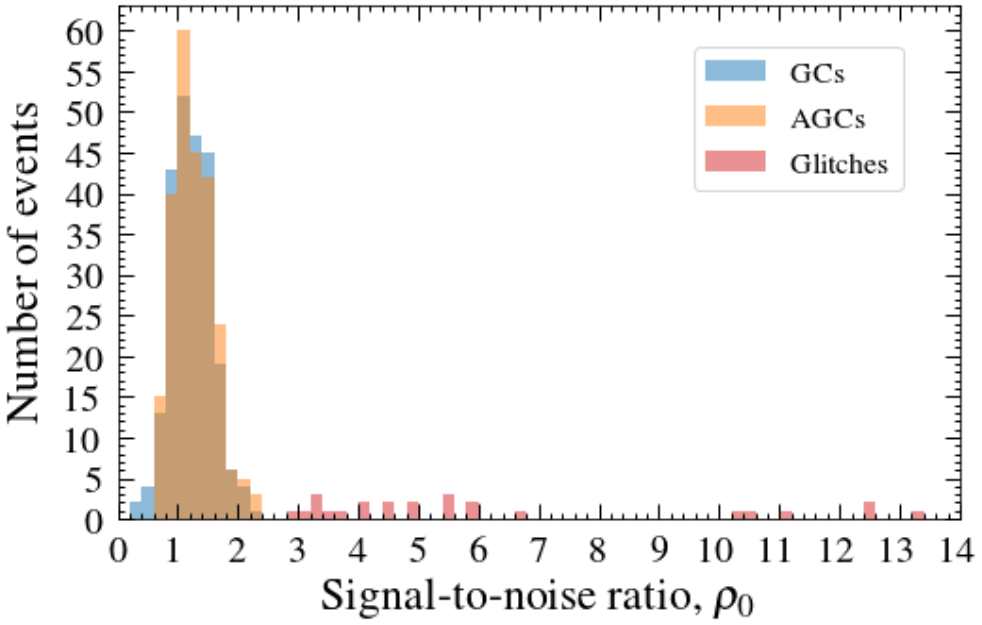

FIGURE 9.4: This histogram shows the SNR attainable by the ET for the predicted GWs from GCs, AGCs and glitches for the Crab pulsar. Some SNRs are not shown for clarity. These are at values of: 20.0, 32.6 and 50.6, all of which belongs to glitches.

of $\Delta\nu$ as our model allows us to change easily between the two via Equation (9.24). Doing so gives

$$\rho_0^2 = \frac{2\pi\sqrt{5G}}{c^3}\frac{1}{S_{\rm n}(f)}M^{\frac{1}{2}}R^{\frac{7}{2}}d^{-2}\Delta\nu \tag{9.40}$$

for $|m| = 2$. Figures 9.4 and 9.5 show histograms of the SNR that one finds when the above equation is applied to Crab and Vela data assuming ET sensitivity. For the Crab, GCs and AGCs have a SNR ~ 1, whereas the SNR is around ~ 5 for Vela. It appears that GWs from individual GCs or AGCs will not be detectable with the ET. However, it might be possible to coherently stack signals which improves the SNR by $\sqrt{N_{\rm excite}}$, with $N_{\rm excite}$ being the number of mode excitation events. This means that, for GCs/AGCs from Vela, one would need to stack between 2 - 5 events before the combined signal has a SNR that exceeds the detection threshold.

What is perhaps equally as interesting, but also fairly speculative, is to suggest that glitches are caused by the excitation and decay of an $m = 2$ mode instead of vortex unpinning or starquakes. This would require $\alpha_{2,2}(0)$ to be sufficiently large. One can find the SNRs that glitches would give (for the ET) in Figures 9.4 and 9.5. Some of the Crab's largest glitches and all of Vela's glitches should be detectable. In fact, Vela's glitch SNRs for the ET are so large that we can consider what they would be for aLIGO (at design sensitivity). The results of this are shown in Figure 9.6.

One can see that even with aLIGO, we will be able to put this idea to the test. For the largest Vela glitch, the corresponding initial mode amplitude needs to be $\alpha_{2,2}(0) =$

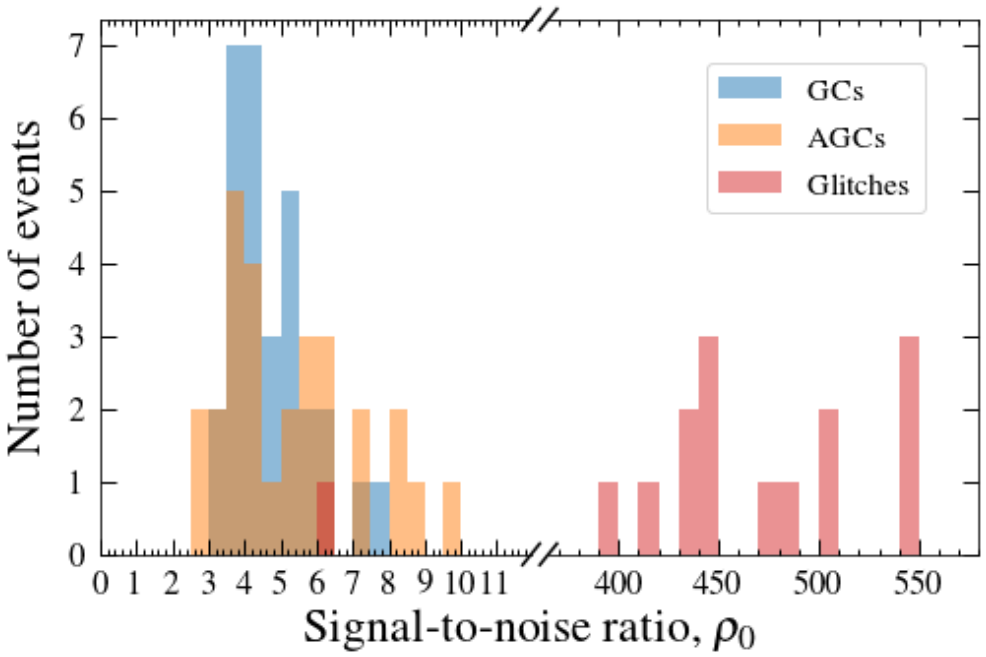

FIGURE 9.5: This histogram shows the SNR attainable by the ET for the predicted GWs from GCs, AGCs and glitches for the Vela pulsar. Note the change in scale after the break on the x-axis. Some SNRs are not shown for clarity. These are at values of: 33.9, 138.0 and 330.9, all of which belongs to glitches.

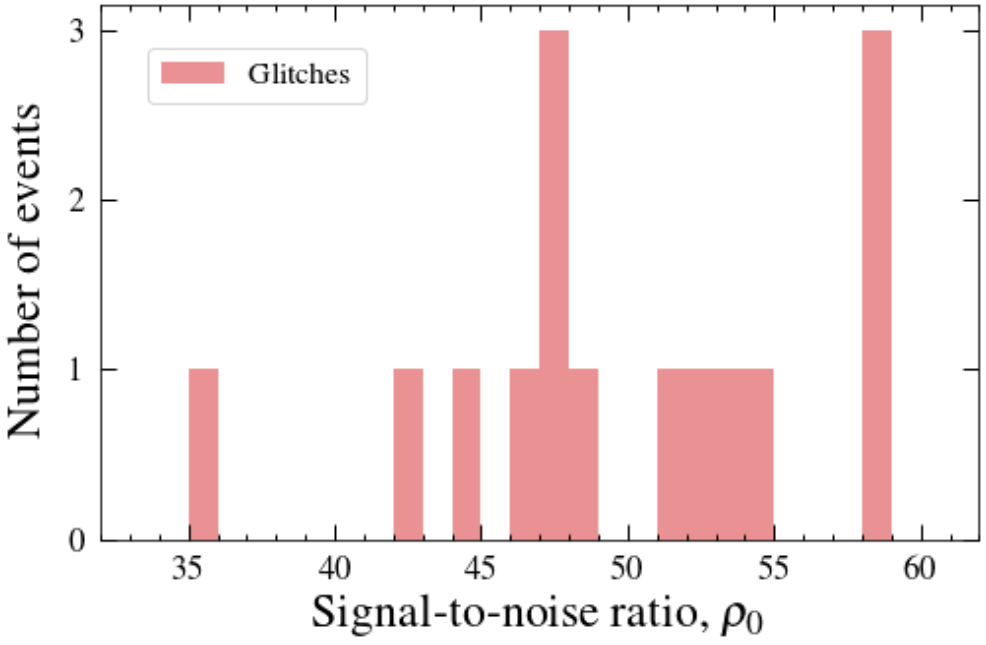

FIGURE 9.6: This histogram shows the SNR attainable by aLIGO at design sensitivity for the predicted GWs from glitches for the Vela pulsar. Some SNRs are not shown for clarity. These are at values of: 0.7, 3.7 and 14.9.

1.2×10^{-4}. From Abadie et al. (2011), we find an observational limit of $\alpha_{2,2}(0) < 2.6 \times 10^{-4}$ when their upper limit on $h_0(0)$ is cast to our model. This means that as far as GW observations are concerned, this idea is still plausible but could probably be ruled out, or upper limits set, with the next GW burst search coincident with a pulsar glitch. Current detectors are much more sensitive than what was used in Abadie et al. (2011).

9.5 Calculating the energies involved

So far, we have only considered the angular momentum of the NS system and like Chapter 7, we will now consider the energetics of our model. There is a slight difference here in that we consider (steady-state) power budgets rather than energies. The quantities we will be calculating are: the power required to sustain the GCs and AGCs, i.e. how much power we will need to give to the modes for them to exist, and the power that can be obtained from elasticity. Both quantities will be given as a fraction of the spin-down power, $\dot{E}_{\text{spin-down}} = -4\pi^2 I \nu \dot{\nu}$.

In the following subsections, it will be useful to know how many GCs/AGCs there were and over what timespan they occurred. For the Crab, there were 381 GCs and 383 AGCs (for a total of 764 events), and they occurred over a timespan of $T_{\text{obs}} \approx 10620$ d (Espinoza et al., 2014). Likewise, for Vela, there were 83 GCs and 66 AGCs (for a total of 149 events) that occurred over a timespan of $T_{\text{obs}} = 6865$ d (Espinoza et al., 2021). Also, so that everything is in one place, $\nu_{\text{Crab}} = 29.6$ Hz, $\dot{\nu}_{\text{Crab}} = -3.68 \times 10^{-10}$ Hz s^{-1}, $\nu_{\text{Vela}} = 11.2$ Hz and $\dot{\nu}_{\text{Vela}} = -1.56 \times 10^{-11}$ Hz s^{-1}.

9.5.1 Energy required to power the Kelvin modes

We already know how much energy it takes to excite an individual Kelvin mode from Equation (8.82), denoted by δE. Therefore, the average power required to power these modes is given by

$$\langle \dot{E}_{\text{mode}} \rangle = \frac{N \langle \delta E \rangle}{T_{\text{obs}}} = \frac{3}{5\pi} \langle \alpha_{2,2}^2 \rangle \frac{GM^2}{R} \frac{N}{T_{\text{obs}}} \tag{9.41}$$

where N is the total number of GCs and AGCs and the angled brackets indicates an average. Using the GC and AGC data from Figures 9.2 and 9.3, we can convert $\Delta\nu$ values into $\alpha_{2,2}^2$ using Equation (9.24) and then take an average. This gives $\langle \alpha_{2,2}^2 \rangle = 4.3 \times 10^{-12}$ for the Crab and $\langle \alpha_{2,2}^2 \rangle = 1.4 \times 10^{-12}$ for Vela. Using these values in the equation above, along with the values of N and T_{obs} from Espinoza et al. (2014, 2021),

we get

$$\text{Crab:}\quad \dot{E}_{\text{mode}} = 3.6\times10^{35}\left(\frac{\sqrt{\langle\alpha_{2,2}^2\rangle}}{2.1\times10^{-6}}\right)^2\left(\frac{M}{1.4\,\text{M}_\odot}\right)^2\left(\frac{R}{10\,\text{km}}\right)^{-1}\text{erg s}^{-1} \tag{9.42}$$

$$\text{Vela:}\quad \dot{E}_{\text{mode}} = 3.5\times10^{34}\left(\frac{\sqrt{\langle\alpha_{2,2}^2\rangle}}{1.2\times10^{-6}}\right)^2\left(\frac{M}{1.4\,\text{M}_\odot}\right)^2\left(\frac{R}{10\,\text{km}}\right)^{-1}\text{erg s}^{-1} \tag{9.43}$$

which, when expressed as a fraction of the spin-down energy, $\dot{E}_{\text{spin-down}} = -4\pi^2 I\nu\dot{\nu}$, is

$$\text{Crab:}\quad \frac{\dot{E}_{\text{mode}}}{\dot{E}_{\text{spin-down}}} \sim 7\times10^{-4} \tag{9.44}$$

$$\text{Vela:}\quad \frac{\dot{E}_{\text{mode}}}{\dot{E}_{\text{spin-down}}} \sim 4\times10^{-3}\,. \tag{9.45}$$

This shows that we need less than 1% of the spin-down power to sustain the excitation of Kelvin modes as frequently as they appear in observations. As for GWs, this means that there is a up to 1% of the spin-down power available for GW emission if this model is to be believed.

9.5.2 Energy attainable from elasticity

We have shown that we need around 10^{-3} of the spin-down power to power our modes but we need some mechanism to explain where this energy comes from. A natural place to look at is the elastic energy that is stored in the crust as the NS spins down. Here, we will do a rough calculation to see how much energy we can extract from the elasticity in the crust.

One can imagine that at some point in time, a NS is rotating at some angular velocity which gives it some oblateness. As the NS spins down, the oblateness wants to decrease due to a weakening centrifugal force, but the rigidity of the crust prevents it from doing so. This then strains the crust so we get a build up of elastic energy that we could harness for the excitation of our modes. This is build up of elastic strain is essentially a part of the starquake model.

Therefore, we return to the Baym and Pines (1971) model for starquakes which is detailed in Section 7.1. The elastic energy can be written as

$$E_{\text{el}} = B(\varepsilon_{\text{ref}} - \varepsilon)^2 \tag{9.46}$$

where $B \approx 6 \times 10^{47}$ erg, and the oblateness can be written as

$$\varepsilon = \frac{I_{\text{sph}}\Omega^2}{4(A+B)} + \frac{B}{A+B}\varepsilon_{\text{ref}} \tag{9.47}$$

which is also stated in Equation (7.8). A is a constant that equals $A \approx 6.3 \times 10^{52}$ erg. ε_{ref} is the reference oblateness which is the oblateness when there is no strain in the crust. This means $\varepsilon_{\text{ref}} > \varepsilon$. One can differentiate the two equations above with respect to time to find

$$\dot{E}_{\text{el}} = -2B\dot{\varepsilon}(\varepsilon_{\text{ref}} - \varepsilon) \tag{9.48}$$

and

$$\dot{\varepsilon} = \frac{I_{\text{sph}}\Omega\dot{\Omega}}{2(A+B)} = \frac{\dot{E}_{\text{spin-down}}}{2(A+B)} \tag{9.49}$$

where we have assumed the reference oblateness does not change during the interglitch period, i.e. $\dot{\varepsilon}_{\text{ref}} = 0$. We then substitute $\dot{\varepsilon}$ into Equation (9.48) and use the fact that the largest strain the NS is able to endure is the breaking strain, $\varepsilon_{\text{ref}} - \varepsilon = u_{\text{break}}$, which is typically taken as 0.1 (Horowitz and Kadau, 2009; Baiko and Chugunov, 2018). This means the power we can get from elasticity is

$$\frac{|\dot{E}_{\text{el}}|}{\dot{E}_{\text{spin-down}}} = \frac{B}{A+B}u_{\text{break}} \sim 10^{-6}\,. \tag{9.50}$$

Clearly this is around 3 orders of magnitude too small to power our Kelvin modes and so elasticity alone cannot be the driver of these modes. In a more realistic situation, one would expect the NS to contain a superfluid, so like with glitches, some energy may be harnessed from there. We will explore this idea in the future.

Chapter 10

Overall summary

In this thesis, we have given an overview of the most important aspects of radio pulsar astronomy, GW astronomy and fluid dynamics. This allowed us to create two separate models for pulsar timing irregularities: one for pulsar glitch recoveries and the other for glitch candidates (GCs) and anti-glitch candidates (AGCs), which can be thought of as small glitches and may play a role in understanding timing noise. Both models include elements of multi-messenger astronomy, with electromagnetic observations being used to make predictions for the GWs emitted. This makes the models falsifiable with future GW observations.

The first of the novel models is the transient mountain model, which could be an explanation for glitch recoveries (Yim and Jones, 2020). In this model, as soon as a NS glitches, a mountain is formed which causes a braking torque on the NS. This is hinted at by observations of $\Delta\dot{\nu} < 0$ immediately after the glitch. Then, during the glitch recovery phase, the value of $\dot{\nu}$ appears to exponentially recover back to pre-glitch values, which in the context of our mountain means it must be decaying away. We found the transient mountain would have a decay time-scale of 2τ, where τ is the recovery time-scale of the glitch as seen in electromagnetic data. We were able to write down the exact GW waveform expected for such a model and this can be easily incorporated into existing GW searches, though limited by computational cost. Using the transient mountain model, we can predict which glitches produce detectable GWs.

We then applied the transient mountain model to several astrophysical scenarios: the glitches of the Crab, Vela and J0537-6910; the long and short term braking index behaviours of J0537-6910; the fast $\sim$ 100 s glitch recovery observed in the 2016 Vela glitch; fast, unresolved glitch recoveries from any pulsar; and the burst GW candidate S200114f.

We found that the negative long term braking index of J0537-6910 could be explained by a small increase to a permanent mountain at every glitch ($\Delta\varepsilon_{\mathrm{p}} \approx 1.6 \times 10^{-9}$ on

average). We also showed that the short term exponential recovery of J0537-6910's post-glitch braking indices is a natural consequence of having transient mountains. Consequently, we provided expressions for the braking index in terms of the model parameters. Future work could involve fitting the braking index model to data.

As for the fast recovery after the 2016 Vela glitch, which was coincident with the O2 run, we found that the transient mountain size would have to be $\varepsilon = 0.19$ in order to explain the large change in $\dot{\nu}$ after the glitch. This, of course, is too large to be physical. Even if it were physically possible, our model still predicts that the associated GWs would not be detectable with aLIGO detectors during O2. Another interesting idea is whether the spin-down reported *pre-glitch* (Ashton et al., 2019) could be evidence of the formation of a transient mountain. In such a scenario, we would expect GWs to be emitted *before* the glitch. As of right now, nobody has carried out a GW search in the appropriate parameter space so this could be a relatively quick extension.

From studying the fast recovery of the 2016 Vela glitch, a question was asked on whether all glitches have a fast recovery and perhaps it is a lack of observational cadence that has prevent us from seeing them previously. We initially explored this idea by proposing every glitch from every pulsar forms a transient mountain of size $\varepsilon = 0.19$ which lasts ~ 200 s. We then calculated the SNR for the GWs emitted and provided a list of pulsars that presented detectable GWs with aLIGO. However, when the mountain size was reduced to a more realistic value, no pulsar produced detectable GWs, but this was not surprising as even conventional CW searches, which last much longer, have not been successful.

Finally, there was an idea based on the scenario where a GW signal is detected but the electromagnetic counterpart is not. There was one such case in O3, S200114f, and it was of particular interest because it was a burst candidate. We tested the idea that S100114f was due to a very short-lived transient mountain on a NS with spin-frequency $\nu = \frac{1}{2}f$, where the GW frequency for S200114f was $f = 64.69$ Hz. It was initially thought that any glitching pulsar, with approximately the correct spin frequency, coincident on the sky with the S100114f, could be a electromagnetic search candidate. However, we found that in order for the signal to be detectable, it would either have a transient mountain much larger than what is physically allowed, or that it is closer than the nearest pulsar ever recorded. We conclude that a transient mountain is unlikely the cause of S200114f.

Throughout all the above calculations, we had not accounted for whether it was energetically possible for transient mountains to form, especially at the large sizes we were calculating them to be. First, we found pessimistic and optimistic estimates of how much elastic energy is available to build mountains. The pessimistic calculation assumed that the elastic strain built up between glitches is completely relieved at each glitch. In other words, we were looking for a steady-state solution. The optimistic

calculation on the other hand assumed that the NS was maximally strained early in its life and that glitches are a way for the NS to divest its stored strain. This was a non-steady-state solution. The estimates were compared to the energy it took to build a mountain and it was found that elasticity alone is not enough to explain mountain formation. More could be done to improve this outlook, for example, if we consider a pinned superfluid which could support larger mountains.

The aim of the latter half of the thesis was to develop a model that could explain pulsar timing noise. Like with the transient mountain model, it was important that there were aspects of GWs included as their (non-)observation could provide an independent test for the model. Although the timing noise model is not fully complete, the main ideas can be easily summarised and some interesting physics has resulted during the development stages of the model.

The novel idea is that NS oscillations could be what is causing timing noise. As a NS evolves, one could imagine a non-axisymmetric oscillation mode being excited by some unspecified mechanism (perhaps related to starquakes) and due to the non-axisymmetric nature of the mode, GWs are emitted. This has the effect of radiating angular momentum away which, by the conservation of angular momentum, changes how much angular momentum the NS has. Through a choice of which mode is excited, the NS could lose negative or positive angular momentum which has the effect of spinning-up or spinning-down the NS. If there are consecutive mode excitations, then the changes in angular frequency could combine coherently to give rise to long time-scale timing phenomena such as timing noise.

In reality, the problem goes much deeper than this. In Chapter 8, we derived from first principle the Kelvin modes, which are f-modes on non-rotating, uniformly-dense and incompressible NSs. These assumptions allowed our work to be completely analytic. We were able to formulate the Kelvin modes (and all other quantities) in terms of the mode amplitude, α_{lm}, which was the small parameter used whenever perturbation theory was required. As GW emission is strongest for $l = 2$, we specialised to the $l = 2$ modes.

Once we had the eigenfunctions and eigenvalues, we were able to calculate the mode energies and angular momenta, which came from the second order formalism of Friedman and Schutz (1978a,b). Then, we computed the rate of change in energy and angular momentum due to GW emission, via the quadrupole formulae. It was found that the mode energies and angular momenta were related by $\delta E = 2\omega_{\rm p}\delta J$ whereas the rates were related by $\dot{E}_{\rm GW} = \omega_{\rm p}\dot{J}_{\rm GW}$, where $\omega_{\rm p}$ is the pattern speed.

This simple result has surprising consequences. If we consider some energy time-scale over which the mode energy is damped, defined as $\tau_{\rm E} = \frac{2\delta E}{\dot{E}_{\rm GW}}$, and we define in a similar way a time-scale for the angular momentum, $\tau_{\rm J}$, then taking the ratio of the equations in the last paragraph reveals that the energy time-scale is two times larger that the angular

momentum time-scale, suggesting angular momentum is being radiated quicker than energy. This cannot be as both δE and δJ depend only on α_{2m}^2 so they must both decay at the same rate, as the mode amplitude damps on only one time-scale.

The resolution to this is to allow the initially non-rotating NS to start rotating, in what we called the "GW back-reaction" (Yim and Jones, 2022). We found that a mode with angular momentum δJ, radiates $2\delta J$ of angular momentum as GWs, which leaves the NS with an angular momentum of $-\delta J$. In other words, the GW emission from a prograde (retrograde) mode causes the NS to rotate in the retrograde (prograde) direction.

In Chapter 9, we utilised what we had learnt about mode damping to find out how much a NS could change its angular frequency. Clearly, the GW back-reaction was important but the initial excitation of the mode also needed to be accounted for. The excitation of a mode of angular momentum δJ leaves the NS with angular momentum $-\delta J$. Then, as the mode damps away, it radiates $2\delta J$ as GWs, which changes the NS's angular momentum by a further $-\delta J$. Collectively, after the excitation and decay of a mode, the NS's angular momentum changes by a total of $-2\delta J$. This is all that is required if timing noise is solely a phenomena that affects the angular frequency. However, we may also need to account for changes in the spin-down rate.

Espinoza et al. (2014, 2021) reported the existence of GCs and AGCs, which are effectively small glitches, but are distinct from the normal glitch population. These GCs and AGCs have a $\Delta\nu$ but they also have a $\Delta\dot{\nu}$. If these GCs and AGCs make up timing noise, then we need to be able to explain values of $\Delta\dot{\nu}$. In fact, the fractional change in spin-up/down rate was observed to be 3 to 4 orders of magnitude greater than the glitch size. To explain this, we had to use a two-component model for the NS, whereby a superfluid and normal component are coupled together by a linear coupling torque. Using this, we found that the fractional change in spin-up/down rate could be related to the glitch size by a factor of the pulsar's age divided by the coupling time-scale.

So, we had an expression for the glitch size, dependent only on the mode amplitude, and we had an expression for the fractional change in spin-up/down rate, which depended on both mode amplitude and coupling time-scale. The coupling time-scale could be further broken down into an electromagnetic glitch recovery time-scale, which we had observations for, and the superfluid moment of inertia fraction. In the absence of detailed modelling, the best we could do was to select a superfluid fraction that allowed our model to fit the data. This is what was done and the results are shown in Figures 9.2 and 9.3 for the Crab and Vela respectively. One can see that our model is able to explain the vast majority of the GCs and AGCs for both the Crab and Vela pulsars.

Since GWs are emitted from the modes, we then calculated the SNR and provided histograms for their distribution. We found that even with the ET, it will not be possible to detect GWs from non-axisymmetric modes if these modes are indeed what causes

GCs and AGCs. However, for Vela, there may be the possibility of stacking a few GW signals during ET which may accumulate enough SNR to be detected with confidence.

Moreover, we suggested that glitches could be caused by the excitation and decay of a single $m = 2$ mode, rather than vortex unpinning or starquakes. This required the initial mode amplitude to be large enough. Currently, constraints from GW observations still allow for a mode amplitude large enough to explain Vela's largest glitch. This speculative idea can be tested immediately with aLIGO if one has GW data that is coincident with a large and/or nearby glitch.

Finally, we looked at the power budget available to power the Kelvin modes. We found that, at the frequency they have been observed, only $< 1\%$ of the spin-down power needed to be utilised to source the modes. However, we found that the build-up of elastic energy between glitches is not enough to power the $l = 2$ Kelvin modes. Unless we can think of another mechanism that could provide an energy source, like harnessing energy from the interior superfluid, then the energetics of the oscillation model seems to be a bit problematic. This should be the first model feature to be improved and further thought about.

In the upcoming years and decades, new GW detectors are planned to come online with sensitivities being multiple times better than what we already have. It is therefore imperative that now, before the new detections arrive, we prepare our arsenal of models so that we are ready for whatever may come our way. This is particularly apparent for the oscillation model above, where we have shown that even with the ET, a detection of an individual non-axisymmetric mode may not be possible. Nevertheless, creating these models still has it uses in interpreting electromagnetic observations, like GCs/AGCs and timing noise. There will become a point when there is so much data that only the most accurate models should be used. Clearly, with the simple assumptions made here, there is still a long way to go, but hopefully, in making a start, the models presented here will be ready for when the detections come in the not-so-distant future.

Appendix A

Simplifying the change in torque during the glitch recovery

This Appendix aims to show that we can simplify the general expression for the change in torque on a NS due to a transient mountain during the post-glitch recovery. We will exploit the size differences between the fractional changes of several variables to allow us, to some approximation, ignore all effects on the torque besides the change in the spin-down rate.

Firstly, the torque $\mathcal{N}$ on the NS is given as

$$\mathcal{N}(t) = \frac{d}{dt}(I(t)\Omega(t)) = \dot{I}(t)\Omega(t) + I(t)\dot{\Omega}(t) \tag{A.1}$$

where I is the moment of inertia about the rotation axis, Ω is the angular velocity of the NS and the dot represents a time derivative. Then, the change in the torque due to a glitch is

$$\Delta\mathcal{N}(t) = 2\pi\left[\nu_0\Delta\dot{I}(t) + \dot{I}_0\Delta\nu(t) + \dot{\nu}_0\Delta I(t) + I_0\Delta\dot{\nu}(t)\right] \tag{A.2}$$

for $t > t_g$ and where the subscript '0' represents the pre-glitch value. This is a general expression for the torque during the post-glitch recovery and each change of a variable is time-dependent. This means a change in $\dot{I}$, ν, I or $\dot{\nu}$ will have an effect on the torque. Our model associates the change in torque purely to a change in $\dot{\nu}$ so therefore we want to show that the first 3 terms are much smaller than the last in order for our assumption

to be justified. The relevant ratios are

$$\frac{\text{Term 1}}{\text{Term 4}} = \frac{\nu_0 \Delta\dot{I}(t)}{I_0 \Delta\dot{\nu}(t)} \tag{A.3}$$

$$\frac{\text{Term 2}}{\text{Term 4}} = \frac{\dot{I}_0 \Delta\nu(t)}{I_0 \Delta\dot{\nu}(t)} \tag{A.4}$$

$$\frac{\text{Term 3}}{\text{Term 4}} = \frac{\dot{\nu}_0 \Delta I(t)}{I_0 \Delta\dot{\nu}(t)} \,. \tag{A.5}$$

These ratios are not trivial and so we will need explore further. In all ratios, the moment of inertia plays an important role so we will start with that. One can imagine that before a NS glitches, it has a stable, but still time-varying, moment of inertia, denoted by $I_{\rm sec}(t)$ where the subscript is short for "secular". Then, immediately after the glitch it has a moment of inertia of $I(t_{\rm g})$. The change of moment of inertia at the glitch is therefore $\Delta I(t_{\rm g}) = I(t_{\rm g}) - I_{\rm sec}(t_{\rm g}) = I(t_{\rm g}) - I_0$. If the moment of inertia exponentially recovers at a rate τ (this can be verified by looking at Equations (B.6), (B.13) and (5.11) but with the time-dependence kept in), then the moment of inertia of the NS goes as

$$I(t) = I_{\rm sec}(t) + \Delta I(t_{\rm g}) e^{-\frac{\Delta t}{\tau}} = I_{\rm sec}(t) + \Delta I(t) \tag{A.6}$$

for $t > t_{\rm g}$, and when we differentiate with respect to time we get

$$\dot{I}(t) = \dot{I}_{\rm sec}(t) - \frac{\Delta I(t)}{\tau} \,. \tag{A.7}$$

We can therefore write

$$\Delta\dot{I}(t) \equiv \dot{I}(t) - \dot{I}_{\rm sec}(t) = -\frac{\Delta I(t)}{\tau} \tag{A.8}$$

which is the difference to the rate of change of the moment of inertia caused by the glitch.

We also need to find an expression for $\dot{I}_0$ to allow us to simplify Equation (A.4). To do this, we need to look at the secular evolution of the NS's moment of inertia which is attributed to the slowing down of the NS over time. We can write the secular moment of inertia in terms of a small parameter, ε_Ω, which parametrises how rotation causes a departure from the moment of inertia of a non-rotating NS. Mathematically, it is

$$I_{\rm sec}(t) = I_{\rm NR}(1 + \varepsilon_\Omega(t)) \tag{A.9}$$

where $I_{\rm NR}$ is the moment of inertia if the NS was not rotating. We immediately see that

$$\dot{I}_{\rm sec}(t) = I_{\rm NR}\dot{\varepsilon}_\Omega(t) \tag{A.10}$$

In general, ε_Ω has the form

$$\varepsilon_\Omega(t) = k\Omega^2(t) \tag{A.11}$$

where k is some constant of proportionality which depends on the detailed model of the NS. To get an idea of the size of ε_Ω, we can take the simple case of a completely fluid and incompressible NS which Baym and Pines (1971) found has

$$\varepsilon_\Omega(t) = \frac{5}{6}\frac{R^3}{GM}\Omega^2(t) \tag{A.12}$$

which results in $\varepsilon_\Omega = 1.58 \times 10^{-4}$ for the Crab and $\varepsilon_\Omega = 2.21 \times 10^{-5}$ for Vela for values of the spin frequency as given in Table 5.1 and using $M = 1.4\,\mathrm{M}_\odot$ and $R = 10$ km. Differentiating Equation (A.11) with respect to time and substituting into Equation (A.10), we find that

$$\dot{I}_{\mathrm{sec}}(t) = 2I_{\mathrm{NR}}\varepsilon_\Omega(t)\frac{\dot{\Omega}(t)}{\Omega(t)}\,. \tag{A.13}$$

From Equation (A.9), we can see that there is only a small correction between using I_{NR} and say the moment of inertia just before the glitch, I_0 ($= I_{\mathrm{sec}}(t_{\mathrm{g}})$), and so we can let $I_{\mathrm{NR}} \approx I_0$. This then allows us to evaluate Equation (A.13) at the moment just before the glitch which gives

$$\frac{\dot{I}_0}{I_0} = 2\varepsilon_{\Omega,0}\frac{\dot{\nu}_0}{\nu_0}\,. \tag{A.14}$$

We now have enough to re-write our ratios without the $\dot{I}_0$ and $\Delta\dot{I}$ terms, and we want all our ratios to be much less than 1. This results in

$$\frac{\Delta I(t)}{I_0} \ll -\frac{\tau\Delta\dot{\nu}(t)}{\nu_0} \tag{A.15}$$

$$2\varepsilon_{\Omega,0}\frac{\Delta\nu(t)}{\nu_0} \ll \frac{\Delta\dot{\nu}(t)}{\dot{\nu}_0} \tag{A.16}$$

$$\frac{\Delta I(t)}{I_0} \ll \frac{\Delta\dot{\nu}(t)}{\dot{\nu}_0} \tag{A.17}$$

where each line represents the ratios in Equations (A.3), (A.4) and (A.5) respectively. Note that these conditions are all still time-dependent. We can remove this by taking the conservative case of $\Delta I(t) = \Delta I(t_{\mathrm{g}})$ and $\Delta\nu(t) = \Delta\nu(t_{\mathrm{g}})$ as both these quantities are always smaller or equal to the value at the time of the glitch. On the right hand side, we can say that during the post-glitch recovery, $\Delta\dot{\nu}(t) \sim \Delta\dot{\nu}_{\mathrm{t}}$. Then, using Equation (5.7) in

Equation (A.15), and Equation (5.33) in Equations (A.16) and (A.17), we finally get

$$\frac{\Delta I(t_g)}{I_0} \ll \mathcal{Q}\left(\frac{\Delta\nu(t_g)}{\nu_0}\right) \tag{A.18}$$

$$2\varepsilon_{\Omega,0}\frac{\Delta\nu(t_g)}{\nu_0} \ll \mathcal{Q}'\left(\frac{\Delta\dot{\nu}(t_g)}{\dot{\nu}_0}\right) \tag{A.19}$$

$$\frac{\Delta I(t_g)}{I_0} \ll \mathcal{Q}'\left(\frac{\Delta\dot{\nu}(t_g)}{\dot{\nu}_0}\right) \tag{A.20}$$

where $\mathcal{Q}$ is the healing parameter of the spin frequency and $\mathcal{Q}'$ is the same but for the time derivative of the spin frequency. They are defined in Equations (5.6) and (5.33) respectively.

Typically, $\mathcal{Q}$ and $\mathcal{Q}'$ are on the order of unity and since the spin frequency of NSs vary by a small amount over secular time-scales, we can say ε_Ω varies by little too, meaning we are able to use the values of ε_Ω which we calculated earlier for $\varepsilon_{\Omega,0}$.

From Appendix B, it was found empirically that $\frac{\Delta I(t_g)}{I_0} \ll \frac{\Delta\nu(t_g)}{\nu_0}$ for both the Crab and Vela. This means Equation (A.18) is satisfied. Then, looking at the JBCA Glitch Catalogue, we find that $\frac{\Delta\nu(t_g)}{\nu_0}$ is about 4 - 6 orders of magnitude smaller than $\frac{\Delta\dot{\nu}(t_g)}{\dot{\nu}_0}$ for both pulsars. Along with $\varepsilon_{\Omega,0} \sim 10^{-5}$ – 10^{-4}, Equation (A.19) is comfortably satisfied. Finally, by simple logic it must be that $\frac{\Delta I(t_g)}{I_0} \ll \frac{\Delta\dot{\nu}(t_g)}{\dot{\nu}_0}$ so Equation (A.20) is also satisfied.

To summarise, we have shown Equations (A.18) – (A.20) to be true. This allows us to ignore the small effects of $\Delta\dot{I}$, $\Delta\nu$ and ΔI on the torque. As a result, the main contributor to the change in torque for our transient mountain model is due to a change in the spin-down rate, $\Delta\dot{\nu}$.

Appendix B

The change in the moment of inertia due to the formation of a mountain

This Appendix addresses the question on whether the change in the moment of inertia about the rotation axis, due to the formation of a transient mountain, can be ignored when: 1) a NS rapidly spins-up during a glitch, and 2) when the NS recovers from a glitch. For a uniformly-dense and incompressible NS, the sudden formation of a mountain causes an increase to the moment of inertia about the rotation axis. This has the effect of decreasing the NS's spin frequency and the subsequent dissipation of the mountain during the recovery causes the NS to spin faster. We show empirically that these effects due to changes in the moment of inertia are negligible compared to the frequency changes caused intrinsically by glitches for the Crab and Vela pulsars. We use the results from this Appendix to simplify the calculation of the GW luminosity and torque during the post-glitch recovery.

For the sake of simplicity, we will assume the NS is of uniform density and is incompressible. This allows for simple analytic results to be calculated. Under the model described in Section 5.1, when a NS glitches, the NS forms a transient mountain turning it into a tri-axial (ellipsoidal) NS. This tri-axial NS will have a volume of

$$V = \frac{4}{3}\pi a_1 a_2 a_3 \tag{B.1}$$

where a_1, a_2 and a_3 are the semi-major axis lengths along the x, y and z axes respectively, with the z-axis defined such that it is aligned with the rotation axis. The initial pre-glitch configuration, shown by a subscript '0', is generally axisymmetric with an initial volume of

$$V_0 = \frac{4}{3}\pi a_{1,0}^2 a_{3,0} \tag{B.2}$$

where we have used $a_{1,0} = a_{2,0}$ for an axisymmetric NS. Keeping all generality, the perturbed semi-major axis length can be written as the sum of the unperturbed semi-major axis length, $a_{i,0}$, and a small perturbation, δa_i, giving

$$a_i = a_{i,0} + \delta a_i \tag{B.3}$$

for $i = 1, 2, 3$. We are interested in spherical harmonic perturbations of the form $l = 2$, $m = 2$ which have the property $\delta a_2 = -\delta a_1$. When enforced with volume conservation, we find a 1-parameter family of solutions, with δa_3 easily calculable if required.

Let the moment of inertia about the rotation axis be I_{zz}. We have similar expressions along the x and y axes which lie along the remaining axes of symmetry. For a uniformly-dense ellipsoid of density $\bar{\rho}$, the moment of inertia about each of the axes can be written analytically as

$$\begin{aligned} I_{xx} &= \frac{1}{5}M(a_2^2 + a_3^2) \\ I_{yy} &= \frac{1}{5}M(a_1^2 + a_3^2) \\ I_{zz} &= \frac{1}{5}M(a_1^2 + a_2^2) \end{aligned} \tag{B.4}$$

where $M = \bar{\rho}V$. Here, when we talk about NS mountains we refer to a non-axisymmetric deformation which leads to an *equatorial* ellipticity, ε_{eq}. It is defined as

$$\varepsilon_{\text{eq}} \equiv \frac{I_{xx} - I_{yy}}{I_{zz}} \tag{B.5}$$

which is a small dimensionless number parametrising how much the NS differs in length between its x and y axes within the equatorial plane (for a NS with a non-zero I_{zz}).

There is another dimensionless parameter we can talk about which is the oblateness parameter, ε_{ob}, defined as

$$\varepsilon_{\text{ob}} \equiv \frac{I_{zz} - I_{zz,0}}{I_{zz,0}} \tag{B.6}$$

where $I_{zz,0} = \frac{2}{5}Ma_{1,0}^2$. This is, again, a small parameter but this time it measures the change in oblateness due to the sudden formation of a mountain. Oblateness can be seen as how elliptical the NS is in a plane perpendicular to the equatorial plane, i.e. within a meridional plane.

We want to show that we can ignore the effects of the change in the moment of inertia about the z-axis whilst still obeying the conservation of angular momentum at the moment of the glitch. The change in the angular momentum at the moment of the glitch,

$\Delta J(t_g)$, is the sum of

$$\Delta J(t_g) = 2\pi \Delta I_{zz}(t_g)\nu_0 + 2\pi I_{zz,0}\Delta\nu(t_g) \tag{B.7}$$

where the parentheses show the quantity is evaluated at the time of the glitch, immediately after the transient mountain has been created. If we can show the first term is smaller than the second, then we can conclude that the change in the moment of inertia can be ignored at the glitch without considerably affecting the "usual" change in angular momentum due to a change in the spin frequency. In other words, we want to show

$$\frac{\Delta I_{zz}(t_g)}{I_{zz,0}} \ll \frac{\Delta\nu(t_g)}{\nu_0} \tag{B.8}$$

where $\Delta I_{zz}(t_g) = I_{zz}(t_g) - I_{zz,0}$. The left hand side of Equation (B.8) is the same as $\varepsilon_{ob}(t_g)$ and the right hand side we know from the JBCA Glitch Catalogue. However, we do not immediately have a numerical value for $\varepsilon_{ob}(t_g)$ but what we can get is a value for $\varepsilon_{eq}(t_g)$. $\varepsilon_{eq}(t_g)$ can be approximated using Equation (5.12) from Section 5.3. Therefore, we proceed by relating ε_{ob} to ε_{eq} which would give us a numerical value to the left hand side of Equation (B.8).

After substituting Equations (B.4) and (B.3) into Equation (B.6), we get

$$\varepsilon_{ob} = \frac{-\left(a_{1,0}^2 - a_{2,0}^2\right) + \left(2a_{1,0}\delta a_1 + 2a_{2,0}\delta a_2\right) + \left(\delta a_1^2 + \delta a_2^2\right)}{2a_{1,0}^2} \tag{B.9}$$

and doing the same substitutions but for Equation (B.5) gives

$$\varepsilon_{eq} = \frac{\left(a_{2,0}^2 - a_{1,0}^2\right) + 2\left(a_{2,0}\delta a_2 - a_{1,0}\delta a_1\right) + \left(\delta a_2^2 - \delta a_1^2\right)}{\left(a_{1,0}^2 + a_{2,0}^2\right) + 2\left(a_{1,0}\delta a_1 + a_{2,0}\delta a_2\right) + \left(\delta a_1^2 + \delta a_2^2\right)}\,. \tag{B.10}$$

Both Equations (B.9) and (B.10) are general results. Then, we specialise to $\delta a_2 = -\delta a_1$ perturbations and account for the axisymmetric initial configuration, $a_{1,0} = a_{2,0}$, so that Equation (B.9) becomes

$$\varepsilon_{ob} = \left(\frac{\delta a_1}{a_{1,0}}\right)^2 \tag{B.11}$$

which is an exact result, and (the square of) Equation (B.10) becomes

$$\varepsilon_{eq}^2 = 4\left(\frac{\delta a_1}{a_{1,0}}\right)^2 + \mathcal{O}\left[\left(\frac{\delta a_1}{a_{1,0}}\right)^4\right] \tag{B.12}$$

TABLE B.1: This table has values of $\varepsilon_{\rm ob}(t_{\rm g})$ calculated from Equation (B.13), the glitch sizes from the JCBA Glitch Catalogue (Espinoza et al., 2011) and the final two columns have the fraction of these two quantities expressed as a percentage, one without being divided by $\mathcal{Q}$ and the other one with the division by $\mathcal{Q}$. The 4th column represents the contribution that the change in the moment of inertia has on the angular momentum at moment of the glitch and 5th column represents the same but for the post-glitch recovery. [O2]This glitch happened during the O2 run of aLIGO. [O3]This glitch occurred during the O3 run of aLIGO. [1]The data for this glitch was taken from Xu et al. (2019).

Crab				
MJD	$\varepsilon_{\rm ob}(t_{\rm g})$	$\frac{\Delta\nu(t_{\rm g})}{\nu_0}$	$\frac{\varepsilon_{\rm ob}(t_{\rm g})\nu_0}{\Delta\nu(t_{\rm g})}$[%]	$\frac{\varepsilon_{\rm ob}(t_{\rm g})\nu_0}{\mathcal{Q}\Delta\nu(t_{\rm g})}$[%]
40491.8	6.3×10^{-11}	7.2×10^{-9}	0.87	1.0
41161.98	2.4×10^{-11}	1.9×10^{-9}	1.3	1.4
41250.32	1.6×10^{-11}	2.1×10^{-9}	0.75	0.89
42447.26	2.3×10^{-10}	3.57×10^{-8}	0.64	0.79
46663.69	7×10^{-11}	6×10^{-9}	1	1
47767.504	4.9×10^{-10}	8.10×10^{-8}	0.60	0.67
48945.6	4.6×10^{-11}	4.2×10^{-9}	1.1	1.3
50020.04	3×10^{-11}	2.1×10^{-9}	1	2
50260.031	2.5×10^{-10}	3.19×10^{-8}	0.77	1.1
50458.94	1.6×10^{-10}	6.1×10^{-9}	2.6	3.0
50489.7	...	8×10^{-10}	...	...
50812.59	8.8×10^{-11}	6.2×10^{-9}	1.4	1.6
51452.02	1×10^{-10}	6.8×10^{-9}	1	2
51740.656	4.1×10^{-10}	2.51×10^{-8}	1.7	2.1
51804.75	7.6×10^{-11}	3.5×10^{-9}	2.2	2.6
52084.072	3.0×10^{-10}	2.26×10^{-8}	1.3	1.6
52146.758	8.1×10^{-11}	8.9×10^{-9}	0.91	1.1
52498.257	1.0×10^{-10}	3.4×10^{-9}	2.9	3.5
52587.2	7×10^{-11}	1.7×10^{-9}	4	5
53067.078	8.8×10^{-10}	2.14×10^{-7}	0.41	0.49
53254.109	3×10^{-11}	4.9×10^{-9}	0.6	0.7
53331.17	1×10^{-10}	2.8×10^{-9}	4	4
53970.19	4.4×10^{-10}	2.18×10^{-8}	2.0	2.4
54580.38	3×10^{-11}	4.7×10^{-9}	1	1
55875.5	...	4.92×10^{-8}	...	...
57839.92[O2]	3.9×10^{-11}	2.14×10^{-9}	1.8	2.6
58064.555	9.9×10^{-10}	5.164×10^{-7}	0.19	0.23
58237.357	6.6×10^{-11}	4.08×10^{-9}	1.6	1.9
58470.939	5.1×10^{-11}	2.36×10^{-9}	2.2	2.6
58687.59[O3]	...	3.60×10^{-8}	...	...

Vela				
MJD	$\varepsilon_{\rm ob}(t_{\rm g})$	$\frac{\Delta\nu(t_{\rm g})}{\nu_0}$	$\frac{\varepsilon_{\rm ob}(t_{\rm g})\nu_0}{\Delta\nu(t_{\rm g})}$[%]	$\frac{\varepsilon_{\rm ob}(t_{\rm g})\nu_0}{\mathcal{Q}\Delta\nu(t_{\rm g})}$[%]
40280	8.1×10^{-9}	2.34×10^{-6}	0.35	10
41192	1.2×10^{-8}	2.05×10^{-6}	0.59	17
41312	2×10^{-9}	1.2×10^{-8}	20	40
42683	8.9×10^{-9}	1.99×10^{-6}	0.45	2.1
43693	1.5×10^{-8}	3.06×10^{-6}	0.48	4.0
44888.4	4.0×10^{-8}	1.145×10^{-6}	3.5	20
45192	1.9×10^{-8}	2.05×10^{-6}	0.91	21
46257.228	1.4×10^{-8}	1.601×10^{-6}	0.86	5.5
47519.8036	6.2×10^{-8}	1.805×10^{-6}	3.5	20
48457.382	4.9×10^{-7}	2.715×10^{-6}	18	110
49559	0	8.35×10^{-7}	0	0
49591.2	9.7×10^{-8}	1.99×10^{-7}	49	290
50369.345	4.8×10^{-9}	2.11×10^{-6}	0.23	0.60
51559.319	5.5×10^{-9}	3.086×10^{-6}	0.18	1.0
53193	...	2.1×10^{-6}	...	...
53960	1.9×10^{-7}	2.62×10^{-6}	7.1	42
55408.8	6.1×10^{-8}	1.94×10^{-6}	3.1	18
56556	1.2×10^{-7}	3.1×10^{-6}	3.9	23
56922	8×10^{-11}	4×10^{-10}	20	100
57734.485[O2,1]	5.9×10^{-8}	1.431×10^{-6}	4.2	24

where the $\mathcal{O}$ notation represents higher order terms we can ignore, coming from a Taylor expansion in $\left(\frac{\delta a_1}{a_{1,0}}\right)$. Therefore to a very good approximation, we can say that

$$\varepsilon_{\rm ob} \approx \frac{1}{4}\varepsilon_{\rm eq}^2 \tag{B.13}$$

at all times during and after the glitch. We can now numerically evaluate Equation (B.8) to see if it is satisfied. We take $\varepsilon_{\rm eq}(t_{\rm g}) = \varepsilon_{\rm approx}(t_{\rm g})$ from Tables 5.2 and 5.3 to calculate $\varepsilon_{\rm ob}(t_{\rm g})$ and we compare $\varepsilon_{\rm ob}(t_{\rm g})$ as a percentage of $\frac{\Delta\nu(t_{\rm g})}{\nu_0}$. The results are shown in Table B.1.

We can see from Table B.1 that $\varepsilon_{\rm ob}(t_{\rm g})$ is typically $\sim$1% of $\frac{\Delta\nu(t_{\rm g})}{\nu_0}$ for the Crab, and typically 1 – 4% for Vela with the odd glitch hitting 20% or even 50%. Therefore, we find that for most glitches, the assumption of ΔI_{zz} being negligible holds at the moment of the glitch, as its contribution to the angular momentum has a relative size of $< 5\%$ when compared to the contribution due to $\Delta\nu$.

We can extend this calculation to include the post-glitch recovery too. If we wanted to show that the change in the moment of inertia is negligible during the post-glitch

recovery, we would need to show

$$\frac{\Delta I_{zz}(t)}{I_{zz,0}} \ll \frac{\Delta\nu(t)}{\nu_0} \tag{B.14}$$

for all $t > t_g$. However, $\Delta I_{zz}(t)$ at most has a value of $\Delta I_{zz}(t_g)$ and the change in the spin frequency during the glitch recovery is typically $\Delta\nu(t) \sim \Delta\nu_t$. Therefore, we have

$$\frac{\Delta I_{zz}(t_g)}{I_{zz,0}} \ll \frac{\Delta\nu_t}{\nu_0} = \mathcal{Q}\left(\frac{\Delta\nu(t_g)}{\nu_0}\right) \tag{B.15}$$

where we used Equation (5.7) in the equality. This condition is simply Equation (B.8) but with an extra factor of $\mathcal{Q}$. If $\mathcal{Q} \sim 1$, then Equations (B.15) and (B.8) are the same and since we have already shown Equation (B.8) to be true, then Equation (B.15) must also be true.

We do however, have values of $\mathcal{Q}$ so we shall use them to calculate the ratio of the left hand side and the right hand side of Equation (B.15). This ratio, expressed as a percentage, is presented in Table B.1. We see that the contribution from the moment of inertia is higher during the post-glitch recovery, though it is still small enough to allow us to justify neglecting it. There are a few Vela glitches which have a large contribution from the moment of inertia, but for the majority, it seems the inequality in Equation (B.15) holds. Therefore, we can and we will ignore the change in the moment of inertia during the post-glitch recovery.

Our assumption of the change in the angular momentum being solely due to a change in spin frequency breaks down whenever the percentages in Table B.1 get larger, like in a few of Vela's glitches. Nonetheless, we could still use the assumption but we would need to proceed with caution as a change in the moment of inertia about the rotation axis would contribute to a change in the NS's angular momentum. A quick way to parametrise how much the moment of inertia contributes to the change in angular momentum would be to look at the following parameters

$$\eta_1 \equiv \frac{\varepsilon_{ob}(t_g)\nu_0}{\Delta\nu(t_g)} = -\frac{5}{32(2\pi)^4}\frac{c^5}{G}\frac{1}{I}\frac{\dot{\nu}_0}{\nu_0^5}\left(\frac{\Delta\dot{\nu}(t_g)}{\dot{\nu}_0}\right)\left(\frac{\Delta\nu(t_g)}{\nu_0}\right)^{-1} \tag{B.16}$$

$$\eta_2 \equiv \frac{\varepsilon_{ob}(t_g)\nu_0}{\mathcal{Q}\Delta\nu(t_g)} = -\frac{5}{32(2\pi)^4}\frac{c^5}{G}\frac{1}{I}\frac{\dot{\nu}_0}{\nu_0^5}\frac{1}{\mathcal{Q}}\left(\frac{\Delta\dot{\nu}(t_g)}{\dot{\nu}_0}\right)\left(\frac{\Delta\nu(t_g)}{\nu_0}\right)^{-1} \tag{B.17}$$

where η_1 represents the fractional contribution to the angular momentum due to a change in the moment of inertia at the glitch and η_2 represents the same but for the post-glitch recovery. If both these parameter are much less than 1, then we can ignore the change in the moment of inertia at the moment of the glitch and during the post-glitch recovery. If η_1 is considerably large, then it would mean there was a sudden

increase in ΔI_{zz} at the glitch which would slow down the NS. This would mean whatever mechanism was producing the spin-up would have to be correspondingly larger than would otherwise be inferred, e.g. a larger starquake, a larger unpinning event. Similarly, a large η_2 would mean ΔI_{zz} is considerable during the recovery, i.e. the decaying mountain would spin-up the NS. To counteract the effect of including ΔI_{zz}, the resultant transient mountain would need to be larger in size during the recovery.

The ratios η_1 and η_2 can be easily evaluated since the JBCA Glitch Catalogue and the ATNF Pulsar Catalogue provides all the information required. All in all, these two parameters are useful tools to assess whether the change in the moment of inertia about the rotation axis is an important factor when calculating a NS's dynamics at the moment of a glitch and during its subsequent recovery.

Appendix C

Virial equation for perturbations

In this Appendix, we will derive the "virial equation for perturbations" which is given by Equation (6.6.14) of Shapiro and Teukolsky (1983). This derivation is specific to non-rotating, uniformly-dense and incompressible stars.

Like in Section 8.3, we begin with Euler's equation, Equation (4.2), but this time perturb it using *Lagrangian* perturbations. This gives

$$\begin{aligned} \frac{d\Delta v^i}{dt} &= \frac{\Delta\rho}{\rho^2}\nabla_i P - \frac{1}{\rho}\nabla_i \Delta P - \nabla_i \Delta\Phi \\ \rightarrow \frac{\partial^2 \xi^i}{\partial t^2} &= -\frac{1}{\rho}\nabla_i \Delta P - \nabla_i \Delta\Phi \end{aligned} \tag{C.1}$$

where we have used Equation (4.3), $\Delta\rho = 0$ and $\Delta v^i = \frac{d\xi^i}{dt} = \frac{\partial \xi^i}{\partial t}$ where the last equality is because our background NS is static ($v^i = 0$). By definition, the Lagrangian change in the pressure at the surface is zero (Equation (8.40)) but if we can show $\Delta P = 0$ inside the perturbed NS too, then we can remove the first term on the right hand side of Equation (C.1).

To do this, we take a theorem from partial differential equations that says if some field, ψ, is zero on the boundary of a system, but we can show $\nabla^2\psi = 0$ everywhere inside the boundary, then it must be that ψ is zero inside the boundary too. This can be thought of as showing the curvature inside the boundary is always zero meaning the values of ψ lie in one plane, and if ψ must equal zero on the boundary, then the only way for everything to be consistent is if ψ inside is also zero.

We can take a partial derivative of Equation (C.1), and on the left hand side, we can commute ∇_i and $\frac{\partial}{\partial t}$, since normally ∇_i commutes with $\frac{d}{dt}$ but $\frac{d}{dt} = \frac{\partial}{\partial t}$ for a static background (e.g. Shapiro and Teukolsky, 1983). Then, for our incompressible NS, we have

$\nabla_i \xi^i = 0$ so we get

$$0 = -\frac{1}{\rho}\nabla^2 \Delta P - \nabla^2 \Delta \Phi \quad \rightarrow \quad \nabla^2 \Delta P = -\rho \nabla^2 \Delta \Phi \,. \tag{C.2}$$

Then, we can also perturb Poisson's equation (Equation (4.4)) with Lagrangian perturbations to give

$$\nabla^2 \Delta \Phi = 4\pi G \Delta \rho = 0 \tag{C.3}$$

where the last equality is because $\Delta\rho = 0$ inside the NS. Therefore, substituting this into Equation (C.2) gives

$$\nabla^2 \Delta P = 0 \tag{C.4}$$

inside the NS, and so we have shown we can remove the first term on the right hand side of Equation (C.1) to leave

$$\frac{\partial^2 \xi^i}{\partial t^2} = -\nabla_i \Delta \Phi \tag{C.5}$$

for our non-rotating, uniformly-dense, incompressible NS. We have not yet calculated $\Delta\Phi$ but we have calculated $\delta\Phi$ and Φ before (Equations (8.50) and (8.11) respectively) so we can use Equation (4.9) to write

$$\begin{aligned} \frac{\partial^2 \xi^i}{\partial t^2} &= -\nabla_i \delta\Phi - \nabla_i(\xi^j \nabla_j \Phi) \\ \rightarrow \rho \frac{\partial^2 \xi^i}{\partial t^2} &= -\rho \nabla_i \delta\Phi - \rho \nabla_i(\xi^j \nabla_j \Phi) \end{aligned} \tag{C.6}$$

where we have multiplied by ρ to get into the form of

$$\rho \frac{\partial^2 \xi^i}{\partial t^2} = L_{ij} \xi^j \tag{C.7}$$

where L_{ij} is the potential operator (Shapiro and Teukolsky, 1983) and is equal to $L_{ij}\xi^j = -\rho\nabla_i\delta\Phi - \rho\nabla_i(\xi^j\nabla_j\Phi)$ for our system. If ξ^i is oscillatory in time, then Equation (C.7) becomes an eigenequation. We then define the total potential energy of the perturbations as being equal to

$$\delta V \equiv -\frac{1}{2}\int_V \xi^i L_{ij} \xi^j dV \tag{C.8}$$

and the kinetic energy of the perturbations as

$$\delta T \equiv \frac{1}{2}\int_V \rho \left(\frac{\partial \xi^i}{\partial t}\right)^2 dV \,. \tag{C.9}$$

Substituting Equation (C.7) into Equation (C.8), we get

$$\delta V = -\frac{1}{2}\int_V \rho \xi^i \frac{\partial^2 \xi^i}{\partial t^2} dV \tag{C.10}$$

and when we calculate the Lagrangian of the Kelvin modes, given by $\mathcal{L} \equiv \delta T - \delta V$, we find

$$\mathcal{L} = \frac{1}{2}\int_V \rho \left[\left(\frac{\partial \xi^i}{\partial t} \right)^2 + \xi^i \frac{\partial^2 \xi^i}{\partial t^2} \right] dV \, . \tag{C.11}$$

Taking two derivatives out of the brackets and moving them in front of the integral (for a static background), we get

$$\mathcal{L} = \frac{1}{4}\frac{d^2}{dt^2}\int_V \rho \xi^i \xi^i dV \, . \tag{C.12}$$

The integral has a similar form to the mass quadrupole moment but has perturbed quantities instead of non-perturbed. Therefore, we perturb the integral quantity to get

$$\begin{aligned} I_{ij} &= \int_V \rho x_i x_j dV \\ \rightarrow \delta I_{ij} &= \int_V \rho \Delta(x_i x_j) dV \\ &= \int_V \rho \left[(x_i + \xi_i)(x_j + \xi_j) - x_i x_j \right] dV \end{aligned} \tag{C.13}$$

where we have used Equation (4.21) in going from $I_{ij} \rightarrow \delta I_{ij}$, and Equation (4.7) in the step after. When we take the trace, we get

$$\delta I_{ii} = \delta I = 2\int_V \rho x_i \xi_i dV + \int_V \rho \xi_i \xi_i dV \, .$$

However, as the Kelvin modes are proportional to the spherical harmonics, the first integral vanishes identically. In this case, we are free to drop that term and we are left with

$$\delta I = \int_V \rho \xi_i \xi_i dV \, . \tag{C.14}$$

Putting this into Equation (C.12), we get the final virial equation of

$$\frac{1}{4}\frac{d^2 \delta I}{dt^2} = \delta T - \delta V \tag{C.15}$$

which agrees with Equation (6.6.14) in Shapiro and Teukolsky (1983).

References

Aasi, J., Abbott, B. P., Abbott, R., Abbott, T., Abernathy, M. R., Ackley, K., Adams, C., Adams, T., Addesso, P., Adhikari, R. X., and et al. (2015). Advanced LIGO. *Classical and Quantum Gravity*, 32(7):074001.

Abadie, J., Abbott, B. P., Abbott, R., Adhikari, R., Ajith, P., Allen, B., Allen, G., Amador Ceron, E., Amin, R. S., Anderson, S. B., and et al. (2011). Search for gravitational waves associated with the August 2006 timing glitch of the Vela pulsar. *Physical Review D*, 83(4):042001.

Abbott, B., Abbott, R., Adhikari, R., Ageev, A., Allen, B., Amin, R., Anderson, S. B., Anderson, W. G., Araya, M., Armandula, H., and et al. (2004). Setting upper limits on the strength of periodic gravitational waves from PSR J1939+2134 using the first science data from the GEO 600 and LIGO detectors. *Physical Review D*, 69(8):082004.

Abbott, B. P., Abbott, R., Abbott, T. D., Abernathy, M. R., Acernese, F., Ackley, K., Adams, C., Adams, T., Addesso, P., Adhikari, R. X., and et al. (2016). Observation of Gravitational Waves from a Binary Black Hole Merger. *Physical Review Letters*, 116 (6):061102.

Abbott, B. P., Abbott, R., Abbott, T. D., Abernathy, M. R., Acernese, F., Ackley, K., Adams, C., Adams, T., Addesso, P., Adhikari, R. X., and et al. (2017)a. Upper Limits on the Stochastic Gravitational-Wave Background from Advanced LIGO's First Observing Run. *Physical Review Letters*, 118(12):121101.

Abbott, B. P., Abbott, R., Abbott, T. D., Acernese, F., Ackley, K., Adams, C., Adams, T., Addesso, P., Adhikari, R. X., Adya, V. B., and et al. (2017)b. GW170817: Observation of Gravitational Waves from a Binary Neutron Star Inspiral. *Physical Review Letters*, 119(16):161101.

Abbott, B. P., Abbott, R., Abbott, T. D., Acernese, F., Ackley, K., Adams, C., Adams, T., Addesso, P., Adhikari, R. X., Adya, V. B., and et al. (2017)c. Gravitational Waves and Gamma-Rays from a Binary Neutron Star Merger: GW170817 and GRB 170817A. *The Astrophysical Journal Letters*, 848:L13.

Abbott, B. P., Abbott, R., Abbott, T. D., Abraham, S., Acernese, F., Ackley, K., Adams, C., Adhikari, R. X., Adya, V. B., Affeldt, C., and et al. (2019)a. GWTC-1: A Gravitational-Wave Transient Catalog of Compact Binary Mergers Observed by LIGO and Virgo during the First and Second Observing Runs. *Physical Review X*, 9(3):031040.

Abbott, B. P., Abbott, R., Abbott, T. D., Abraham, S., Acernese, F., Ackley, K., Adams, C., Adhikari, R. X., Adya, V. B., Affeldt, C., and et al. (2019)b. All-sky search for long-duration gravitational-wave transients in the second Advanced LIGO observing run. *Physical Review D*, 99(10):104033.

Abbott, B. P., Abbott, R., Abbott, T. D., Acernese, F., Ackley, K., Adams, C., Adams, T., Addesso, P., Adhikari, R. X., Adya, V. B., Affeldt, C., and et al. (2019)c. Search for Gravitational Waves from a Long-lived Remnant of the Binary Neutron Star Merger GW170817. *The Astrophysical Journal*, 875(2):160.

Abbott, R., Abbott, T. D., Abraham, S., Acernese, F., Ackley, K., Adams, A., Adams, C., Adhikari, R. X., Adya, V. B., Affeldt, C., and et al. (2020). Gravitational-wave Constraints on the Equatorial Ellipticity of Millisecond Pulsars. *The Astrophysical Journal Letters*, 902(1):L21.

Abbott, R., Abbott, T. D., Abraham, S., Acernese, F., Ackley, K., Adams, A., Adams, C., Adhikari, R. X., Adya, V. B., Affeldt, C., and et al. (2021)a. GWTC-2: Compact Binary Coalescences Observed by LIGO and Virgo during the First Half of the Third Observing Run. *Physical Review X*, 11(2):021053.

Abbott, R., Abbott, T. D., Abraham, S., Acernese, F., Ackley, K., Adams, A., Adams, C., Adhikari, R. X., Adya, V. B., Affeldt, C., and et al. (2021)b. Diving below the Spin-down Limit: Constraints on Gravitational Waves from the Energetic Young Pulsar PSR J0537-6910. *The Astrophysical Journal Letters*, 913(2):L27.

Abbott, R., Abbott, T. D., Abraham, S., Acernese, F., Ackley, K., Adams, A., Adams, C., Adhikari, R. X., Adya, V. B., Affeldt, C., and et al. (2021)c. All-sky search in early O3 LIGO data for continuous gravitational-wave signals from unknown neutron stars in binary systems. *Physical Review D*, 103(6):064017.

Abbott, R., Abbott, T. D., Abraham, S., Acernese, F., Ackley, K., Adams, A., Adams, C., Adhikari, R. X., Adya, V. B., Affeldt, C., and et al. (2021)d. Constraints from LIGO O3 data on gravitational-wave emission due to r-modes in the glitching pulsar PSR J0537-6910. *arXiv e-prints*, art. arXiv:2104.14417

Akbal, O. and Alpar, M. A. (2018). Minimum glitch of the Crab pulsar and the crustquake as a trigger mechanism. *Monthly Notices of the Royal Astronomical Society*, 473(1):621–624.

Allen, M. P. and Horvath, J. E. (1997). Glitches, torque evolution and the dynamics of young pulsars. *Monthly Notices of the Royal Astronomical Society*, 287(3):615–621.

Alpar, M. A. and Pines, D. Pulsar Glitches and Neutron Star Superfluidity - A 1992 Perspective. In van Riper, K. A., Epstein, R. I., and Ho, C., editors, *Isolated Pulsars*, page 18, (1993)

Alpar, M. A., Pines, D., Anderson, P. W., and Shaham, J. (1984). Vortex creep and the internal temperature of neutron stars. I - General theory. *The Astrophysical Journal*, 276:325–334.

Alpar, M. A., Nandkumar, R., and Pines, D. (1986). Vortex creep and the internal temperature of neutron stars Timing noise in pulsars. *The Astrophysical Journal*, 311: 197–213.

Alpar, M. A., Cheng, K. S., and Pines, D. (1989). Vortex Creep and the Internal Temperature of Neutron Stars: Linear and Nonlinear Response to a Glitch. *The Astrophysical Journal*, 346:823.

Alpar, M. A., Chau, H. F., Cheng, K. S., and Pines, D. (1996). Postglitch Relaxation of the Crab Pulsar after Its First Four Major Glitches: The Combined Effects of Crust Cracking, Formation of Vortex Depletion Region and Vortex Creep. *The Astrophysical Journal*, 459:706.

Anderson, P. W. and Itoh, N. (1975). Pulsar glitches and restlessness as a hard superfluidity phenomenon. *Nature*, 256:25–27.

Andersson, N. (1998). A New Class of Unstable Modes of Rotating Relativistic Stars. *The Astrophysical Journal*, 502:708–713.

Andersson, N., Glampedakis, K., Ho, W. C. G., and Espinoza, C. M. (2012). Pulsar Glitches: The Crust is not Enough. *Physical Review Letters*, 109(24):241103.

Andersson, N., Antonopoulou, D., Espinoza, C. M., Haskell, B., and Ho, W. C. G. (2018). The Enigmatic Spin Evolution of PSR J0537-6910: r-modes, Gravitational Waves, and the Case for Continued Timing. *The Astrophysical Journal*, 864:137.

Andersson, N. (2019). *Gravitational-Wave Astronomy: Exploring the Dark Side of the Universe*. Oxford Graduate Texts. Oxford University Press. ISBN 9780198568032

Antonopoulou, D., Weltevrede, P., Espinoza, C. M., Watts, A. L., Johnston, S., Shannon, R. M., and Kerr, M. (2015). The unusual glitch recoveries of the high-magnetic-field pulsar J1119-6127. *Monthly Notices of the Royal Astronomical Society*, 447(4):3924–3935.

Antonopoulou, D., Espinoza, C. M., Kuiper, L., and Andersson, N. (2018). Pulsar spin-down: the glitch-dominated rotation of PSR J0537-6910. *Monthly Notices of the Royal Astronomical Society*, 473:1644–1655.

Archibald, R. F., Kaspi, V. M., Ng, C. Y., Gourgouliatos, K. N., Tsang, D., Scholz, P., Beardmore, A. P., Gehrels, N., and Kennea, J. A. (2013). An anti-glitch in a magnetar. *Nature*, 497(7451):591–593.

Arzoumanian, Z., Nice, D. J., Taylor, J. H., and Thorsett, S. E. (1994). Timing behavior of 96 radio pulsars. *The Astrophysical Journal*, 422:671–680.

Ashton, G., Lasky, P. D., Graber, V., and Palfreyman, J. (2019). Rotational evolution of the Vela pulsar during the 2016 glitch. *Nature Astronomy*, 3:1143–1148.

Baade, W. and Zwicky, F. (1934). Cosmic Rays from Super-novae. *Proceedings of the National Academy of Science*, 20:259–263.

Baiko, D. A. and Chugunov, A. I. (2018). Breaking properties of neutron star crust. *Monthly Notices of the Royal Astronomical Society*, 480(4):5511–5516.

Basu, A., Joshi, B. C., Krishnakumar, M. A., Bhattacharya, D., Nandi, R., Bandhopadhay, D., Char, P., and Manoharan, P. K. (2020). Observed glitches in eight young pulsars. *Monthly Notices of the Royal Astronomical Society*, 491(3):3182–3191.

Baym, G. and Pines, D. (1971). Neutron starquakes and pulsar speedup. *Annals of Physics*, 66:816–835.

Baym, G., Pethick, C., and Pines, D. (1969)a. Superfluidity in Neutron Stars. *Nature*, 224(5220):673–674.

Baym, G., Pethick, C., Pines, D., and Ruderman, M. (1969)b. Spin Up in Neutron Stars : The Future of the Vela Pulsar. *Nature*, 224(5222):872–874.

Bennett, M. F., van Eysden, C. A., and Melatos, A. (2010). Continuous-wave gravitational radiation from pulsar glitch recovery. *Monthly Notices of the Royal Astronomical Society*, 409(4):1705–1718.

Bonazzola, S. and Gourgoulhon, E. (1996). Gravitational waves from pulsars: emission by the magnetic-field-induced distortion. *Astronomy & Astrophysics*, 312:675–690

Boynton, P. E., Groth, E. J., Hutchinson, D. P., Nanos, Jr., G. P., Partridge, R. B., and Wilkinson, D. T. (1972). Optical Timing of the Crab Pulsar, NP 0532. *The Astrophysical Journal*, 175:217.

Burke, W. L. (1971). Gravitational radiation damping of slowly moving systems calculated using matched asymptotic expansions. *Journal of Mathematical Physics*, 12: 401–418.

Burke, W. L. *The coupling of gravitational radiation to nonrelativistic sources*. PhD thesis, California Institute of Technology, (1969)

Chadwick, J. (1932). The Existence of a Neutron. *Proceedings of the Royal Society of London Series A*, 136:692–708.

Chandrasekhar, S. (1964). A General Variational Principle Governing the Radial and the Non-Radial Oscillations of Gaseous Masses. *The Astrophysical Journal*, 139:664.

Chandrasekhar, S. (1969). *Ellipsoidal Figures of Equilibrium*. Yale University Press

Chandrasekhar, S. (1970). Solutions of Two Problems in the Theory of Gravitational Radiation. *Physical Review Letters*, 24(11):611–615.

Chandrasekhar, S. and Lebovitz, N. R. (1962). On the Oscillations and the Stability of Rotating Gaseous Masses. *The Astrophysical Journal*, 135:248.

Chandrasekhar, S. (1961). *Hydrodynamic and hydromagnetic stability*. Clarendon Press

Chau, W.-Y. (1967). Gravitational Radiation from Neutron Stars. *The Astrophysical Journal*, 147:664.

Cheng, K. S. (1987)a. Outer Magnetospheric Fluctuations and Pulsar Timing Noise. *The Astrophysical Journal*, 321:799.

Cheng, K. S. (1987)b. Could Glitches Inducing Magnetospheric Fluctuations Produce Low-Frequency Pulsar Timing Noise? *The Astrophysical Journal*, 321:805.

Cheng, K. S., Alpar, M. A., Pines, D., and Shaham, J. (1988). Spontaneous superfluid unpinning and the inhomogeneous distribution of vortex lines in neutron stars. *The Astrophysical Journal*, 330:835–846.

Clement, M. J. (1964). A General Variational Principle Governing the Oscillations of a Rotating Gaseous Mass. *The Astrophysical Journal*, 140:1045.

Cognard, I. and Backer, D. C. (2004). A Microglitch in the Millisecond Pulsar PSR B1821-24 in M28. *The Astrophysical Journal Letters*, 612(2):L125–L127.

Coles, W., Hobbs, G., Champion, D. J., Manchester, R. N., and Verbiest, J. P. W. (2011). Pulsar timing analysis in the presence of correlated noise. *Monthly Notices of the Royal Astronomical Society*, 418(1):561–570.

Comins, N. (1979). On secular instabilities of rigidly rotating stars in general relativity - I. Theoretical formalism. *Monthly Notices of the Royal Astronomical Society*, 189:233–253.

Cordes, J. M. and Downs, G. S. (1985). JPL pulsar timing observations. III - Pulsar rotation fluctuations. *The Astrophysical Journal Supplement Series*, 59:343–382.

Cordes, J. M. and Helfand, D. J. (1980). Pulsar timing. III - Timing noise of 50 pulsars. *The Astrophysical Journal*, 239:640–650.

Cordes, J. M., Downs, G. S., and Krause-Polstorff, J. (1988). JPL pulsar timing observations. V - MACRO and microjumps in the VELA pulsar 0833-45. *The Astrophysical Journal*, 330:847–869.

Crawford, F. and Demiański, M. (2003). A Comparison of Measured Crab and Vela Glitch Healing Parameters with Predictions of Neutron Star Models. *The Astrophysical Journal*, 595:1052–1057.

Cromartie, H. T., Fonseca, E., Ransom, S. M., Demorest, P. B., Arzoumanian, Z., Blumer, H., Brook, P. R., DeCesar, M. E., Dolch, T., Ellis, J. A., Ferdman, R. D., Ferrara, E. C., Garver-Daniels, N., Gentile, P. A., Jones, M. L., Lam, M. T., Lorimer, D. R., Lynch, R. S., McLaughlin, M. A., Ng, C., Nice, D. J., Pennucci, T. T., Spiewak, R., Stairs, I. H., Stovall, K., Swiggum, J. K., and Zhu, W. W. (2020). Relativistic Shapiro delay measurements of an extremely massive millisecond pulsar. *Nature Astronomy*, 4:72–76.

Detweiler, S. L. (1975). A variational calculation of the fundamental frequencies of quadrupole pulsation of fluid spheres in general relativity. *The Astrophysical Journal*, 197:203–217.

Dodson, R., Lewis, D., and McCulloch, P. (2007). Two decades of pulsar timing of Vela. *Astrophysics and Space Science*, 308(1-4):585–589.

Downs, G. S. (1981). JPL pulsar timing observations. I. The VELA pulsar. *The Astrophysical Journal*, 249:687–697.

Dreissigacker, C., Prix, R., and Wette, K. (2018). Fast and accurate sensitivity estimation for continuous-gravitational-wave searches. *Physical Review D*, 98(8):084058.

Edwards, R. T., Hobbs, G. B., and Manchester, R. N. (2006). TEMPO2, a new pulsar timing package - II. The timing model and precision estimates. *Monthly Notices of the Royal Astronomical Society*, 372(4):1549–1574.

Espinoza, C. M., Lyne, A. G., Stappers, B. W., and Kramer, M. (2011). A study of 315 glitches in the rotation of 102 pulsars. *Monthly Notices of the Royal Astronomical Society*, 414:1679–1704.

Espinoza, C. M., Antonopoulou, D., Stappers, B. W., Watts, A., and Lyne, A. G. (2014). Neutron star glitches have a substantial minimum size. *Monthly Notices of the Royal Astronomical Society*, 440:2755–2762.

Espinoza, C. M., Antonopoulou, D., Dodson, R., Stepanova, M., and Scherer, A. (2021). Small glitches and other rotational irregularities of the Vela pulsar. *Astronomy & Astrophysics*, 647:A25.

Ferdman, R. D., Archibald, R. F., Gourgouliatos, K. N., and Kaspi, V. M. (2018). The Glitches and Rotational History of the Highly Energetic Young Pulsar PSR J0537-6910. *The Astrophysical Journal*, 852(2):123.

Fesik, L. and Papa, M. A. (2020). First Search for r-mode Gravitational Waves from PSR J0537-6910. *The Astrophysical Journal*, 895(1):11.

Flanagan, C. S. (1990). Rapid recovery of the Vela pulsar from a giant glitch. *Nature*, 345(6274):416–417.

Fonseca, E., Cromartie, H. T., Pennucci, T. T., Ray, P. S., Kirichenko, A. Y., Ransom, S. M., Demorest, P. B., Stairs, I. H., Arzoumanian, Z., Guillemot, L., Parthasarathy, A., Kerr, M., Cognard, I., Baker, P. T., Blumer, H., Brook, P. R., DeCesar, M., Dolch, T., Dong, F. A., Ferrara, E. C., Fiore, W., Garver-Daniels, N., Good, D. C., Jennings, R., Jones, M. L., Kaspi, V. M., Lam, M. T., Lorimer, D. R., Luo, J., McEwen, A., McKee, J. W., McLaughlin, M. A., McMann, N., Meyers, B. W., Naidu, A., Ng, C., Nice, D. J., Pol, N., Radovan, H. A., Shapiro-Albert, B., Tan, C. M., Tendulkar, S. P., Swiggum, J. K., Wahl, H. M., and Zhu, W. W. (2021). Refined Mass and Geometric Measurements of the High-mass PSR J0740+6620. *The Astrophysical Journal Letters*, 915(1):L12.

Franco, L. M., Link, B., and Epstein, R. I. (2000). Quaking Neutron Stars. *The Astrophysical Journal*, 543(2):987–994.

Freise, A., Chelkowski, S., Hild, S., Del Pozzo, W., Perreca, A., and Vecchio, A. (2009). Triple Michelson interferometer for a third-generation gravitational wave detector. *Classical and Quantum Gravity*, 26(8):085012.

Friedman, J. L. and Schutz, B. F. (1978)a. Lagrangian perturbation theory of nonrelativistic fluids. *The Astrophysical Journal*, 221:937–957.

Friedman, J. L. and Schutz, B. F. (1978)b. Secular instability of rotating Newtonian stars. *The Astrophysical Journal*, 222:281–296.

Fuentes, J. R., Espinoza, C. M., and Reisenegger, A. (2019). Glitch time series and size distributions in eight prolific pulsars. *Astronomy & Astrophysics*, 630:A115.

Gavriil, F. P., Dib, R., and Kaspi, V. M. (2011). The 2006-2007 Active Phase of Anomalous X-ray Pulsar 4U 0142+61: Radiative and Timing Changes, Bursts, and Burst Spectral Features. *The Astrophysical Journal*, 736(2):138.

Ge, M. Y., Zhang, S. N., Lu, F. J., Li, T. P., Yuan, J. P., Zheng, X. P., Huang, Y., Zheng, S. J., Chen, Y. P., Chang, Z., Tuo, Y. L., Cheng, Q., Güngör, C., Song, L. M., Xu, Y. P., Cao, X. L., Chen, Y., Liu, C. Z., Zhang, S., Qu, J. L., Bu, Q. C., Cai, C., Chen, G., Chen, L., Chen, M. Z., Chen, T. X., Chen, Y. B., Cui, W., Cui, W. W., Deng, J. K., Dong, Y. W., Du, Y. Y., Fu, M. X., Gao, G. H., Gao, H., Gao, M., Gu, Y. D., Guan, J., Guo, C. C., Han, D. W., Hao, L. F., Huo, J., Jia, S. M., Jiang, L. H., Jiang, W. C., Jin, C. J., Jin, J., Jin, Y. J., Kong, L. D., Li, B., Li, D., Li, C. K., Li, G., Li, M. S., Li, W., Li, X., Li, X. B., Li, X. F., Li, Y. G., Li, Z. W., Li, Z. X., Liu, Z. Y., Liang, X. H., Liao, J. Y., Liu, G. Q., Liu, H. W., Liu, X. J., Liu, Y. N., Lu, B., Lu, X. F., Luo, Q., Luo, T., Ma, X., Meng, B., Nang, Y., Nie, J. Y., Ou, G., Sai, N., Shang, R. C., Song, X. Y., Sun, L., Tan, Y., Tao, L., Wang, C., Wang, G. F., Wang, J., Wang, J. B., Wang, M., Wang, N., Wang, W. S., Wang, Y. D., Wang, Y. S., Wen, X. Y., Wen, Z. G., Wu, B. B., Wu, B. Y., Wu, M., Xiao, G. C., Xiao, S., Xiong, S. L.,

Xu, Y. H., Yan, W. M., Yang, J. W., Yang, S., Yang, Y. J., Yang, Y. J., Yi, Q. B., Yin, Q. Q., You, Y., Yue, Y. L., Zhang, A. M., Zhang, C. M., Zhang, D. P., Zhang, F., Zhang, H. M., Zhang, J., Zhang, T., Zhang, W. C., Zhang, W., Zhang, W. Z., Zhang, Y., Zhang, Y. F., Zhang, Y. J., Zhang, Y., Zhang, Z., Zhang, Z., Zhang, Z. L., Zhao, H. S., Zhao, X. F., Zheng, W., Zhou, D. K., Zhou, J. F., Zhou, X., Zhuang, R. L., Zhu, Y. X., and Zhu, Y. (2020). Discovery of Delayed Spin-up Behavior Following Two Large Glitches in the Crab Pulsar, and the Statistics of Such Processes. *The Astrophysical Journal*, 896(1):55.

Gittins, F., Andersson, N., and Jones, D. I. (2021). Modelling neutron star mountains. *Monthly Notices of the Royal Astronomical Society*, 500(4):5570–5582.

Gold, T. (1968). Rotating neutron stars as the origin of the pulsating radio sources. *Nature*, 218:731–732.

Goldreich, P. and Julian, W. H. (1969). Pulsar Electrodynamics. *The Astrophysical Journal*, 157:869.

Graber, V., Andersson, N., and Hogg, M. (2017). Neutron stars in the laboratory. *International Journal of Modern Physics D*, 26(8):1730015-347.

Griffiths, D. J. (2013). *Introduction to Electrodynamics*. Pearson. 4th edition. ISBN 9780321856562

Groth, E. J. (1975). Timing of the Crab Pulsar III. The Slowing Down and the Nature of the Random Process. *The Astrophysical Journal Supplement Series*, 29.

Groth, III, E. J. *Absolute Timing of the Crab Nebula Pulsar, NPO532.* PhD thesis, Princeton University., (1971)

Gügercinoğlu, E. and Alpar, M. A. (2020). The 2016 Vela glitch: a key to neutron star internal structure and dynamics. *Monthly Notices of the Royal Astronomical Society*, 496 (2):2506–2515.

Gügercinoğlu, E. and Alpar, M. A. (2019). The largest Crab glitch and the vortex creep model. *Monthly Notices of the Royal Astronomical Society*, 488(2):2275–2282.

Harding, A. K., Muslimov, A. G., and Zhang, B. (2002). Regimes of Pulsar Pair Formation and Particle Energetics. *The Astrophysical Journal*, 576:366–375.

Haskell, B. and Melatos, A. (2015). Models of pulsar glitches. *International Journal of Modern Physics D*, 24:1530008.

Haskell, B., Pizzochero, P. M., and Sidery, T. (2012). Modelling pulsar glitches with realistic pinning forces: a hydrodynamical approach. *Monthly Notices of the Royal Astronomical Society*, 420(1):658–671.

Hessels, J. W. T., Ransom, S. M., Stairs, I. H., Freire, P. C. C., Kaspi, V. M., and Camilo, F. (2006). A Radio Pulsar Spinning at 716 Hz. *Science*, 311:1901–1904.

Hewish, A., Bell, S. J., Pilkington, J. D. H., Scott, P. F., and Collins, R. A. (1968). Observation of a rapidly pulsating radio source. *Nature*, 217:709–713.

Hild, S., Abernathy, M., Acernese, F., Amaro-Seoane, P., Andersson, N., Arun, K., Barone, F., and et al. (2011). Sensitivity studies for third-generation gravitational wave observatories. *Classical and Quantum Gravity*, 28(9):094013.

Ho, W. C. G., Espinoza, C. M., Arzoumanian, Z., Enoto, T., Tamba, T., Antonopoulou, D., Bejger, M., Guillot, S., Haskell, B., and Ray, P. S. (2020)a. Return of the Big Glitcher: NICER timing and glitches of PSR J0537-6910. *Monthly Notices of the Royal Astronomical Society*, 498(4):4605–4614.

Ho, W. C. G., Jones, D. I., Andersson, N., and Espinoza, C. M. (2020)b. Gravitational waves from transient neutron star f -mode oscillations. *Physical Review D*, 101(10): 103009.

Hobbs, G., Lyne, A. G., Kramer, M., Martin, C. E., and Jordan, C. (2004). Long-term timing observations of 374 pulsars. *Monthly Notices of the Royal Astronomical Society*, 353:1311–1344.

Hobbs, G., Lyne, A. G., and Kramer, M. (2010). An analysis of the timing irregularities for 366 pulsars. *Monthly Notices of the Royal Astronomical Society*, 402:1027–1048.

Hobbs, G. B., Edwards, R. T., and Manchester, R. N. (2006). TEMPO2, a new pulsar-timing package - I. An overview. *Monthly Notices of the Royal Astronomical Society*, 369:655–672.

Horowitz, C. J. and Kadau, K. (2009). Breaking Strain of Neutron Star Crust and Gravitational Waves. *Physical Review Letters*, 102(19):191102.

Howitt, G., Melatos, A., and Delaigle, A. (2018). Nonparametric Estimation of the Size and Waiting Time Distributions of Pulsar Glitches. *The Astrophysical Journal*, 867(1): 60.

Ipser, J. R. and Lindblom, L. (1991). The Oscillations of Rapidly Rotating Newtonian Stellar Models. II. Dissipative Effects. *The Astrophysical Journal*, 373:213.

Janssen, G. H. and Stappers, B. W. (2006). 30 glitches in slow pulsars. *Astronomy & Astrophysics*, 457:611–618.

Jaranowski, P., Królak, A., and Schutz, B. F. (1998). Data analysis of gravitational-wave signals from spinning neutron stars: The signal and its detection. *Physical Review D*, 58(6):063001.

Johnson-McDaniel, N. K. and Owen, B. J. (2013). Maximum elastic deformations of relativistic stars. *Physical Review D*, 88(4):044004.

Jones, D. I. (2010). Gravitational wave emission from rotating superfluid neutron stars. *Monthly Notices of the Royal Astronomical Society*, 402(4):2503–2519.

Jones, D. I. (2012). Pulsar state switching, timing noise and free precession. *Monthly Notices of the Royal Astronomical Society*, 420(3):2325–2338.

Jones, D. I. and Andersson, N. (2002). Gravitational waves from freely precessing neutron stars. *Monthly Notices of the Royal Astronomical Society*, 331(1):203–220.

Jones, P. B. (1990). The generation of timing noise by superfluid rotation in pulsars. *Monthly Notices of the Royal Astronomical Society*, 246:364

Jones, P. B. (1991). Rotation of the Neutron-Drip Superfluid in Pulsars: The Interaction and Pinning of Vortices. *The Astrophysical Journal*, 373:208.

Kashiyama, K. and Ioka, K. (2011). Magnetar asteroseismology with long-term gravitational waves. *Physical Review D*, 83(8):081302.

Kaspi, V. M. and Beloborodov, A. M. (2017). Magnetars. *Annual Review of Astronomy and Astrophysics*, 55:261–301.

Keer, L. and Jones, D. I. (2015). Developing a model for neutron star oscillations following starquakes. *Monthly Notices of the Royal Astronomical Society*, 446:865–891.

Keitel, D., Woan, G., Pitkin, M., Schumacher, C., Pearlstone, B., Riles, K., Lyne, A. G., Palfreyman, J., Stappers, B., and Weltevrede, P. (2019). First search for long-duration transient gravitational waves after glitches in the Vela and Crab pulsars. *Physical Review D*, 100(6):064058.

Klimenko, S., Vedovato, G., Drago, M., Salemi, F., Tiwari, V., Prodi, G. A., Lazzaro, C., Ackley, K., Tiwari, S., Da Silva, C. F., and Mitselmakher, G. (2016). Method for detection and reconstruction of gravitational wave transients with networks of advanced detectors. *Physical Review D*, 93(4):042004.

Large, M. I., Vaughan, A. E., and Mills, B. Y. (1968). A Pulsar Supernova Association? *Nature*, 220:340–341.

Lentati, L., Alexander, P., Hobson, M. P., Feroz, F., van Haasteren, R., Lee, K. J., and Shannon, R. M. (2014). TEMPONEST: a Bayesian approach to pulsar timing analysis. *Monthly Notices of the Royal Astronomical Society*, 437(3):3004–3023.

Lindblom, L., Owen, B. J., and Morsink, S. M. (1998). Gravitational Radiation Instability in Hot Young Neutron Stars. *Physical Review Letters*, 80(22):4843–4846.

Link, B. (2014). Thermally Activated Post-glitch Response of the Neutron Star Inner Crust and Core. I. Theory. *The Astrophysical Journal*, 789(2):141.

Link, B., Epstein, R. I., and Baym, G. (1992). Postglitch Behavior of the Crab Pulsar: Evidence for External Torque Variations. *The Astrophysical Journal Letters*, 390:L21.

Link, B., Franco, L. M., and Epstein, R. I. (1998). Starquake-induced Magnetic Field and Torque Evolution in Neutron Stars. *The Astrophysical Journal*, 508(2):838–843.

Link, B., Epstein, R. I., and Lattimer, J. M. (1999). Pulsar Constraints on Neutron Star Structure and Equation of State. *Physical Review Letters*, 83(17):3362–3365.

Livingstone, M. A., Kaspi, V. M., and Gavriil, F. P. (2010). Timing Behavior of the Magnetically Active Rotation-Powered Pulsar in the Supernova Remnant Kesteven 75. *The Astrophysical Journal*, 710(2):1710–1717.

Lower, M. E., Bailes, M., Shannon, R. M., Johnston, S., Flynn, C., Osłowski, S., Gupta, V., Farah, W., Bateman, T., Green, A. J., Hunstead, R., Jameson, A., Jankowski, F., Parthasarathy, A., Price, D. C., Sutherland , A., Temby, D., and Venkatraman Krishnan, V. (2020). The UTMOST pulsar timing programme - II. Timing noise across the pulsar population. *Monthly Notices of the Royal Astronomical Society*, 494(1):228–245.

Lynden-Bell, D. and Ostriker, J. P. (1967). On the stability of differentially rotating bodies. *Monthly Notices of the Royal Astronomical Society*, 136:293.

Lyne, A., Hobbs, G., Kramer, M., Stairs, I., and Stappers, B. (2010). Switched Magnetospheric Regulation of Pulsar Spin-Down. *Science*, 329:408.

Lyne, A. G., Pritchard, R. S., and Graham-Smith, F. (1993). Twenty-Three Years of Crab Pulsar Rotational History. *Monthly Notices of the Royal Astronomical Society*, 265:1003.

Lyne, A. G., Pritchard, R. S., Graham-Smith, F., and Camilo, F. (1996). Very low braking index for the Vela pulsar. *Nature*, 381(6582):497–498.

Lyne, A. G., Shemar, S. L., and Smith, F. G. (2000). Statistical studies of pulsar glitches. *Monthly Notices of the Royal Astronomical Society*, 315:534–542.

Lyne, A. G., Jordan, C. A., Graham-Smith, F., Espinoza, C. M., Stappers, B. W., and Weltevrede, P. (2015). 45 years of rotation of the Crab pulsar. *Monthly Notices of the Royal Astronomical Society*, 446:857–864.

Maggiore, M., Van Den Broeck, C., Bartolo, N., Belgacem, E., Bertacca, D., Bizouard, M. A., Branchesi, M., Clesse, S., Foffa, S., García-Bellido, J., Grimm, S., Harms, J., Hinderer, T., Matarrese, S., Palomba, C., Peloso, M., Ricciardone, A., and Sakellariadou, M. (2020). Science case for the Einstein telescope. *Journal of Cosmology and Astroparticle Physics*, 2020(3):050.

Manchester, R. N., Hobbs, G. B., Teoh, A., and Hobbs, M. (2005). The Australia Telescope National Facility Pulsar Catalogue. *The Astronomical Journal*, 129:1993–2006.

Marshall, F. E., Gotthelf, E. V., Zhang, W., Middleditch, J., and Wang, Q. D. (1998). Discovery of an Ultrafast X-Ray Pulsar in the Supernova Remnant N157B. *The Astrophysical Journal Letters*, 499(2):L179–L182.

Matsakis, D. N., Taylor, J. H., and Eubanks, T. M. (1997). A statistic for describing pulsar and clock stabilities. *Astronomy & Astrophysics*, 326:924–928

McCulloch, P. M., Klekociuk, A. R., Hamilton, P. A., and Royle, G. W. R. (1987). Daily observations of three period jumps of the VELA pulsar. *Australian Journal of Physics*, 40:725–730.

McCulloch, P. M., Hamilton, P. A., McConnell, D., and King, E. A. (1990). The Vela glitch of Christmas 1988. *Nature*, 346(6287):822–824.

McKee, J. W., Janssen, G. H., Stappers, B. W., Lyne, A. G., Caballero, R. N., Lentati, L., Desvignes, G., Jessner, A., Jordan, C. A., Karuppusamy, R., Kramer, M., Cognard, I., Champion, D. J., Graikou, E., Lazarus, P., Osłowski, S., Perrodin, D., Shaifullah, G., Tiburzi, C., and Verbiest, J. P. W. (2016). A glitch in the millisecond pulsar J0613-0200. *Monthly Notices of the Royal Astronomical Society*, 461(3):2809–2817.

Melatos, A., Peralta, C., and Wyithe, J. S. B. (2008). Avalanche Dynamics of Radio Pulsar Glitches. *The Astrophysical Journal*, 672:1103–1118.

Melatos, A. and Link, B. (2014). Pulsar timing noise from superfluid turbulence. *Monthly Notices of the Royal Astronomical Society*, 437(1):21–31.

Mignani, R. P. (2011). Optical, ultraviolet, and infrared observations of isolated neutron stars. *Advances in Space Research*, 47(8):1281–1293.

Miller, M. C., Lamb, F. K., Dittmann, A. J., Bogdanov, S., Arzoumanian, Z., Gendreau, K. C., Guillot, S., Ho, W. C. G., Lattimer, J. M., Loewenstein, M., Morsink, S. M., Ray, P. S., Wolff, M. T., Baker, C. L., Cazeau, T., Manthripragada, S., Markwardt, C. B., Okajima, T., Pollard, S., Cognard, I., Cromartie, H. T., Fonseca, E., Guillemot, L., Kerr, M., Parthasarathy, A., Pennucci, T. T., Ransom, S., and Stairs, I. (2021). The Radius of PSR J0740+6620 from NICER and XMM-Newton Data. *arXiv e-prints*, art. arXiv:2105.06979

Misner, C. W., Thorne, K. S., and Wheeler, J. A. (1973). *Gravitation*. W.H. Freeman and Co.

Namkham, N., Jaroenjittichai, P., and Johnston, S. (2019). Diagnostics of timing noise in middle-aged pulsars. *Monthly Notices of the Royal Astronomical Society*, 487(4):5854–5861.

Owen, B. J. (2010). How to adapt broad-band gravitational-wave searches for r-modes. *Physical Review D*, 82(10):104002.

Owen, B. J., Lindblom, L., Cutler, C., Schutz, B. F., Vecchio, A., and Andersson, N. (1998). Gravitational waves from hot young rapidly rotating neutron stars. *Physical Review D*, 58(8):084020.

Özel, F. and Freire, P. (2016). Masses, Radii, and the Equation of State of Neutron Stars. *Annual Review of Astronomy and Astrophysics*, 54:401–440.

Pacini, F. (1967). Energy emission from a neutron star. *Nature*, 216:567–568.

Pacini, F. (1968). Rotating Neutron Stars, Pulsars and Supernova Remnants. *Nature*, 219:145–146.

Palfreyman, J., Dickey, J. M., Hotan, A., Ellingsen, S., and van Straten, W. (2018). Alteration of the magnetosphere of the Vela pulsar during a glitch. *Nature*, 556(7700): 219–222.

Parthasarathy, A., Shannon, R. M., Johnston, S., Lentati, L., Bailes, M., Dai, S., Kerr, M., Manchester, R. N., Osłowski, S., Sobey, C., van Straten, W., and Weltevrede, P. (2019). Timing of young radio pulsars - I. Timing noise, periodic modulation, and proper motion. *Monthly Notices of the Royal Astronomical Society*, 489(3):3810–3826.

Pitkin, M. (2018). psrqpy: a python interface for querying the ATNF pulsar catalogue. *The Journal of Open Source Software*, 3(22):538.

Prix, R., Giampanis, S., and Messenger, C. (2011). Search method for long-duration gravitational-wave transients from neutron stars. *Physical Review D*, 84(2):023007.

Radhakrishnan, V. and Manchester, R. N. (1969). Detection of a Change of State in the Pulsar PSR 0833-45. *Nature*, 222:228–229.

Ravenhall, D. G. and Pethick, C. J. (1994). Neutron Star Moments of Inertia. *The Astrophysical Journal*, 424:846.

Rayleigh, J. (1945). *The Theory of Sound*, volume 2. Dover Publications. ISBN 9780486602936. §364

Reichley, P. E. and Downs, G. S. (1969). Observed Decrease in the Periods of Pulsar PSR 0833-45. *Nature*, 222:229–230.

Richards, D. W. and Comella, J. M. (1969). The Period of Pulsar NP 0532. *Nature*, 222: 551–552.

Riley, T. E., Watts, A. L., Ray, P. S., Bogdanov, S., Guillot, S., Morsink, S. M., Bilous, A. V., Arzoumanian, Z., Choudhury, D., Deneva, J. S., Gendreau, K. C., Harding, A. K., Ho, W. C. G., Lattimer, J. M., Loewenstein, M., Ludlam, R. M., Markwardt, C. B., Okajima, T., Prescod-Weinstein, C., Remillard, R. A., Wolff, M. T., Fonseca, E., Cromartie, H. T., Kerr, M., Pennucci, T. T., Parthasarathy, A., Ransom, S., Stairs, I., Guillemot, L., and Cognard, I. (2021). A NICER View of the Massive Pulsar PSR J0740+6620 Informed by Radio Timing and XMM-Newton Spectroscopy. *arXiv e-prints*, art. arXiv:2105.06980

Ruderman, M. (1969). Neutron starquakes and pulsar periods. *Nature*, 223:597 – 598

Sathyaprakash, B., Abernathy, M., Acernese, F., Ajith, P., Allen, B., Amaro-Seoane, P., Andersson, N., Aoudia, S., Arun, K., Astone, P., Krishnan, B., Barack, L., Barone, F., Barr, B., Barsuglia, M., Bassan, M., Bassiri, R., Beker, M., Beveridge, N., Bizouard, M., Bond, C., Bose, S., Bosi, L., Braccini, S., Bradaschia, C., Britzger, M., Brueckner, F., Bulik, T., Bulten, H. J., Burmeister, O., Calloni, E., Campsie, P., Carbone, L., Cella, G., Chalkley, E., Chassande-Mottin, E., Chelkowski, S., Chincarini, A., Di Cintio, A., Clark, J., Coccia, E., Colacino, C. N., Colas, J., Colla, A., Corsi, A., Cumming, A., Cunningham, L., Cuoco, E., Danilishin, S., Danzmann, K., Daw, E., De Salvo, R., Del Pozzo, W., Dent, T., De Rosa, R., Di Fiore, L., Emilio, M. D. P., Di Virgilio, A., Dietz, A., Doets, M., Dueck, J., Edwards, M., Fafone, V., Fairhurst, S., Falferi, P., Favata, M., Ferrari, V., Ferrini, F., Fidecaro, F., Flaminio, R., Franc, J., Frasconi, F., Freise, A., Friedrich, D., Fulda, P., Gair, J., Galimberti, M., Gemme, G., Genin, E., Gennai, A., Giazotto, A., Glampedakis, K., Gossan, S., Gouaty, R., Graef, C., Graham, W., Granata, M., Grote, H., Guidi, G., Hallam, J., Hammond, G., Hannam, M., Harms, J., Haughian, K., Hawke, I., Heinert, D., Hendry, M., Heng, I., Hennes, E., Hild, S., Hough, J., Huet, D., Husa, S., Huttner, S., Iyer, B., Jones, D. I., Jones, G., Kamaretsos, I., Kant Mishra, C., Kawazoe, F., Khalili, F., Kley, B., Kokeyama, K., Kokkotas, K., Kroker, S., Kumar, R., Kuroda, K., Lagrange, B., Lastzka, N., Li, T. G. F., Lorenzini, M., Losurdo, G., Lück, H., Majorana, E., Malvezzi, V., Mandel, I., Mandic, V., Marka, S., Marin, F., Marion, F., Marque, J., Martin, I., McLeod, D., Mckechan, D., Mehmet, M., Michel, C., Minenkov, Y., Morgado, N., Morgia, A., Mosca, S., Moscatelli, L., Mours, B., Müller-Ebhardt, H., Murray, P., Naticchioni, L., Nawrodt, R., Nelson, J., O' Shaughnessy, R., Ott, C. D., Palomba, C., Paoli, A., Parguez, G., Pasqualetti, A., Passaquieti, R., Passuello, D., Perciballi, M., Piergiovanni, F., Pinard, L., Pitkin, M., Plastino, W., Plissi, M., Poggiani, R., Popolizio, P., Porter, E., Prato, M., Prodi, G., Punturo, M., Puppo, P., Rabeling, D., Racz, I., Rapagnani, P., Re, V., Read, J., Regimbau, T., Rehbein, H., Reid, S., Ricci, F., Richard, F., Robinson, C., Rocchi, A., Romano, R., Rowan, S., Rüdiger, A., Samblowski, A., Santamaría, L., Sassolas, B., Schilling, R., Schmidt, P., Schnabel, R., Schutz, B., Schwarz, C., Scott, J., Seidel, P., Sintes, A. M., Somiya, K., Sopuerta, C. F., Sorazu, B., Speirits, F., Storchi, L., Strain, K., Strigin, S., Sutton, P., Tarabrin, S., Taylor, B., Thürin, A., Tokmakov, K., Tonelli, M., Tournefier, H., Vaccarone, R., Vahlbruch, H., van den Brand, J. F. J., Van Den Broeck, C., van der Putten, S., van Veggel, M., Vecchio, A., Veitch, J., Vetrano, F., Vicere, A., Vyatchanin, S., Weßels, P., Willke, B., Winkler, W., Woan, G., Woodcraft, A., and Yamamoto, K. (2012). Scientific objectives of Einstein Telescope. *Classical and Quantum Gravity*, 29(12):124013.

Schutz, B. F. (1985). *A First Course in General Relativity*. Cambridge University Press

Schutz, B. F. (1989). Gravitational wave sources and their detectability. *Classical and Quantum Gravity*, 6:1761–1780.

Schutz, B. F. and Sorkin, R. (1977). Variational aspects of relativistic field theories, with application to perfect fluids. *Annals of Physics*, 107:1–43.

Shannon, R. M., Lentati, L. T., Kerr, M., Johnston, S., Hobbs, G., and Manchester, R. N. (2016). Characterizing the rotational irregularities of the Vela pulsar from 21 yr of phase-coherent timing. *Monthly Notices of the Royal Astronomical Society*, 459(3):3104–3111.

Shapiro, S. L. and Teukolsky, S. A. (1983). *Black holes, white dwarfs, and neutron stars: The physics of compact objects*. Wiley-Interscience

Shaw, B., Lyne, A. G., Stappers, B. W., Weltevrede, P., Bassa, C. G., Lien, A. Y., Mickaliger, M. B., Breton, R. P., Jordan, C. A., Keith, M. J., and Krimm, H. A. (2018). The largest glitch observed in the Crab pulsar. *Monthly Notices of the Royal Astronomical Society*, 478:3832–3840.

Shemar, S. L. and Lyne, A. G. (1996). Observations of pulsar glitches. *Monthly Notices of the Royal Astronomical Society*, 282:677–690.

Singh, A. (2017). Gravitational wave transient signal emission via Ekman pumping in neutron stars during post-glitch relaxation phase. *Physical Review D*, 95(2):024022.

Smartt, S. J. (2009). Progenitors of Core-Collapse Supernovae. *Annual Review of Astronomy and Astrophysics*, 47:63–106.

Staelin, D. H. and Reifenstein, III, E. C. (1968). Pulsating Radio Sources near the Crab Nebula. *Science*, 162:1481–1483.

Strohmayer, T., Ogata, S., Iyetomi, H., Ichimaru, S., and van Horn, H. M. (1991). The shear modulus of the neutron star crust and nonradial oscillations of neutron stars. *The Astrophysical Journal*, 375:679–686.

Tan, C. M., Bassa, C. G., Cooper, S., Dijkema, T. J., Esposito, P., Hessels, J. W. T., Kondratiev, V. I., Kramer, M., Michilli, D., Sanidas, S., Shimwell, T. W., Stappers, B. W., van Leeuwen, J., Cognard, I., Grießmeier, J. M., Karastergiou, A., Keane, E. F., Sobey, C., and Weltevrede, P. (2018). LOFAR Discovery of a 23.5 s Radio Pulsar. *The Astrophysical Journal*, 866(1):54.

The LIGO Scientific Collaboration, the Virgo Collaboration, and the KAGRA Collaboration. (2021). Search for intermediate mass black hole binaries in the third observing run of Advanced LIGO and Advanced Virgo. *arXiv e-prints*, art. arXiv:2105.15120

Thomson, W. (1863). Dynamical Problems Regarding Elastic Spheroidal Shells and Spheroids of Incompressible Liquid. *Philosophical Transactions of the Royal Society of London Series I*, 153:583–616

Thorne, K. S. (1969). Nonradial Pulsation of General-Relativistic Stellar Models.IV. The Weakfield Limit. *The Astrophysical Journal*, 158:997.

Thorne, K. S. (1980). Multipole expansions of gravitational radiation. *Reviews of Modern Physics*, 52(2):299–340.

Thorne, K. S. and Blandford, R. D. (2017). *Modern Classical Physics: Optics, Fluids, Plasmas, Elasticity, Relativity, and Statistical Physics*. Princeton University Press

Tong, H. (2014). The Anti-glitch of Magnetar 1E 2259+586 in the Wind Braking Scenario. *The Astrophysical Journal*, 784(2):86.

van Eysden, C. A. and Melatos, A. (2008). Gravitational radiation from pulsar glitches. *Classical and Quantum Gravity*, 25(22):225020.

Vivekanand, M. (2020). NICER observations of the Crab pulsar glitch of 2017 November. *Astronomy & Astrophysics*, 633:A57.

Walsh, S., Pitkin, M., Oliver, M., D'Antonio, S., Dergachev, V., Królak, A., Astone, P., Bejger, M., Di Giovanni, M., Dorosh, O., Frasca, S., Leaci, P., Mastrogiovanni, S., Miller, A., Palomba, C., Papa, M. A., Piccinni, O. J., Riles, K., Sauter, O., and Sintes, A. M. (2016). Comparison of methods for the detection of gravitational waves from unknown neutron stars. *Physical Review D*, 94(12):124010.

Wang, J., Wang, N., Tong, H., and Yuan, J. (2012). Recent glitches detected in the Crab pulsar. *Astrophysics and Space Science*, 340(2):307–315.

Wang, N., Manchester, R. N., Zhang, J., Wu, X. J., Yusup, A., Lyne, A. G., Cheng, K. S., and Chen, M. Z. (2001). Pulsar timing at Urumqi Astronomical Observatory: observing system and results. *Monthly Notices of the Royal Astronomical Society*, 328(3): 855–866.

Weltevrede, P., Johnston, S., and Espinoza, C. M. (2011). The glitch-induced identity changes of PSR J1119-6127. *Monthly Notices of the Royal Astronomical Society*, 411(3): 1917–1934.

Wong, T., Backer, D. C., and Lyne, A. G. (2001). Observations of a Series of Six Recent Glitches in the Crab Pulsar. *The Astrophysical Journal*, 548:447–459.

Xu, Y. H., Yuan, J. P., Lee, K. J., Hao, L. F., Wang, N., Wang, M., Yu, M., Li, Z. X., Yue, Y. L., Liu, Z. Y., Yuen, R., Wen, Z. G., Dang, S. J., Bai, J. M., Chen, W., Huang, Y. X., and Yan, W. M. (2019). The 2016 glitch in the Vela pulsar. *Astrophysics and Space Science*, 364:11.

Yim, G. and Jones, D. I. (2020). Transient gravitational waves from pulsar post-glitch recoveries. *Monthly Notices of the Royal Astronomical Society*.

Yim, G. and Jones, D. I. (2022). Gravitational radiation back-reaction from f-modes on neutron stars. *Monthly Notices of the Royal Astronomical Society*.

Yu, M., Manchester, R. N., Hobbs, G., Johnston, S., Kaspi, V. M., Keith, M., Lyne, A. G., Qiao, G. J., Ravi, V., Sarkissian, J. M., Shannon, R., and Xu, R. X. (2013). Detection of 107 glitches in 36 southern pulsars. *Monthly Notices of the Royal Astronomical Society*, 429:688–724.

Zhang, X., Shuai, P., Huang, L., Chen, S., and Du, Y. (2018). X-Ray Observation of the 2017 November Glitch in the Crab Pulsar. *The Astrophysical Journal*, 866(2):82.